

https://dspace.org/

Augmenting the magnetotelluric response function: an integrated geophysical approach

Harrison, Wesley

2020
https://hdl.handle.net/10539/35612

Downloaded from a DSpace repository. https://dspace.org/

AUGMENTING THE MAGNETOTELLURIC RESPONSE FUNCTION: AN INTEGRATED GEOPHYSICAL APPROACH

Wesley Harrison

A thesis submitted to the Faculty of Science, University of the Witwatersrand, Johannesburg, in fulfilment of the requirements for the degree of Doctor of Philosophy.

Johannesburg, 2020

School of Geosciences, University of the Witwatersrand



UNIVERSITY OF THE
WITWATERSRAND,
JOHANNESBURG

Declaration

I declare that this thesis is my own, unaided work. It is being submitted for the Degree of Doctor of Philosophy at the University of the Witwatersrand, Johannesburg. It has not been submitted before for any degree or examination at any other University.



(Signature of candidate)

15th day of April 2020 at the University of the Witwatersrand.

Abstract

We show, in a typical groundwater study, a well know problem in electromagnetic exploration that near-surface (<40 m deep) electrically conductive layers can mask deeper resistive features. This is also true for the magnetotelluric (MT) method since the MT method is naturally sensitive to conductive bodies, especially in the near-surface, and insensitive to resistive features. To solve this problem, we use the electrical resistivity tomography (ERT) method to constrain the near-surface electrical resistivity structure missing in the MT method. The combination of ERT data to a depth of 40 m with audio magnetotelluric (AMT) data starting at a depth of ~30 m will improve lateral and vertical resolution of the top 30 m and reduce the masking effect, of near-surface conductors, on deeper resistors. Using Maxwell's equations and Ohm's Law we derive the well-known current density equations for both the MT and ERT methods. We then equate both the MT and ERT current density equations, through the common layer conductivity value in Ohm's Law. The resulting newly derived equation is simplified so that a pseudo-MT impedance tensor can be calculated from ERT data. The resulting pseudo-MT impedance tensor is used to calculate both the phase and resistivity values for each ERT data point used in the conversion. The pseudo-MT data is then combined with MT data at the same location to form, what we named, the augmented ERT-MT response function. The augmented ERT-MT response function is then inverted, resulting in an improvement of up to ~ 90 % in recovered electrical resistivity structures. This improvement is observed in multiple resistivity inverse models when compared to the true electrical resistivity structure for both the synthetic layered one-dimensional (1-D) case and

a two-dimensional (2-D) half-space. Both 1-D and 2-D synthetic models, using the augmented ERT-MT response function, mapped resistive features below conductive layers that are absent in resistivity inversions using MT data only. The augmented ERT-MT response function is applied to AMT data collected over an electrically resistive dyke beneath a conductive overburden. The augmented ERT-MT response function again assisted in mapping the resistive (~1000 Ω·m - ~10000 Ω·m) dyke that was absent in the AMT only resistivity inverse model. The augmented ERT-MT response function is used on a second site to map an aquifer system contained in the Malmani Group dolomites. As expected, greater detail is seen in the near-surface (< 100 m deep) in the augmented ERT-MT response function resistivity inverse model while retaining the deeper features from the standard AMT resistivity inverse model. The fault zone, ~120 m along the profile at the second research site, is seen in the resistivity inverse model using the augmented ERT-MT response function, which is missing in the AMT resistivity inverse model. Therefore, for both conductive and resistive features, the augmented ERT-MT response function improved the AMT resistivity inverse models by recovering features that are generally masked by near-surface conductive layering for both the synthetic and case study experiments.

Acknowledgments

I would like to thank DST-NRF Centre of Excellence for Integrated Mineral and Energy Resource Analysis (CIMERA) for funding the research contained in this thesis. Without the financial support provided by CIMERA, the important conclusions contained in this thesis would have been unattainable.

I would also like to acknowledge Dr Louise Pellerin for her constant support and assistance throughout my Ph.D. career. Her valuable experience and knowledge in the electromagnetic field proved vital for many of the findings in this thesis.

Prof Susan J. Webb first supervised me on a third-year project in 2015. Now five years later Sue has transformed me from an immature aspiring scientist to a competent researcher in geophysics resulting in my research pushing the boundaries forward of the electromagnetic field.

Finally, I would like to thank God and my family for the continual faith, love and support throughout my research career.

Table of Contents

Declaration i
Abstract ii
Acknowledgments iv
Table of Contents v
List of Figures viii
List of Tables xxi
List of Acronyms xxii
List of Symbols xxiii
Chapter 1 : Introduction 1

1.1. Thesis Objective 1
1.2. Organisation of thesis 1
1.3. Contribution of Thesis 3
Chapter 2 : Theoretical Background 5

2.1. Brief history of the magnetotelluric method 5
2.2. Material conductivity theory 6
2.3. MT Theory 12
2.3.1. Maxwell's equations and the MT response function 12
2.3.2. MT source fields 19
2.3.3. MT data acquisition 22
2.3.5. Basic description of MT processing 32
2.4. Electrical resistivity tomography 36
2.4.1. Electrical resistivity tomography theory 36
2.2.3 Basic processing of ERT data 41
2.5. Basic Inversion Theory 42
2.5.1. Introduction 42
2.5.2. The inversion method 44
2.5.3. Joint and cooperative inversion methods 52
Chapter 3 : Buried Resistors Masked by Conductive layers 55

3.1. Abstract 58
3.2. Introduction 59
3.3. Hopefield Regional Geological and Hydrogeological Setting 60
3.4. Audio Magnetotelluric and Aeromagnetic Measurements and Data Processing 63

3.5. Audio Magnetotelluric and Magnetics Results and Interpretation 73
3.6. Discussion 83
3.7. Conclusions 92
3.8. Acknowledgments 93
Chapter 4 : Augmented ERT-MT Response Function 94

4.1. Abstract 97
4.2. Introduction 98
4.3. Calculating augmented ERT-MT response function 99
4.3.1. Analytical derivation 99
4.3.2. Theoretical models 103
4.5. Case study 122
4.5.1. Introduction 122
4.5.2. Survey design 127
4.5.3. Results 128
4.5.4. Discussion 139
4.5.5. Conclusion 142
4.5.6. Acknowledgments 142
Chapter 5 : Evaluating the Augmented ERT-MT Response Function on Conductive Targets 144

5.1. Introduction 144
5.2. Regional Geological and Hydrogeological Setting 145
5.3. Legacy Seismic Data 148
5.4. Seismic Low Velocity Zone Investigation 158
5.5. Discussion 171
5.6. Conclusion 175
5.7. Acknowledgments 176
Chapter 6 : Concluding Remarks 177

6.1. Conclusion 177
6.2. Future studies 179
Chapter 7 : References 181

Chapter 8 : Appendix 194

A.1. Magnetotelluric forward modelling MATLAB code 194

A.2. Magnetotelluric inversion modelling MATLAB code 197
A.2.1. Constrained tandem random model generator one dimensional magnetotelluric layer resistivity least squares damped weighted inversion MatLab code 197
A.2.2. Constrained tandem random model generator one dimensional magnetotelluric layer thickness least squares damped weighted inversion MatLab code 203
A.2.3. Constrained tandem random model generator joint one-dimensional magnetotelluric layer thickness and resistivity least squares damped weighted inversion MatLab code 210
A.3. Augmented ERT-MT response function MatLab code 219
A.4. ERT Lines 223
A.5. Publications 223
A.5.1. Conference abstracts 223
A.5.2. Publications 225

List of Figures

Figure 2.1 Electron energy spectra at absolute zero for different systems. 7

Figure 2.2. Resistivity chart for different materials (modified and consolidated after Palacky, 1987 and Dentith and Mudge, 2014)..... 12

Figure 2.3. Sketch showing the strike of the electric and magnetic field for both the transvers magnetic and electric modes in a heterogenous half space. The transvers magnetic mode is perpendicular to geological strike while the transvers electric mode is parallel to geological strike. 18

Figure 2.4. Lightning storms near the equatorial regions generate electromagnetic fields, known as spherics, that travel along a wave guide between the Earth's surface and the ionosphere. These electromagnetic fields are the main source field for magnetotelluric signal > 1Hz. The electromagnetic fields are vertically incident plane waves at the Earth's surface and propagate through the Earth to ~2 km deep. 20

Figure 2.5. Micropulsations, caused by the interaction of solar winds and the Earth's magnetic field, induces telluric currents deep in the earth's surface through magnetospheric induction (modified from Constable, 2016)..... 21

Figure 2.6. Skin depth for both spherics and micropulsations electromagnetic source fields. The exponential decay of the propagating electromagnetic wave is greater for the higher frequency (>1 Hz) spherics source fields than for the lower frequency (< 1 Hz) micropulsations source fields. Therefore, the penetration depth for the spherics source fields are up to ~ 2 km deep while the micropulsations source fields can penetrate to depths > 20 km..... 23

Figure 2.7. (A) A typical MT station setup with two dipoles in the X and Y direction and three induction coils in the X, Y and Z directions. This system will be used for deeper (up to ~40 km deep) exploration where the measured electromagnetic signals are < ~1Hz. (B) A typical AMT system also has two dipoles in the X and Y direction but only two magnetic induction coils in the X and Y direction. This system will be used for shallower (up to ~2 km deep) exploration where the measured electromagnetic signals are > ~1Hz. The Z direction magnetic induction coil is usually left out in AMT soundings since it is sensitive to high frequency noise in the magnetic field. 24

Figure 2.8. (A) Resistivity model with a 10 Ω·m conductor 7.5 km deep. (B) Resistivity and phase measurements between 10-10000 Hz. Data is 1-D in nature indicating the absence of the deeper conductor. (C) Resistivity and

phase measurements between 0.00001-10 Hz. Data is 2-D in nature, showing indications of the 7.5 km deep conductor. 25

Figure 2.9. (A) True resistivity model, with a 10 Ω·m conductor 15 km deep. (B) Resistivity inverse model using AMT data measured between 1-100000 Hz. The conductor is absent in the resistivity inverse model since the MT data used is too high frequency to measure at the depth of the conductor. (C) A Resistivity inverse model using MT data measured between 0.00001-1 Hz shows the conductor at 15 km deep. 27

Figure 2.10. (A) True resistivity model with an 800 m thick 10 Ω·m conductive overburden above a 1000 Ω·m half-space. An 8000 Ω·m resistive vertical dyke is embedded within the half space. (B) MT resistivity inverse model shows how the conductive overburden obscures the resistive dyke beneath. The frequency range used is 0.00001 Hz – 100 000 Hz. 29

Figure 2.11: Example of the static shift effect over a local conductive body. Local near surface conductor shown in blue. The geological model consists of an upper medium resistive lithological layer, in orange, underlain by a highly resistive half-space, shown in red. The static shift effect is shown within the apparent resistivity curve plot. 31

Figure 2.12. (A) Rotated resistivity plot of MT data. (B) Rotated phase plot of MT data. The green block shows the ~ 1 kHz dead band that affects MT data quality and the red block shows low energy levels in the high frequencies. 34

Figure 2.13. (A) Rotated and edited resistivity plot of MT data. (B) Rotated and edited phase plot of MT data. 35

Figure 2.14: Four-point electrode configuration sketch, where E represents electrodes. 37

Figure 2.15: Sketch of a typical two-dimensional resistivity array setup. The potential difference between electrodes is used to calculate an apparent resistivity value as shown in the apparent resistivity pseudo-section. 39

Figure 2.16: Common ERT configurations and corresponding geometric factors (modified from Dentith and Mudge, 2014). C represents current electrodes, P represents potential electrodes, a is the spacing between electrodes and n is a spacing modifier as the array is extended. I is the amp meter for the applied current and V is the voltmeter required for measuring the change in potential. 40

Figure 2.17: A dipole-dipole and Wenner array equipotential surface interaction comparison for both vertical and horizontal conductive geological structures represented by the brown rectangles, the black line represent current flow lines (modified from Dentith and Mudge, 2014). 41

Figure 2.18. (A) Electrical resistivity tomography raw data plot. (B) Electrical resistivity tomography smoothed and spiked removed data. 42

Figure 2.19. Magnetic data collected in the field is used to calculate a magnetic susceptibility 3-D inverse model. White dots represent magnetic data points. The magnetic susceptibility 3-D inverse model shows the isovolume of the dyke that we are interested in. 43

Figure 2.20. A plot shows the root mean square (RMS) error for models calculated using the Monte Carlo simulation. 48

Figure 2.21. Algorithm workflow map for the Monte Carlo random model gubernators 50

Figure 2.22. Algorithm workflow map for the least squares inversion. 51

Figure 2.23. A 1-D MT inverse model calculated using the algorithm developed in this thesis (Appendix A.2.). The green line represents the actual resistivity model, the red dashed line is the starting model calculated from the Monte Carlo simulations and the blue line is the lowest root mean square resistivity inverse model. 52

Figure 3.1. Geological map of the surrounding Hopefield area (modified from Theron, 1990, and Visser and Theron, 1973). The purple square on the map outlines the study area, the Waterboerskraal farm. 62

Figure 3.2. Geological map of Waterboerskraal. Audio magnetotelluric stations are indicated as red triangles. Ten audio magnetotelluric traverses were collected in total around the farm. A simplified geological cross-section based on borehole (green dots) data, of the study area, is shown with expected electrical resistivity values, taken from the South African Council for Geoscience publicly available physical property database (Mare, 1999). The yellow Sandveld group was mapped using satellite images, where the color and texture of sediments seen at dune plumes in the surrounding area matched the color and texture in our research site. . 65

Figure 3.3. (A) Representative quality AMT field data. (B) Rotated AMT data so the X and Y direction is perpendicular and parallel to geological strike respectively. (C) Masked data in the 1 kHz dead band and >31 kHz where

signal strength was low. (D) Removed noise spikes and fitted smooth (D+) curves to the remaining data points..... 68

Figure 3.4. This schematic map illustrates the procedure followed by the model confidence assessment algorithm. The misfit for both the resistivity and phase data, for both the TE and TM mode, are calculated. The misfit for the resistivity and phase data is summed and normalized to create a total misfit map for the inverse model. The total misfit model is transformed into an alpha map that controls the translucency of cells within the inverse model. Transparent cells indicate regions of low confidence. 70

Figure 3.5. (A) Reduced total magnetic intensity aeromagnetic map. (B) Levelled total magnetic intensity aeromagnetic map. (C) Reduced to pole total magnetic intensity aeromagnetic map. AMT stations are represented by white triangles. 72

Figure 3.6. (A) A locality map that shows the position of the 5 AMT sites, from L1 represented as red triangles, used for the inverse model. The AMT impedance tensor for these sites is rotated by 156 ° to lineup the TM and TE modes perpendicular and parallel to the lithological strike respectively. (B) The resistivity inverse model maps a conductive layer between ~50-20 mamsl deep. This layer is interpreted as the calcrete and clay aquitard present on the farm. A break in the conductor, between 40 m and 80 m along the profile, where a lite blue resistor is preventing the formation of the aquitard in this area. One of the farms' flagship freshwater wells is sunk in the area of the break in the conductor. Between 50-0 mamsl and 0-40 m along the profile, white cells show a region of low confidence calculated by the model confidence assessment algorithm. The root mean square error of the model is 2.9. (C) A geological model interpreted from the resistivity inverse model..... 74

Figure 3.7. (A) This locality map shows the positions of the 7 AMT stations, from L2, used for the resistivity inverse model. The impedance tensor is rotated 133°, which rotates the TM mode perpendicular to the strike of wells and vegetation at this site. (B) The resistivity inverse model again maps the conductive clay and calcrete aquitard at the surface of the model. A resistor breaks the continuity of the aquitard. A well sunk near the edge of the clay and calcrete aquitard intersect slightly more saline groundwater than the well at line L1. The calcrete and clay aquitard mapped by the borehole matches the conductivity layer. The course fluvial sands match with the green layer of the resistivity inverse model, which is the target aquifer in the area. The root mean square error of the model is 2.5. (C) A geological model interpreted from the resistivity inverse model. 76

Figure 3.8. (A) This locality map shows the position of 6 AMT stations along survey line L4. The impedance tensor for these stations is rotated by 120° to follow the vegetation strike in the area. (B) The resistivity inverse

model for this line shows two resistors recharging a single operational well that is positioned between them. The resistors again disrupt the conductive aquitard layer. Below the two resistors the basement Malmesbury Supergroup seems to form a channel, due to folding, from a depth of -25 mamsl on the east to -100 mamsl on the western side of the inverse model. Zone of low confidence in the inverse model is shown as white cells. The root mean square error of the model is 1.9. (C) The geological model interpreted from the resistivity inverse model shows that the well is primarily being recharged by two breaks in the conductive aquitard. 78

Figure 3.9. (A) The locality map shows the position of 9 AMT stations along survey line L7. This is one of the longest lines of AMT data collected on the farm. The impedance tensor for the stations is rotated by 64° following the strike of the wells. (B) The resistivity inverse model shows the resistor, in this case, is buried by a layer of fine sands (green). Even though the resistor is buried two wells still recharge from the buried resistive area. The root mean square error of the model is 1.6. (C) A geological model interpreted from the resistivity inverse model shows that both wells intersect the break in the conductive aquitard. 79

Figure 3.10. (A) The location of the 6 AMT stations, along L5, used in the resistivity inverse model is shown on this map. The rotation angle for these stations is 100°. (B) The resistivity inverse model shows a continuous conductor at a depth of 55 mamsl. This conductor is interpreted as the clay and calcrete aquitard. White cells with low confidence are present below -140 mamsl. The root mean square error of the model is 1.6. (C) The geological model shows that the non-productive well intersects the aquifer below the aquitard but the groundwater conductivity in the aquifer is > ~2000 µS/cm. 81

Figure 3.11. (A) A cross-section, along a traverse between M1 and M2, from the 3-D magnetic susceptibility inverse model. (B) Resistivity inverse models along lines L2 and L4 overlain on the magnetic susceptibility inverse model cross-section. The resistivity inverse models map the edges of inferred channels formed much later in Cenozoic times by exploiting possible minor synclinal folds in the basement Malmesbury Supergroup and correlate with the edges of channels seen in the basement Malmesbury Supergroup in the magnetic susceptibility inverse model. (C) The geological model interpreted from the magnetic susceptibility inverse model. 83

Figure 3.12. (A) Geological model interpreted from resistivity inverse model calculated from AMT line L1. (B) Geological model interpreted from resistivity inverse model calculated from AMT line L4. (C) Geological model interpreted from resistivity inverse model calculated from AMT line L7. (A) Geological model modified from Kandel et al. (2003), showing ancient dunes preserved in the calcrete layer near the

Yzerfontein–Geelbek dune cordon. The breaks in the calcrete layer seen in all the resistivity inverse models resemble the same breaks in the Kandel et al. (2003) geological model. Therefore, the breaks in the calcrete in our study area are likely as a result of preserved ancient dune fields. 85

Figure 3.13. A shuttle radar topography mission elevation map of the geological map shows that operational (groundwater conductivity <500 µS/cm) have an average elevation range of ~50-58 mamsl, while non-operational wells (groundwater conductivity >500 µS/cm) have an average elevation range of ~65-78 mamsl. This is likely due to the faster rate of weathering in the preserved dunes when compared to the calcrete aquitard. Most of the operational groundwater wells are situated on or near the yellow ancient dune outcrops mapped by satellite images on the geological map. 87

Figure 3.14. Outcropping paleochannel outlined on the satellite image. There is a clear contrast between the coarse orange color ancient dune sediments and the fine grain grey color sediments overlying the calcrete and clay aquitard. The operational well is recharged by the ancient dune outcrop and is used to replenish a farm dam just east of the well. 88

Figure 3.15. The proposed geological model interpreted from both the resistivity and magnetic susceptibility inverse models. Groundwater infiltrates the Cenozoic sedimentary succession through preserved ancient dune outcrops by disrupting the calcrete and clay aquitard above. 90

Figure 3.16. The red line marks the previously mapped Pliocene shoreline from Roberts et al. (2011). We make use of the satellite imagery and geophysical mapping to extend (blue line) the Pliocene shoreline further north-east. (A) Shows the location of the Yzerfontein–Geelbek dune cordon. (B) Orange colored matured dunes stabilized by vegetation in our study area. (C) Shows matured dunes furthest east from the present-day shoreline, marking the boundary of the Pliocene shoreline. 91

Figure 4.1. Sketch of a typical ERT array. C1 and C2 are current electrodes while P1 and P2 are potential electrodes. The distance between current electrodes and potential electrodes is represented as distances r1, r2, r3 and r4 respectively. Jx is the current density in the horizontal direction. J_{DCx} is the horizontal current density measured at that point, with a depth of z and distance R1 and R2 away from current electrodes C1 and C2 respectively. 100

Figure 4.2. (A) True resistivity model of a 1000 Ω·m half space. (B) True resistivity model of a 1000 Ω·m half space with an embedded 10 Ω·m conductor. (C) Sensitivity model for the inverse model calculation from forward modeled MT data of the 1000 Ω·m half space, with a frequency range of 10 - 10000000 Hz. Most of the model sensitivity is in a

distinctive cone shape distribution throughout the half space. (D) Sensitivity model for the inverse model calculation from forward modeled MT data of the 1000 Ω·m half space with the embedded 10 Ω·m conductor, with a frequency range of 10 - 10000000 Hz. Most of the model sensitivity is located near the center of the conductor. 105

Figure 4.3. (A) True resistivity model. (B) Resistivity inverse model of the augmented ERT-MT response function without the use of smooth D+ curves. (C) Resistivity inverse model of the augmented ERT-MT response function with the use of smooth D+ curves. (D) Inverse model sensitivity map of the augmented ERT-MT response function without the use of smooth D+ curves. Sensitivities are spread throughout the inverse model. (E) Inverse model sensitivity map of the augmented ERT-MT response function with the use of smooth D+ curves. Sensitivities are isolated in the top 10 m where the conductive layer is situated. (F) Augmented ERT-MT response function, without D+ curve data filling the gap, apparent resistivity and phase plots with calculated inverse model apparent resistivity and phase. (G) Augmented ERT-MT response function, with D+ curve data filling the gap, apparent resistivity and phase plots with calculated inverse model apparent resistivity and phase..... 107

Figure 4.4. (A) Calculated apparent MT resistivity response from ERT (red) and MT (blue) data. (B) Calculated apparent MT phase response from ERT (red) and MT (blue) data. (C) True 1-D resistivity model with a 10 Ω·m overburden to a depth of 10 m overlaying a 1000 Ω·m half-space..... 109

Figure 4.5. Augmented ERT-MT response function (blue to purple) and MT (red to yellow) 1-D resistivity inverse models. The true resistivity model is represented by a black line. The augmented ERT-MT response function resulted in a 1-D inverse models that depicts an improvement of up to ~91% in recovering the true resistivity model. 111

Figure 4.6. (A) True resistivity model with a conductive (100 Ω·m) overburden, to a depth of 10 m, and an underlying resistive (8000 Ω·m) dyke embedded in a 1000 Ω·m half-space. (B) ERT inverse model with an RMSE of 0.36. The ERT inverse model recovers both the conductive overburden and the dyke. 113

Figure 4.7. (A) Calculated apparent magnetotelluric resistivity response from augmented ERT-MT response function (red) and audio magnetotelluric (blue) data. (B) Calculated apparent magnetotelluric phase response from augmented ERT-MT response function (red) and audio magnetotelluric (blue) data. (C) ERT inverse model used to calculate the augmented ERT-MT response function. The black dots show the location of data points derived from the augmented ERT-MT response function. The gap between ~1000 Hz- 100000 Hz is due to the shorter ERT array so the depth penetration is insufficient for frequency overlap. 114

Figure 4.8. (A) True resistivity model that we are trying to recover has a conductive (100 Ω·m) overburden, to a depth of 10 m, and an underlying resistive (8000 Ω·m) dyke embedded in a 1000 Ω·m half-space. (B) Resistivity inverse model only using audio magnetotelluric data. A resistor is mapped at 300 m along the profile but is at a depth of ~150 m. The conductive overburden is absent from this model. The RMSE for this model is 0.6. (C) Resistivity inverse model using the augmented ERT-MT response function. A resistor is again mapped at 300 m along the profile but is constrained to ~100-200 m wide. Also, the conductive overburden is mapped in this inverse model to a depth of 10 m. The RMSE for this model is 0.5. 117

Figure 4.9. (A) True resistivity model with a conductive (100 Ω·m) overburden to a depth of 10 m and an underlying resistive (8000 Ω·m) dyke embedded in a 1000 Ω·m half-space. (B) ERT inverse model with an RMSE of 0.3. The resistive dyke and the conductive overburden is recovered in the inverse model. 119

Figure 4.10. (A) Calculated apparent magnetotelluric resistivity response from ERT (red) and audio magnetotelluric (blue) data. Calculated phase response from ERT (red) and MT (blue) data. (C) ERT inverse model used to calculate the augmented ERT-MT response function. The black dots show the location of data points derived from the augmented ERT-MT response function. The gap between ~1000 Hz- 100000 Hz is due to the shorter ERT array so the depth penetration is insufficient for frequency overlap 120

Figure 4.11. (A) The true resistivity model has a conductive (100 Ω·m) overburden, to a depth of 10 m, and an underlying resistive (8000 Ω·m) dyke embedded in a 1000 Ω·m half-space. The model is 238 m in length almost half the size of the previous model tested. (B) Resistivity inverse model only using audio magnetotelluric data. No clear resistor is mapped at 300 m along the profile. Again, the conductive overburden is absent in this inverse model. The inverse model had an RMSE of 0.3. (C) Resistivity inverse model using the augmented ERT-MT response function. A resistor is mapped at 300 m along the profile but is constrained to ~100 m. Also, the conductive overburden is again mapped in this inverse model. The inverse model had an RMSE of 0.3. 121

Figure 4.12. Regional geology map showing the ERT and MT survey site as a red circle and the dark blue lines represent aeromagnetic lineaments interpreted as a dyke swarm in the area (modified from Steyn, 1990). .. 123

Figure 4.13. (A) The observed magnetic data collected over our research site. (B) Predicted magnetic data calculated from the inversion algorithm. (C) The misfit map is created by subtracting the predicted data from the observed

data and the resulting difference is mapped as a misfit value on the map. 125

Figure 4.14. (A) Total magnetic intensity map of the magnetic data collected over the study area. White dots indicate actual magnetic readings from the magnetometer. (B) Total magnetic intensity observation data grid used for the 3-D magnetic susceptibility inverse model calculation. (C) The 3-D magnetic susceptibility inverse model shows a ~30 m wide dyke isovolume with a magnetic susceptibility of ~0.6 SI with a north-south strike in our study area. 126

Figure 4.15. Total magnetic intensity map of the study area. White squares represent ERT electrode positions. Blue triangles show AMT station positions. The east-west survey lines run perpendicular to the strike of the target dyke in our study area. 128

Figure 4.16. (A) East-west ERT 2-D inversion model highlighting the dolerite dyke location with a dashed red box. The resistivity inverse model has a root mean square error of 1.8. (B) North-south ERT 2-D inversion model. The dyke was intersected twice along the ERT line indicated by the two red dashed boxes. The resistivity inverse model has a root mean square error of 1.7..... 129

Figure 4.17. (A) Calculated apparent magnetotelluric resistivity response from ERT data (red) and collected audio magnetotelluric (blue) data. (B) Calculated apparent magnetotelluric phase response from ERT data (red) and collected audio magnetotelluric (blue) data. (C) The ERT inverse model used to calculate the augmented ERT-MT response function. The black dots show the location of data points used for the augmented ERT-MT response function. 130

Figure 4.18. (A) Calculated apparent magnetotelluric resistivity response from ERT data (red) and collected audio magnetotelluric (blue) data. (B) Calculated apparent magnetotelluric phase response from ERT data (red) and collected audio magnetotelluric (blue) data. (C) The ERT inverse model used to calculate the augmented ERT-MT response function. The black dots show the location of data points used for the augmented ERT-MT response function. For this station the high frequency data calculated from the ERT data overlap with the AMT data. 131

Figure 4.19. (A) Edited augmented ERT-MT response function resistivity data. (B) Edited augmented ERT-MT response function phase data. 132

Figure 4.20. Edited augmented ERT-MT response function resistivity and phase curve (red squares). The calculated D+ smooth curve is represented as a blue line..... 133

Figure 4.21. (A) Resistivity inverse model only using audio magnetotelluric data. The conductive (15-20 Ω·m) overburden is mapped to a depth of ~15 m. The inverse model had an RMSE of 2.9. (B) Resistivity inverse model using the augmented ERT-MT response function. A resistor is mapped at 150 m along the profile, which was absent in the inverse model using audio magnetotelluric data only. The inverse model had an RMSE of 2.1. 136

Figure 4.22. (A) Augmented ERT-MT response function resistivity and phase data fit from station 8 for the 2-D inverse model calculation shown in Figure 4.21. (B) . (A) AMT response function resistivity and phase data fit from station 8 for the 2-D inverse model calculation shown in Figure 4.21. .. 137

Figure 4.23. (A) East-west ERT inverse model over the audiomagnetotelluric line. (B) Resistivity inverse model using the augmented ERT-MT response function. The resistor at 150 m is mapped in both the ERT and augmented ERT-MT response function inverse model. 138

Figure 4.24. (A) A slice from the magnetic susceptibility inverse model along the AMT line shows the magnetic dyke, labeled “A”, and the north-south fault, labeled “B”. (B) The resistivity inverse model, calculated from the augmented ERT-MT response function, shows that both the dyke and the fault zone in both inverse models line up..... 139

Figure 5.1. Geological map (modified from the following maps sheets, Wilkinson, K.J., and Coetsee, F., 1986; Retief, P.F., 2000) of surrounding the study area at the edge of the Klerksdorp Goldfield situated on the Witwatersrand Basin..... 147

Figure 5.2. Geological map (modified from the following maps sheets, Wilkinson, K.J., and Coetsee, F., 1986; Retief, P.F., 2000) with seismic line positions collected by Gold Division of the Anglo-American Corporation in 1983. 149

Figure 5.3 Shot gather taken from seismic line AV 1 showing the location of picked first breaks. 151

Figure 5.4. (A) P-wave seismic tomography inverse model of seismic line AV 1. The inverse model has a root mean square error of 6 ms. (B) The seismic ray paths raytraced through the velocity model. Black areas indicate zones with no ray traces. 152

Figure 5.5. (A) P-wave seismic tomography inverse model of seismic line AV 1 with a root mean square error of 6 ms. A fault zone, with low velocities dipping down to a ~350 m depth, shown at position f1 maps the continuation of the fault depicted on the existing geological map of the

area. Velocities between ~5000-6000 m/s (blue) represent the Malmani subgroup, and velocities between ~3000-4500 m/s indicate the Vryheid Formation, part of the Karoo supergroup, overlaying the Malmani subgroup, part of the Transvaal Supergroup. Dykes and faults are mapped from underground mapping and subsurface boreholes. (B) P-wave seismic tomography inverse model of seismic line AV 2 with a root mean square error of 7 ms. Position f2 shows the fault zone continuing from AV 1 with a low-velocity zone being traced down to a ~300 m deep. Dykes and faults are mapped from underground mapping and subsurface boreholes. (C) Geological map showing the position of the seismic lines and boreholes being indicated by yellow circles. The continuation of the existing fault zone between position f1 and f2 is indicated with a red line between AV 1 and AV 2. 154

Figure 5.6. (A) P-wave seismic tomography inverse model of seismic line AV 4 with a root mean square error of 5 ms. Two fault zones are mapped in the dolomites. (B) P-wave seismic tomography inverse model of seismic line AV 5 with a root mean square error of 4 ms. Velocities between ~3000-4500 m/s map the Karoo supergroup and matches the borehole log MGR5. Velocities between ~5000-6000 m/s (blue) representing the Malmani subgroup also match the borehole log. A fault zone is mapped at ~2500 m along the profile. (C) P-wave seismic tomography inverse model of seismic line AV 6 with a root mean square error of 9 ms. Faults and dykes can be seen clearly compartmentalizing the dolomites in the inverse model. (D) P-wave seismic tomography inverse model of seismic line AV 7 with a root mean square error of 7 ms. Velocities between ~5000-6000 m/s (blue) in the Malmani subgroup correlate with all three boreholes along the survey line. Again, faults and dykes can be seen compartmentalizing the dolomites. Dykes and faults are mapped from underground mapping and subsurface boreholes. 156

Figure 5.7. A three-dimensional spatial representation of all 6 seismic lines in our study area. Low velocity zones at Position f1 and f2 correspond with the fault continuation. The red line labeled f3 shows a love velocity zone propagating through P-wave seismic tomography inverse models associated with seismic lines AV 2, AV 5, AV 6 and AV 7. 157

Figure 5.8. A geological map showing the planned survey site targeting low-velocity zones mapped in the P-wave seismic tomography inverse model. We collected data from 5 electrical resistivity tomography survey lines, 11 audio magnetotelluric stations, and 15 magnetic survey lines. Seismic line AV 6 runs through the center of our research site. 158

Figure 5.9. (A) Reduced and leveled magnetic map with black dots representing the magnetic readings collected along the survey lines. Black squares show the receiver positions for a portion of the seismic line AV 6. (B) Reduced and leveled magnetic data collected at our research site. Positions

A and B show two negative residual magnetic intensity (~-11 nT) zones. Zone C, marked by the black stippled line, offsets the positive residual magnetic intensity lineament marked as D. Position f3 shows the location of the low velocity zone seen along P-wave seismic tomography inverse model for seismic line AV 6. 161

Figure 5.10. (A) Reduced and leveled magnetic map. Positions A and B show two negative magnetic intensity (~-11 nT) zones. Zone C, marked by the black stippled line, offsets the positive magnetic intensity lineament marked as D. Position f3 shows the location of the low velocity zone seen along P-wave seismic tomography inverse model for seismic line AV 6. (B) A top down view of the magnetic susceptibility inverse model calculated from the reduced and leveled residual magnetic grid. An isovolume of susceptibilities between 0.0004 and 0.0006 SI shows a 'break' in the dolomites in the area labeled C. The residual negative magnetic intensity (~-11 nT) zone at position A, correlates with a cavity in the dolomites at that same position in the magnetic susceptibility inverse model. (C) Easterly side view of the magnetic susceptibility inverse model. An isovolume of susceptibilities between 0.0004 and 0.0006 SI shows a drop in depth in the dolomites from ~15 m to ~110 m deep in the area labeled C. 163

Figure 5.11. (A) Reduced and leveled magnetic map with black dots representing the magnetic readings collected along the survey lines. Green lines show the position of the ERT lines and 11 audio magnetotelluric stations are shown as grey triangles. Black squares show the receiver positions for a portion of seismic line AV 6. (B) Resistivity inverse model for ERT2, with a root mean square error of 5. The resistive dolomites (~ 800 Ω·m) are discontinued ~170 m along the profile by a conductor (~100 Ω·m) interpreted as a fault zone, labeled B. A vertical resistor (1200-1400 Ω·m), labeled A, ~60-150 m along the profile, is situated in the same location as the inferred cavity mapped on the reduced and leveled magnetic map. (C) 3-D Magnetic susceptibility inverse model slice along survey line ERT2. Both the position of the low susceptibility (~0.0001) fault zone and the inferred cavity match the position seen in the resistivity inverse model for the same line..... 166

Figure 5.12. (A) TE and TM resistivity values collected from AMT station AMT1. (B) TE and TM phase values collected from AMT station AMT1. The TE mode is more susceptible to noise saturation since the TE mode strikes parallel with the surrounding powerlines in the study area. 168

Figure 5.13. (A) Standard AMT resistivity inverse model with a minimum root mean square error of 5. (B) Augmented ERT-MT response function resistivity inverse model with a root mean square error of 2.3. Greater detail is seen in the near surface (< 100 m deep) of the augmented response function resistivity inverse model while retaining the deeper

features from the standard AMT resistivity inverse model. f3 marks the location of the low velocity zone in the P-wave seismic tomography inverse model for a portion seismic line AV 6. Position A marks the location of the cavity seen in both the ERT and magnetic susceptibility inverse models. The white cells in these models represent cells with low confidence calculated from the model confidence assessment algorithm. 171

Figure 5.14. (A) Augmented ERT-MT response function resistivity inverse model along survey line ERT2. The white cells in this model represent cells with low confidence calculated from the model confidence assessment algorithm. (B) A geological model interpreted from the augmented ERT-MT response function resistivity inverse model along survey line ERT2. The fractured karst aquifer is confined between ~100-400 m deep. A inferred cavity is interpreted at position A..... 174

Figure 8.1. (A) ERT inverse model for ERT line: ERT1 with a root mean square error of 4.7. (B) ERT inverse model for ERT line: ERT2 with a root mean square error of 5. (C) ERT inverse model for ERT line: ERT3 with a root mean square error of 3.1. (D) ERT inverse model for ERT line: ERT4 with a root mean square error of 5.4. (E) ERT inverse model for ERT line: ERT5 with a root mean square error of 3.2. (F) ERT line locality map. 223

List of Tables

Table 2.1. General micropulsations energy sources utilized in the MT method (modified from Vozoff (1991)). 22

Table 4.1: Processing sequence of MT data..... 134

Table 5.1: Field acquisition parameters for 1983 2D Moab Khotsong seismic.. 150

List of Acronyms

Acronym	Meaning
MT	Magnetotellurics
AMT	Audio magnetotellurics
ERT	Electrical resistivity tomography
BLR	Black Reef Formation
TM	Transverse magnetic
TE	Transverse electric
SPI	Standard precipitation index
EM	Electromagnetic
DC	Direct current
RMSE	Root mean square error

List of Symbols

Symbol	Meaning
K	Kelvin
Ω	Ohm
R	Resistance
V	Voltage
I	Current
ρ	Bulk resistivity
J	Current density
E	Electric field strength
B	Magnetic flux density
D	Electric displacement
q	Electric charge
T	Period
H	Magnetic field strength
μ	Magnetic permeability
ε	Electric permittivity
σ	Electric conductivity
i	Imaginary number
ω	Angular frequency
ϕ	Phase
δ	Skin depth
Z	Impedance tensor

Chapter 1 : Introduction

1.1. Thesis Objective

The objective of this thesis is to investigate which, if any, geophysical method can be used to constrain the near-surface (<40 m) in MT inverse model calculations. Additionally, to develop an analytical solution, algorithms and new processing flow, for the magnetotelluric (MT) method, which can be used to reduce the effects of conductive layering over deeper resistive features. The new processing flow and algorithms will be tested on synthetic layered one-dimensional (1-D) and a two-dimensional (2-D) half-space models and through case study experiments at various research sites.

1.2. Organisation of thesis

This thesis is set out in six chapters where two of these chapters are papers produced from the research contained in this thesis.

The first chapter is designed as an outline and describes the structure, objectives and contributions of this thesis.

The second chapter reviews the background theory used throughout this research. This includes a short description of conductivity theory required to fully understand the outcomes of this study. A review of the MT method is also covered, principally aspects such as important derivations needed to appreciate findings in the following chapter. A second review on the electrical resistivity tomography (ERT) method is also included. Basic inversion theory is similarly covered with practical examples using algorithms developed for this thesis. This

chapter is designed to provide the background needed to appreciate the conclusion in the following chapters.

Chapter 3 includes the following paper:

1. "Geophysical Investigation of Groundwater Control in the Semi-Arid Swartland Terrane, South Africa".
   (In preparation for submission for review)

In this chapter, we use audio magnetotelluric (AMT) and regional magnetic data to map stratigraphy and ancient dune networks that are recharging producing groundwater wells on a farm located in the semi-arid Hopefield region of South Africa. The AMT inverse models show an electrically conductive (5-10 Ω·m) calcrete and clay layered aquitard with an approximate thickness of ~ 20 m overlying a resistive Cenozoic sedimentary succession and ancient dune networks. The chapter describes a link between groundwater salinity and the proximity of wells to ancient dune network locations. The AMT inverse models in this chapter clearly show the masking effect of conductive layers over resistive features.

Chapter 4 includes the following paper:

2. "Augmented ERT-MT Response Function for Resistive Target Amplification".

(In preparation for submission for review)

This chapter covers a newly developed analytical solution, processing flow and algorithms, for the MT method, designed to reduce the effects of conductive layering over deeper resistive features. The new processing flow and algorithms is

tested on synthetic layered 1-D and 2-D half-space models and through a case study experiment over an electrically restive dyke overlain by a conductive overburden in the Bushveld Complex, South Africa.

Chapter 5 covers research on dolomites or dolostone of the Transvaal Supergroup which host groundwater aquifers recharged by surface water flow. It is unknown if the fissures below the dolomites and faults in the dolomites are connected. The research site is of interest since active groundwater biodiversity is being studied in the fissures and faults. The augmented ERT-MT response function, developed in Chapter 3, is used to assist in the mapping of a fault zone and a fracture karst aquifer in the dolomites. The resulting resistivity inverse model is compared to additional geophysical data sets such as three dimensional (3-D) near surface electrical resistivity and magnetic susceptibility inverse models and legacy seismic P-wave tomography inverse models.

The final chapter (Chapter 6) provides a summary of all the conclusions found in this thesis and possible opportunities for future research on the main topics contained in this writeup.

1.3.Contribution of Thesis

The research conducted in this thesis led to the development of a new method to constrain near-surface features in MT resistivity inverse models and improve MT sensitivity towards resistive features previously masked by overlying conductive layers. This includes the development of an analytical derivation, algorithms and methodology linking MT and ERT data sets.

A secondary contribution, from this thesis, that fall outside the original objectives include the discovery and mapping of a new ancient dune network in the Swartland Terrane. A relationship is discovered between the proximity of productive groundwater wells to ancient dune networks. The Pliocene shoreline boundary in the Swartland Terrane was extended using geophysical techniques. This case shows that the near-surface biosphere and the deep biosphere is disconnected in our study area on the Witwatersrand Basin. This finding proves that the deep gold mines in South Africa can be an ideal example of how archaeal biospheres can be preserved in deep confined fissures on other planets.

Chapter 2 : Theoretical Background

2.1. Brief history of the magnetotelluric method

Earth is described and modelled today as a conductive body, becoming increasingly conductive with depth, thanks to the pioneering work in electromagnetic induction studies from Lamb (1883), Schuster (1889), Chapman (1919) and Chapman & Price (1930). Our understanding of the Earth's resistivity structure was further developed by measuring the geomagnetic field with a method called geomagnetic depth sounding (Tarits,1994). At this point, the electric field is left out of the measurement scheme, but the physics used in the geomagnetic depth sounding method forms the bases of the MT method.

During the same period, the ERT method is described, by the Schlumberger brothers, and used successfully in active exploration (Nabighian,1987; Nabighian, 1991). Both the development of the ERT and geomagnetic depth sounding methods laid down the required foundation for the development of the MT method.

Hirayama (1934) and Rikitake (1948) introduced the concept of a relationship between the orthogonal electric and magnetic field components. A few years later the MT method was formally proposed by Tikhonov (1950) and Cagniard (1953) as a geophysical exploration tool. Initially, the MT method, proposed by Tikhonov and Cagniard, was vigorously debated because the proposed plane-

wave source model inadequately and incorrectly assumed electromagnetic induction would take place from the proposed source. Price (1962) finally developed a more general theory for the MT method, still referenced today.

The MT method has grown in popularity over the past few years due to substantial progress made in both acquisition and modelling techniques. The recent wide adoption of the MT method has also revealed a prevalent electromagnetic issue. This major problem, facing the MT method, is when conductive layers mask resistive features laying beneath (Constable, and Weiss, 2006). This is a result of the MT methods' natural sensitivity to conductive bodies as we will show in the following chapters. The consequence of this sensitivity is that conductive layering, such as a conductive overburden, will mask details in resistive targets, for example, a sandstone aquifer confined by a conductive clay aquitard. This problem is also present in other electromagnetic methods, for example, time-domain electromagnetics, but this challenge will be further investigated in the context of the MT method for the remainder of this thesis.

2.2. Material conductivity theory

To understand conductivity within materials we must consider their electron energy level make up. Quantum mechanics helps explain these levels by grouping them into discreet “bands”.

An electron energy spectrum is shown in Figure 2.1, the particle states are shown along the vertical axis. In quantum mechanics, the allowed energy levels begin from 0 and tend to infinity (Ashcroft and Mermin, 1976). Even though Figure 2.1 shows hatching for the energy levels, the energy levels are more tightly spaced

and for practical purposes we consider the energy levels to form a continuum. The different electron energy spectra will determine whether a material will be electrically conductive or resistive. The electrons will fill the lowest energy levels first, shown as a red hash. One electron will only fill one state at a time, adhering to the Pauli Exclusion Principle (Pauli, 1925). In free electron gas, we assume that the electrons are distributed homogeneously and that any electron forces are cancelled out (Lee, 1950; Mestel, 1950).

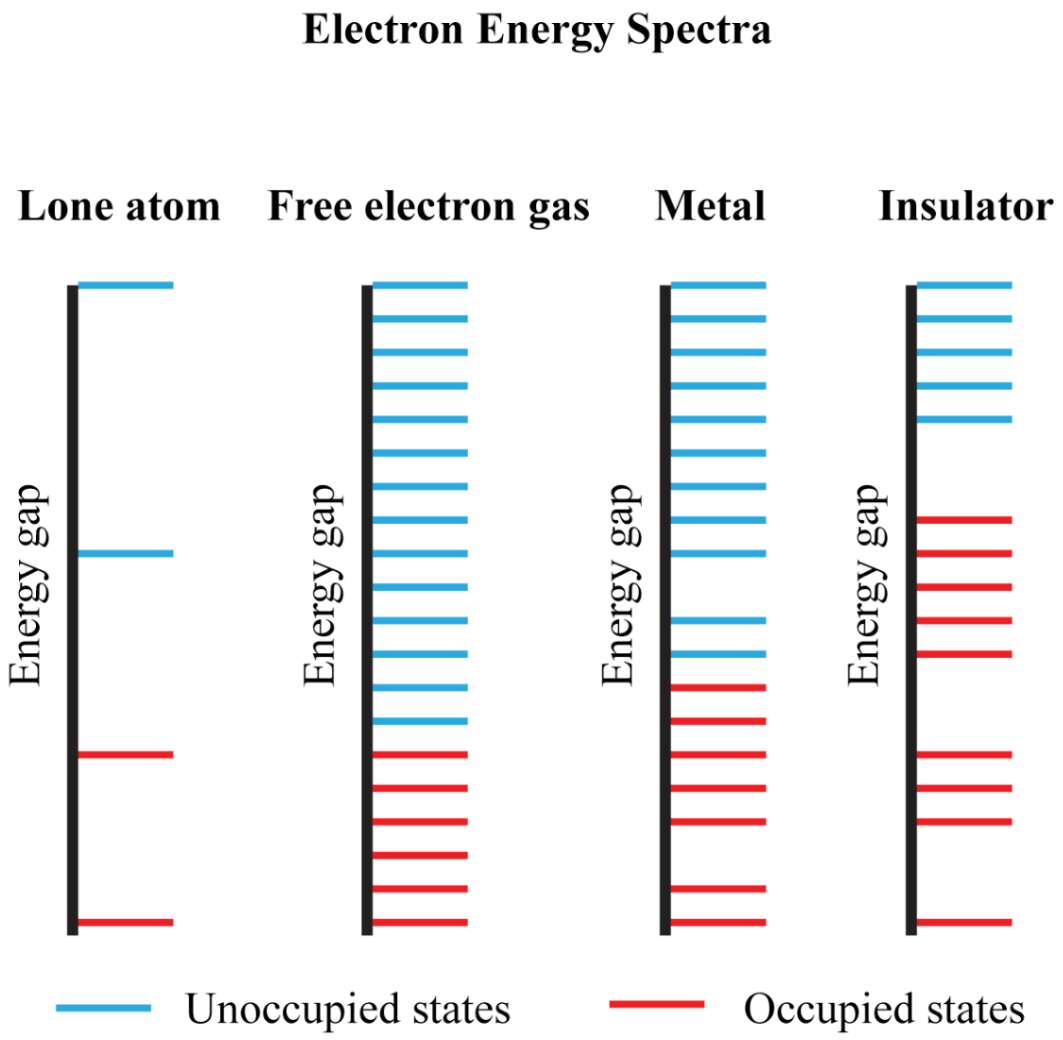


Figure 2.1 Electron energy spectra at absolute zero for different systems.

Realistically this is improbable, indeed some of the electron forces will cancel out but some will persist. In the lone atom case, the atoms are so far apart that the solid is essentially a gas. Lone atoms have the same discrete energy levels, assuming there is insufficient energy present to ionize the atoms and conduction will never occur.

In metals, conduction is possible when the Fermi energy, the maximum energy an electron occupies at 0 K, is reached. Electrons at this energy level can be moved to a higher energy level in a specific direction. This overall motion produces a current within the metal. In insulators, the highest occupied energy band (valence band) is filled. The gap between the highest occupied band and the conduction band above it is large enough that the jump will require substantial energy to induce a state of net motion. The bandgap energy needed by the electrons to reach the conduction band is of the order of electron volts, which is comparable to ionization energies. Without this required energy the electrons are essentially "stuck", preventing any net motion, hence preventing current flow resulting in infinite resistance. Therefore, band gaps are the reason for the large difference in resistance between metals and insulators at 0 K.

Resistors can become semiconductors if their electrons gain energy by increasing the materials temperature. The gained energy can move the electrons into the conduction band if the energy received is equal to or greater than the bandgap energy of the material. If these conditions are met, the material will gain the ability to conduct a current (Peter and Cardona, 2010).

We can predict the conducting behaviour of certain materials by modifying Ohm's law from an intrinsic to an extrinsic property. Ohm's law is defined as the resistance across a circuit and is described as the ratio of the voltage applied to the electrical current. The unit for resistance is ohm (Ω)

$$R = \frac{V}{I}, \tag{2.1}$$

where R is the resistance, V is given as the voltage and I the current.

If the range of voltage applied is considerably large and the resistance stays constant over this range, Ohm's Law can then be applied to predict the electrical behaviour of the material.

A material violates Ohm's law, where resistance changes throughout the material or voltage is disproportionate to current since resistance is an extrinsic property that depends on the size and shape of the resistor. A materials resistance can be described in terms of its bulk resistivity, which states that the resistance is temperature dependent and requires a temperature coefficient as described on pages 488-490 in Alenitsyn et al., (1997).

Ohm's Law can be modified to calculate resistivity which is the physical property that describes the nature of the material. Even though resistivity is temperature dependent, it can be used to find the resistance of a material for its geometry at a specific temperature. The resistivity for an ideal case, a homogenous material with a uniform electric current, can be calculated with the following equation:

$$\rho = R\frac{L}{A}, \tag{2.2}$$

where ρ is the bulk resistivity, L is the length of the material and A is the cross-sectional area of the sample and R is the resistance of the material (Van Zijl, 1977). In a general case, if the material is inhomogeneous and both the electrical field and current vary in the sample, the following equation is used to calculate resistivity:

$$\rho = \frac{J}{E}, \tag{2.3}$$

where J is the current density magnitude and E is electric field. In Geophysics the resistivity of rocks is used by multiple methods to map the earth conductivity structure.

The resistivity within rocks is affected by a wide variety of geological parameters. These parameters include the type of mineral that formed the rock during its formation stage, porosity, permeability, and the salinity of pore water. Minerals such as clay and metal ores are generally conductive and decrease resistivity within the lithology, while resistive minerals such as quartz increase the resistivity within the same lithology. Metallic conductors and even graphite as thin wafers in the rock matrix can alter the resistivity of a rock body dramatically, separately from pore fluids such as saline water (Van Zijl, 1977).

The porosity of the rock also plays a large role in the resistivity of the rock type. The greater the porosity of the rock the more volume of water the rock can hold, and this will result in a reduced resistivity value for that rock. Permeability refers to how well pore spaces are connected, the better connected these spaces are the easier water can travel between and fill these pores resulting in lower bulk

resistivity. Both the porosity and permeability are used to calculate the cementation factor, which quantifies the connectedness of pores in a lithology.

Electrolytic conductions from water in these pores will also play a role in the resistance of the rock. Therefore, rocks resemble electrolytic conductors, where current propagates by ionic conduction, otherwise the resistance in rocks will always be exceedingly high (Telford et al., 2001). The greater the concentration of ions in the pore water, the greater the conductivity within the lithology. Other factors including temperature, saturation capacity and even the weathering of the rock will affect its ability to conduct a current.

The effects on resistivity due to porosity are expressed by Archie's Law:

$$\rho_{rock} = \rho_{fluid}\, A\gamma^{-m}, \tag{2.4}$$

where ρ_{rock} is the resistivity of the lithology, ρ_{fluid} is the resistivity of the pore fluid, A and m are empirical constants based on clean sandstone, where A is dependent on the pore geometry and connectivity while m is the cementation factor, and γ is the porosity (Salem and Chilingarian, 1999).

The generalised Archie's Law was derived by Glover (2010) and is given as:

$$\rho_{rock} = \sum \rho_{fluid}\gamma^{m}, \tag{2.5}$$

where we sum the resistivity of pore fluids with associating cementation factors and porosities.

Hence, due to all these variables within rocks, there is a large range of resistivity values for a single type of lithology. This large variability of resistivity within rocks implies that even rocks of the same type can have different values for

resistivity. The following Figure 2.2 demonstrates a typical resistivity chart. The colour scheme is set to indicate that reddish hues imply electrically conductive and blue hues imply resistive rock types and this colour scheme will be used for the rest of the thesis.

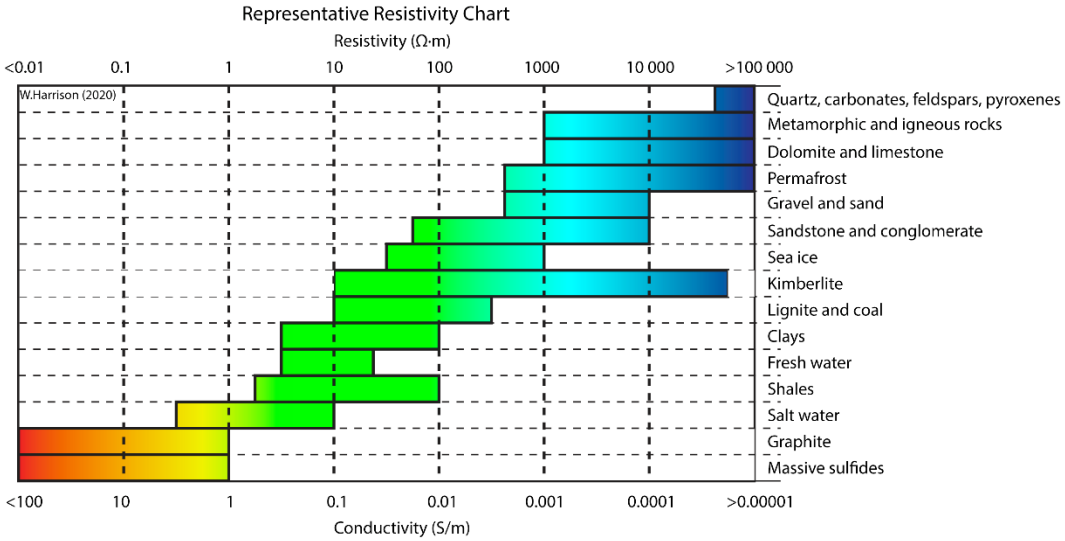


Figure 2.2. Resistivity chart for different materials (modified and consolidated after Palacky, 1987 and Dentith and Mudge, 2014).

2.3. MT Theory

2.3.1. Maxwell's equations and the MT response function

A brief derivation and description of the magnetotelluric response function, based on Maxwell's equations formulated in the frequency domain, is presented here and follows a more detailed derivation described in the following publications Chave and Jones (2012), Berdichevsky and Dmitriev (2002) and Telford et al., (2001).

Some of the important assumptions made when deriving the MT response function are:

- All source fields are vertically incident plane waves at the Earth's surface.

- The Earth only dissipates or absorbs electromagnetic (EM) energy, it does not generate it.
- The Earth acts like a conductor that obeys Ohm's law.
- Displacement currents are negligible compared to induction currents.
- When compared to changes in bulk conductivity, electrical permittivity and magnetic permeability is negligible.

The magnetotelluric method is governed by the following famous Maxwell equations developed in the textbook "*A Treatise on Electricity and Magnetism*" (Maxwell, 1873) written in modern mathematical form as:

$$\nabla \cdot \vec{B} = 0, \tag{2.6}$$

which is Gauss's Law for magnetic fields, where $\vec{B}$ is the magnetic flux. The following equation is Gauss's Law for electric fields,

$$\nabla \cdot \vec{D} = q, \tag{2.7}$$

where q is the electric charge density and $\vec{D}$ is the electric displacement. Faraday's Law is given as follows,

$$\nabla \times \vec{E} = -\frac{\partial \vec{B}}{\partial t}, \tag{2.8}$$

where $\vec{E}$ represents the electric field.

$$\nabla \times \vec{H} = \vec{J} + \frac{\partial \vec{D}}{\partial t}, \tag{2.9}$$

which is Ampere's Law with the Maxwell term, where $\vec{H}$ is the magnetic field and $\vec{J}$ is the electric current density.

Also,

$$\vec{B} = \mu\vec{H}, \tag{2.10}$$

where μ is the magnetic permeability,

$$\vec{D} = \varepsilon\vec{E}, \tag{2.11}$$

where ε is the electric permittivity and

$$\vec{J} = \sigma\vec{E}, \tag{2.12}$$

where σ is the conductivity.

The above equations govern how electromagnetic waves travel through a medium, there are also important boundary conditions that must be satisfied. When an electromagnetic wave reaches a boundary between two different conductive mediums, the normal component of the current density and magnetic field must have the same values immediately before and after the boundary, hence they must be continuous (Chave and Jones, 2012; Berdichevsky and Dmitriev, 2002). The same boundary condition applies to the transverse component of the electric field at a boundary. The boundary conditions require $E_z = 0$, therefore the E_z component is excluded in measurements (Vozoff, 1991).

Rewriting Ampere and Faraday's Laws with the time dependence, defined as $e^{i\omega t}$ we have:

$$\nabla \times \vec{E} = -\frac{\partial \vec{B}}{\partial t} = -i\omega\mu\vec{H}, \tag{2.13}$$

where ω is the angular frequency and i is the imaginary number,

$$\nabla \times \vec{H} = \vec{J} + \frac{\partial \vec{D}}{\partial t} = (\sigma + i\omega\varepsilon)\vec{E}. \quad (2.14)$$

If we expand the curl operator for equation 2.13, we have the following relationship between the E and H fields given as follows:

$$\frac{dE_z}{dy} - \frac{dE_y}{dz} = -i\omega\mu H_x, \quad (2.15)$$

$$\frac{dE_x}{dz} - \frac{dE_z}{dx} = -i\omega\mu H_y, \quad (2.16)$$

$$\frac{dE_y}{dx} - \frac{dE_x}{dy} = -i\omega\mu H_z, \quad (2.17)$$

According to the plane wave assumption, the inducing magnetic field will only have horizontal components, therefore both $E_z = 0$ and $B_z = 0$. The scalar form of equation 2.13 and equation 2.14 in the x and y directions and assuming homogeneous subsurface conductivity is therefore:

$$\frac{dE_y}{dz} = -i\omega\mu_0 H_{x,} \quad (2.18)$$

$$\frac{dE_x}{dz} = -i\omega\mu_0 H_{y,} \quad (2.19)$$

and

$$\frac{dH_y}{dz} = -\sigma E_{x,} \quad (2.20)$$

$$\frac{dH_x}{dz} = -\sigma E_{y,} \quad (2.21)$$

where the negative sign is required in order to maintain a consistent right-hand rule (Chave and Jones, 2012). Differentiating equation 2.18 to 2.21 again with respect to z we have:

$$\frac{d^2E_x}{dz^2} = -i\omega\mu_0 E_{x,} \tag{2.22}$$

$$\frac{d^2E_y}{dz^2} = -i\omega\mu_0 E_{y,} \tag{2.23}$$

and

$$\frac{d^2H_x}{dz^2} = -i\omega\mu_0\sigma H_{x,} \tag{2.24}$$

$$\frac{d^2H_y}{dz^2} = -i\omega\mu_0\sigma H_{y,} \tag{2.25}$$

therefore equations 2.22 to 2.25 have solutions in the following form:

$$\vec{E} = Ae^{-i\omega\mu_0\sigma t} + Be^{i\omega\mu_0\sigma t}, \tag{2.26}$$

and

$$\vec{H} = \frac{\sqrt{\omega\mu_0\sigma}}{\omega\mu_0}\left(Ae^{-i\omega\mu_0\sigma t} + Be^{i\omega\mu_0\sigma t}\right). \tag{2.27}$$

Hence, the impedance within a medium is given as:

$$Z_{xy} = \frac{E_x}{H_y} = -\frac{i\omega\mu_0}{\sqrt{i\omega\mu_0\sigma}} = -\frac{i\omega\mu_0}{k}, \tag{2.28}$$

$$Z_{yx} = \frac{E_y}{H_x} = -\frac{i\omega\mu_0}{\sqrt{i\omega\mu_0\sigma}} = -\frac{i\omega\mu_0}{k}, \tag{2.29}$$

where

$$k = \sqrt{i\omega\mu_0\sigma}. \tag{2.30}$$

Now the apparent resistivity and phase lag between the electric and magnetic fields is calculated by:

$$\rho_{xy}(\omega) = \frac{1}{\omega\mu_0}\left|\frac{E_x(\omega)}{H_y(\omega)}\right|^2, \tag{2.31}$$

$$\rho_{yx}(\omega) = \frac{1}{\omega\mu_0}\left|\frac{E_y(\omega)}{H_x(\omega)}\right|^2, \quad (2.32)$$

$$\varphi_{xy}(\omega) = \tan^{-1}\left(\frac{E_x(\omega)}{H_y(\omega)}\right), \quad (2.33)$$

$$\varphi_{yx}(\omega) = \tan^{-1}\left(\frac{E_y(\omega)}{H_x(\omega)}\right), \quad (2.34)$$

where ρ is the apparent resistivity, φ is the phase lag between the electric and magnetic fields. Since the electromagnetic fields are orthogonal to each other they can be decomposed into two modes that relate to the polarisation of the electromagnetic fields. The first mode is known as the transverse magnetic (TM) mode where the magnetic field is polarised parallel to the lithological strike (Figure 2.3). The second mode is called the transverse electric (TE) mode where the electric field is polarised parallel to lithological strike. The TM mode apparent resistivity and phase are represented as follows:

$$\rho_{xy}(\omega) = \frac{1}{\omega\mu_0}\left|\frac{E_x(\omega)}{H_y(\omega)}\right|^2, \quad (2.35)$$

$$\varphi_{xy}(\omega) = \tan^{-1}\left(\frac{E_x(\omega)}{H_y(\omega)}\right). \quad (2.36)$$

The TE mode apparent resistivity and phase are:

$$\rho_{yx}(\omega) = \frac{1}{\omega\mu_0}\left|\frac{E_y(\omega)}{H_x(\omega)}\right|^2, \quad (2.37)$$

$$\varphi_{yx}(\omega) = \tan^{-1}\left(\frac{E_y(\omega)}{H_x(\omega)}\right). \quad (2.38)$$

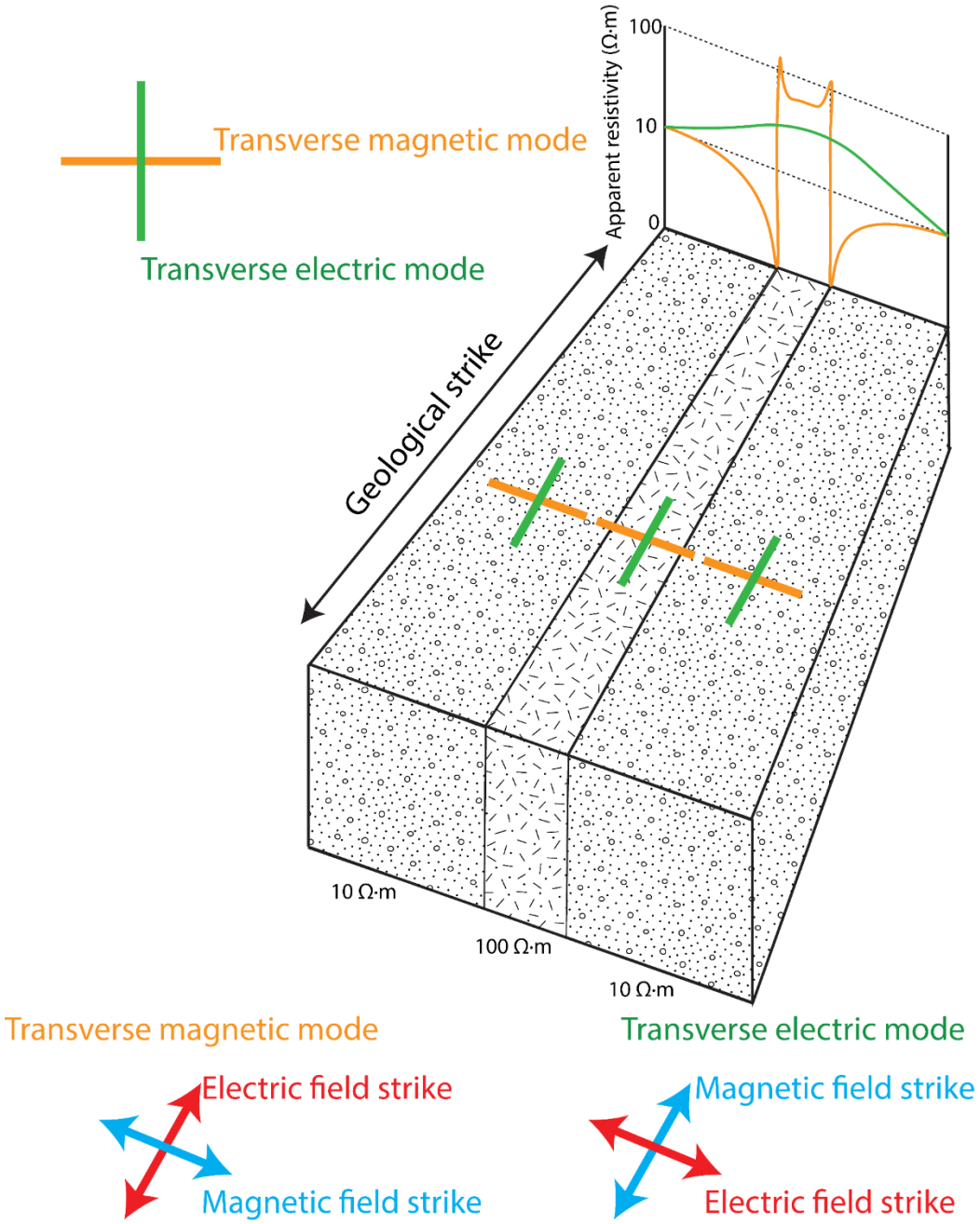


Figure 2.3. Sketch showing the strike of the electric and magnetic field for both the transvers magnetic and electric modes in a heterogenous half space. The transvers magnetic mode is perpendicular to geological strike while the transvers electric mode is parallel to geological strike.

Both the TM and TE modes, at a certain period, can be described by the MT

impedance tensor:

$$\vec{E} = \vec{Z}\vec{H} = \begin{pmatrix} E_x \\ E_y \end{pmatrix} = \begin{pmatrix} Z_{xx} & Z_{xy} \\ Z_{yx} & Z_{yy} \end{pmatrix} \begin{pmatrix} H_x \\ H_y \end{pmatrix}. \quad (2.39)$$

The detection of lateral and vertical resistivity changes of the geological subsurface is essential for the magnetotelluric method as an effective exploration tool in geophysics. Thankfully, many geological environments fit this criterion of resistivity contrast, hence the magnetotelluric method can provide much-needed information about the underlying geological structure, which can be later used for geological model interpretation. Two types of magnetotelluric surveys can be conducted, namely large-scale regional reconnaissance and local detailed surveys. Regional reconnaissance involves the study of large, 100 km to 1000 km, geological structures such as sedimentary basins under lithological cover or general regional structure interpretation, the survey grid spacing is typically 2 to 6 km for regional reconnaissance surveys. Detailed local, 10 m to 1 km, surveys involve mapping the resistivity contrast of a desired resource at higher resolutions due to the smaller station spacing. Examples of local targets include mapping aquifers, mineralized zones, petroleum traps and geothermal horizons. Detailed local surveys usually have a grid spacing of 0.1 to 1 km.

2.3.2. MT source fields

Since the magnetotelluric method is a passive-source inductive electromagnetic method it relies on natural sources of electromagnetic waves. These electromagnetic waves induce currents in the earth, known as telluric currents, which can be measured at the surface of the earth. There are two primary sources of EM energy namely spherics and micropulsations.

At frequencies greater than 1 Hz spherics is the main source of energy for the MT method. Figure 2.4 shows Lightning near the equatorial regions generating EM fields, known as spherics, that travel along a waveguide between the Earth's

surface and the ionosphere (Campbell et al., 1998). Since these EM waves travel in this waveguide over long distances, they are essentially plane waves. This phenomenon, in the 5-50 Hz band is also called Schumann resonances and is described in detail in Heckman et al., (1998) and Surkov and Hayakawa (2014).

There is a dead band between 0.5-5 Hz, due to absorption in the photo-ionised atmosphere, where there is little EM energy which usually results in poor data quality. The dead band usually results in a "v" shaped minimum in the MT response curves. MT data collected Above 1 Hz is referred to as audio-magnetotellurics (AMT) data.

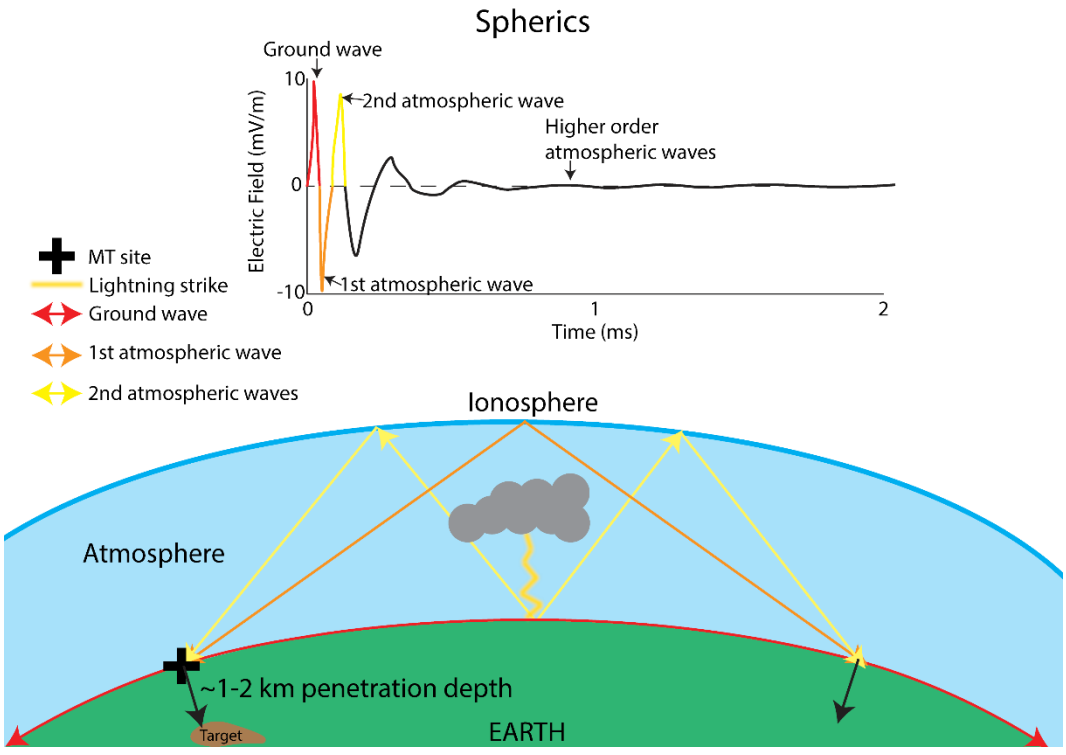


Figure 2.4. Lightning storms near the equatorial regions generate electromagnetic fields, known as spherics, that travel along a wave guide between the Earth's surface and the ionosphere. These electromagnetic fields are the main source field for magnetotelluric signal > 1Hz. The electromagnetic fields are vertically incident plane waves at the Earth's surface and propagate through the Earth to ~2 km deep.

The second source of natural EM energy below 1 Hz is micropulsations (Figure 2.5). Micropulsations are a result of the interaction between the Earth's magnetic field and solar winds. The continues stream of plasma, carried by solar winds, has a small magnetic field. The solar winds themselves vary in density, intensity and velocity and when they interact and ultimately distort the Earth's magnetic field, time-varying EM fields are produced. The types of micropulsations used in the MT method is described in Table 2.1.

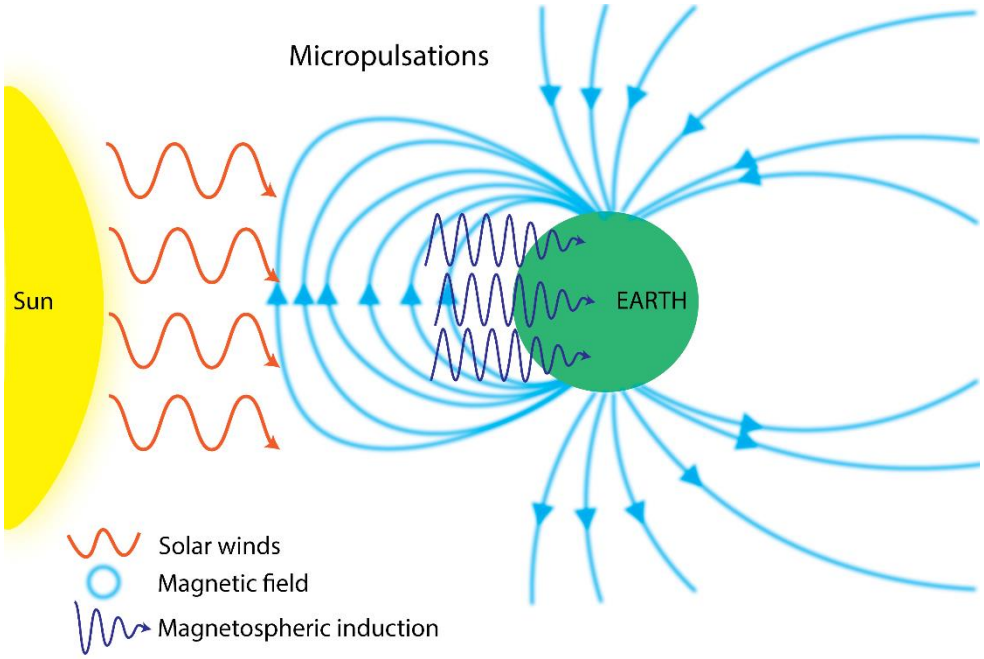


Figure 2.5. Micropulsations, caused by the interaction of solar winds and the Earth's magnetic field, induces telluric currents deep in the earth's surface through magnetospheric induction (modified from Constable, 2016).

Table 2.1. General micropulsations energy sources utilized in the MT method (modified from Vozoff (1991)).

Name	Frequency
Pc1	3-30 GHz
Pc2	0.3-3 GHz
Pc3	30-300 MHz
Pc4	3-30 MHz
Pc5	0.3-3 MHz
Pi1	3-30 kHz
Pi2	3-3000 Hz
sc, si	<3 Hz

2.3.3. MT data acquisition

When acquiring MT data, the following should be considered before planning a survey:

1. The depth of your target.
2. Conductivity contrast of your target.
3. Proximity to noise sources.
4. The conductivity of the overburden.
5. Strike orientation of your target.

When Considering the depth of a target we first must study the MT skin depth. Skin depth is defined as the depth at which the EM source field's exponential decay reduces the field to ≈ 37 % of its original value (Figure 2.6) (Chave and Jones, 2012). The skin depth is governed by the following equation:

$$\delta = \sqrt{\frac{2}{\omega \mu_0 \sigma}} \approx 0.5\sqrt{\rho T}, \tag{2.40}$$

where T represents the period. The skin depth equation states that the depth at which the EM source field penetrates is dependent on the bulk conductivity of the overlying lithology and the frequency of the source EM wave. Hence if the overlying lithology is conductive and/or the EM source wave is high frequency, the EM wave will only penetrate the ground a few meters. The EM source wave will penetrate the earth deeper if is low frequency and/or the overlying lithology is resistive. The skin depth will govern what type of MT system will be used for a specific survey (Figure 2.7). If the target is shallow (20 m-2 km deep) a high frequency (0,1-10000 Hz) AMT system setup should be used. If the target is deep (~100 m - >20 km) a low frequency (~0,0005 Hz-1 Hz) MT system should be used (Figure 2.8 and Figure 2.9).

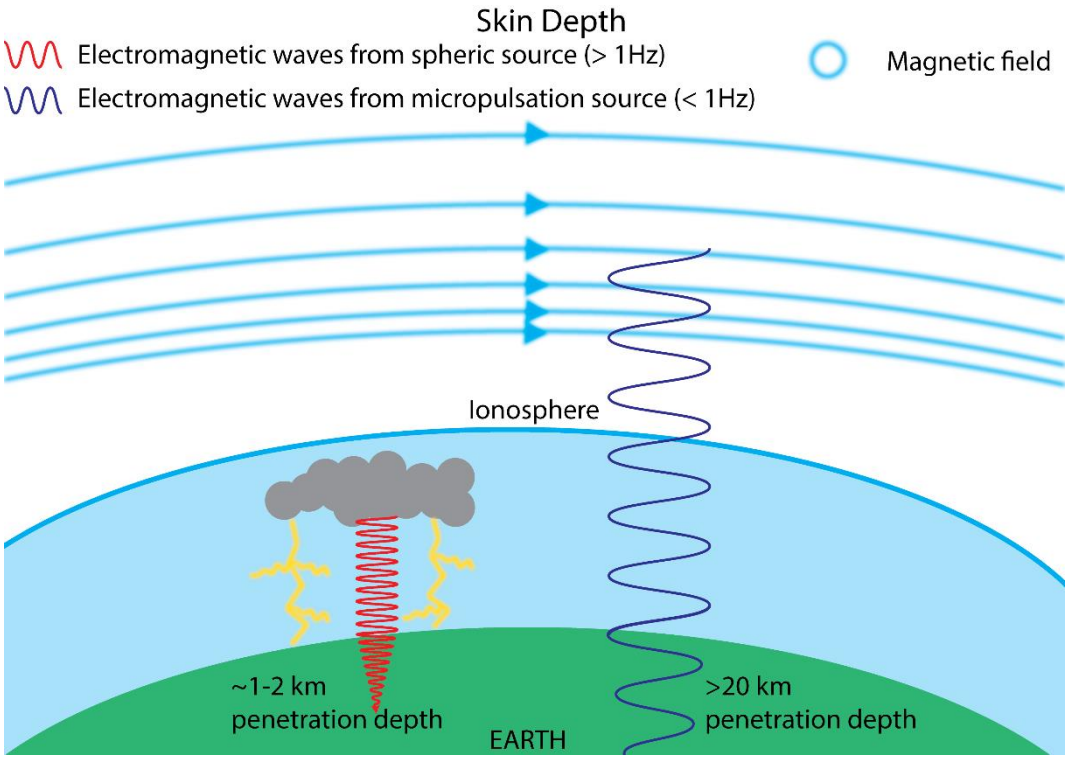


Figure 2.6. Skin depth for both spherics and micropulsations electromagnetic source fields. The exponential decay of the propagating electromagnetic wave is greater for the higher frequency (>1 Hz) spherics source fields than for the lower frequency (< 1 Hz) micropulsations source fields. Therefore, the penetration depth

for the spherics source fields are up to ~ 2 km deep while the micropulsations source fields can penetrate to depths > 20 km.

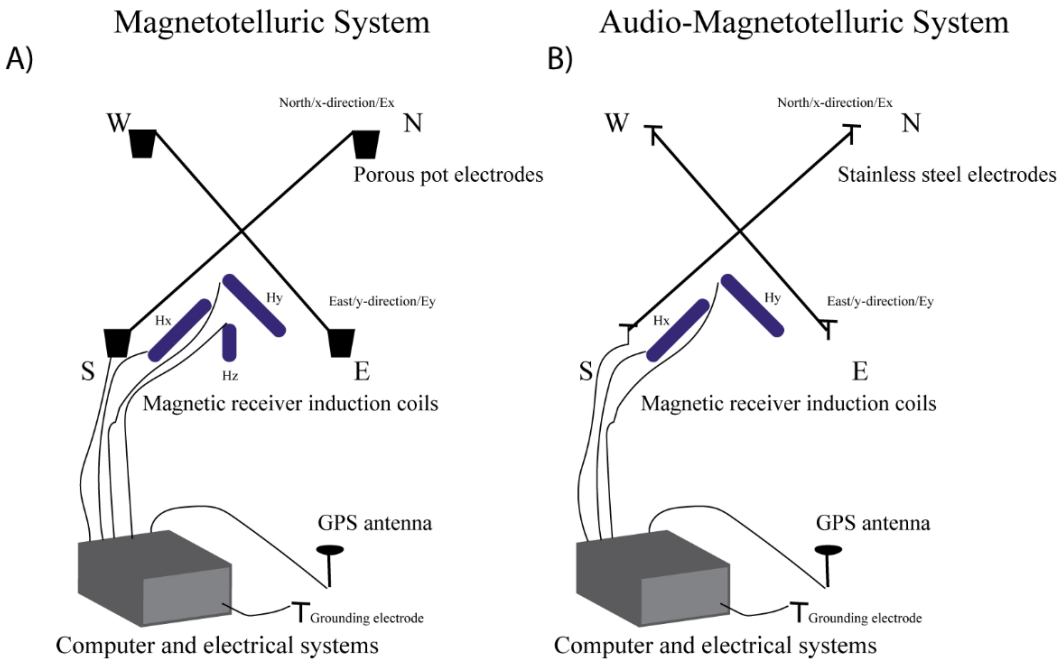


Figure 2.7. (A) A typical MT station setup with two dipoles in the X and Y direction and three induction coils in the X, Y and Z directions. This system will be used for deeper (up to ~40 km deep) exploration where the measured electromagnetic signals are < ~1Hz. (B) A typical AMT system also has two dipoles in the X and Y direction but only two magnetic induction coils in the X and Y direction. This system will be used for shallower (up to ~2 km deep) exploration where the measured electromagnetic signals are > ~1Hz. The Z direction magnetic induction coil is usually left out in AMT soundings since it is sensitive to high frequency noise in the magnetic field.

Figure 2.8 shows a resistivity model with a 10 Ω·m conductor 7.5 km deep, embedded in a 1000 Ω·m half-space. When calculating the forward MT response, in the AMT frequency range, the resistivity and phase data is 1-D in nature indicating that the deeper conductor is missed since the depth of investigation is too shallow (Figure 2.8(B)). When calculating the forward MT response, in the MT frequency range, the data is 2-D in nature indicating that the depth of investigation is deep enough to detect the conductor (Figure 2.8(C)).

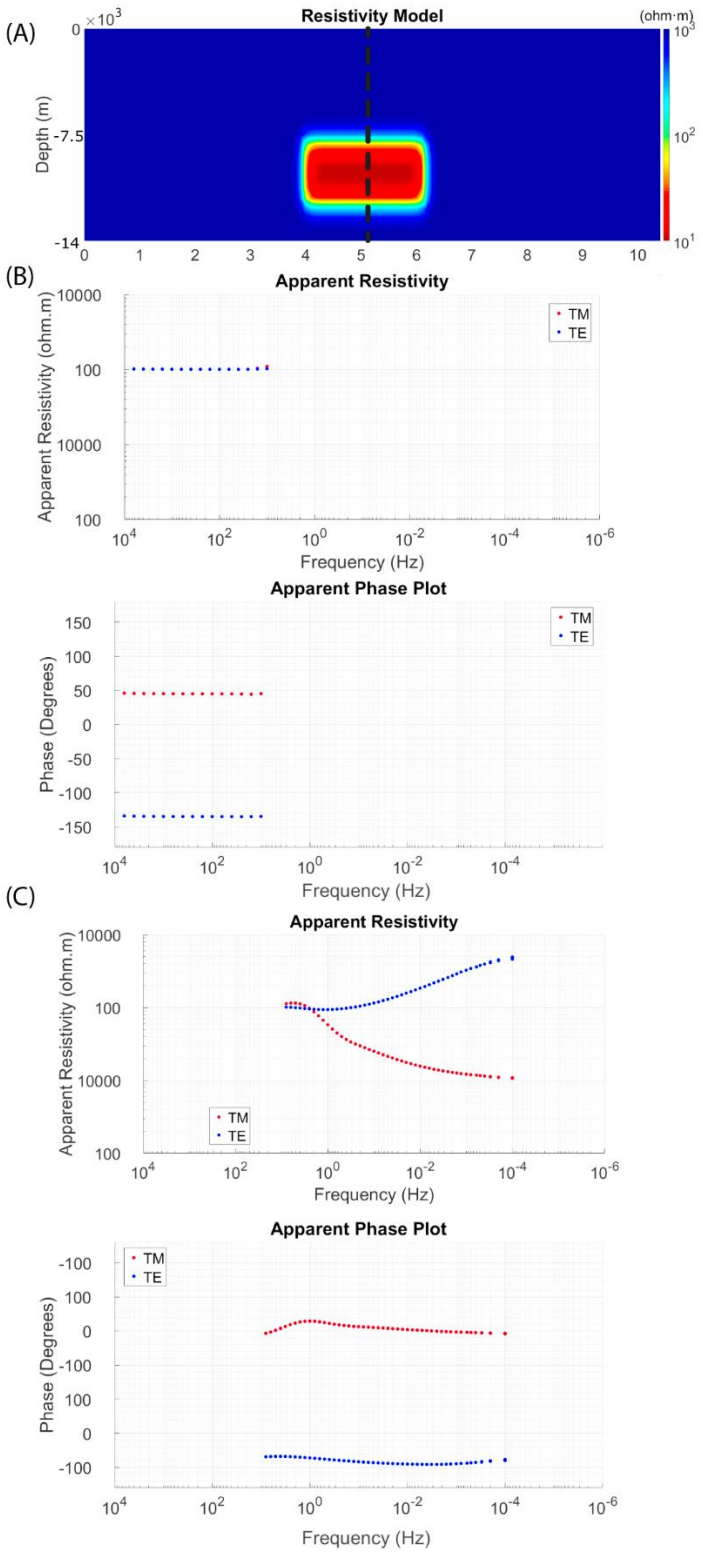


Figure 2.8. (A) Resistivity model with a 10 Ω·m conductor 7.5 km deep. (B) Resistivity and phase measurements between 10-10000 Hz. Data is 1-D in nature

indicating the absence of the deeper conductor. (C) Resistivity and phase measurements between 0.00001-10 Hz. Data is 2-D in nature, showing indications of the 7.5 km deep conductor.

The resistivity inverse model using AMT data, measured between 1-100000 Hz, only recovers the 1000 Ω·m half-space. The conductor is absent in the AMT resistivity inverse model (Figure 2.9(B)). While in the resistivity inverse model using the MT data the conductor is revered at a depth of 15 km deep (Figure 2.9(C)). This is a practical example of how the skin depth works in the MT method and why it is important to understand the capability of the MT system chosen for a specific target depth.

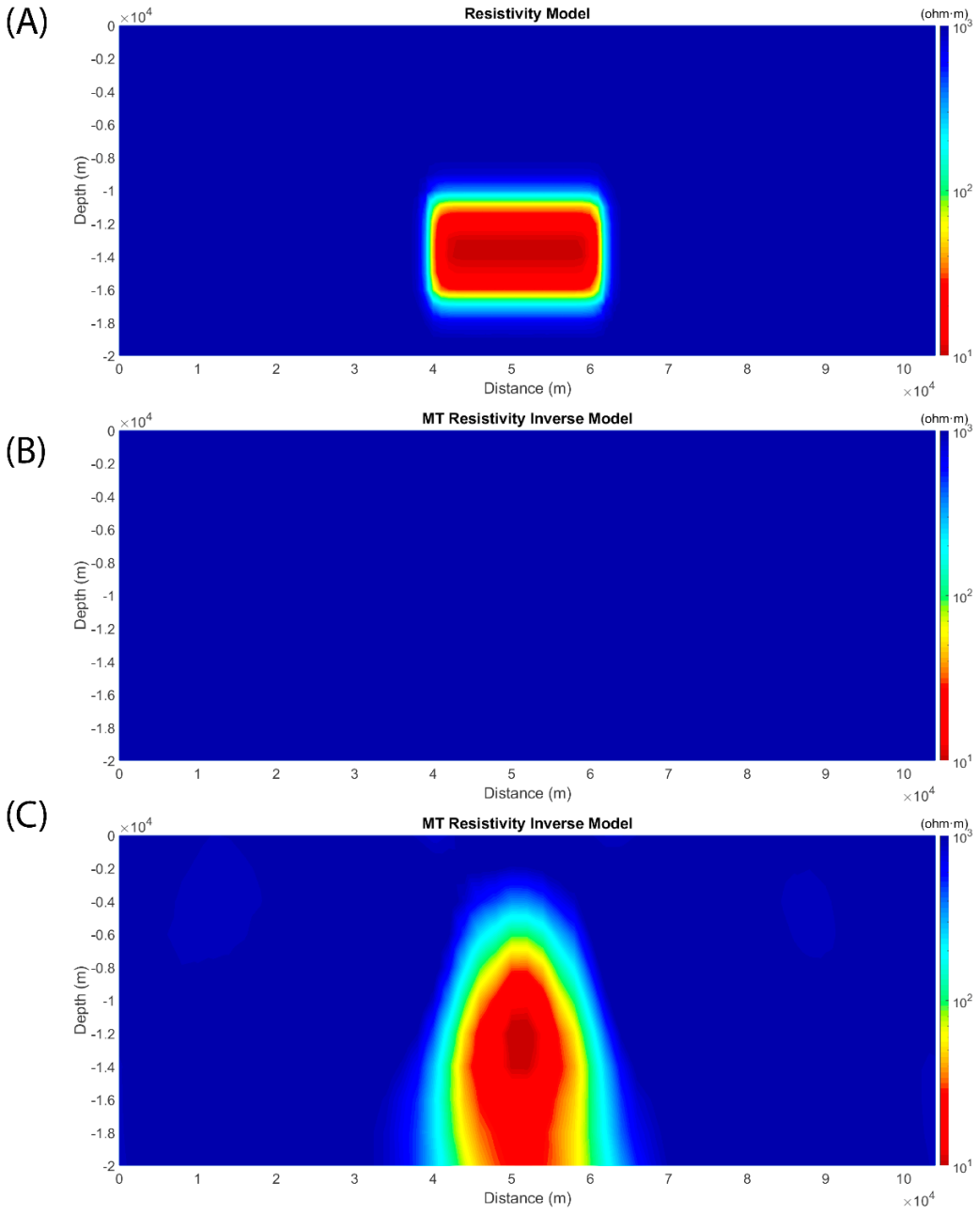


Figure 2.9. (A) True resistivity model, with a 10 Ω·m conductor 15 km deep. (B) Resistivity inverse model using AMT data measured between 1-100000 Hz. The conductor is absent in the resistivity inverse model since the MT data used is too high frequency to measure at the depth of the conductor. (C) A Resistivity inverse model using MT data measured between 0.00001-1 Hz shows the conductor at 15 km deep.

In electromagnetics, if conductors are present above resistors, the resistor is obscured or completely missed in calculated inverse models (Constable, and Weiss, 2006). Conductors can make resolving resistive structures difficult in the MT method (Pedersen and Gharibi, 2000). A real problem in MT data is when a conductive overburden distorts deeper resistors, dulling the MT sensitivity to these resistive structures as shown in Figure 2.10 (Park and Livelybrook, 1989). This is a result of the MT methods natural sensitivity to conductive layering and poor sensitivity to resistive features (Streich et al., 2010).

As described in chapter 2.2.1. the strike direction of the target lithology plays an important role when planning the strike of a survey. When we calculate the MT response function, we assume that the TM is perpendicular to lithological strike and the TE mode strikes parallel to the lithological strike. If the strike direction of TM mode is parallel to the lithological strike, the impedance tensor will have to be mathematically rotated. If the impedance tensor is left as is, the resolution and data quality collected by this MT station will be negatively affected. Hence, knowing the ideal strike direction for an MT survey is vital.

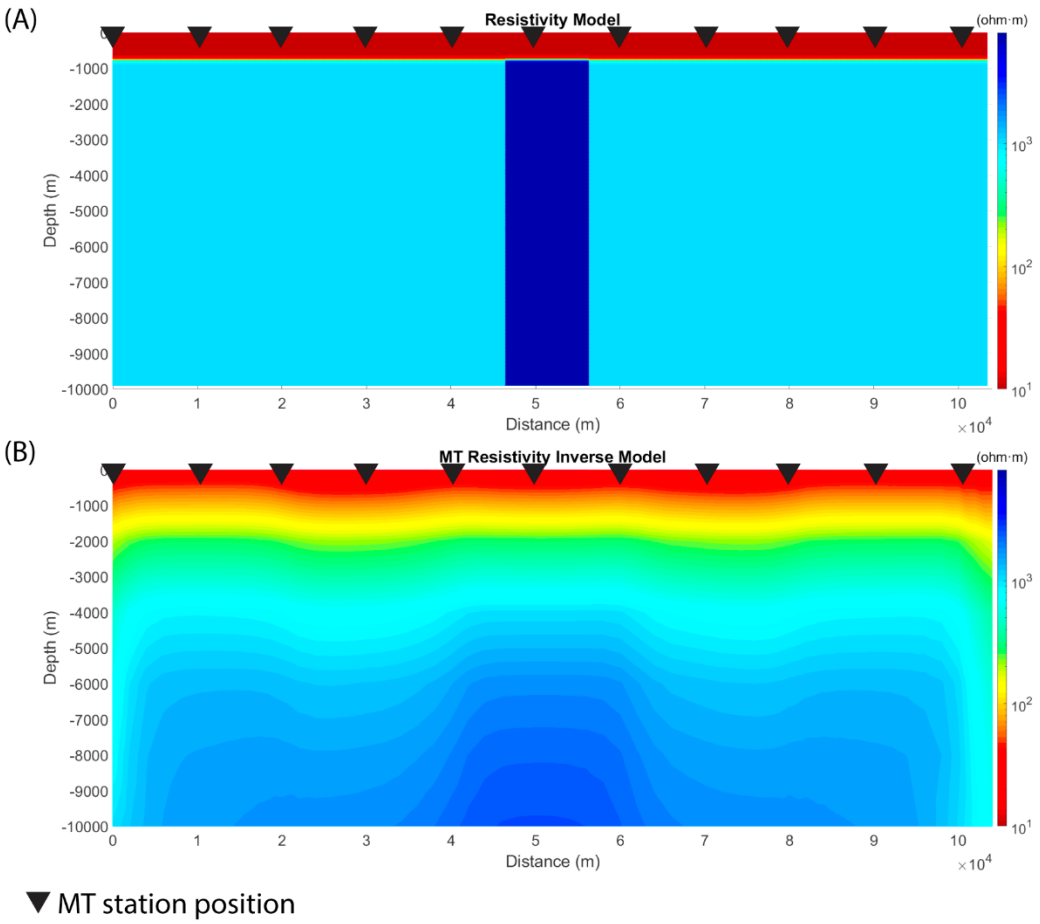


Figure 2.10. (A) True resistivity model with an 800 m thick 10 Ω·m conductive overburden above a 1000 Ω·m half-space. An 8000 Ω·m resistive vertical dyke is embedded within the half space. (B) MT resistivity inverse model shows how the conductive overburden obscures the resistive dyke beneath. The frequency range used is 0.00001 Hz – 100 000 Hz.

2.3.4. Static Shift Effect

The magnetotelluric geophysical exploration technique is vulnerable to static shift or telluric effects (Dentith and Mudge, 2014; Jones, 1988; Sternberg et al., 1988). The static shift effect is caused by heterogeneous electrical properties of geological structures with dimensions less than the skin depth at the highest frequency (near-surface) of a magnetotelluric sounding (Dentith and Mudge, 2014; Jones, 1988; Sternberg et al., 1988).

Electrical charges accumulate at the boundary of the conductive medium, resulting in a secondary electric field, independent of frequency, which leads to a shift in the detected resistivity values (deGroot-Hedlin, 1991).

This static shift effect can lead to misinterpretation of magnetotelluric sounding data due to the shifting of resistivity curves, which are interpolated from resistivity data points at different frequencies (Sternberg et al., 1988). Magnetotelluric sounding curves from sites nearby generally have a similar curvature but are often shifted parallel to one another by some unknown multiplier (Figure 2.11) (Sternberg et al., 1988). The MT phase is not affected by static shift. Therefore, MT specialists rely less on fitting the apparent resistivity and put more emphasis on fitting the phases during inversion modelling (e.g. Tietze et al., 2015).

This shift within the apparent resistivity curves will greatly distort resistivity inverse models since both the inverted resistivities and depth approximations will be shifted by the curvature shift (Sternberg et al., 1988; Dentith and Mudge, 2014). A magnetotelluric survey conducted over a local conductive body will have a more conductive resistivity curve compared to a magnetotelluric survey in the same area where the local conductive body is absent (Figure 2.11).

At high frequency (>100 Hz) the magnetic field is distorted less, but the electric field can be significantly altered by galvanic distortion and Eddy currents caused by local conductors (Sternberg et al., 1988). At lower frequencies, the electric field tends to be the only field affected by galvanic distortion (Sternberg et al., 1988; Jones, 1988). Therefore, the static shift effect is unperturbed with large

scale inhomogeneity, since this would cause a frequency-dependent shift instead of a parallel shift in the apparent resistivity curves (Sternberg et al., 1988). Hence the static shift problem is most prominent during near-surface magnetotelluric measurements (Sternberg et al., 1988; Jones, 1988). The issue is that our most advanced magnetotelluric systems can only start taking readings around 30 m deep, hence a local body within the first 30 m that might be causing the static shift will be undetected and the error will go unnoticed.

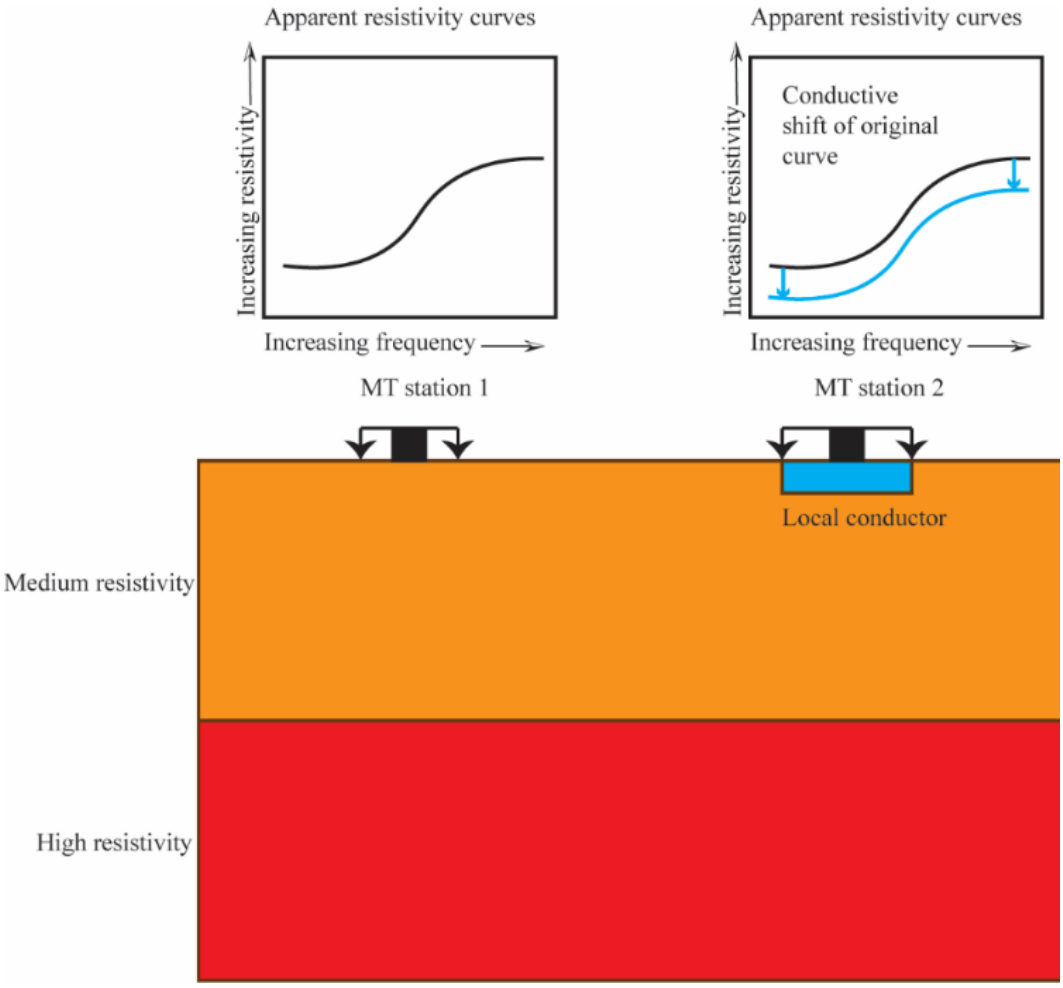


Figure 2.11: Example of the static shift effect over a local conductive body. Local near surface conductor shown in blue. The geological model consists of an upper medium resistive lithological layer, in orange, underlain by a highly resistive half-space, shown in red. The static shift effect is shown within the apparent resistivity curve plot.

2.3.5. Basic description of MT processing

2.3.5.1. Calculating the MT response function from field data

Typically, the five components (three magnetic and two electric field components) measured at an MT station is in the form of a time series in the specific MT systems frequency range. Generally, there is a notch filter applied at either 50 Hz or 60 Hz depending on the power line frequency of the country that the data is collected in. The time series is then split up into fixed time length segments and are cosine tapered. A Fourier-transform is calculated for each segment and the Fourier coefficients are corrected for any instrument noise. The segments are stacked to reduce random noise and the auto-spectra and cross-spectra are calculated. From these statistical parameters, the MT response function is calculated. A more detailed description can be found in Chave and Jones (2012) and Weckmann et al., (2005).

2.3.5.2. MT impedance tensor rotation

Once the TM and TE modes are assigned, the TM mode must be rotated perpendicular to geological strike. The TE mode should be rotated parallel to geological strike. The MT impedance tensor can be rotated using the following rotation matrix calculation:

$$\mathrm{Z}^{R} = \mathrm{RZR}^{\mathrm{T}}, \tag{2.41}$$

where Z and Z^{R} is the MT impedance and rotated MT impedance tensor respectively. R is the rotation matrix given as follows:

$$\mathrm{R} = \begin{pmatrix} \cos\theta & \sin\theta \\ -\sin\theta & \cos\theta \end{pmatrix}, \tag{2.42}$$

where θ is the rotation angle. The rotation angle is determined by the offset angle between the resistivity boundary and the impendence tensor coordinate frame.

2.3.5.3. Masking spikes and dead band data

The next step in MT processing is to mask data that is saturated by cultural noise or where very little energy is present in the dead band or high frequencies (Figure 2.12). This is to guarantee a smooth MT response function for further modelling and analysis (Figure 2.13). Traditionally error bars would also be used to characterise spikes but the AMT system used in the thesis, the Geometrics EH-4 Stratagem, does not export error bars on field data.

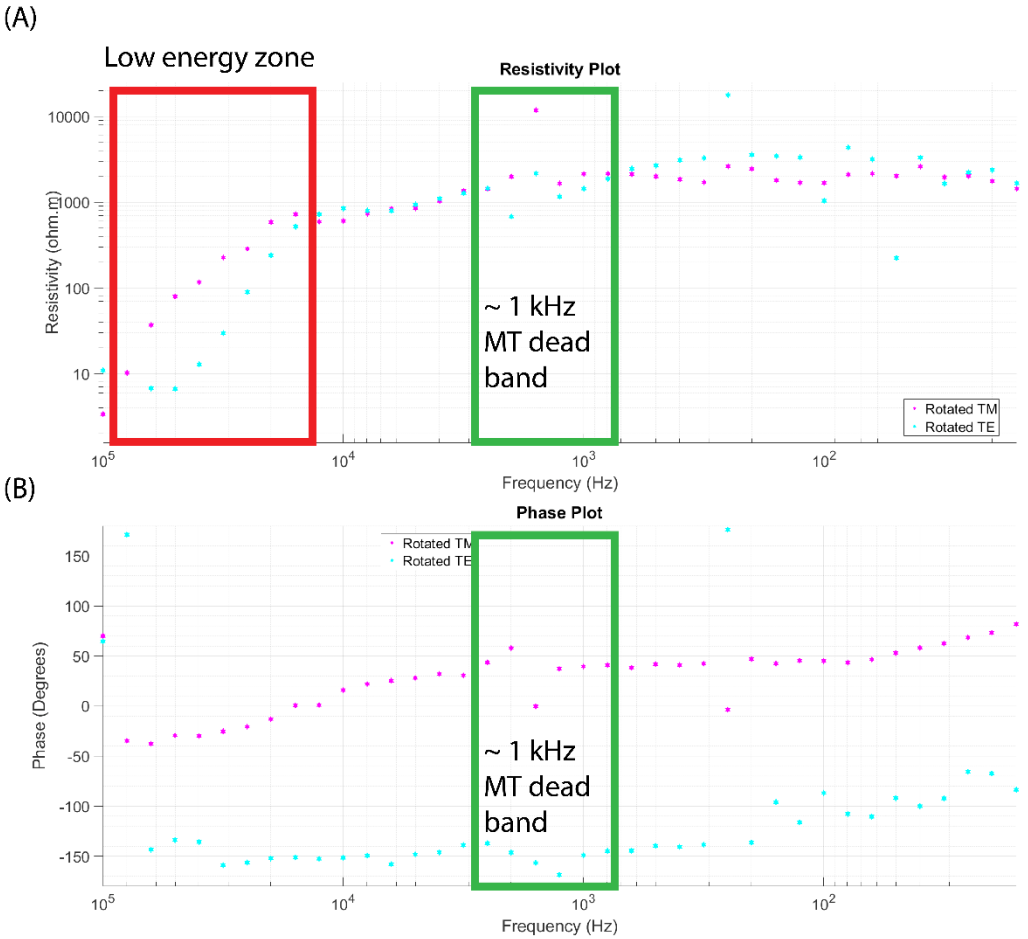


Figure 2.12. (A) Rotated resistivity plot of MT data. (B) Rotated phase plot of MT data. The green block shows the ~ 1 kHz dead band that affects MT data quality and the red block shows low energy levels in the high frequencies.

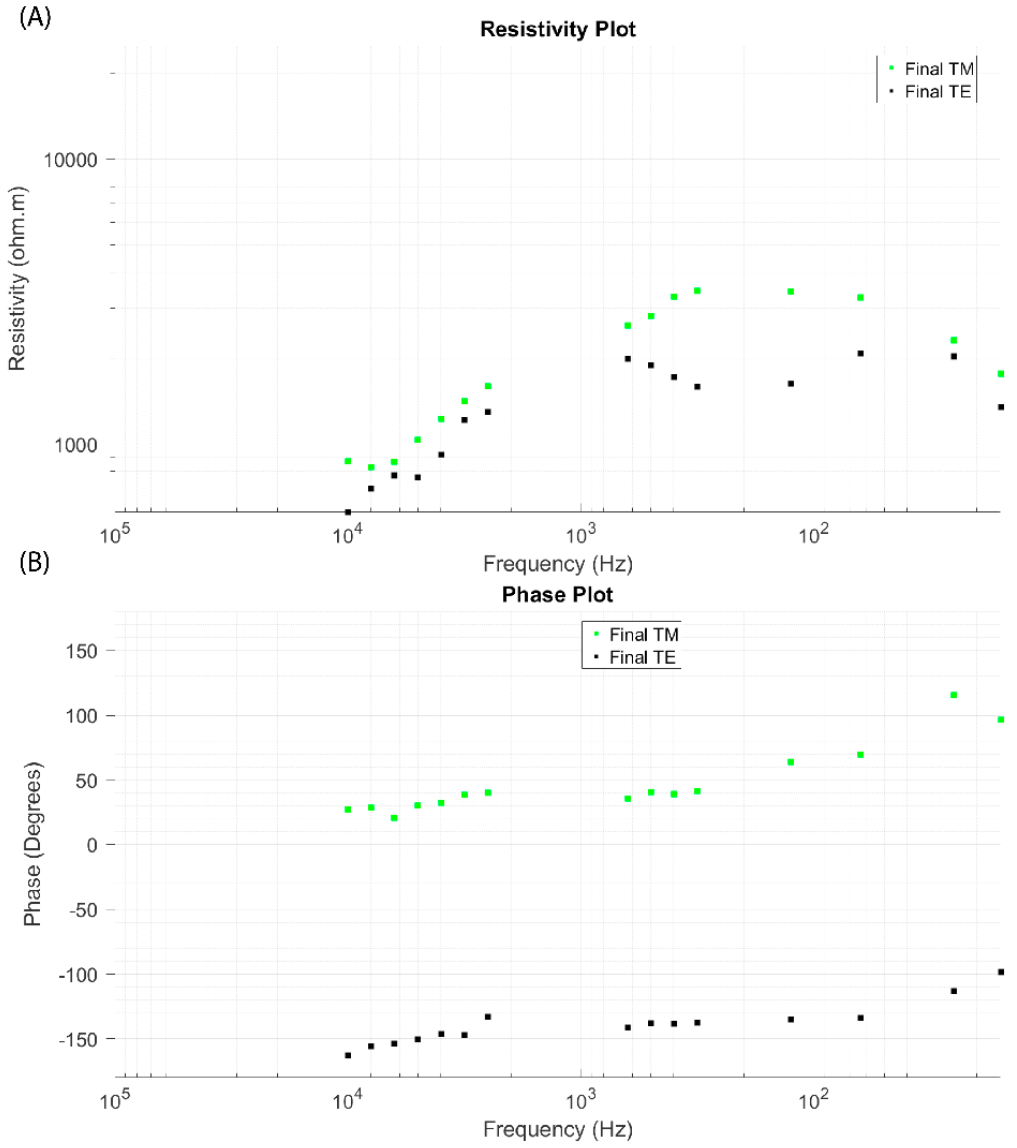


Figure 2.13. (A) Rotated and edited resistivity plot of MT data. (B) Rotated and edited phase plot of MT data.

2.4.Electrical resistivity tomography

2.4.1. Electrical resistivity tomography theory

The resistivity of a wire is given by:

$$R = \frac{\rho L}{A}, \tag{2.43}$$

where ρ is the resistivity, L is the length of the wire and A is the cross-sectional area of the sample and R is the measured resistance (Herman, 2001).

The four-point collinear resistivity method, which most modern-day electrical resistivity tomography (ERT) meters make use of, uses four electrodes (Figure 2.14) (Majid, 2011). Four electrodes are placed on the surface of a material and a known current is then passed through the two outermost current electrodes (Majid, 2011). A voltmeter is connected to the two inner electrodes and a voltage is observed. The resistivity of the earth (ρ) can be measured using this four-point collinear method, which is governed by the following equation modified from equation (2.43):

$$\rho = 2\pi a K \frac{V}{I}, \tag{2.44}$$

where a is the distance between each electrode, V is the potential voltage, I is the current and K is the geometrical correction factor, which is given by:

$$K = \left[\left(\frac{1}{E_1E_2} - \frac{1}{E_2E_4}\right) - \left(\frac{1}{E_1E_3} - \frac{1}{E_3E_4}\right)\right]^{-1}, \tag{2.45}$$

where E stands for electrode, E_1E_2 is the distance between electrode 1 and electrode 2, E_2E_4 is the distance between electrode 2 and 4, E_1E_3 is the distance

between electrode 1 and 3 and E_3E_4 is the distance between electrode 2 and 4 (Figure 2.14).

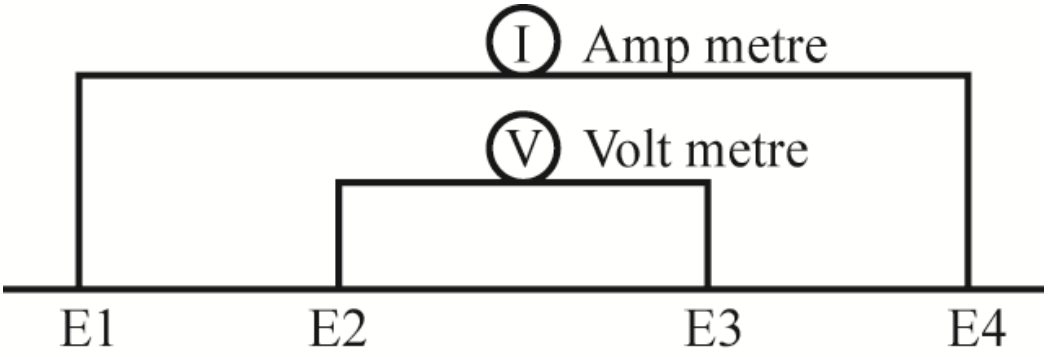


Figure 2.14: Four-point electrode configuration sketch, where E represents electrodes.

The resistivity of lithology, measured by ERT surveys, is again affected by porosity, hydraulic permeability, moisture content, type of minerals that form the lithology, temperature and phase of pore fluids, concentration of dissolved electrolytes and the amount and composition of colloids (Brace and Orange, 1968; Herman, 2001).

Minerals found in clay and metal ores are generally conductive and decrease the measured resistivity within the lithology. Highly resistive minerals such as quartz (SiO_2) increase the resistivity within the same lithology (Herman, 2001; González-Álvarez et al., 2016). Minerals such as pyrrhotite (FeS), pyrite (FeS_2), graphite (C), galena (PbS) and magnetite (Fe_3O_4) are examples of conductive minerals (González-Álvarez et al., 2016).

Pore space and pore geometry of a lithology also play a significant role in the resistivity of the lithology. Joints, fractures, intergranular voids and vugs affect the porosity of lithology, which then governs the resistivity of that lithology. The

greater the porosity of lithology the greater the volume of fluid the lithology can hold, which will result in a reduced resistivity value within that lithology (Herman, 2001; González-Álvarez et al., 2016).

The salinity of the fluid in pores will also play a role in the resistivity of a lithology. The greater the concentration of ions in the fluid, the greater the conductivity within the lithology (Herman, 2001). Other factors including temperature, saturation capacity and even the alteration of the lithology will affect its ability to conduct current (Herman, 2001; González-Álvarez et al., 2016).

Hence, due to all these features within lithology, there can be a large range of resistivity values for a single type of lithology. This large variability of resistivity within lithology means that lithology of the same type can have different values for resistivity measured by the ERT method.

2.4.2. Types of direct current resistivity method surveys

Two- and three-dimensional ERT methods make use of an array of electrodes positioned in the ground to input a current into the earths subsurface (Figure 2.15), as previously described in the four-point method. The potential that results from the voltage input is measured and used to calculate the resistivity of the underlying geology. The depth of the resistivity measurements is generally calculated to be around ~20 % of the maximum length between the first and last electrode in a four-point electrode array. This depth estimate is affected by the conductivity of the overburden and the total length of the array used.

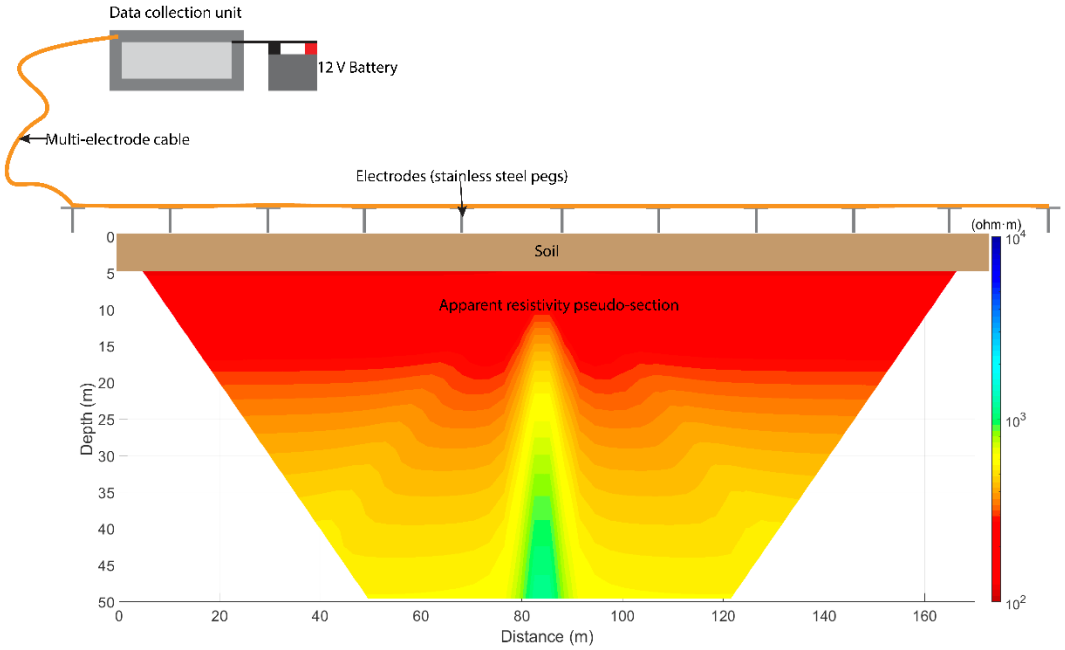


Figure 2.15: Sketch of a typical two-dimensional resistivity array setup. The potential difference between electrodes is used to calculate an apparent resistivity value as shown in the apparent resistivity pseudo-section.

The ERT methods make use of multiple array types (Figure 2.16), where the different arrays have diverse advantages and disadvantages (Furman and Ferré et al., 2003). The most common array types are the Wenner, dipole-dipole, Schlumberger, pole-pole and pole-dipole (Binley and Kemna, 2005).

The pole-pole array has the deepest depth of investigation (how deep the array can penetrate the lithology) but the poorest resolution. While the dipole-dipole array is best-suited mapping vertical structure but poor in mapping horizontal structures. The Wenner and Schlumberger array is the best at resolving vertical changes but poor at resolving horizontal changes (Dentith and Mudge, 2014).

The resolving power of a certain array is determined by how the equipotential surfaces and electrical field lines interact with different types of geological structures (Figure 2.17). The change in the recorded potential is determined by

how the field lines deflect and interact with lithology, hence decreasing or increasing the electric field flux detected at a certain point by the array (Dentith and Mudge, 2014). If the electric field lines are undisturbed by lithology, potential will stay constant and information on the underlying lithology will be absent.

Therefore, each array is suited for specific types of near surfaces geological structures. If the incorrect array is chosen for the type of geological structure, the resulting geological model will be incorrectly interpreted.

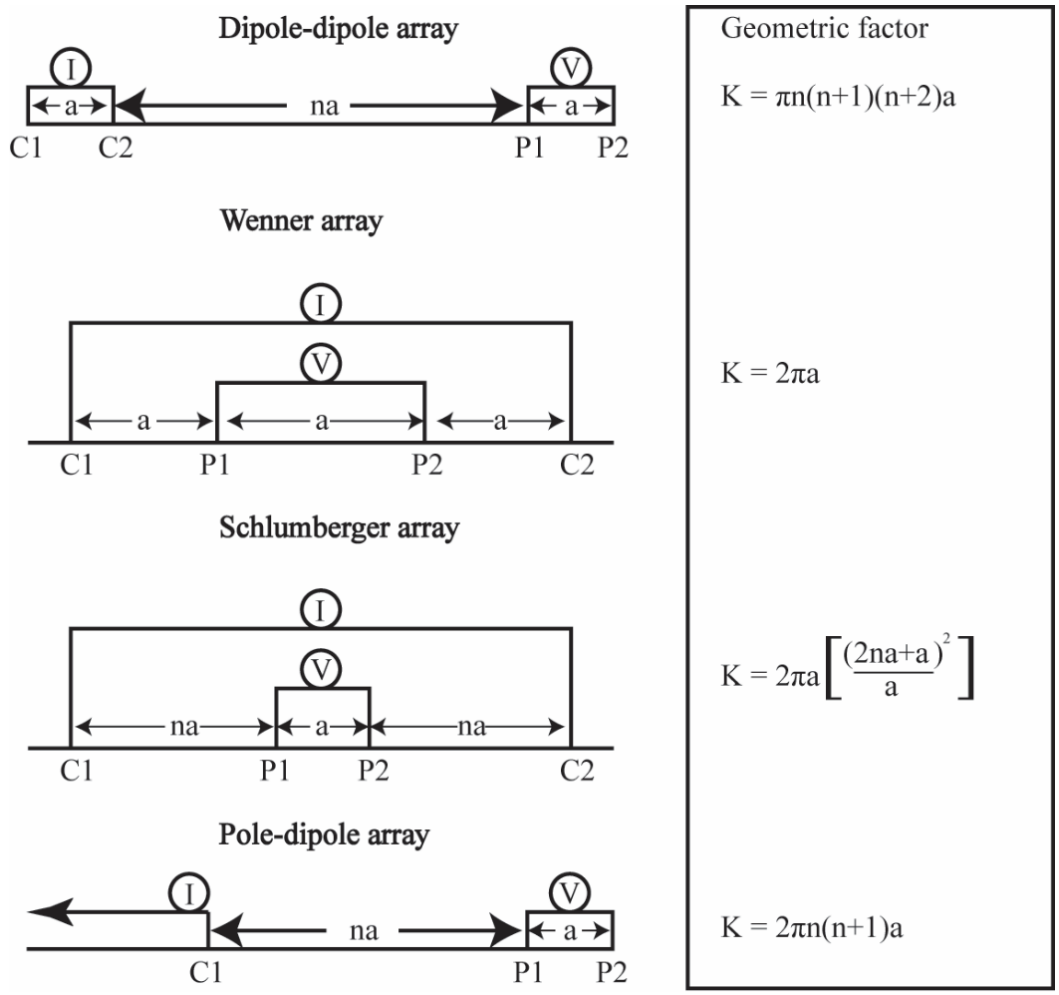


Figure 2.16: Common ERT configurations and corresponding geometric factors (modified from Dentith and Mudge, 2014). C represents current electrodes, P represents potential electrodes, a is the spacing between electrodes and n is a spacing modifier as the array is extended. I is the amp meter for the applied current and V is the voltmeter required for measuring the change in potential.

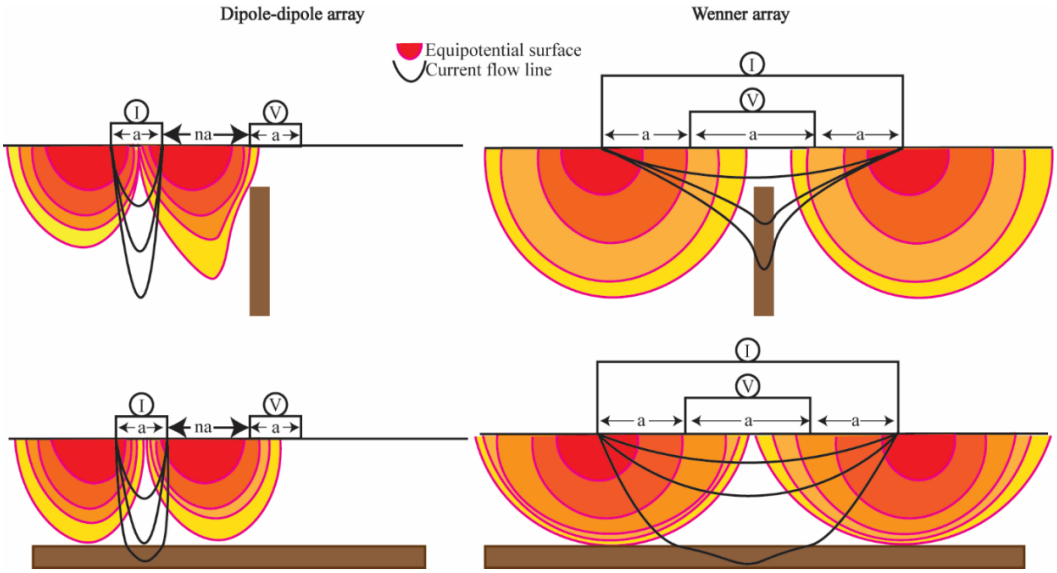


Figure 2.17: A dipole-dipole and Wenner array equipotential surface interaction comparison for both vertical and horizontal conductive geological structures represented by the brown rectangles, the black line represent current flow lines (modified from Dentith and Mudge, 2014).

2.2.3 Basic processing of ERT data

ERT data is one of the easier geophysical data sets to process if the data quality is good. Sometimes all that is needed is to remove spikes in the data that is usually caused by poor electrode ground contact or a faulty electrode (Figure 2.18(A)). If the ERT data is noisy due to cultural noise, smoothing can be performed on the data set. Once the smoothing is complete any extra spikes can be removed but keep in mind that smoothing a data set will diminish the resolution of the ERT survey (Figure 2.18(B)).

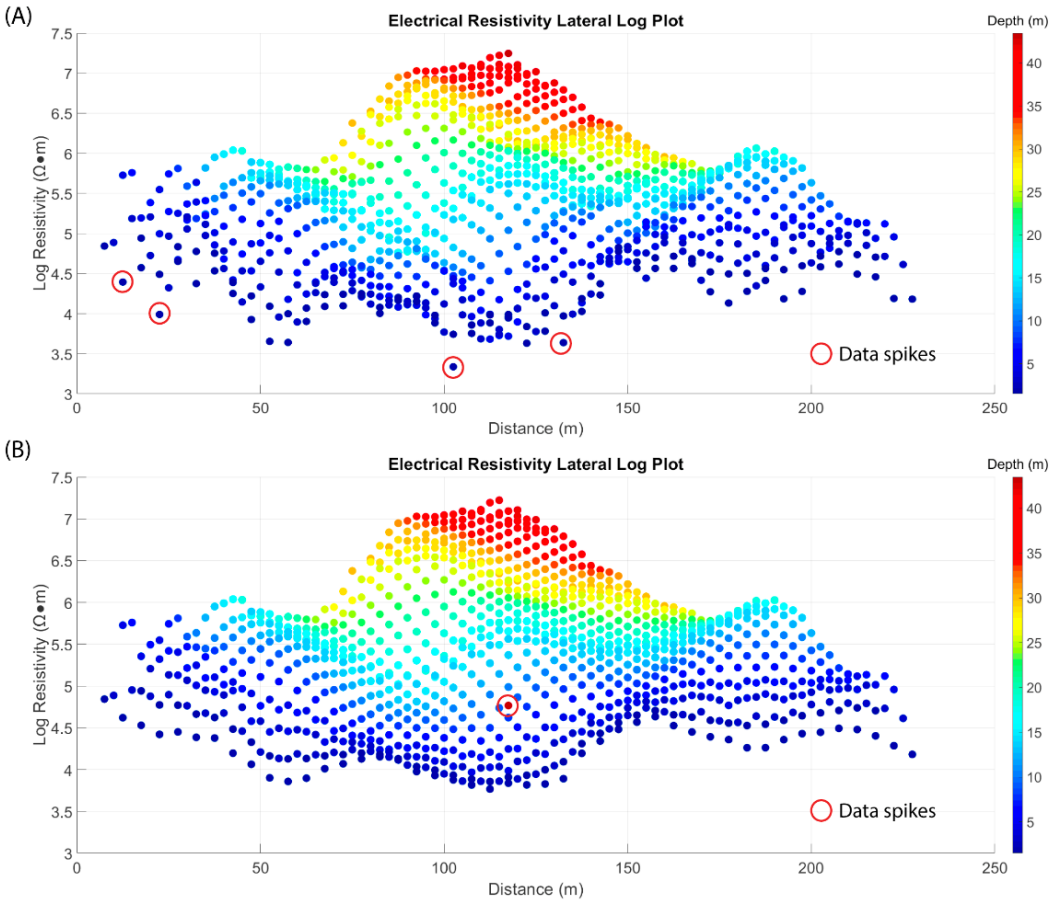


Figure 2.18. (A) Electrical resistivity tomography raw data plot. (B) Electrical resistivity tomography smoothed and spiked removed data.

2.5. Basic Inversion Theory

2.5.1. Introduction

Geophysical surveys and data sets are widely used in solving practical engineering, exploration, site safety analysis and environmental problems. In most geophysics modeling there is a heavy reliance on the inversion technique due to large data sets that need to be modeled and interpreted in a set amount of time.

The inversion technique makes use of a set of geophysical observations and statistically predicts the parameters associated with a hypothesized earth model (Lines and Treitel, 1984; Sambridge, 1999). For example, Figure 2.19 shows magnetic data collected over a dyke. The observed data is then used in an

inversion algorithm to calculate a magnetic susceptibility inverse model of the target dyke seen in Figure 2.19.

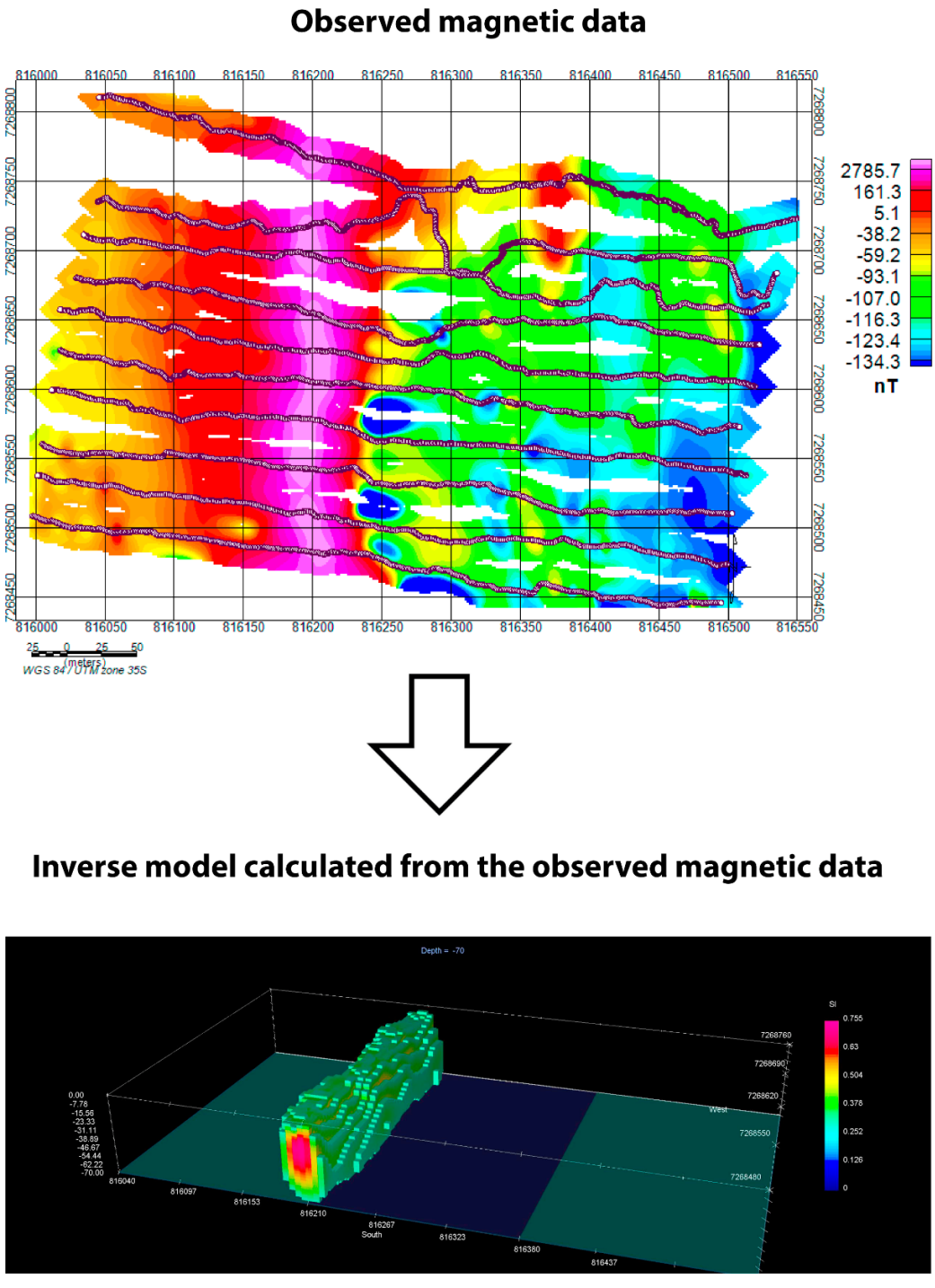


Figure 2.19. Magnetic data collected in the field is used to calculate a magnetic susceptibility 3-D inverse model. White dots represent magnetic data points. The magnetic susceptibility 3-D inverse model shows the isovolume of the dyke that we are interested in.

Inversion techniques are growing in popularity in the Earth science due to the inversion techniques ability to provide rapid constraints on lithological structures, from geophysical data sets (Sambridge, 1999).

However, inversion algorithms are affected by non-uniqueness issues (Moorkamp et al., 2011). Earth models developed by inversion data are generally affected by noise and in any given situation, several models can fit the observed solution space, adding to ambiguity present within the geophysical models. The ambiguity arises since most inverse models will have a digitized earth model with more cells than observations making it almost impossible to find a unique solution, this is known as the problem of non-uniqueness. Other information such as borehole data is generally included in inverse models to reduce the ambiguity and the number of proposed models that fit the observation data. Geophysical inverse theory is still a popular topic of research, particularly 3-D inverse models.

To calculate a useful inverse model from geophysical data the following is needed:

- Observed geophysical data.
- Any prior information, such as borehole data, to assist in the constraining of the inverse model.
- A suitable inversion algorithm.

2.5.2. The inversion method

The inversion algorithm is controlled by an objective function that ultimately evaluates the best inverse model, that fits a criterion, for the provided observed data and is one of the few ways a priori information can be included in the

inversion process. To visualize the role of the objective function, we will go through a simple 1-D MT inversion algorithm I developed for this purpose (Appendix A.2.1. and A 2.2.).

The inversion algorithm is coded for one-dimensional magnetotelluric data and makes use of the following ridge regression objective function, also known as the model change vector,

$$\delta m = (J^T W^T W J + KI)^{-1}\left(J^T W^T W (d^{obs} - F[m])\right). \quad (2.46)$$

Where d^{obs} is the observed data, $F[m]$ is the calculated response of the model parameters (Appendix A.1), K is the dampening factor matrix, I is the identity matrix, J is the sensitivity matrix and W is the weighting matrix (Penrose, 1955; Farquharson and Oldenburg, 1998). Smoothing constraints are absent in the algorithm to prevent the smoothing out of edges within the inverse models.

The surface apparent resistivity function is stated as,

$$\rho_0(\omega) = \frac{1}{\omega \mu_0} |Z_0(0)|^2, \quad (2.47)$$

where ω is the angular frequency, μ is the magnetic permeability and $Z_0(0)$ is the surface magnetotelluric impedance tensor (Chave and Jones, 2012; Berdichevsky and Dmitriev, 2002).

The surface phase function is given as,

$$\varphi_0(\omega) = \tan^{-1}\left(\frac{E(\omega)}{H(\omega)}\right) = \tan^{-1}\left(Z_0(0)\right), \quad (2.48)$$

where $E(\omega)$ and $H(\omega)$ are the electric and magnetic fields respectively as shown on pages 343-355 in Telford et al., (1990).

The sensitivity matrix, also known as the Jacobean matrix, is a set of first-order partial derivatives of the forward function, equation 2.47 and 2.48, with respect to the inverting parameter cell resistivity or thickness. The sensitivity matrix can be calculated numerically but for the discussed inversion an analytical solution is derived and used. The partial derivative for the apparent resistivity forward function described in equation 2.47 is derived as:

$$\frac{\partial F[m_n]}{\partial m} = \frac{\partial \rho_0(\omega)}{\partial Z}\frac{\partial Z}{\partial \rho_m} = \frac{Z}{\sqrt{\rho_0 \mu \omega}}, \tag{2.49}$$

where ρ_m is the layer resistivity of the conductivity model. The partial derivative for the phase forward function, stated in equation 2.48, has also been derived and follows as:

$$\frac{\partial F[m_n]}{\partial m} = \frac{\partial \varphi_0(\omega)}{\partial Z}\frac{\partial Z}{\partial h}, \tag{2.50}$$

$$\frac{\partial \varphi_0(\omega)}{\partial Z}\frac{\partial Z}{\partial h} = \left(\frac{i\omega\mu}{Z_2^2+1}\right)\operatorname{csch}^2\left[ik_1 h - \coth^{-1}\left(\frac{k_1 Z_2}{\omega\mu}\right)\right], \tag{2.51}$$

where Z_2 is the impedance between the second and third model conductivity layers. k_1 is given as:

$$k_1 = \sqrt{\omega\mu_0\sigma_1}, \tag{2.52}$$

σ_1 is the conductivity of the first model layer. Once the partial derivatives are calculated for the respective forward functions, the partial derivatives are placed into a matrix as follows:

$$J = \begin{bmatrix} \frac{\partial F[m]_1}{\partial m_1} & \cdots & \frac{\partial F[m]_1}{\partial m_n} \\ \vdots & \ddots & \vdots \\ \frac{\partial F[m]_n}{\partial m_1} & \cdots & \frac{\partial F[m]_n}{\partial m_n} \end{bmatrix}. \tag{2.53}$$

The sensitivity matrix is an n by m matrix, where n is the number of calculated data points and m is the number model parameters. The model parameters in these two inversion algorithms are the layer resistivity and layer thickness, respectively.

The objective function also makes use of a dampening matrix K. The dampening matrix K is a diagonal matrix occupied with dampening factors relating to the sensitivity matrix by the following equation:

$$K_0 = \sqrt{\sum_1^n \sum_1^m J_{n,m}^2}. \tag{2.54}$$

The dampening factors prevent singularities within the $J^T J$ matrix and minimises unbound oscillations throughout the inversion (Lines and Treitel, 1984). The damping matrix K is dynamic since the dampening factors are changed after every iteration depending on the calculated root mean square error (RMSE). If RMSE is increasing, the dampening factors are doubled but if the RMSE is decreasing the dampening factors are halved. The RMSE equation used in this inversion is modified from Willmott et al., 1985:

$$RMSE = \sqrt{\frac{\sum_1^n (d^{obs} - F[m])^2}{n}}. \tag{2.55}$$

A proportional weighting matrix is used for both inversions. This weighting matrix is well suited for a resistivity inversion since the values of the parameters can vary widely and the weightings prevent large values from dominating the inversion. The weightings are calculated as follows and are set to a fixed proportion of the observed data, in this case 1% is used:

$$W_n = \frac{100}{d^{obs}}. \tag{2.56}$$

This inversion algorithm also makes use of a set of Monte Carlo generators which assist in calculating the best starting model for the inversion process. The model with the lowest RMSE is chosen as the starting model for the least square's inversion (Figure 2.20).

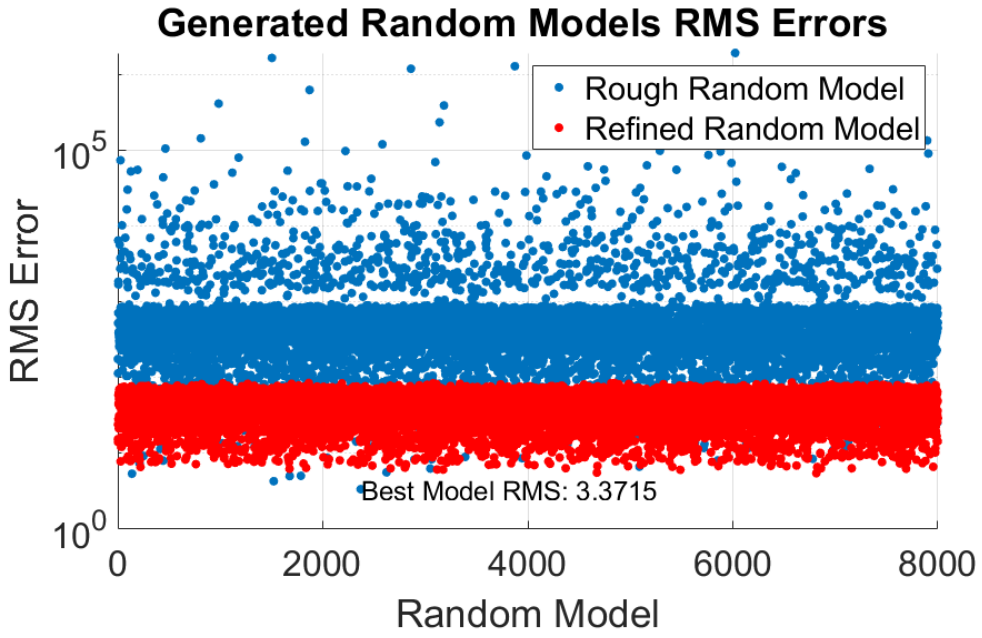


Figure 2.20. A plot shows the root mean square (RMS) error for models calculated using the Monte Carlo simulation.

The algorithm has three different forms, it can invert just layer thickness (Appendix A.2.1.), layer resistivity (Appendix A.2.2.) or a joint inversion where both the layer thickness and resistivity are inverted (Appendix A.2.3.).

An algorithm flow chart for the Monte Carlo starting models and the least-squares inversion algorithm is shown in Figure 2.21 and Figure 2.22. Figure 2.23 shows the results of running the inversion algorithm to calculate a model that fits the observed data. The green line is the real resistivity earth model that we are trying to find with the inversion calculation. The blue line shows the calculated inverse

resistivity model, the inverse algorithm was able to find a resistivity model that fits the real resistivity earth model observation data within an RSME of 0.01.

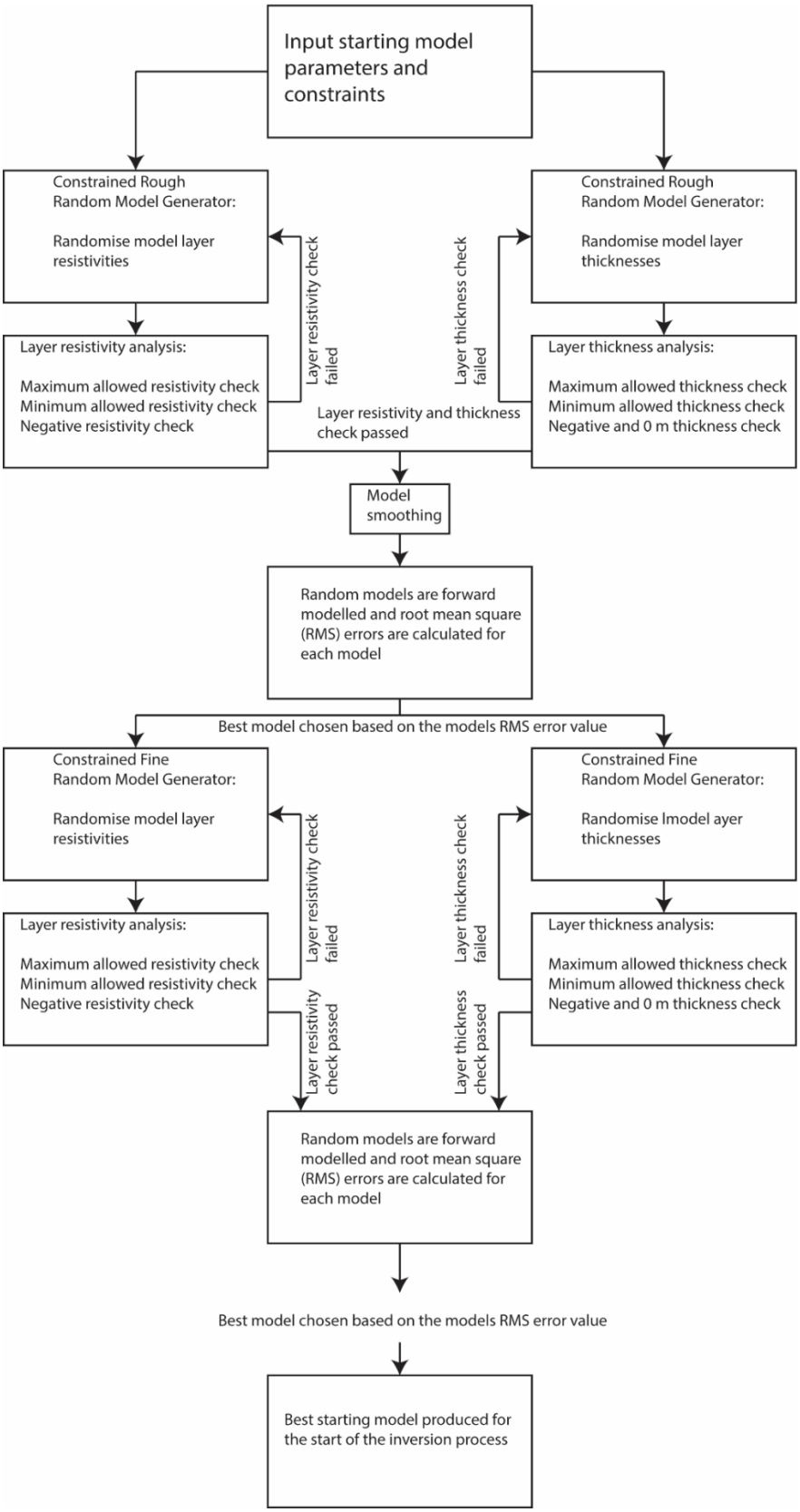


Figure 2.21. Algorithm workflow map for the Monte Carlo random model gubernators

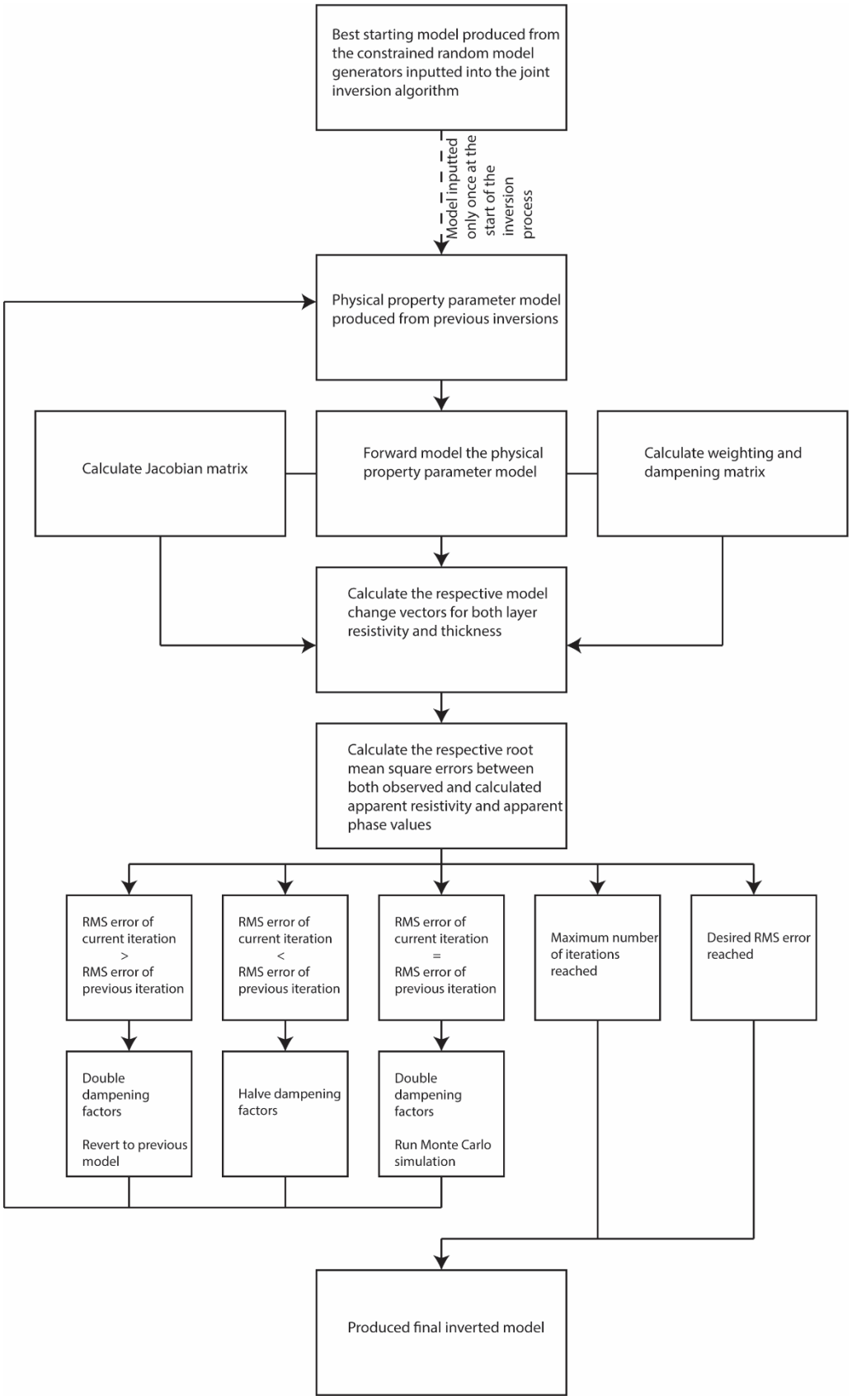


Figure 2.22. Algorithm workflow map for the least squares inversion.

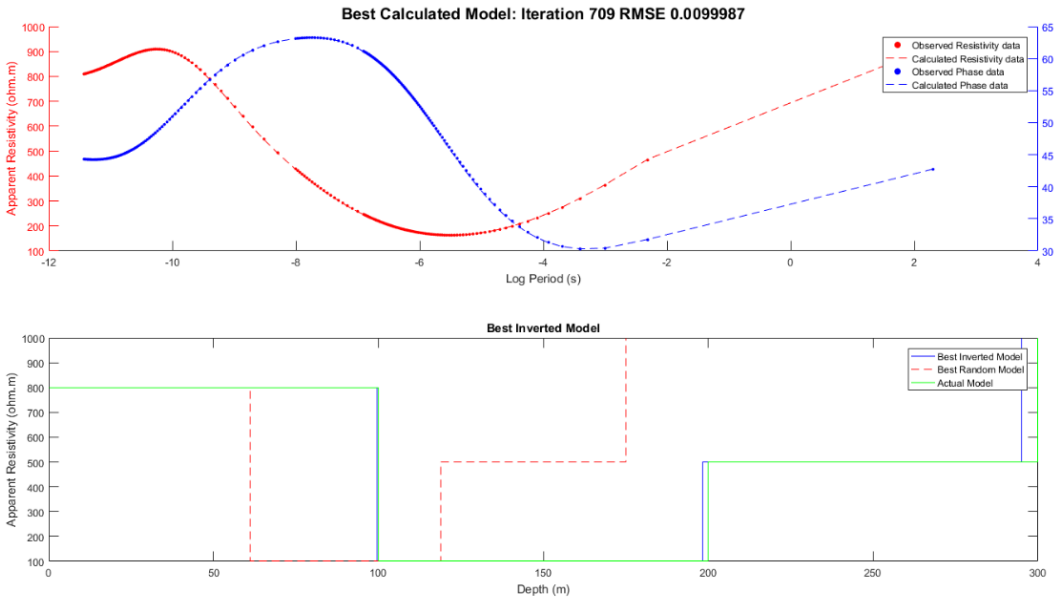


Figure 2.23. A 1-D MT inverse model calculated using the algorithm developed in this thesis (Appendix A.2.). The green line represents the actual resistivity model, the red dashed line is the starting model calculated from the Monte Carlo simulations and the blue line is the lowest root mean square resistivity inverse model.

2.5.3. Joint and cooperative inversion methods

An attempt in reducing the ambiguity of the inversion technique resulted in the formulation of multiple solver inversion algorithms. The inversion of two different datasets is generally more robust since each method is affected by different types of noise and if one method is insensitive and struggles to resolve a certain type of geological unit the supplementary method usually can (Moorkamp et al., 2010). There are two main categories that the multiple solver inversion algorithms fall in, namely joint inversion and cooperative inversion.

Joint inversion, sometimes known as simultaneous inversion, is an inversion process where different types of data are inverted simultaneously with a single inversion algorithm. The data sets used usually share some commonality between

physical property changes and different resolutions otherwise the joint inversion is unconstrained. If the relationship between the physical properties is unreasonable a useful geological interpretation from the model is difficult to defend. For example, seismic and gravity data are usually jointly inverted, since with increasing lithological density we have a larger gravity response and faster seismic travel times, therefore the different data sets can be used to constrain each other during an inversion process (Lelièvre et al., 2012). Resolution also plays a role with jointly inverting data sets, when considering the gravity and seismic joint inversion, the gravity data set has higher resolution at shallow depths, but seismic data has a greater resolution at greater depths (Lelièvre et al., 2012). Therefore, during a joint inversion process, the resolution of different data sets at different depths can be used to produce a higher resolution geological model than if the data sets where inverted individually (Lelièvre et al., 2012).

The cooperative or sequential inversion technique is different from the joint inversion technique since during a cooperative inversion different data sets are inverted in parallel or sequentially (Lines et al., 1988). The cooperative inversion method aims to build up a geological model over a series of steps rather than satisfying both datasets simultaneously as with a joint inversion algorithm (Lines et al., 1988; Moorkamp et al., 2011). If we make use of the seismic and gravity data sets again, with cooperative inversion the gravity data set will be inverted first and generate an initial starting model for the seismic inversion once the initial inversion criteria are met (Lines et al., 1988; Moorkamp et al., 2010). The gravity model provides a more realistic starting model for the seismic inversion and this means that the inversion will converge at a faster rate and still retain a higher

resolution at shallower depths than if the seismic data was inverted independently (Lines et al., 1988; Moorkamp et al., 2011). Cooperative inversions also require less computing power than joint inversions since less data is being inverted at a single time (Lines et al., 1988; Moorkamp et al., 2011).

Chapter 3 : Buried Resistors Masked by Conductive layers

This chapter includes a manuscript that is being prepared for peer-review publication. This research came from an opportunity to assist in a typical groundwater exploration project in the Western Cape province in South Africa during the 2018 drought. In this chapter, we use AMT and regional magnetic data to map stratigraphy and ancient dune networks that are recharging producing groundwater wells on a farm located in the semi-arid Hopefield region of South Africa. The chapter describes a link between groundwater salinity and the proximity of wells to ancient dune network locations. The resistivity inverse models calculated in this paper show how conductive clay and calcrete aquitard layers masked the resistive aquifer beneath. The aquifer can only be seen when there is a break in the conductive layer. This is a general problem in the MT method, that an overlying conductive layer can mask details of a resistor that lays beneath. The findings in this paper led to the development, in the next chapter, of a method to correct resistive layer distortion beneath conductive layers in the MT method.

Percentage of work done, and role played by authors on this paper:

Harrison, W.:

90% (Collected field data, processed field data, modelled data, wrote the manuscript).

Pellerin, L.:

5% (assisted with numerical analyses and interpretation. Also reviewed the manuscript).

Webb, S.J.:

5% (supervisor, assisted in interpretation and reviewed the manuscript).

Geophysical Investigation of Groundwater Control in the Semi-Arid Swartland Terrane, South Africa

Wesley Harrison, University of the Witwatersrand, School of Geosciences, 1 Jan Smuts Avenue, Braamfontein, Johannesburg, 2000,

email: Wesley.Harrison@students.wits.ac.za

Louise Pellerin, Green Geophysics, Inc. 2215 Curtis St, Berkeley, California 94702,

email: pellerin@greengeophysics.com

Susan Jane Webb, University of the Witwatersrand, School of Geosciences, 1 Jan Smuts Avenue, Braamfontein, Johannesburg, 2000,

email: Susan.Webb@wits.ac.za

3.1. Abstract

The semi-arid Hopefield region in the Western Cape Province of South Africa, has recently (2014-2018) experienced a severe drought. Audio magnetotelluric (AMT) and magnetic data is used to map the local stratigraphy and ancient dune outcrops that are recharging groundwater extraction wells on the farm, Waterboerskraal, 9 km north-east from the town of Hopefield. AMT resistivity inverse models show an electrically conductive (5-10 Ω·m) calcrete and clay layered aquitard with an approximate thickness of 20-30 m with depths and thicknesses in agreement with borehole data. Magnetic susceptibility inverse models shows the slightly magnetic (0.0003 SI) basement Malmesbury Supergroup containing channels caused by folding, beneath the ancient dune outcrops and correlate with AMT resistivity inverse models. The ancient dune outcrops allow surface groundwater to infiltrate a Cenozoic sedimentary succession below the aquitard by preventing the overlying calcrete and clay aquitard to form. There is a link between groundwater salinity and the proximity of wells to the ancient dune outcrops which are recharging and filtering water moving into these groundwater wells, with surface water, which results in a groundwater conductivity <500 μS/cm. Wells 2 km from the mapped ancient dune outcrops have a groundwater conductivity >2000 μS/cm, which is too saline for farming activities. With this study the previously mapped Pliocene shoreline extent was enlarged by recognizing and mapping a new ancient dune field in the research area from satellite imagery and geophysical data. In conclusion, ancient dune fields, like the one mapped in this study, should be the future primary target

for groundwater exploration on Waterboerskraal and possibly the greater semi-arid Swartland Terrane.

3.2. Introduction

The Western Cape Province in South Africa recently (2014-2018) experienced a severe drought with a standard precipitation index (SPI) of only -2 to -1.5 over 24 months (Masante et al., 2018). Where 0 SPI indicates normal precipitation conditions and -3 represents extremely dry conditions. The provincial response to this crisis included groundwater abstraction projects, utilizing exploration borehole drilling, and the development of desalination plants, primarily around the City of Cape Town.

The farming community in the Hopefield region, 90 km north of the City of Cape Town, relies on finding new groundwater sources to supplement their depleted surface water supply. The exploration, for these sources of groundwater, is usually confined to individual farm boundaries. The farming community relies on limited exploration boreholes to harvest the available groundwater sources with varying success. The study area is situated on the farm, Waterboerskraa, which lies in the semi-arid Swartland tectonostratigraphic Terrane. The Swartland Terrane has a complex deformation history and is poorly understood adding to the complexity of groundwater exploration in this area.

We found that AMT and regional magnetic data can be used to efficiently distinguish variations in geology of the basement Malmesbury Supergroup associated with the development of ancient dunes systems hosting fresh water on the Waterboerskraal farm. By understanding where these ancient dunes are

located, future groundwater exploration can be improved in the Swartland Terrane**.**

3.3. Hopefield Regional Geological and Hydrogeological Setting

Waterboerskraal farm lies in the Swartland tectonostratigraphic Terrane on the west coast of South Africa (Figure 3.1). A pull-apart basin tectonic setting has been suggested for the Swartland Terrane with a maximum depositional age of 600±5 Ma but this setting is still poorly understood (Belcher, 2003; Frimmel et al., 2013; Kisters and Belcher, 2018). After the break-up of the Rodinia supercontinent at approximately 780-750 Ma sedimentation commenced in stepped rift basins (Dalziel, 1994). After the rifting caused by the Rodinia breakup, the Adamastor Ocean closed resulting in sinistral transpression from oblique subduction. This subduction caused the intrusion of the Cape Granite Suite and folding of the Malmesbury Supergroup (Dalziel, 1994; Rozendaal et al., 1999). This folding provided channels for the preservation of dune formations resulting in possible pathways for surface water to infiltrate underlying aquifers. This is known as the Saldania orogenic event and produced the Saldania Belt.

Two northwest-southeast treading faults, the Colenso and Piketberg-Wellington faults, border this terrane (Kisters et al., 2002). The regional geological map (Figure 3.1) shows faults trending northeast-southwest, perpendicular to the Colenso and Piketberg-Wellington faults. Faults and fracture zones are one of the mechanisms controlling water infiltration and flow in the semi-arid Swartland Terrane (Conrad et al., 2004).

The regionally the area also hosts significant dune formations, with extensive sequences of dune stratigraphy, from underwater dunes in Langebaan Lagoon (Flemming, 1977) to Pleistocene and present-day age coastal dune plumes to the west (Compton, 2001). The Yzerfontein–Geelbek dune cordon, runs just east of our study area and is used to study Holocene sea-level fluctuations (Compton, 2001; Franceschini and Compton, 2006). These aeolian sands also host extensive calcrete sheets which underly these dune fields (Tankard, 1976; Compton and Franceschini, 2005). These calcrete sheets preserve the base of ancient dunes, providing a window into the dune history of the surrounding study area (Kandel et al., 2003).

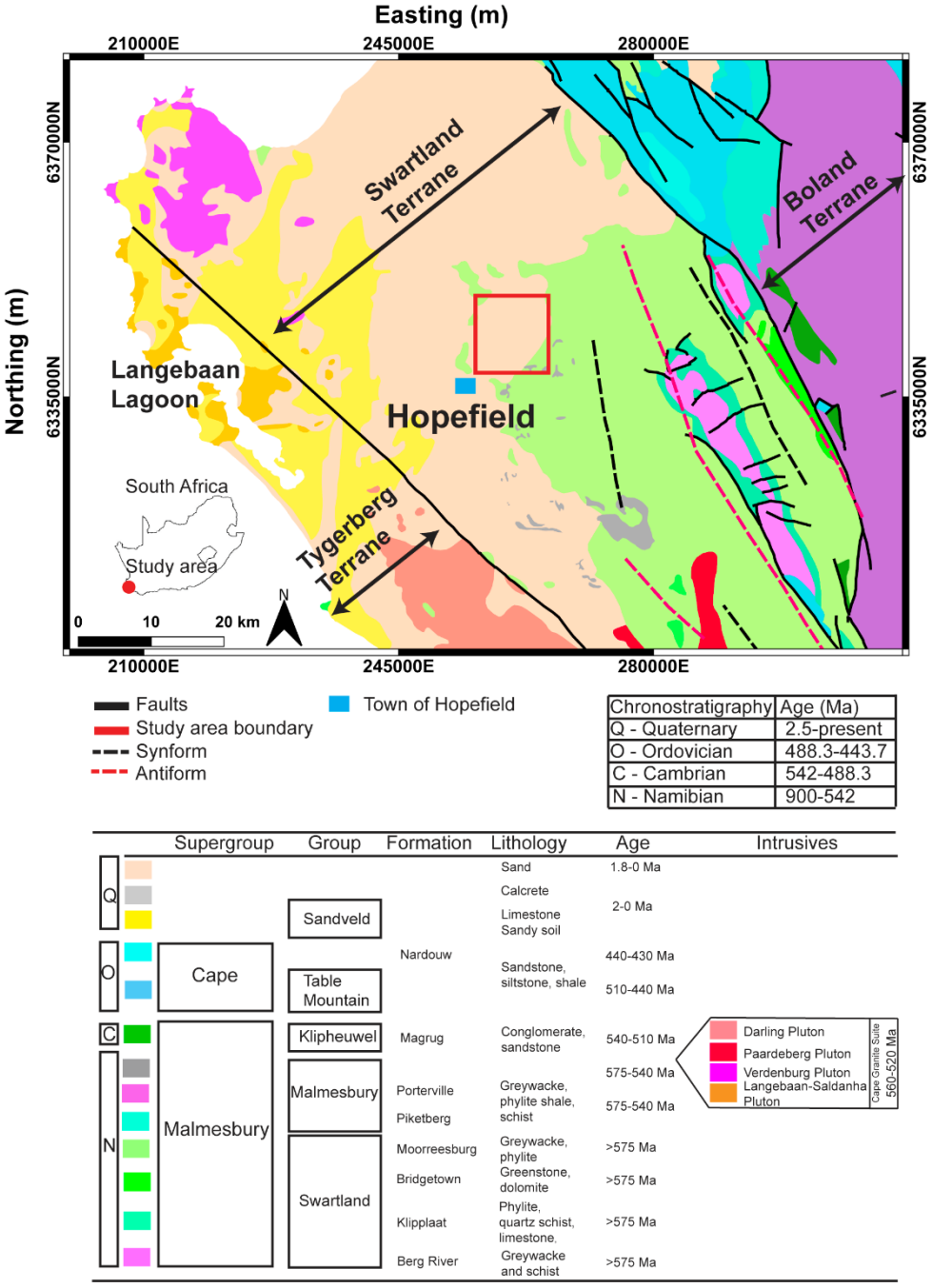


Figure 3.1. Geological map of the surrounding Hopefield area (modified from Theron, 1990, and Visser and Theron, 1973). The purple square on the map outlines the study area, the Waterboerskraal farm.

Generally, the groundwater in the study area is brackish, due to high evaporation rates (Potts, 2015) and slow recharge, except where rock fractures reach the

surface. These fractures allow for the infiltration of fresh surface water into a Cenozoic (65 Ma to present) sedimentary succession that serves as an aquifer. This aquifer lies at a depth of ~25 mamsl according to borehole and exploration drilling records in the area. A ~ 20-30 m thick calcrete and clay layered suite lies above and confines the Cenozoic aquifer. Below the Cenozoic sedimentary succession lies the Malmesbury Supergroup basement. The Malmesbury Supergroup contains shales which, when weathered, are responsible for the saline groundwater in the overlying aquifers (Flügel, 1995; Kamish, 2008).

The fractures in the Cenozoic sedimentary succession and basement Malmesbury Supergroup are the main targets for groundwater exploration on this farm, but these targets are rare as significant aeolian sands cover the study area.

3.4. Audio Magnetotelluric and Aeromagnetic Measurements and Data Processing

The passive-source AMT method was employed to map the electrical resistivity contrast between the electrically conductive calcrete layered aquitard (< 20 Ω·m) and the more electrically resistive (> 500 Ω·m) Cenozoic sediment aquifer and basement Malmesbury Supergroup. Gravelly sand outcrops are mapped from satellite images (Figure 3.2) that matched the color and texture of sediments seen at dune plumes in the surrounding area. These dune features could be possible groundwater infiltration sites and were also investigated with the planned AMT sites.

AMT data from 74 stations were acquired, using a Stratagem EH-4 AMT system, along 10 profiles, designated L1 to L10, of 300-400 m lengths around the farm

(Figure 3.2). Data was acquired for a period of ~10-15 minutes per station. Each station had a dipole length of 10 m with coherency limits set between 0.35 and 0.75.

The survey is planed around producing groundwater wells to assist in the investigation of the lithological features recharging these wells. Since there is little or no rock outcrops, lithological strike directions were estimated by studying satellite images and the general direction of vegetative growth, which likely indicates the strike direction of features enabling vegetation an access groundwater. Most of the wells also lined up in a general strike direction which was also used to estimate the general strike direction of our groundwater structural targets.

Once the AMT data was acquired, it was rotated in the standard way, so the X and Y direction are perpendicular and parallel to the geological strike respectively (Figure 3.3(B)). Then transverse magnetic (TM) and the transverse electric (TE) modes were assigned to the phase and resistivity curves. The TM mode is perpendicular to the predicted lithological strike direction as inferred from satellite images, well locations and vegetative growth. The TE mode is parallel to the general geological/lithological strike direction.

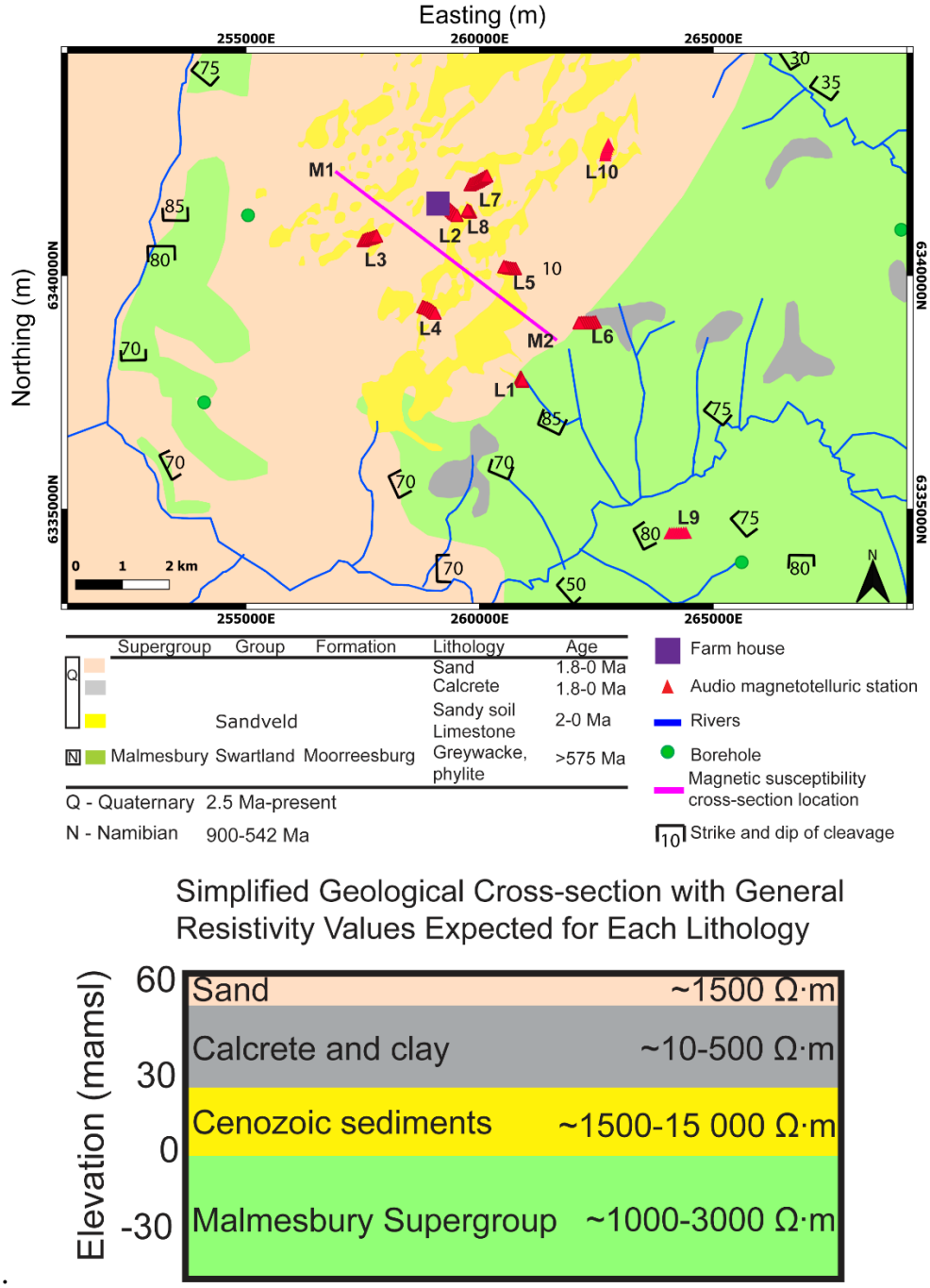


Figure 3.2. Geological map of Waterboerskraal. Audio magnetotelluric stations are indicated as red triangles. Ten audio magnetotelluric traverses were collected in total around the farm. A simplified geological cross-section based on borehole (green dots) data, of the study area, is shown with expected electrical resistivity values, taken from the South African Council for Geoscience publicly available physical property database (Mare, 1999). The yellow Sandveld group was mapped using satellite images, where the color and texture of sediments seen at dune plumes in the surrounding area matched the color and texture in our research site.

Data points in the 1 kHz dead band and >31 kHz were masked where signal strength was low (Figure 3.3(C)). Noisy spikes were removed and fitted smooth (D+) curves to the remaining data points, since magnetotelluric data is smooth (Figure 3.3(D)). The D+ function relates apparent resistivity and phase by finding a one-dimensional earth model that fits both parameters by recalculating a continuous response function for a physically valid earth model (Beamish and Travassos, 1992). Figure 3.3 shows the editing steps taken for the resistivity and phase data sets that represent the average quality of the measurements collected for this paper.

From the edited and processed data, one-dimensional (1-D) and two-dimensional (2-D) resistivity inverse models were calculated using the conjugant gradient code developed by Rodi and Mackie, 2001. The minimum and maximum frequencies set for the inverse model calculations is 15.6 Hz and 100000 Hz respectively, which replicates the frequency range of the data collected. A starting model of 1000 Ω·m is used for the initial inverse calculation. The objective function is set to first find the smoothest model with a standard Laplacian operator focusing on minimizing the integral of the gradients of the model with a Tau value of 3. Once the first inverse model is calculated the resulting model is used as a starting model for the second inverse model calculation. The objective function is now set to solve for the smoothest variation away from the starting model with a standard Laplacian operator focusing on minimizing the integral of the Laplacian. For this inverse calculation, the Tau operator is set as 1 with weighting functions enabled to prevent the model from becoming too blocky. This inversion methodology allows for an initial smooth model to be calculated from a 1000 Ω·m half-space

and then the resulting smooth model is used as a starting model for a second inverse calculation that is focused on fitting the observed data. We found that this procedure, in our case, helped to map minor features in the inverse models that would have been missed if just a single inversion model was calculated. 2-D resistivity inverse models calculated from both the TM and TE modes are used to interpret the underlying lithological structures.

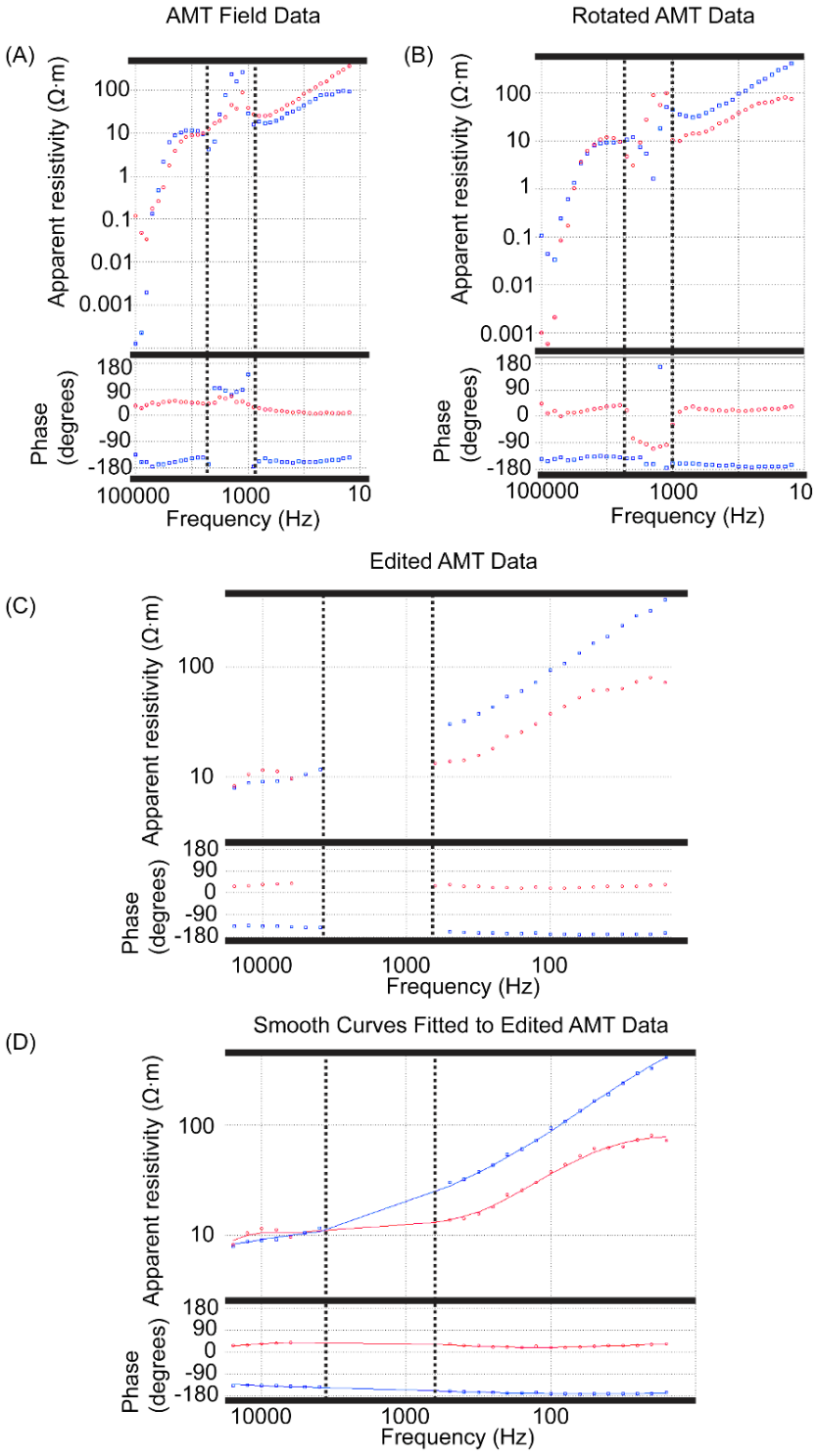


Figure 3.3. (A) Representative quality AMT field data. (B) Rotated AMT data so the X and Y direction is perpendicular and parallel to geological strike respectively. (C) Masked data in the 1 kHz dead band and >31 kHz where signal strength was low. (D) Removed noise spikes and fitted smooth (D+) curves to the remaining data points.

Once the 2-D inverse models are calculated, a model confidence assessment algorithm that we developed is run on the model (Figure 3.4). The routine starts by calculating the misfit, for both the TE and TM mode phase and resistivity data, between the field data and the calculated data produced from the inversion routine. The TE and TM mode misfit data is then summed together and normalized to create the total misfit for both the resistivity and phase data. The total misfit data for both resistivity and phase are summed together then normalized to create the total misfit for the inverse model. Since the total misfit is normalized between 0 and 1, it is well suited to make an alpha map that can control the translucency of cells in the model. The alpha map is transformed from the frequency domain to the spatial domain by using the skin depth formula. The new alpha map is gridded onto the inverse model and the cell translucency is changed to represent the confidence level of that cell. White cells indicate regions of the maximum misfit in the inverse model. This method is used to supplement the standard root mean square error evaluation of an inverse model.

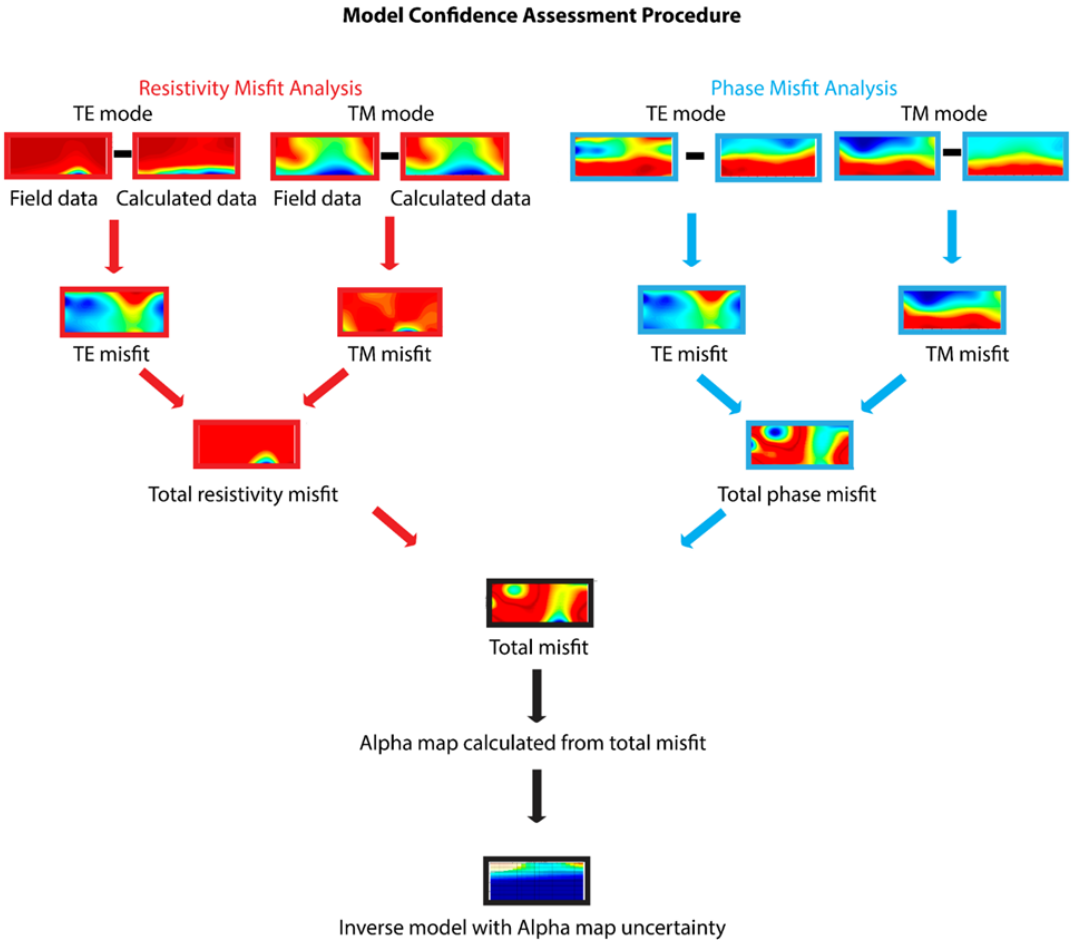


Figure 3.4. This schematic map illustrates the procedure followed by the model confidence assessment algorithm. The misfit for both the resistivity and phase data, for both the TE and TM mode, are calculated. The misfit for the resistivity and phase data is summed and normalized to create a total misfit map for the inverse model. The total misfit model is transformed into an alpha map that controls the translucency of cells within the inverse model. Transparent cells indicate regions of low confidence.

We also used publicly available aeromagnetic data collected in 1976 by the Geological Survey of South African now renamed the Council for Geoscience (Ledwaba et al., 2009). A Digital Gulf Mark III Fluxgate magnetometer was used to collect the aeromagnetic data. The survey had a north-south flight direction at a 100 m flight height with a sampling rate of 8 times a second. A line spacing of 1 km was used with a tie line spacing of 10 km.

A grid using a minimum curvature gridding algorithm with a 250 × 250 m cell size is created. A first-order trend surface was removed to subtract the regional magnetic field from our magnetic grid. This results in a residual aeromagnetic grid (Figure 3.5(A)) that was leveled with the aeromagnetic data with the use of the Naudy-Fuller space domain filter which incorporates both a Butterworth and directional cosine filter (Fraser et al., 1966; Naudy and Dreyer, 1968). An 8th order Butterworth high-pass filter window is set to four times the line spacing (4000 m) so to only pass frequencies of a similar scale to the flight line spacing. The directional cosine filter is set to 90° to only allow wavelengths through in the same north-south flight direction. The resulting grid contains the leveling errors at each grid cell. This error grid is subtracted from the reduced aeromagnetic grid resulting in a leveled aeromagnetic grid (Figure 3.5(B)). The leveled grid is then reduced to pole (RTP) (Figure 3.5(C)) to remove asymmetry in the magnetic anomaly caused by the inclination of the Earth's magnetic field (Baranov and Naudy, 1964).

The magnetic grid is then used in the 3-D magnetic inversion algorithms MAG3D, developed by the University of British Columbia Geophysical Inversion Facility (UBC-GIF), to calculate a 3-D magnetic susceptibility inverse model (Li and Oldenburg, 1996; Li and Oldenburg, 1997). The inverse model had a mesh with 196 × 180 × 150 with a cell dimension of 50 × 50 m with a total of 5292000 cells in the inverse model. The initial model used for the inverse calculations is a 0.001 SI half-space and the upper and lower bounds for the inverse model were set to 0 and 1 SI respectively. The inverse model reached its target $\chi 2$ misfit of 1020 in 6 iterations.

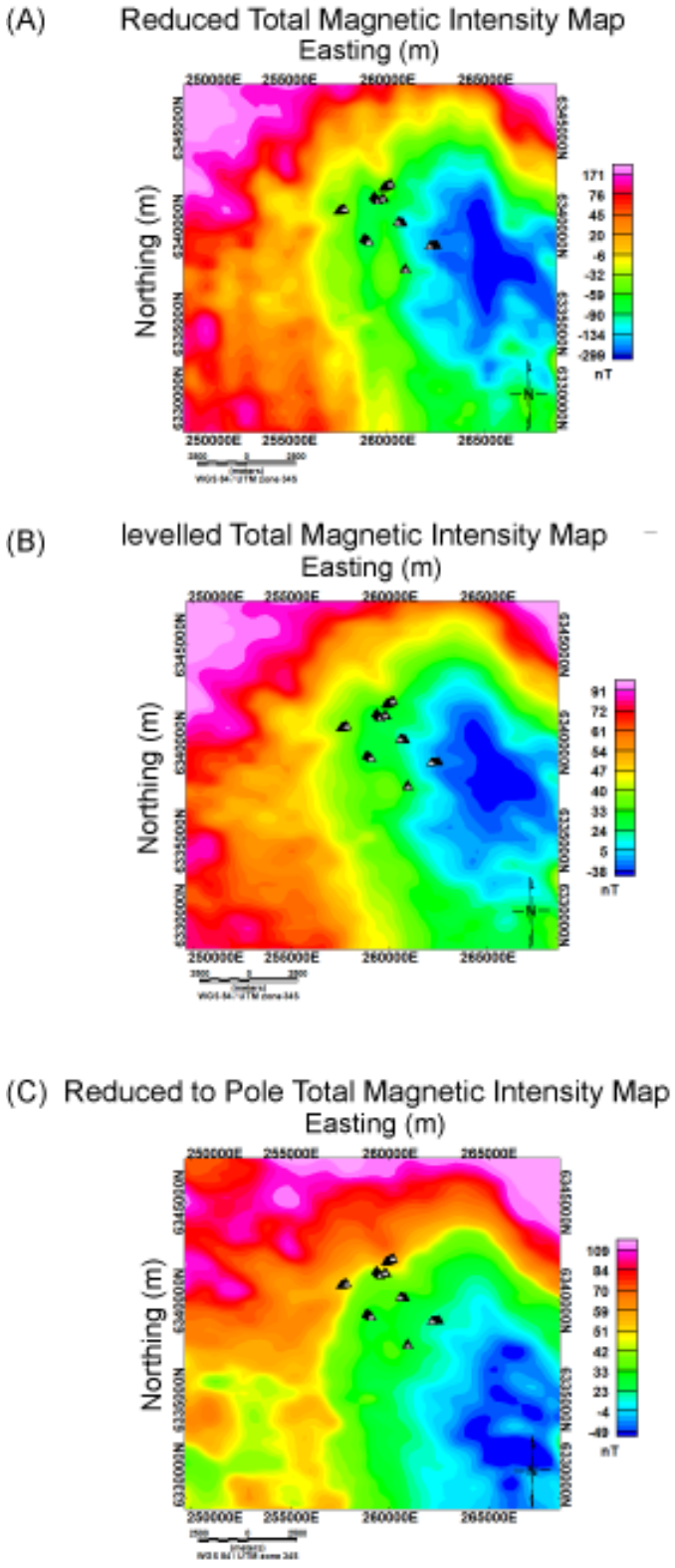


Figure 3.5. (A) Reduced total magnetic intensity aeromagnetic map. (B) Levelled total magnetic intensity aeromagnetic map. (C) Reduced to pole total magnetic intensity aeromagnetic map. AMT stations are represented by white triangles.

3.5. Audio Magnetotelluric and Magnetics Results and Interpretation

To study the geological structures recharging the extraction wells on the farm we first investigate the calibration AMT traverses.

Survey traverse L1 passes by a flagship operational freshwater well on the farm that supplies most of the stored fresh groundwater for irrigation. The resistivity inverse model shows a break in the electrically conductive upper layer near the surface of the calculated model as depicted in Figure 3.6B. The conductive layer is interpreted as being the calcrete and clay aquitard situated between ~50-20 mamsl depth (Figure 3.6). The break in the aquitard, between distances 40 m and 80 m along the profile, coincides with the productive freshwater well location. The discontinuity in the aquitard resulted in this well, being in direct contact with the underlying Cenozoic sediments which, consisting of coarse sand and gravel beds, function as an aquifer in this area. The break in the aquitard is most probably allowing fresh surface water to recharge the underlying aquifer. On surface, coarse sand and gravel sediments surround the producing well. Slightly resistive geology indicated by the light blue resistor is seen on Figure3.6B, penetrates the overlying conductive aquitard. Therefore, the inferred break in the aquitard is acting as a freshwater conduit recharging the underlying aquifer. The groundwater conductivity in this well is < 30 μS/cm. The underlying resistive (dark blue) basement Malmesbury Supergroup is between -50 and -55 mamsl deep, which correlates with depths of Malmesbury Supergroup rocks as seen in a nearby borehole.

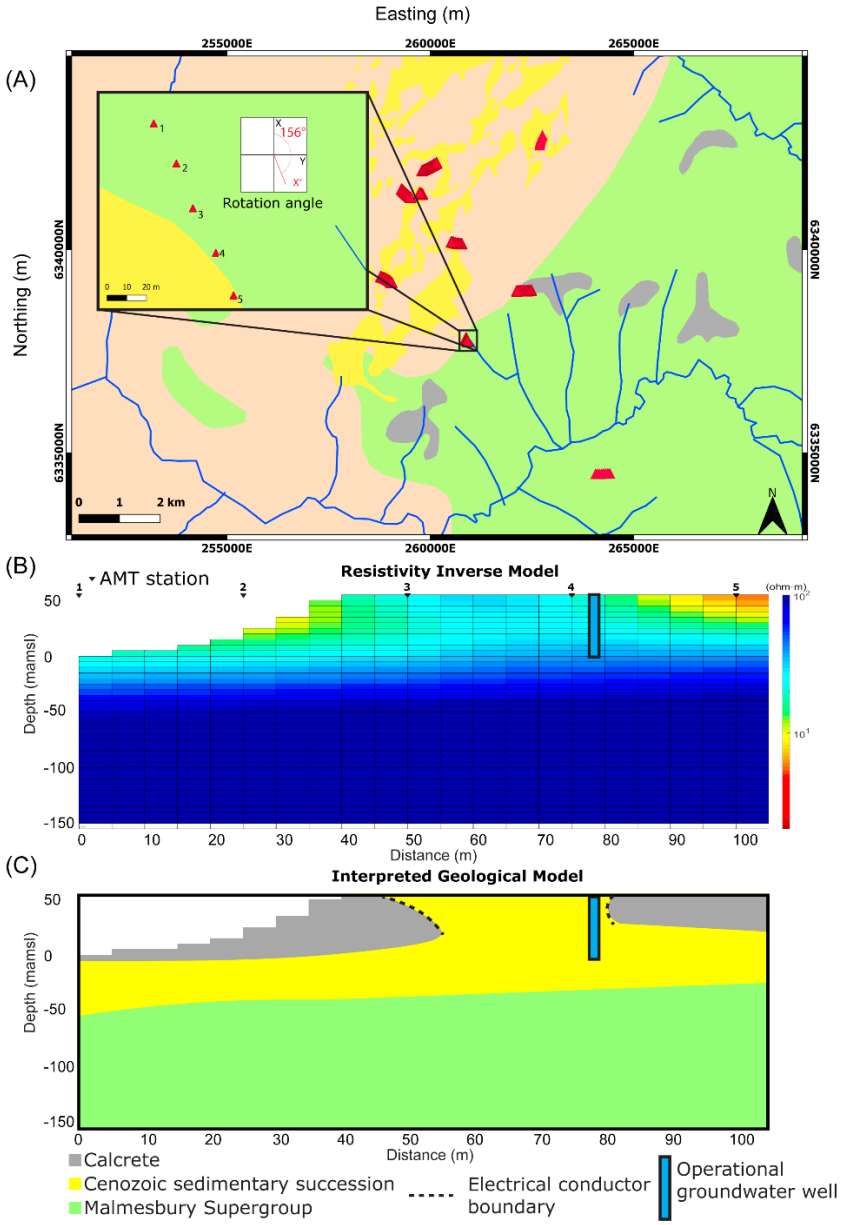


Figure 3.6. (A) A locality map that shows the position of the 5 AMT sites, from L1 represented as red triangles, used for the inverse model. The AMT impedance tensor for these sites is rotated by 156 ° to lineup the TM and TE modes perpendicular and parallel to the lithological strike respectively. (B) The resistivity inverse model maps a conductive layer between ~50-20 mamsl deep. This layer is interpreted as the calcrete and clay aquitard present on the farm. A break in the conductor, between 40 m and 80 m along the profile, where a lite blue resistor is preventing the formation of the aquitard in this area. One of the farms' flagship freshwater wells is sunk in the area of the break in the conductor. Between 50-0 mamsl and 0-40 m along the profile, white cells show a region of low confidence calculated by the model confidence assessment algorithm. The root mean square error of the model is 2.9. (C) A geological model interpreted from the resistivity inverse model.

A second calibration resistivity inverse model, along the survey line L2, is shown in figure 3.7. The resistive basement Malmesbury Supergroup lies at a depth of ~ -55 mamsl which correlates with the basement Malmesbury Supergroup depth of ~ -55 mamsl in a borehole west of the line. A borehole drilled ~ 205 m along the line shows the depth of the surface sands to ~ 45 mamsl. The underlying calcrete and clay aquitard is ~ 20 m thick and ends at a depth of ~28 mamsl which correlates with the electrical conductor (5-10 Ω·m) seen in the resistivity inverse model. Below the aquitard lies coarse fluvial sands and gravels which is represented by the green (15-50 Ω·m) layer in the resistivity inverse model. Again, the electrically conductive calcrete aquitard is disrupted at ~210 m along the line by a resistor. Coarse sand and gravel sediments are again outcropping at the surface. Yet again, the resistor is acting as a recharging conduit for the underlying aquifer that the well is extracting groundwater from. The groundwater extracted from this well is <500 µS/cm. The higher conductivity in the groundwater is likely as a result of the position of the well on the edge of the calcrete and clay aquitard. The calcrete and clay aquitard layer logged in the borehole matches the conductive layer mapped by a red color in the electrical model. The coarse fluvial sands match the green layer of the resistivity inverse model, which is the target aquifer in this area.

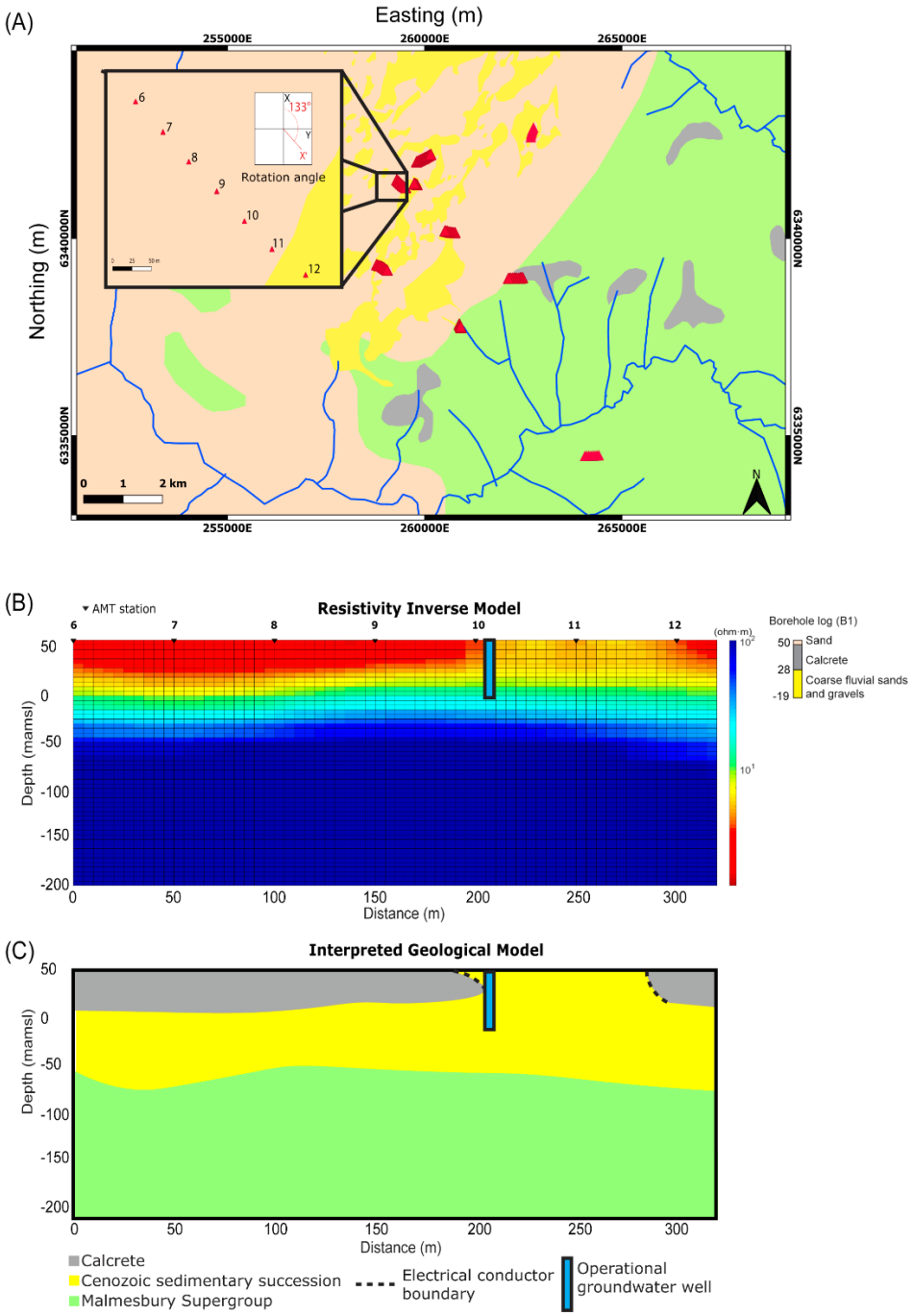


Figure 3.7. (A) This locality map shows the positions of the 7 AMT stations, from L2, used for the resistivity inverse model. The impedance tensor is rotated 133°, which rotates the TM mode perpendicular to the strike of wells and vegetation at this site. (B) The resistivity inverse model again maps the conductive clay and calcrete aquitard at the surface of the model. A resistor breaks the continuity of the aquitard. A well sunk near the edge of the clay and calcrete aquitard intersect slightly more saline groundwater than the well at line L1. The calcrete and clay aquitard mapped by the borehole matches the conductivity layer. The course fluvial sands match with the green layer of the resistivity inverse model, which is the target aquifer in the area. The root mean square error of the model is 2.5. (C) A geological model interpreted from the resistivity inverse model.

The resistivity inverse model along survey line L4 shows two resistors disrupting the conductive aquitard (Figure 3.8). Between the two resistors is a productive well with groundwater conductivity of <50 µS/cm. Below the two resistors the basement Malmesbury Supergroup possibly hosts a channel, from a distance 0-200 m along the line, due to folding of the Malmesbury Supergroup in the area with dip of ~ 75° similar to the cleavage dip mapped on the geological map (Figure 3.2).

Along survey line L7, coarse sand and gravelly sediments are absent at the surface, which usually indicates the possible absence of a break in the conductive aquitard, but two producing wells are stationed along this profile. On the resistivity inverse model, between ~60-150 m along this traverse, shows a resistor (blue) approaching the surface but is cut off by a less resistive layer (colored green) (Figure 3.9). In this case, the resistor is covered by a fine sandy soil which still allows freshwater to infiltrate into the underlying aquifer since the formation of the calcrete and clay aquitard is inferred to have been curtailed. The groundwater conductivity from these wells is also <50 µS/cm. The four calibration traverses just discussed is a representative sample of all the calibration AMT lines performed near productive wells on the farm to obtain a possible understanding of the recharge mechanism and formulate a hypothesis to be applied to the exploration of new ground water resources.

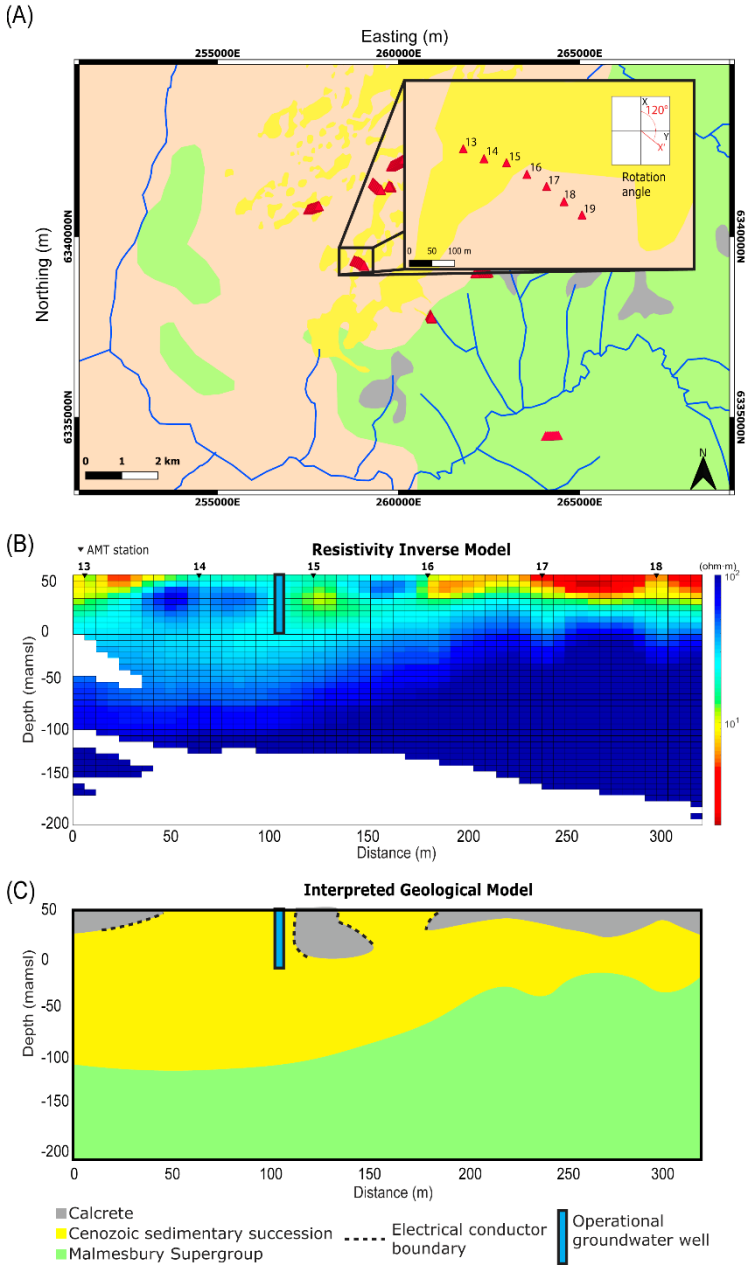


Figure 3.8. (A) This locality map shows the position of 6 AMT stations along survey line L4. The impedance tensor for these stations is rotated by 120° to follow the vegetation strike in the area. (B) The resistivity inverse model for this line shows two resistors recharging a single operational well that is positioned between them. The resistors again disrupt the conductive aquitard layer. Below the two resistors the basement Malmesbury Supergroup seems to form a channel, due to folding, from a depth of -25 mamsl on the east to -100 mamsl on the western side of the inverse model. Zone of low confidence in the inverse model is shown as white cells. The root mean square error of the model is 1.9. (C) The geological model interpreted from the resistivity inverse model shows that the well is primarily being recharged by two breaks in the conductive aquitard.

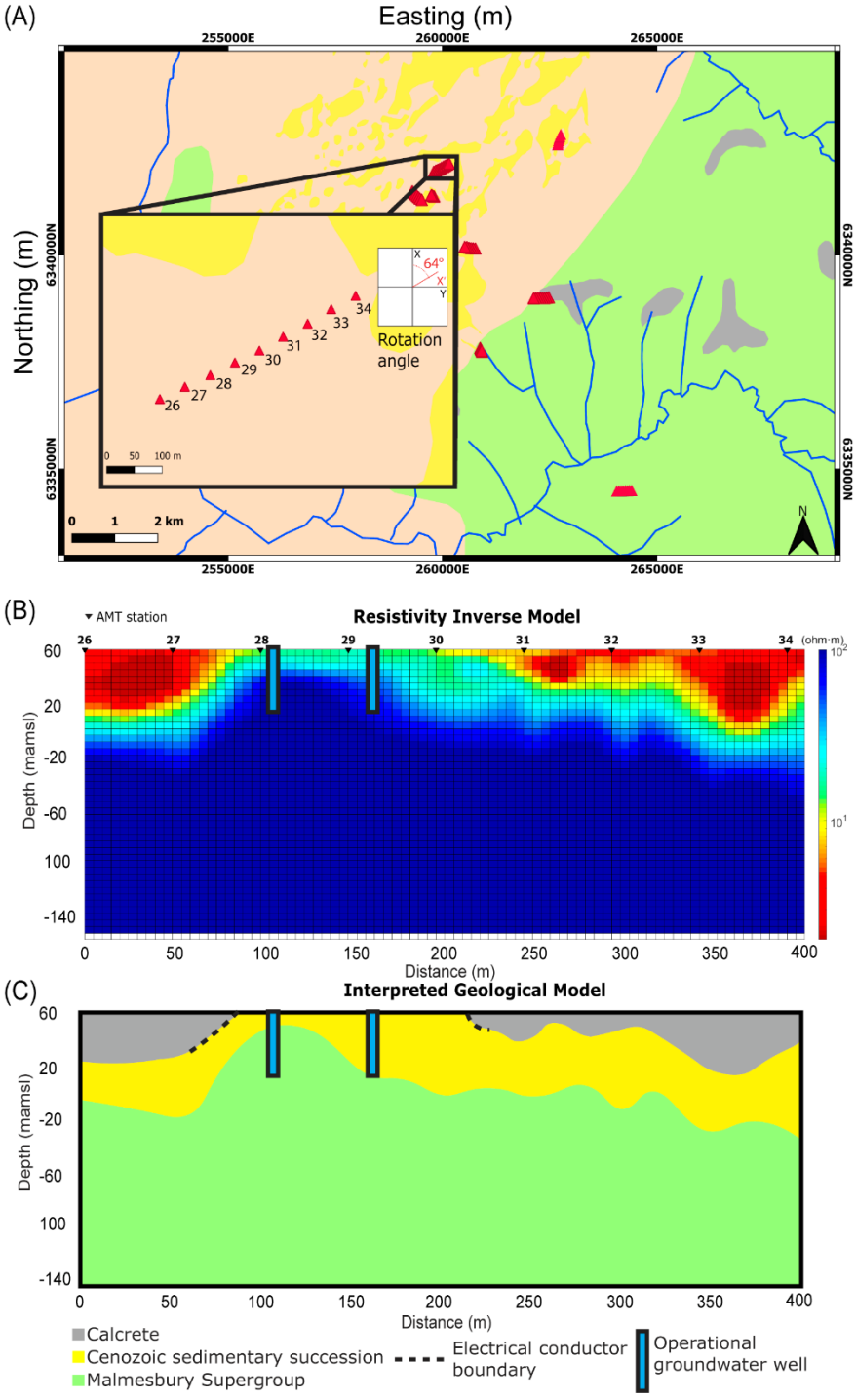


Figure 3.9. (A) The locality map shows the position of 9 AMT stations along survey line L7. This is one of the longest lines of AMT data collected on the farm. The impedance tensor for the stations is rotated by 64° following the strike of the wells. (B) The resistivity inverse model shows the resistor, in this case, is buried by a layer of fine sands (green). Even though the resistor is buried two wells still recharge from the buried resistive area. The root mean square error of the model is 1.6. (C) A geological model interpreted from the resistivity inverse model shows that both wells intersect the break in the conductive aquitard.

Survey line L5 is situated near a non-operational well that has groundwater conductivity measurements of > ~2000 µS/cm. This water is too saline for farm use. The resistivity inverse models show a consistent conductor at a depth of 55 mamsl (Figure 3.10). This conductor is interpreted as the calcrete and clay aquitard. Since the aquitard is continuous, fresh surface water cannot infiltrate the underlying aquifer. This resistivity inverse model from L5 is a representative model of similar resistivity inverse models calculated near other saline or dry wells on the farm.

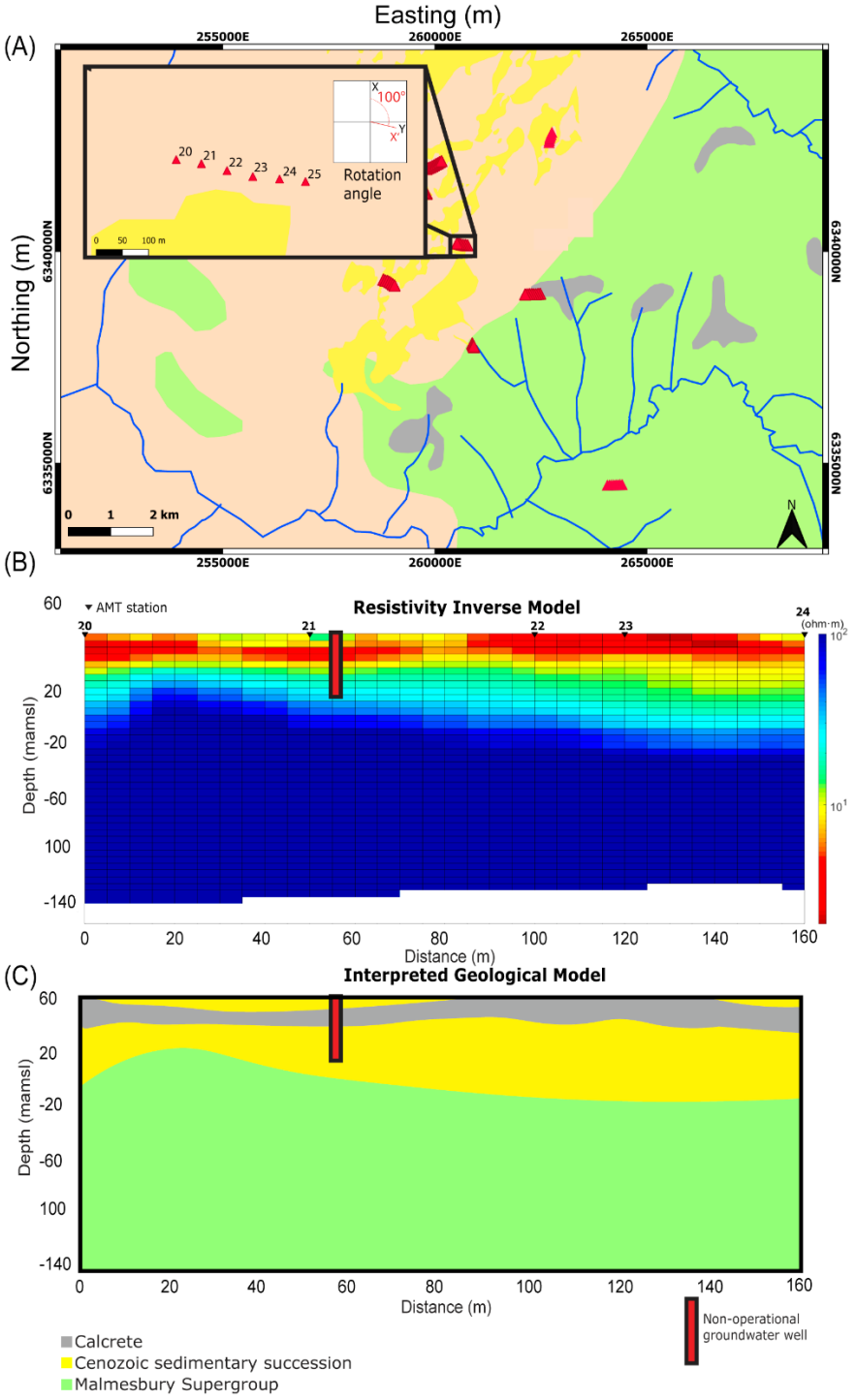


Figure 3.10. (A) The location of the 6 AMT stations, along L5, used in the resistivity inverse model is shown on this map. The rotation angle for these stations is 100°. (B) The resistivity inverse model shows a continuous conductor at a depth of 55 mamsl. This conductor is interpreted as the clay and calcrete aquitard. White cells with low confidence are present below -140 mamsl. The root mean square error of the model is 1.6. (C) The geological model shows that the non-productive well intersects the aquifer below the aquitard but the groundwater conductivity in the aquifer is > ~2000 µS/cm.

A cross-section from the 3-D magnetic susceptibility inverse model is shown in Figure 3.11(A). The basement Malmesbury Supergroup is interpreted as the pink 0.0003 SI feature seen in the magnetic susceptibility inverse model. Two channels are present in the basement Malmesbury Supergroup at 2300 m and 4000 m along the cross-section. The electrically resistive basement Malmesbury Supergroup correlates with a relative magnetic basement Waterboerskraal farm seen in the magnetic susceptibility inverse model (Figure 3.11(B)). The location of the edges of the outcropping channels is seen in the resistivity inverse models along L2 and L4 correlates with the channels, formed from folding in the Malmesbury Supergroup, seen in the magnetic susceptibility inverse model. These channels are filled with much younger Cenozoic sediments which exploited these possible minor synclinal folds in the basement. Therefore, both channels are seen in the magnetic susceptibility and electrical resistivity inverse models.

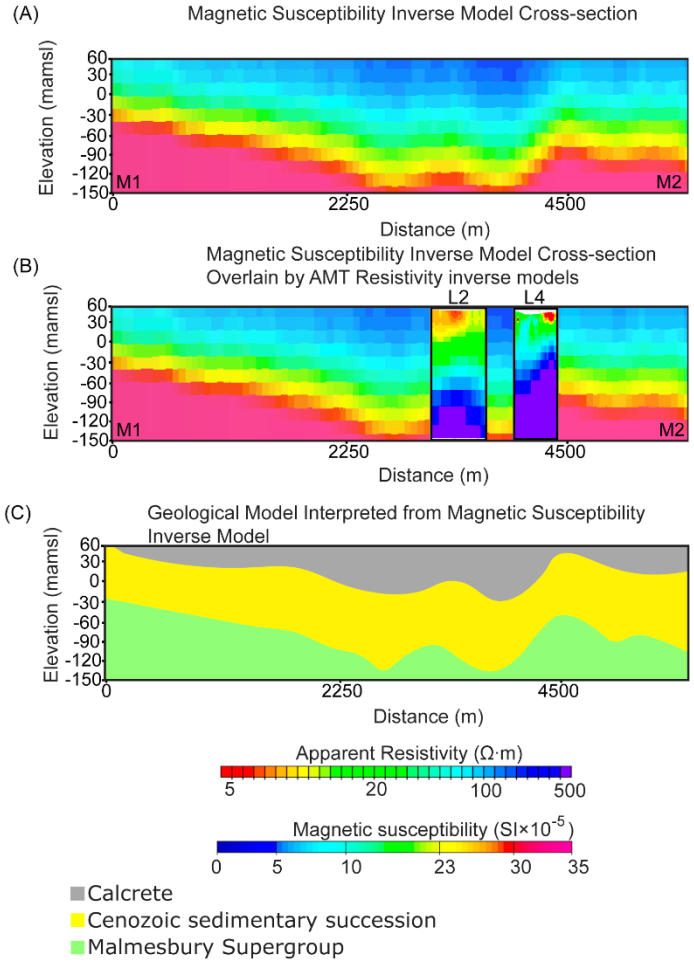


Figure 3.11. (A) A cross-section, along a traverse between M1 and M2, from the 3-D magnetic susceptibility inverse model. (B) Resistivity inverse models along lines L2 and L4 overlain on the magnetic susceptibility inverse model cross-section. The resistivity inverse models map the edges of inferred channels formed much later in Cenozoic times by exploiting possible minor synclinal folds in the basement Malmesbury Supergroup and correlate with the edges of channels seen in the basement Malmesbury Supergroup in the magnetic susceptibility inverse model. (C) The geological model interpreted from the magnetic susceptibility inverse model.

3.6. Discussion

The resistive breaks seen in the resistivity inverse models resemble the breaks in calcrete layers caused by ancient dunes near the Yzerfontein–Geelbek dune cordon as described by Kandel et al. (2003) (Figure 3.12). The dunes that make up the Yzerfontein–Geelbek dune cordon form part of the Sandveld formation, which

is the same formation that contains the Cenozoic sedimentary succession aquifer targeted in our study area. Therefore, we conclude that the resistive breaks in the conductive calcrete aquitard are due to the preservation of ancient Pleistocene and Holocene dunes, like the dunes described in Kandel et al. (2003), and that formed in erosional channels in Cenozoic times that formed by exploiting weak zones on the exposed ~570 Ma Malmesbury floor rocks. As vegetation stabilized these ancient dunes, the formation of calcrete through bicarbonate leaching was confined to deeper sections of the dune. Through deflation and erosion of the dunes, the calcrete layers could be exposed on the surface, and during rainy seasons, ultimately dissolving and resulting in breaks in the calcrete layer. Aeolian dune sand would settle in the resulting depression, preserving the base of the dune in the calcrete layer.

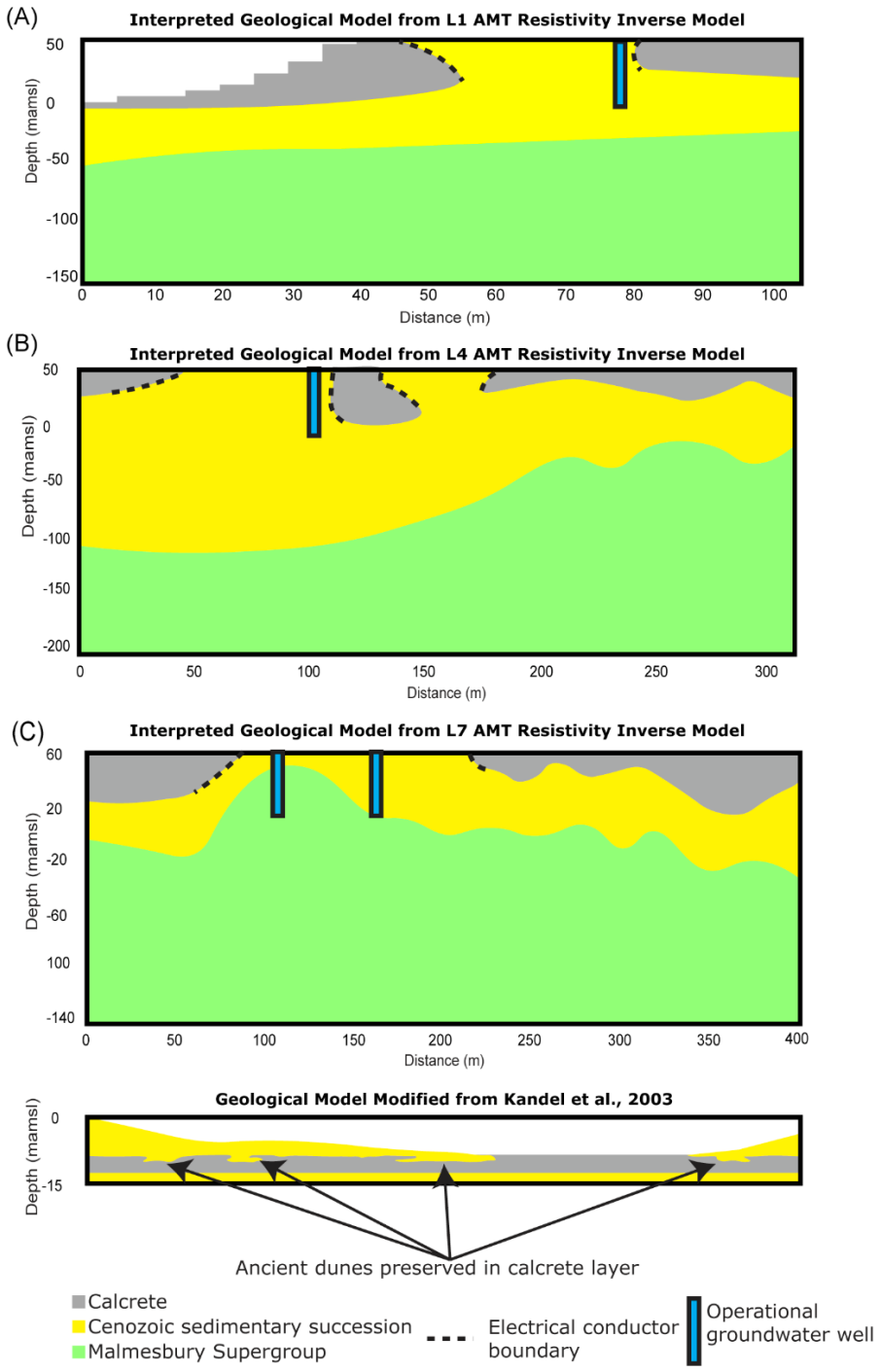


Figure 3.12. (A) Geological model interpreted from resistivity inverse model calculated from AMT line L1. (B) Geological model interpreted from resistivity inverse model calculated from AMT line L4. (C) Geological model interpreted from resistivity inverse model calculated from AMT line L7. (A) Geological model modified from Kandel et al. (2003), showing ancient dunes preserved in the calcrete layer near the Yzerfontein–Geelbek dune cordon. The breaks in the calcrete layer seen in all the resistivity inverse models resemble the same breaks in the Kandel et al. (2003) geological model. Therefore, the breaks in the calcrete in our study area are likely as a result of preserved ancient dune fields.

Operational groundwater wells, with groundwater electrical conductivity <500 µS/cm, line up along these preserved dunes mapped from the AMT resistivity inverse models and satellite images (Figure 3.13). The preserved dunes are recharging these groundwater wells, with surface water, which results in the lowering of the groundwater conductivity being <500 µS/cm. The low groundwater conductivity is likely due to further purification of surface water through the preserved sandy dunes. Dunes have been used as natural water purification systems before, particularly in the Netherlands (Stuyfzand, 1995; Jones et al., 2006; Everard, 2010).

Wells 2 km away from the mapped preserved dunes have groundwater conductivity >2000 µS/cm, which is too saline for farming activities due to dissolved salts from the weathering shale in the underlying Malmesbury Supergroup. The high conductivity of the groundwater in these wells is also a result of the absence of surface water recharge of the Cenozoic sedimentary succession aquifer. From the shuttle radar topography mission (SRTM) elevation data (Farr et al., 2007), all the non-productive wells with groundwater conductivity >500 µS/cm have an average elevation range of ~65-78 mamsl, while the average elevation range for productive wells is ~50-58 mamsl. This is as a result of the ancient dunes weathering at a faster rate than the calcrete layers that preserved these dunes. Therefore, we conclude that the proximity of wells to a preserved dune can be related to the groundwater quality and the reliability of that well on this farm.

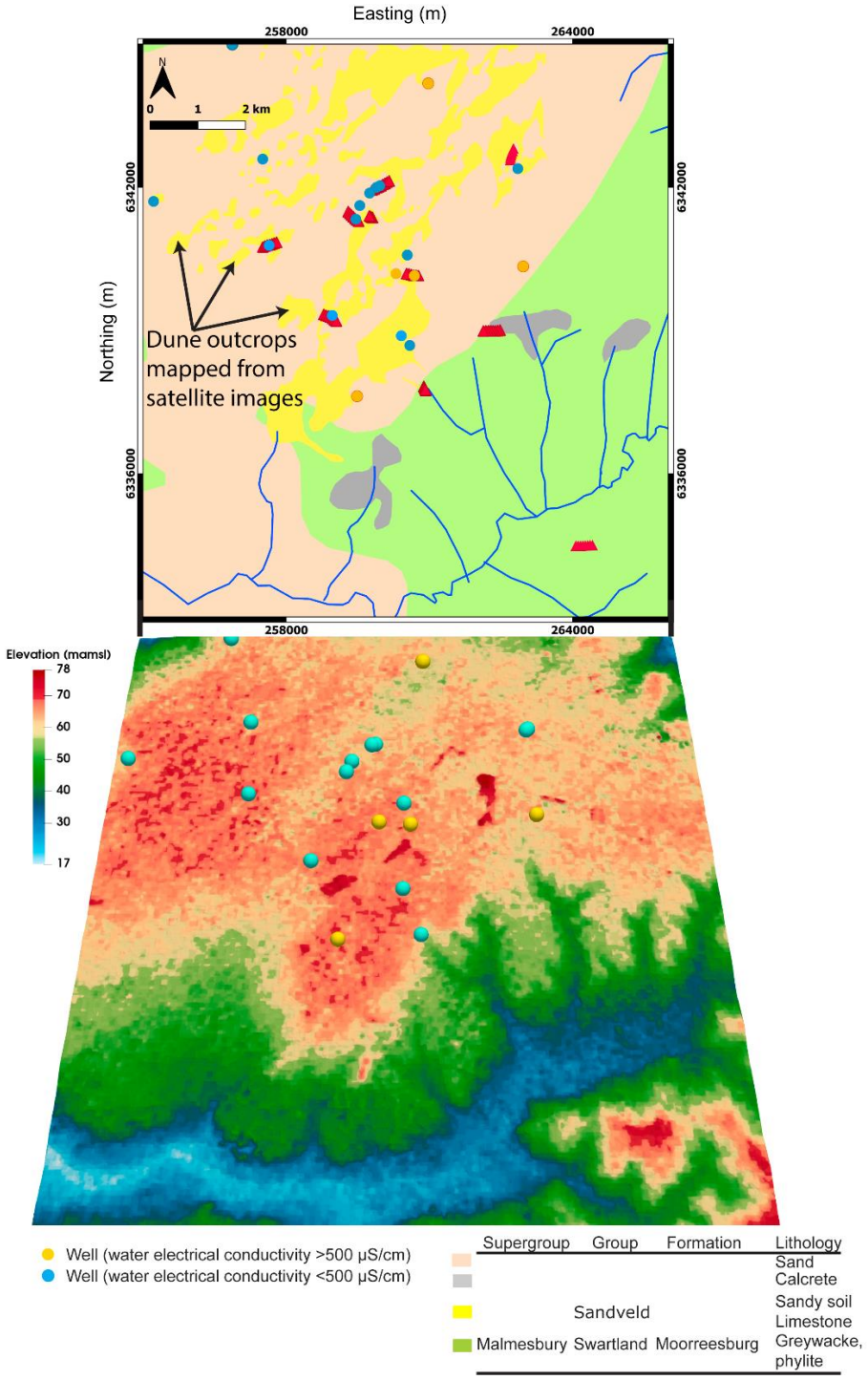


Figure 3.13. A shuttle radar topography mission elevation map of the geological map shows that operational (groundwater conductivity <500 µS/cm) have an average elevation range of ~50-58 mamsl, while non-operational wells (groundwater conductivity >500 µS/cm) have an average elevation range of ~65-78 mamsl. This is likely due to the faster rate of weathering in the preserved dunes when compared to the calcrete aquitard. Most of the operational groundwater wells are situated on or near the yellow ancient dune outcrops mapped by satellite images on the geological map.

As an example of how ancient dune outcrops are mapped from satellite imagery, we mapped gravelly sand outcrops from satellite images that matched the color and texture of sediments from surrounding dune plumes (Figure 3.14). The mapped sediments highlight possible areas where ancient dune outcrops could be. The satellite image in Figure 3.14 shows an outcropping ancient dune, gravelly sand sediments, recharging the operational flagship well described along survey line L1. This well is used to fill a farm dam east of the well. There is a clear contrast between the coarse orange color ancient dune sediments and the fine grain grey colored sediments overlying the calcrete and clay aquitard. Vegetation can be seen growing on the ancient dune outcrop, this is due to the direct access to stored fresh surface water in the aquifer.

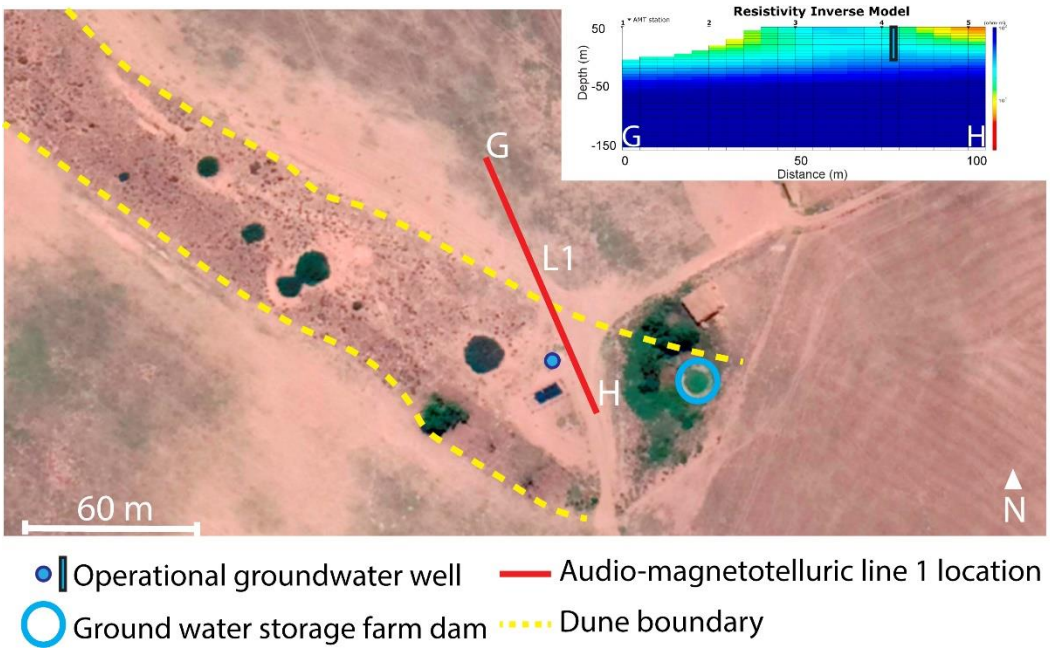


Figure 3.14. Outcropping paleochannel outlined on the satellite image. There is a clear contrast between the coarse orange color ancient dune sediments and the fine grain grey color sediments overlying the calcrete and clay aquitard. The operational well is recharged by the ancient dune outcrop and is used to replenish a farm dam just east of the well.

Ancient dunes allow surface groundwater to infiltrate the Cenozoic sedimentary succession aquifer by providing a conduit between the overlying calcrete and clay aquitard to allow surface water ingress (Figure 3.15). This is reflected by the producing wells (blue circles in Figure 3.13), with groundwater electrical conductivity <500 μS/cm, concentrations around ancient dune outcrops. While decommissioned wells (yellow circles in Figure 3.13) with groundwater electrical conductivity >500 μS/cm are located away from the outcropping ancient dunes. This result indicates that the groundwater salinity can be related to the distance away from an ancient dune outcrop. The further the well is away from an ancient dune outcrop, the more likely the freshwater will mix with the existing saline groundwater and become too saline for operational wells. Therefore, ancient dunes should be the primary target for usable groundwater within the Waterboerskraal farm and possibly the greater Swartland Terrane region. The ancient dune field found on the Waterboerskraal farm has similar lithology to the Yzerfontein–Geelbek dune cordon south-west of the town of Hopefield.

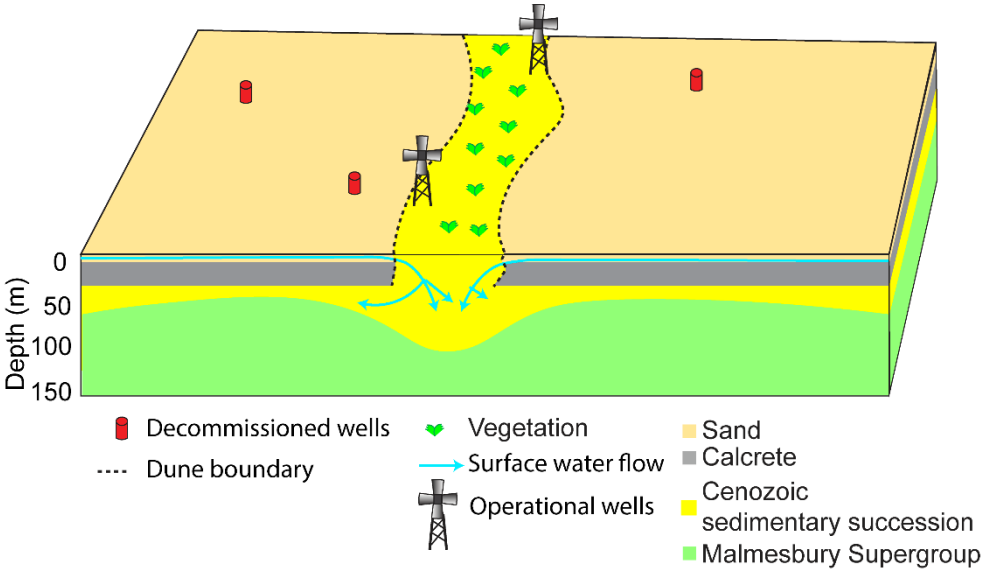


Figure 3.15. The proposed geological model interpreted from both the resistivity and magnetic susceptibility inverse models. Groundwater infiltrates the Cenozoic sedimentary succession through preserved ancient dune outcrops by disrupting the calcrete and clay aquitard above.

Roberts et al. (2011) made use of the coastal dune history near Langebaan Lagoon to map the position of the shoreline during the Pliocene. By making use of the newly mapped ancient dune field in our study area, we have extended the Pliocene shoreline further north-east (Figure 3.16). Figure 3.16(A) shows the location of the Yzerfontein–Geelbek dune cordon south-west of the town of Hopefield. Figure 3.16(B and C) shows orange-colored matured dunes stabilized by vegetation. These matured dunes mark the edge of the Pliocene shoreline since these are the furthest dunes east of the present-day shoreline that have been preserved. The presence of persistent vegetation to the east of these dunes would have stabilized any other dunes further east if they were present at the time. Exploration for usable groundwater, that has been filtered by ancient dunes, should be confined within the Pliocene shoreline boundary.

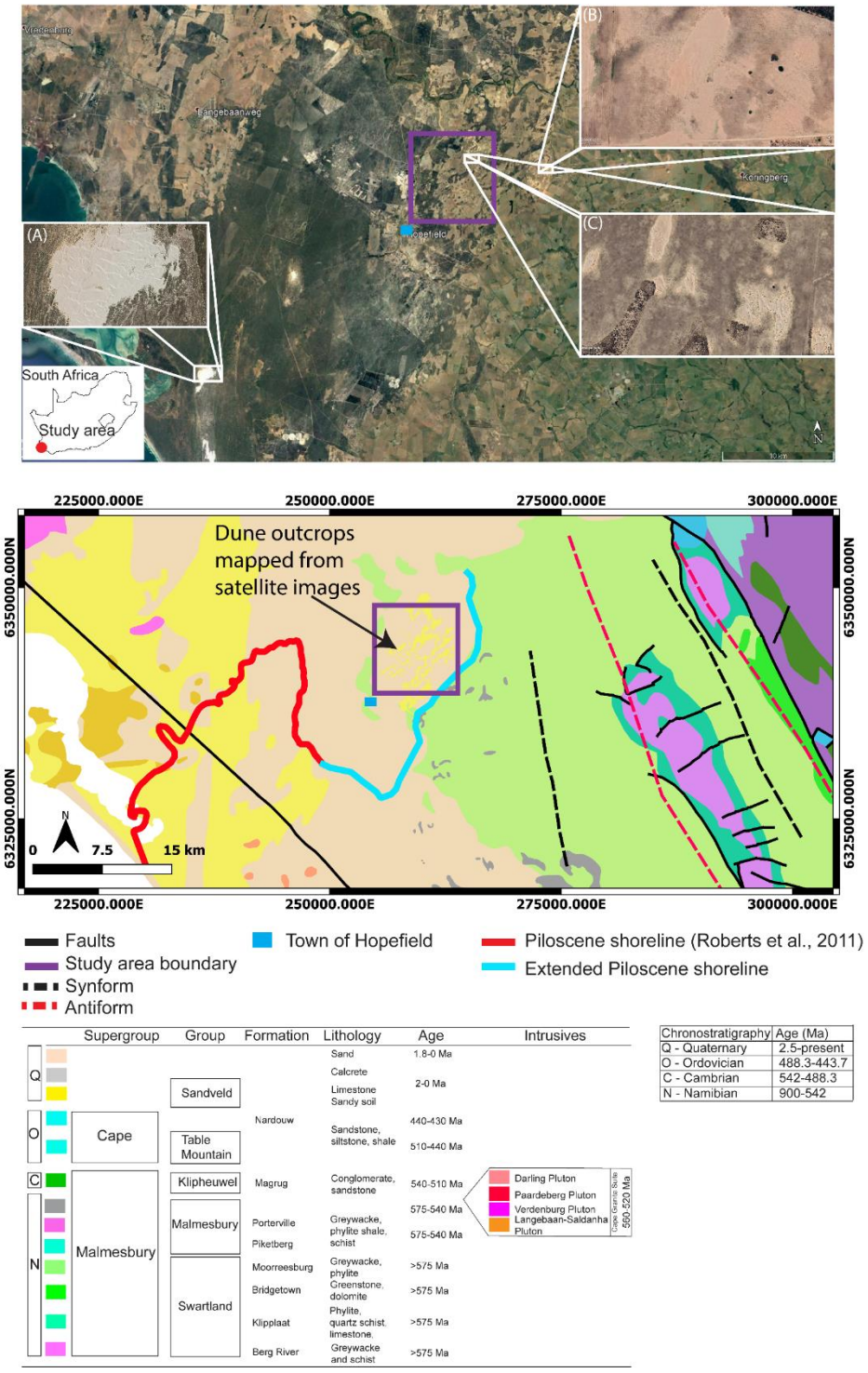


Figure 3.16. The red line marks the previously mapped Pliocene shoreline from Roberts et al. (2011). We make use of the satellite imagery and geophysical mapping to extend (blue line) the Pliocene shoreline further north-east. (A) Shows the location of the Yzerfontein–Geelbek dune cordon. (B) Orange colored matured dunes stabilized by vegetation in our study area. (C) Shows matured dunes furthest east from the present-day shoreline, marking the boundary of the Pliocene shoreline.

It is important notice that the conductive clay and calcrete aquitard masked the resistive aquifer beneath. Details in the resistive aquifer can only be seen when there is a break in the conductive clay and calcrete aquitard. This is a general problem in the MT method, that an overlying conductive layer can mask details of a resistor that lays beneath.

3.7. Conclusions

We have shown that AMT, satellite imagery and regional magnetic data can assist in the mapping of ancient dunes, preserved by calcrete layers, that recharge groundwater wells Around the Waterboerskraal farm. The ancient dune outcrops allow for the storage, filtration, and transmittance of fresh surface water in a Cenozoic sedimentary succession aquifer over the electrically resistive and partially magnetic basement Malmesbury Supergroup. The electrically conductive calcrete and clay aquitard is disrupted, by outcropping ancient dunes on the Waterboerskraal farm, and would otherwise prevent the transmission of surface water into the Cenozoic sedimentary succession aquifer.

Operational groundwater wells align with outcropping ancient dunes. While decommissioned groundwater wells lie away from ancient dune outcrops. The groundwater salinity is related to the proximity of wells to ancient dune outcrops. Therefore, ancient dune outcrops should be the primary target for usable groundwater within the Waterboerskraal farm and possibly the greater Swartland Terrane region. We also extended the previously mapped Pliocene shoreline by mapping a new ancient dune field in our research area with satellite imagery and geophysical data. Exploration for potable groundwater by targeting ancient dune

filtered water, should be confined within the newly mapped Pliocene shoreline boundary.

3.8. Acknowledgments

The support of the DST-NRF Centre of Excellence for Integrated Mineral and Energy Resource Analysis (DST-NRF CIMERA) towards this research is hereby acknowledged. Opinions expressed and conclusions arrived at, are those of the author and are not necessarily to be attributed to the CoE.

The South African Council for Geoscience and Jan van der Walt from GES Geophysics is also acknowledged for their support in providing regional geophysical data and an EH-4 Stratagem AMT system respectively.

We would also like to acknowledge the UBC-Geophysical Inversion Facility from the Department of Earth and Ocean Sciences at University of British Columbia for providing us with MAG3D. MAG3D is a program library for the forward modeling and inversion of magnetic data over 3-D structures.

Chapter 4 : Augmented ERT-MT Response Function

This chapter includes a manuscript that is being prepared for peer-review publication. It is important to notice that in the previous chapter, Chapter 3, the conductive clay and calcrete aquitard masked the resistive aquifer beneath. Details in the resistive aquifer can only be seen when there is a break in the conductive clay and calcrete layers overlying the aquifer. This is a general problem in the MT method, that an overlying conductive layer can mask details of a resistor that lays beneath. This research described in this paper is a direct response to the poor sensitivity of the MT method for resolving the resistive aquifers below a conductive aquitard in the previous chapter. This chapter covers a newly developed analytical solution, processing flow, and algorithms, for the MT method, designed to reduce the effects of conductive layering over deeper resistive features. The new processing flow and algorithms is tested on synthetic layered 1-D and 2-D half-space models and through a case study experiment over an electrically restive dyke overlain by a conductive overburden in the Bushveld Complex, South Africa.

Percentage of work done, and role played by authors on this paper:

Harrison, W.:

90% (Collected field data, processed field data, wrote and developed new algorithms, derived analytical solutions, modelled data, wrote the manuscript).

Pellerin, L.:

5% (assisted with numerical analyses and interpretation).

Webb, S.J.:

5% (supervisor, assisted in interpretation and reviewed the manuscript).

Augmented ERT-MT Response Function for Resistive Target Amplification

Wesley Harrison, University of the Witwatersrand, School of Geosciences, 1 Jan Smuts Avenue, Braamfontein, Johannesburg, 2000,

Email: wesley.harrison@students.wits.ac.za

Louise Pellerin, Green Geophysics, Inc. 2215 Curtis St, Berkeley, California 94702,

Email: pellerin@greengeophysics.com

Susan Jane Webb, University of the Witwatersrand, School of Geosciences, 1 Jan Smuts Avenue, Braamfontein, Johannesburg, 2000,

Email: Susan.Webb@wits.ac.za

4.1. Abstract

With the magnetotelluric (MT) method, conductive layers can mask deeper resistors. We derive an analytical relationship between electrical resistivity tomography (ERT) and MT data to calculate an augmented ERT-MT response function. The augmented ERT-MT response function adds additional high-frequency content in the MT response function. This allows us to model the near-surface conductive layer from the ERT data and resolve deeper resistive structures with the MT data. In general, for the one-dimensional (1-D) case, the augmented ERT-MT response function resulted in 1-D inverse model that showed an improvement of up to ~91% in recovering the true resistivity model. We also tested the augmented ERT-MT response function on theoretical 2-D models. Two electrical resistivity models are used for the 2-D tests. For both 2-D models, the resistive dyke and conductive overburden that was initially concealed was recovered when using the augmented ERT-MT response function. The augmented ERT-MT response function is also applied to field data, allowing us to map a resistive dyke below a conductive overburden that was absent in the standard MT inverse model. The recovered dyke and fault zone in the augmented ERT-MT response function resistivity inverse model correlates with the same features seen in a magnetic susceptibility inverse model. The augmented ERT-MT response function technique improves the resolution of MT to recover resistors beneath a conductive layer for both the theoretical and experimental case.

4.2. Introduction

It is well known in electromagnetics that resistors are masked or distorted when beneath a conductor and particularly so for the magnetotelluric (MT) method (Park and Livelybrook, 1989; Pedersen and Gharibi, 2000 and Constable and Weiss, 2006). This is because of the MT methods natural sensitivity to conductive bodies and poor sensitivity to resistive features (Streich et al., 2010).

To overcome this natural insensitivity to resistors below near-surface conductors, that effects the MT method, we will make use of electrical resistivity tomography (ERT), which has a higher near-surface resolution than the MT method, to increase the high-frequency content in the MT response function. Since both the ERT and MT methods measure the electrical field, we can combine the two data sets through a transformation that augments both data sets into one. We describe a method to calculate an augmented MT response function, that we name the augmented ERT-MT response function, calculated from both MT and ERT data. This allows us to model the near-surface conductive layer from the ERT data and resolve deeper resistive structures with the MT data.

To accomplish this, we derive an analytical relationship between ERT data and the MT impedance tensor. We can then augment the traditional MT response function with higher frequency data. This results in resistivity inverse models that can recover resistive features that are absent in traditional MT inverse models.

4.3. Calculating augmented ERT-MT response function

4.3.1. Analytical derivation

Here we derive a relationship between ERT data and the MT impedance. First, we start with Ohm's Law:

$$J=\sigma E=-\sigma \nabla V, \tag{4.1}$$

J is the current density (A/m^2), σ is the conductivity of the medium (S/m), E is the electric field (V/m) and V it the potential (V).

Considering the ERT current and potential electrodes array shown in Figure 4.1. For the current density in the half space at the center between the two current electrodes we may just consider the horizontal flowing current density (J_{DCx}) since the vertical flowing current density (J_{DCz}) is minimal.

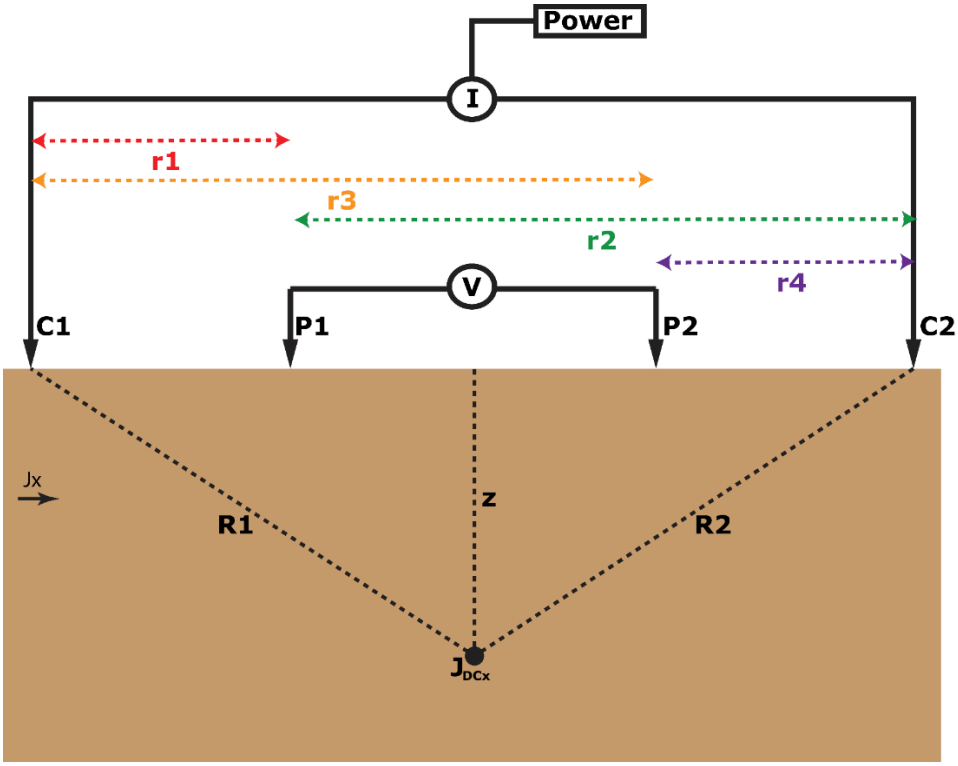


Figure 4.1. Sketch of a typical ERT array. C1 and C2 are current electrodes while P1 and P2 are potential electrodes. The distance between current electrodes and potential electrodes is represented as distances r1, r2, r3 and r4 respectively. Jx is the current density in the horizontal direction. J_{DCx} is the horizontal current density measured at that point, with a depth of z and distance R1 and R2 away from current electrodes C1 and C2 respectively.

The potential (V_1) from C1 at P1 is:

$$V_1 = -\frac{I\rho}{2\pi r_1}. \tag{4.2}$$

The potential (V_2) from C2 at P1 is:

$$V_2 = \frac{I\rho}{2\pi r_2}, \tag{4.3}$$

where I represents current (A), ρ is resistivity of the medium (Ω·m). For the total potential in a half space due to the two current electrodes we add equation 4.2 and 4.4:

$$V = V_1 + V_2 = \frac{I\rho}{2\pi}\left(\frac{1}{r_1} - \frac{1}{r_2}\right). \tag{4.4}$$

For the current density in the half space we just consider the horizontal current density (J_{DCx}) since the vertical current density ($J_{DCz)}$ is zero.

$$J_{DCx} = -\frac{1}{\rho}\frac{\partial V}{\partial x}$$

$$J_{DCx} = \frac{I}{2\pi}\left[\left(\frac{x}{R_1^3} - \frac{x-L}{R_2^3}\right)\right]. \quad (4.5)$$

For a plane polarised wave in a homogenous and isotropic medium we neglect the $\partial\vec{E}/\partial t$ term because ωε << σ from the quasi static approximation. The quasi static approximation states that when compared to changes in bulk conductivity, electrical permittivity and magnetic permeability is negligible so we drop the ε term. As shown on pages 308-309, in Telford et al. (2001), the magnetotelluric current density is given as:

$$\nabla \times \vec{H} = \sigma\vec{E} + \varepsilon\frac{\partial\vec{E}}{\partial t} = \sigma\vec{E} = \vec{J},$$

therefore, we assume the electromagnetic wave is propagating in the z axis then the xy plane is the polarisation plane. H is given as:

$$\mathrm{H}_y = \mathrm{H}_0 e^{-\sqrt{\frac{\omega\mu\sigma}{2}}z + i(wt - \sqrt{\frac{\omega\mu\sigma}{2}}z)},$$

taking the real part as the required solution as shown on page 309 in Telford et al. (2001):

$$\mathrm{H}_y = \mathrm{H}_0 e^{-\sqrt{\frac{\omega\mu\sigma}{2}}z}\cos\left(\omega t - \sqrt{\frac{\omega\mu\sigma}{2}}z\right),$$

therefore, when considering the curl of H_y, there will be current in the x direction only:

$$J_{MTy} = J_{MTz} = 0,$$

then we are left with the special case:

$$J_{MTx} = -\frac{\partial}{\partial z}\left[H_0 e^{-z\sqrt{\frac{\omega\mu\sigma}{2}}} \cos\left(\omega t - z\sqrt{\frac{\omega\mu\sigma}{2}}\right)\right],$$

$$J_{MTx} = [\sqrt{\omega\mu\sigma}]\left[H_0 e^{-z\sqrt{\frac{\omega\mu\sigma}{2}}} \cos\left(\omega t - z\sqrt{\frac{\omega\mu\sigma}{2}} + \frac{\pi}{4}\right)\right], \quad (4.6)$$

where H_0 is the magnetic field intensity, ω is the angular frequency of the field, μ is the relative magnetic permeability of the medium and t is time. The magnetotelluric current density is generally difficult to solve for even simple shapes, such as 2-D slabs in a half space, but we show that this simplified equation provides value by recovering the true resistivity inverse model by up to 90% for the MT method in our study area. The effects of more complicated geometry, for example 3-D lithology, may be under modelled and the true resistivity model might not be fully recovered but in the examples shown, in this thesis, the equation provides greater resistivity model recovery when calculating resistivity inverse models. Deriving a general form of equation 4.6 for 3-D geometry will be part of future work and is outside the scope of this thesis. From the previously derived MT current density in equation 4.6 we can equate the ratio between the electric field strength and current density for both the MT and ERT method.

From equation 4.1 we have:

$$E_{DC} = \frac{J_{DCx}}{\sigma} \tag{4.7}$$

$$E_{MT} = \frac{J_{MTx}}{\sigma} \tag{4.8}$$

We then set equation 4.7 equal to equation 4.8:

$$\frac{J_{DCx}}{E_{DC}} = \frac{J_{MTx}}{E_{MT}}$$

$$E_{MT} = \frac{J_{MTx}}{J_{DCx}} E_{DC}$$

$$E_{DC} = \frac{\frac{I}{2\pi}\left[\left(\frac{x}{r_1^3} - \frac{x-L}{r_2^3}\right)\right]}{[\sqrt{\omega\mu\sigma}]\left[H_0 e^{-z\sqrt{\frac{\omega\mu\sigma}{2}}} \cos\left(\omega t - z\sqrt{\frac{\omega\mu\sigma}{2}} + \frac{\pi}{4}\right)\right]} E_{MT} \tag{4.9}$$

Equation 4.9 shows that the electric field for the MT method can be calculated from the electrical resistivity method and the converse is also true. We can also calculate the MT impedance tensor from electrical resistivity data:

$$\rho_a = \frac{1}{2\pi\mu f}|Z|^2 = \frac{1}{2\pi\mu f}\left|\frac{E}{H}\right|^2$$

$$E_{DC} = \frac{\frac{I}{2\pi}\left[\left(\frac{x}{r_1^3} - \frac{x-L}{r_2^3}\right)\right]}{[\sqrt{\omega\mu\sigma}]}\sqrt{\omega\mu\rho_a}$$

$$Z_{MT} = \frac{[\sqrt{\omega\mu\sigma}]}{\frac{I}{2\pi}\left[\left(\frac{x}{r_1^3} - \frac{x-L}{r_2^3}\right)\right]} \tag{4.10}$$

4.3.2. Theoretical models

To test equation 4.10, we calculated the forward response of a theoretical one-dimensional (1-D) resistivity model for both ERT and MT methods. First the ERT data is calculated from a theoretical resistivity model and then used to calculate the pseudo-MT response function from equation 4.10 This is then compared to the

estimated 1-D MT response function. The estimated and predicted responses are then inverted to demonstrate that MT alone has trouble at high frequencies and needs to be augmented (Figure 4.3). The finite difference forward modelling and inversion routine used for the ERT data is RES2DMOD and RES2DINV. The inversion routine is based on l_2-norm smoothness-constrained least-squares method developed by Loke and Barker (1996). A value of 0.16 is used for the initial damping factor value for the first iteration then halved after each iteration with a minimum allowed value of 0.015 to counteract instability. The subsurface is discretized into rectangular cells, based on the position of available data points calculated from the resistivity array geometry. The deepest layer in the model is equivalent to the depth of investigation. The total number of cells equals the number of available data points in the mesh. Topography values are also included in the mesh if available. The medium conductivity value in equation 4.10 is taken from the resistivity inverse model cell values corresponding to the cell value at the same skin depth of the MT frequency used.

Inversion sensitivity maps show regions in a MT resistivity inverse model which significantly change the MT response function curves. Sensitivities generally consolidate near conductive features in a model since small changes in conductive cells can cause significant changes in the MT response function curves. While changes in resistive features result in a slight change in the MT response function curves. For example, in Figure 4.2(A), we have a 1000 Ω·m half space. The sensitivity map, calculated in WingLink, for the inverse model of the half space is shown in Figure 4.2(C) and distinctive cone shape sensitivity regions is distributed throughout the half space. A 10 Ω·m conductor is embedded in the

center of the 1000 Ω·m, as shown in Figure 4.2(B). The sensitivity map for this model shows that most of the sensitivity is located near the center of the conductor. Since this is where changes in conductivity of a conductor will have a significant effect on the MT response function curves. Therefore, sensitivity maps can be used in MT inverse models to evaluate if the MT data used for the inverse calculation is sufficiently dense in a certain depth range. If the sensitivity map resembles the map shown in Figure 4.2(C), then there is insufficient MT data to identify the conductor at ~25-75 m depth.

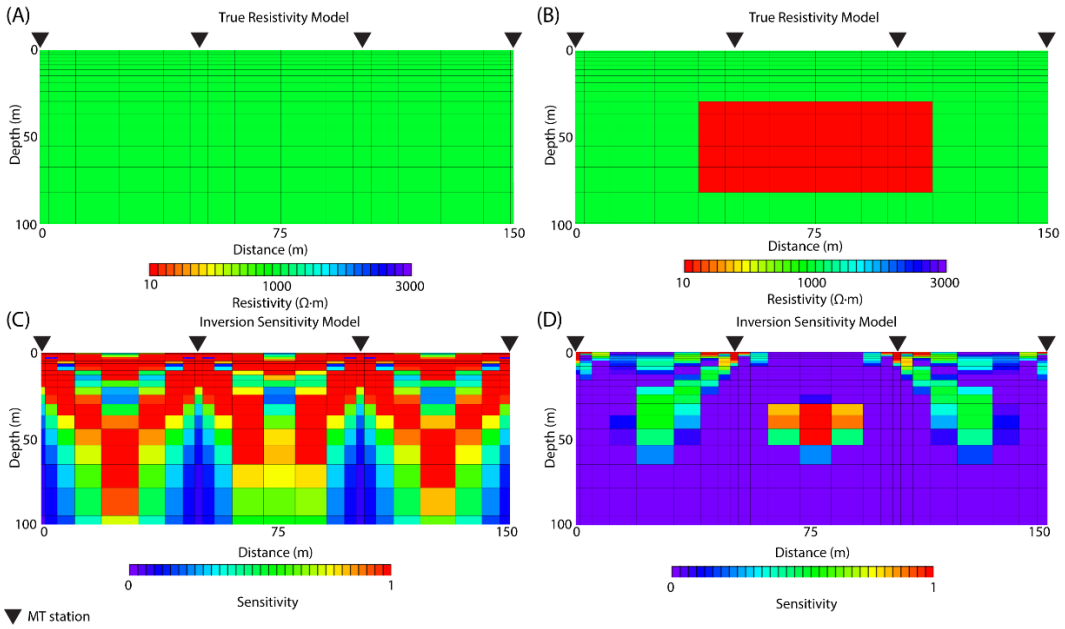


Figure 4.2. (A) True resistivity model of a 1000 Ω·m half space. (B) True resistivity model of a 1000 Ω·m half space with an embedded 10 Ω·m conductor. (C) Sensitivity model for the inverse model calculation from forward modeled MT data of the 1000 Ω·m half space, with a frequency range of 10 - 10000000 Hz. Most of the model sensitivity is in a distinctive cone shape distribution throughout the half space. (D) Sensitivity model for the inverse model calculation from forward modeled MT data of the 1000 Ω·m half space with the embedded 10 Ω·m conductor, with a frequency range of 10 - 10000000 Hz. Most of the model sensitivity is located near the center of the conductor.

To bridge possible gaps between the pseudo-MT and real MT data, we fit smooth (D+) curves to the data set (Figure 4.3). The D+ function relates apparent

resistivity and phase by finding a 1-D earth model that fits both parameters by recalculating a physically valid continuous response function (Beamish and Travassos, 1992). As shown in Figure 4.3 ((B) and (C)), when joining the pseudo-MT data calculated, from the ERT data, with the MT data by using the D+ curves, we recover more of the true resistivity model then if we left the gap between the two response functions. The normalized inversion model sensitivity maps (Figure 4.3(D) and (E)) show regions in the models that have the highest sensitivity to the data, which in MT inversion calculations would relate to conductive zones in the model. Therefore, most of the sensitivity in the model should be consolidated in the top 10 m of the inverse model, where the conductive 10 m layer is situated. This is shown in Figure 4.3(E) where the D+ curves are used to connect the pseudo-MT and real MT data. While in Figure 4.3(D), the sensitivities are spread throughout the model, resembling the half space sensitivity model seen in Figure 4.2(C). Therefore we will apply the D+ curves to all the augmented ERT-MT response functions to bridge any possible gaps caused by ERT arrays with insufficient depth penetration or dead bands in the MT data resulting in discontinuities between the pseudo-MT and real MT data.

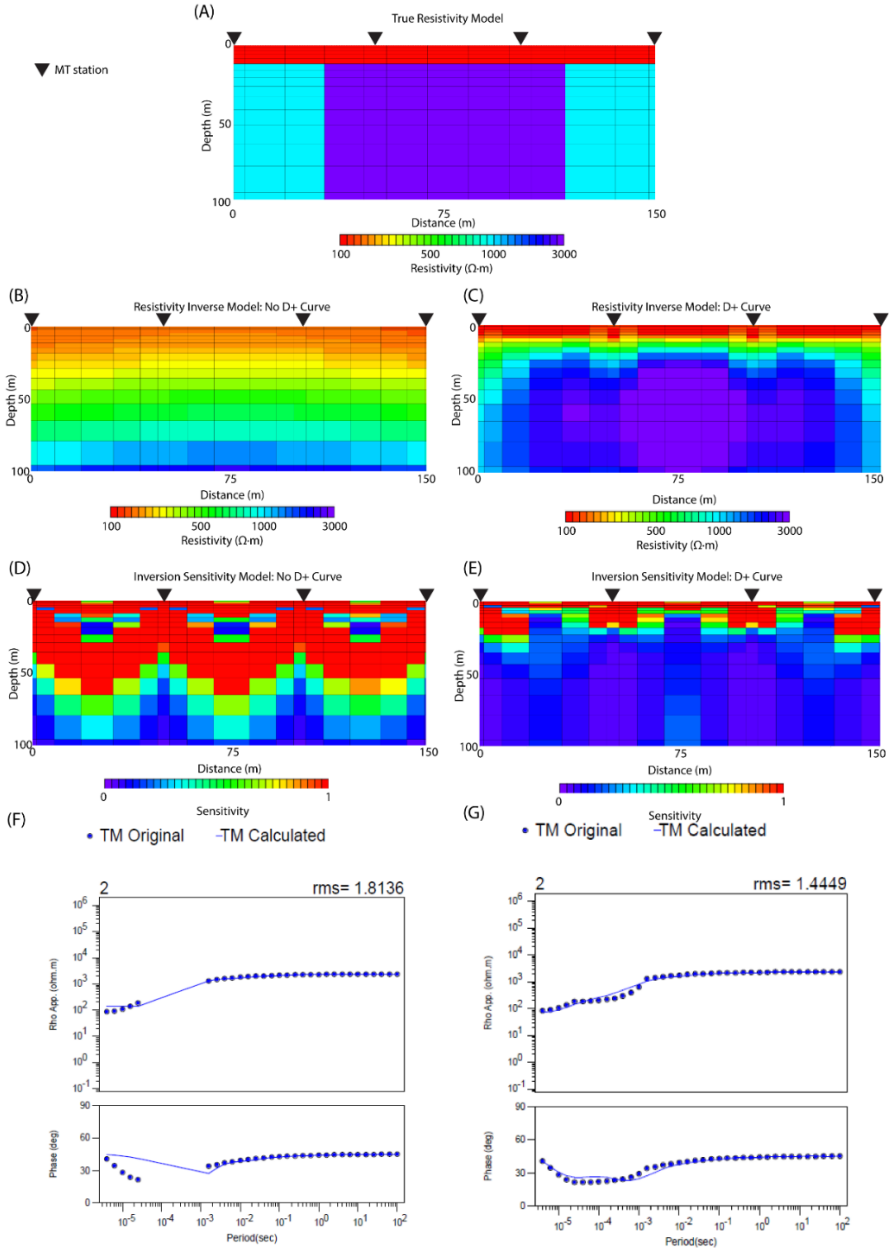


Figure 4.3. (A) True resistivity model. (B) Resistivity inverse model of the augmented ERT-MT response function without the use of smooth D+ curves. (C) Resistivity inverse model of the augmented ERT-MT response function with the use of smooth D+ curves. (D) Inverse model sensitivity map of the augmented ERT-MT response function without the use of smooth D+ curves. Sensitivities are spread throughout the inverse model. (E) Inverse model sensitivity map of the augmented ERT-MT response function with the use of smooth D+ curves. Sensitivities are isolated in the top 10 m where the conductive layer is situated. (F) Augmented ERT-MT response function, without D+ curve data filling the gap, apparent resistivity and phase plots with calculated inverse model apparent resistivity and phase. (G) Augmented ERT-MT response function, with D+ curve data filling the gap, apparent resistivity and phase plots with calculated inverse model apparent resistivity and phase.

Using ERT data can help constrain the near surface as demonstrated in the following models.

The model has a conductive 10 Ω·m overburden that is 10 m thick. Below the overburden is a resistive 1000 Ω·m half-space. Equation 4.10 is used to calculate the MT impedance from the ERT data. The medium conductivity (σ) is calculated from the 1-D ERT inverse model. With the calculated MT impedances, we can calculate both the phase and apparent resistivity response function from the ERT data. The MT response function, calculated from the ERT data (red line), has a higher frequency than the MT data but it allows us to augment the MT data with high-frequency MT data (Figure 4.4). Both the actual MT data and the MT data from the ERT data overlap.

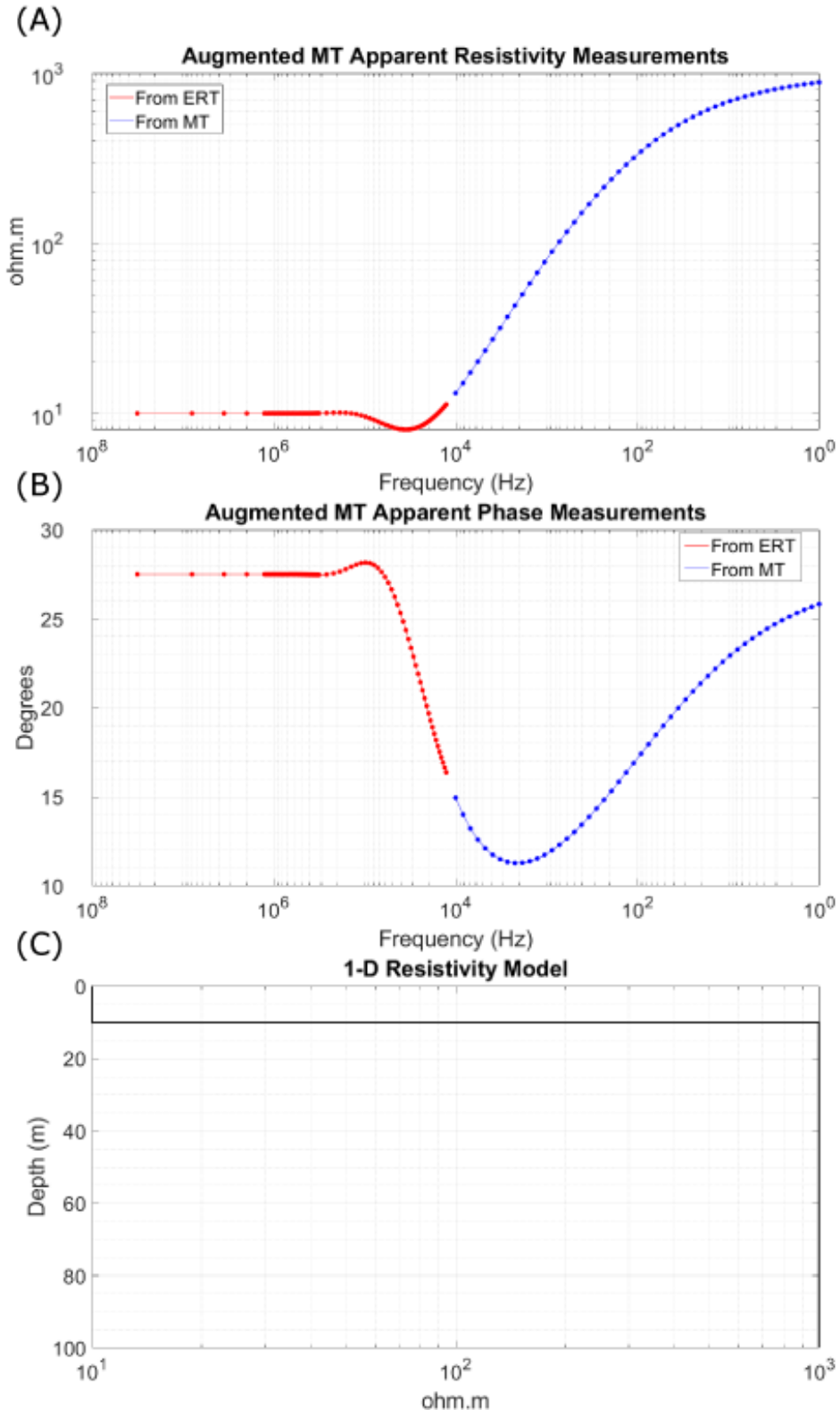


Figure 4.4. (A) Calculated apparent MT resistivity response from ERT (red) and MT (blue) data. (B) Calculated apparent MT phase response from ERT (red) and MT (blue) data. (C) True 1-D resistivity model with a 10 Ω·m overburden to a depth of 10 m overlaying a 1000 Ω·m half-space.

For the second test, we used the same 1-D resistivity model seen in Figure 4.4(C) and calculated both the augmented ERT-MT (blue dots) and MT only (red dots) response functions. We then inverted both response functions using the conjugant gradient code developed by Rodi and Mackie (2001) (Figure 4.5). Adding a differing number of layers to different models to test how each set of data resolves the model with increasing complexity. The augmented ERT-MT response function resulted in a 1-D inverse model where the 10 Ω·m surface conductor is mapped down to a depth of between 10 and 48 m. The half-space resistivity values obtained by applying the augmented ERT-MT response function, are between 1000 Ω·m and 1200 Ω·m for the infinite second layer. When using the standard audio magnetotelluric (AMT) data recording range (ie without ERT augmentation), the inversion routine confined the near-surface conductor to a depth of 125 m and 450 m and the resistive half-space recovered a resistivity of between 1000 Ω·m and 1400 Ω·m. These results must be compared against the true resistivity of the model which is a 10 Ω·m conductive layer to a depth of 10 m and an underlying half-space of 1000 Ω·m.

Keep in mind that the true resistivity of the model is 10 Ω·m to a depth of 10 m and an underlying half-space of 1000 Ω·m. In general, for the 1-D case, the augmented ERT-MT response function resulted in a 1-D inverse model that showed an improvement of up to ~91% in recovering the true resistivity model.

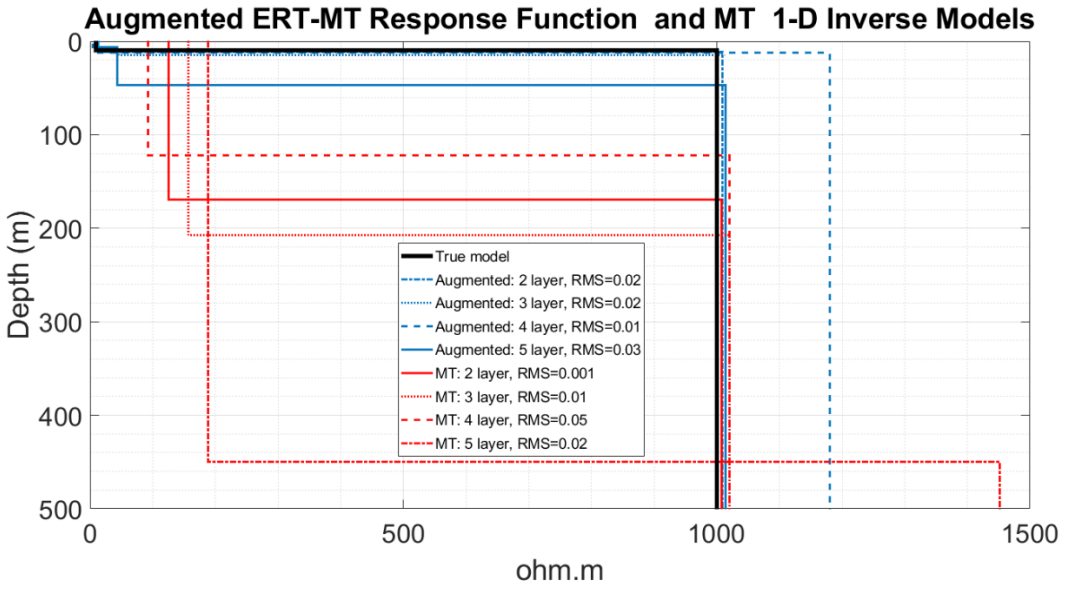


Figure 4.5. Augmented ERT-MT response function (blue to purple) and MT (red to yellow) 1-D resistivity inverse models. The true resistivity model is represented by a black line. The augmented ERT-MT response function resulted in a 1-D inverse models that depicts an improvement of up to ~91% in recovering the true resistivity model.

Applying the augmented ERT-MT response function approach to two-dimensional (2-D) MT data is our next step by using two electrical resistivity models for the 2-D tests. The first model has a conductive 100 Ω·m, 10 m thick overburden. Below the overburden is a 1000 Ω·m half-space. Embedded in the half-space is an 8000 Ω·m dyke 20 m wide. The dyke is placed 300 m along the resistivity model, the model itself is 595 m wide. The second resistivity model is identical to the first model, but the dyke is 40 m wide and the model is only 238 m wide.

Using the Wenner-Schlumberger ERT configuration with a 5 m electrode spacing and a total of 120 electrodes the ERT forward response is calculated followed by the inverse model from the forward response. The 2-D ERT resistivity inverse model is again used to calculate σ for equation 4.10. For the first resistivity model,

the ERT inverse model recovered the dyke at 300 m along the inverse model (Figure 4.6). The ERT inverse model quantify error in the model using an L2-norm data misfit root mean square error (RMSE) calculation. The ERT inverse model had a root mean square error of 0.36. Even though the ERT inverse model recovers the dyke, by adding the MT data we allow for deeper investigation of the dyke. Since the ERT method recovers the true resistivity model effectively we can use this model to compare how well the augmented ERT-MT response function performs at these shallow depths. The ERT inverse model is used to calculate the augmented ERT-MT response function with the forward modeled MT data from the same resistivity model (Figure 4.7). The black dots shown in Figure 4.7 are the calculated pseudo-MT data point from the ERT inverse model. The MT survey design for the forward calculation consists of 13 MT stations with a station spacing of 50 m. The gap between the pseudo-MT and MT data will be connected using a D+ curve.

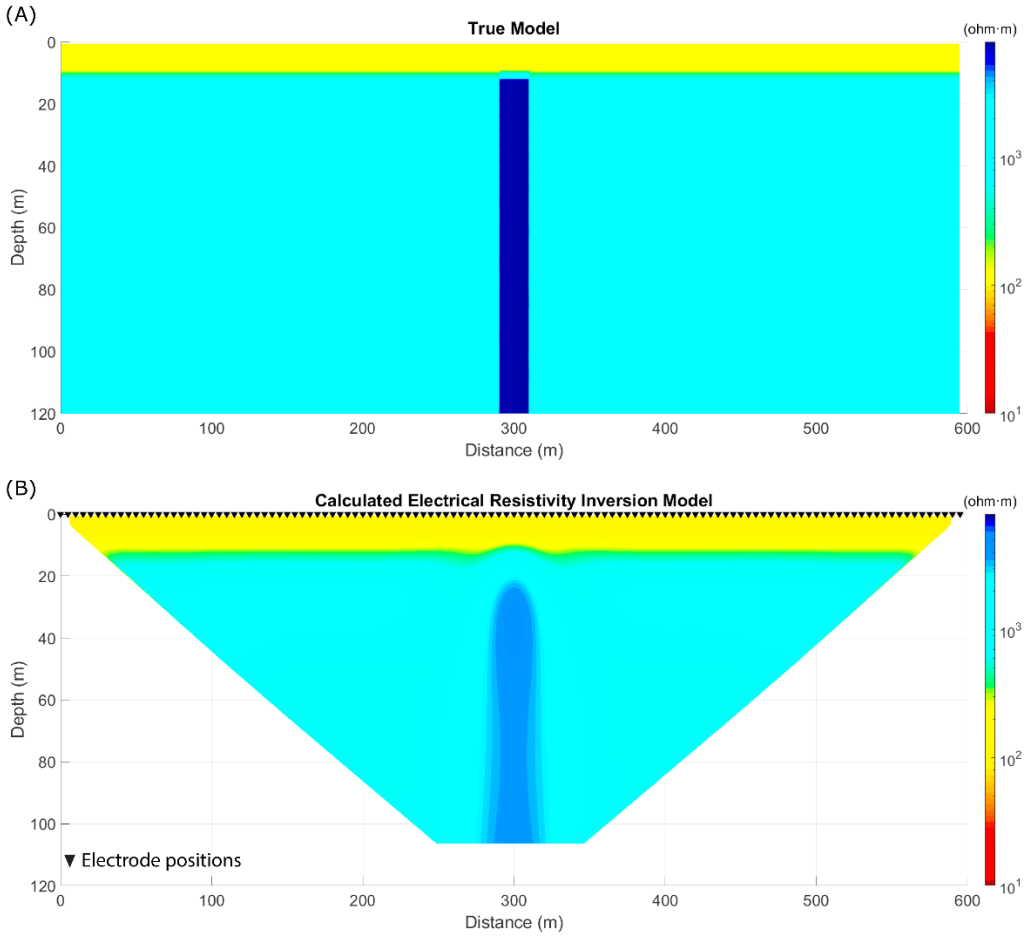


Figure 4.6. (A) True resistivity model with a conductive (100 Ω·m) overburden, to a depth of 10 m, and an underlying resistive (8000 Ω·m) dyke embedded in a 1000 Ω·m half-space. (B) ERT inverse model with an RMSE of 0.36. The ERT inverse model recovers both the conductive overburden and the dyke.

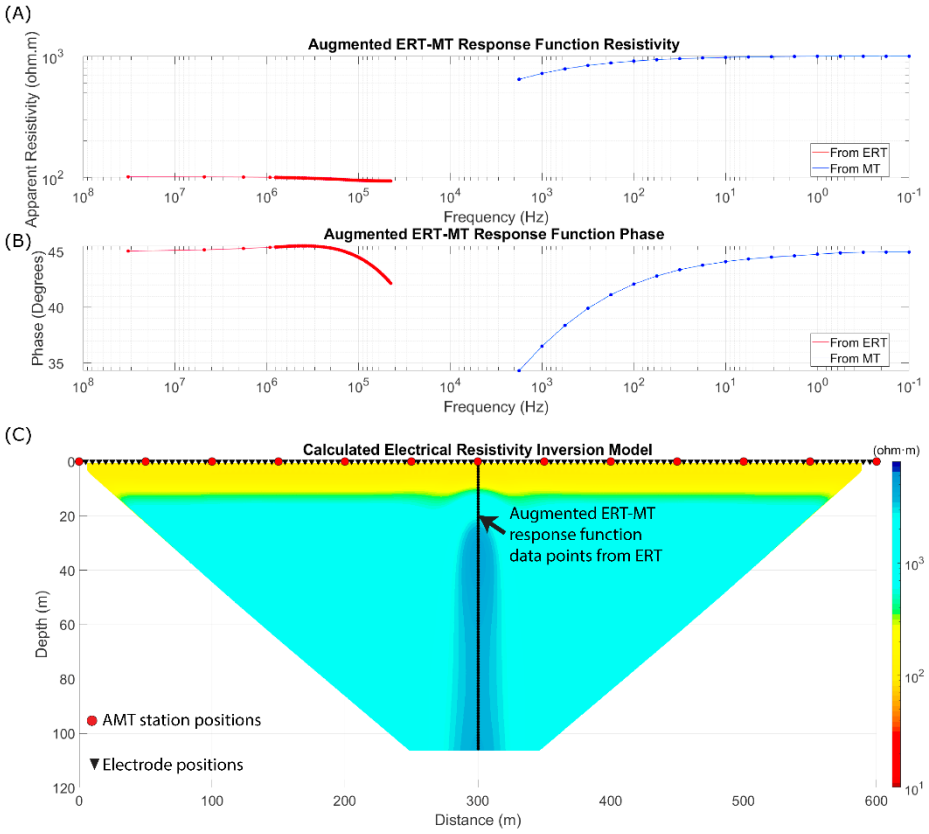


Figure 4.7. (A) Calculated apparent magnetotelluric resistivity response from augmented ERT-MT response function (red) and audio magnetotelluric (blue) data. (B) Calculated apparent magnetotelluric phase response from augmented ERT-MT response function (red) and audio magnetotelluric (blue) data. (C) ERT inverse model used to calculate the augmented ERT-MT response function. The black dots show the location of data points derived from the augmented ERT-MT response function. The gap between ~1000 Hz- 100000 Hz is due to the shorter ERT array so the depth penetration is insufficient for frequency overlap.

Since the electromagnetic fields are orthogonal to each other they can be decomposed into two modes that relate to the polarization of the electromagnetic fields. The first mode is known as the transverse magnetic (TM) mode where the magnetic field is polarized parallel to the lithological strike. The second mode is called the transverse electric (TE) mode where the electric field is polarized parallel to lithological strike. For this paper, we will only study the TM mode since we are only considering ERT data along the profile line. Future work will

consider three-dimensional (3-D) ERT inverse models to augmented both the TM and the TE modes.

The minimum and maximum frequency set for the 2-D inverse model calculations is 0.1 Hz and 10000000 Hz respectively, which replicates the frequency range of the typical data collected in my study areas. A starting model of 1000 Ω·m is used for the initial inverse calculation. The objective function is set to first find the smoothest model with a standard Laplacian operator focusing on minimizing the integral of the gradients of the model with a tau value of 3. Once the first inverse model is calculated the resulting model is used as a starting model for the second inverse model calculation. The objective function is now set to solve for the smoothest variation away from the starting model with a standard Laplacian operator focusing on minimizing the integral of the Laplacian. For this inverse calculation, the Tau operator is set as 1 with weighting functions enabled to prevent the model from becoming too blocky. This inversion methodology allows for an initial smooth model to be calculated from a 1000 Ω·m half-space and then the resulting smooth model is used as starting model for a second inverse calculation that is focused on fitting the observed data. This inversion methodology will also be used later in this chapter for the MT data collected in our study site.

The first inverse model, using only MT data, shows a resistor (~ 2700 Ω·m) at 300 m along the profile but the resistive structure is at a depth of ~150 m (Figure 4.8(B)). The conductive overburden is absent in this inverse model. The resistivity inverse model using the augmented ERT-MT response function also models a resistor (~7900 Ω·m) at 300 m along the profile (Figure 4.8(C)). The resistor

ranges from ~100 m wide at 50 m deep to ~200 m wide at 150 m deep. The dyke is better constrained with the augmented ERT-MT response function. The resistivity inverse model, for the augmented ERT-MT response function, maps the conductive (~20 Ω·m) overburden to a depth ~10 m. The higher conductivity contrast is sometimes caused by the smoothness constrained inversion attempting to fit the very high frequencies (> 10^7 Hz). The MT inverse modeling routines in WingLink also seem to make the apparent resistivity above 10000000 Hz very conductive on Windows 10. This is possibly an algorithm error since when using my own 1-D MatLab forward modeling code this does not happen at these high frequencies. But I still make use of the WingLink code for its 2-D modeling capabilities instead of my 1-D MatLab forward modeling code.

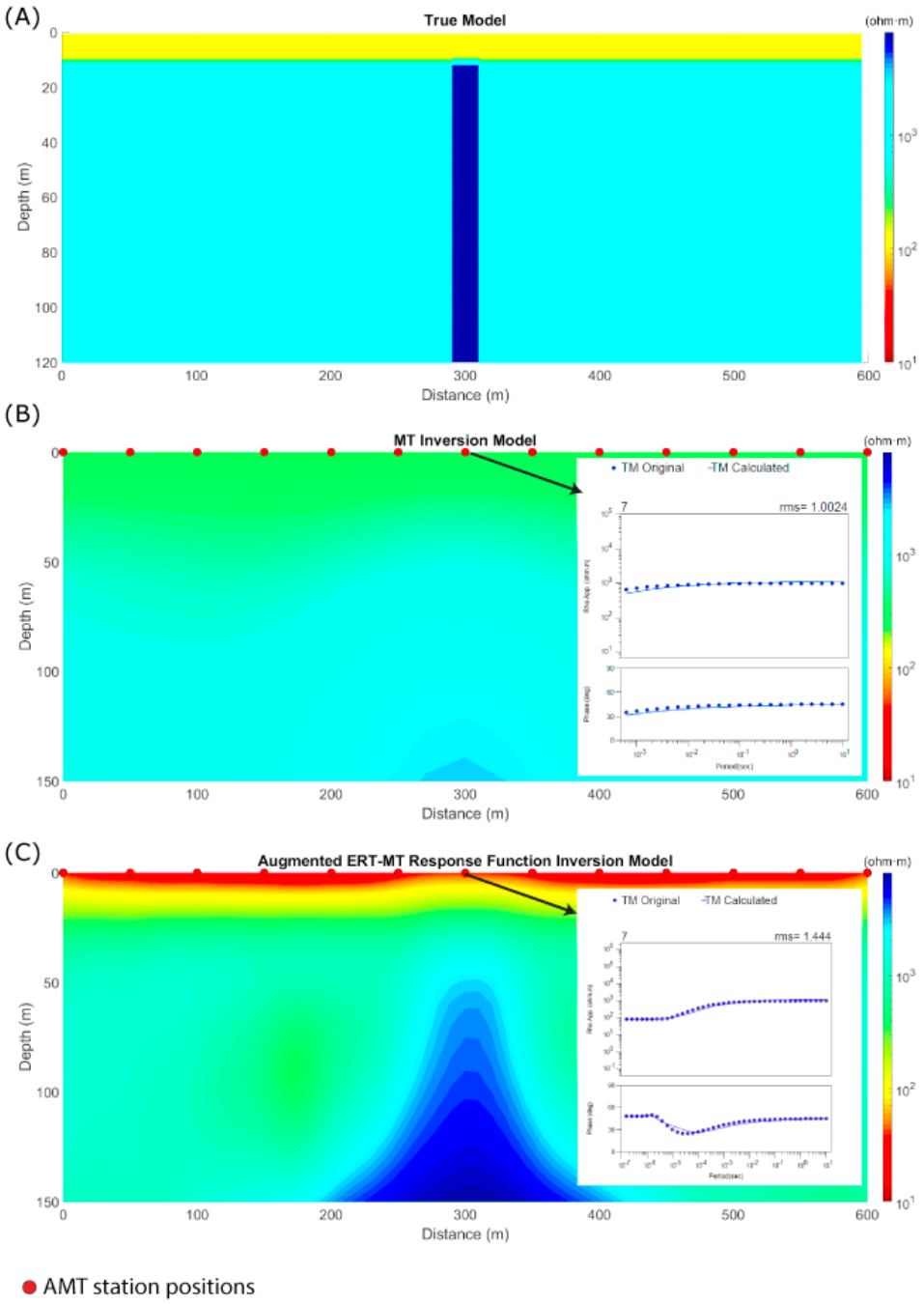


Figure 4.8. (A) True resistivity model that we are trying to recover has a conductive (100 Ω·m) overburden, to a depth of 10 m, and an underlying resistive (8000 Ω·m) dyke embedded in a 1000 Ω·m half-space. (B) Resistivity inverse model only using audio magnetotelluric data. A resistor is mapped at 300 m along the profile but is at a depth of ~150 m. The conductive overburden is absent from this model. The RMSE for this model is 0.6. (C) Resistivity inverse model using the augmented ERT-MT response function. A resistor is again mapped at 300 m along the profile but is constrained to ~100-200 m wide. Also, the conductive overburden is mapped in this inverse model to a depth of 10 m. The RMSE for this model is 0.5.

To test the limits of the augmented ERT-MT response function method we shortened the ERT array to 238 m, which will result in shallower depth penetration. The ERT survey has an electrode spacing of 2 m and the MT survey has a station spacing of 25 m. The ERT inverse model, with an RMSE of 0.2, again mapped a resistor (~8000 Ω·m) at 300 m along the profile (Figure 4.9(B)). The result of again calculating the augmented ERT-MT response function from the ERT and MT data is illustrated in Figure 4.10.

The inverse model using only the MT response function shows no clear resistor that could be the dyke that we aim to recover (Figure 4.11(B)). The model resembles a 1-D layered model and masks the resistor under the conductive overburden. The inverse model using the augmented ERT-MT response function does map a resistor (~4000-8000 Ω·m) at 300 m along the profile. The resistor is again better constrained using the augmented ERT-MT response function even for this case.

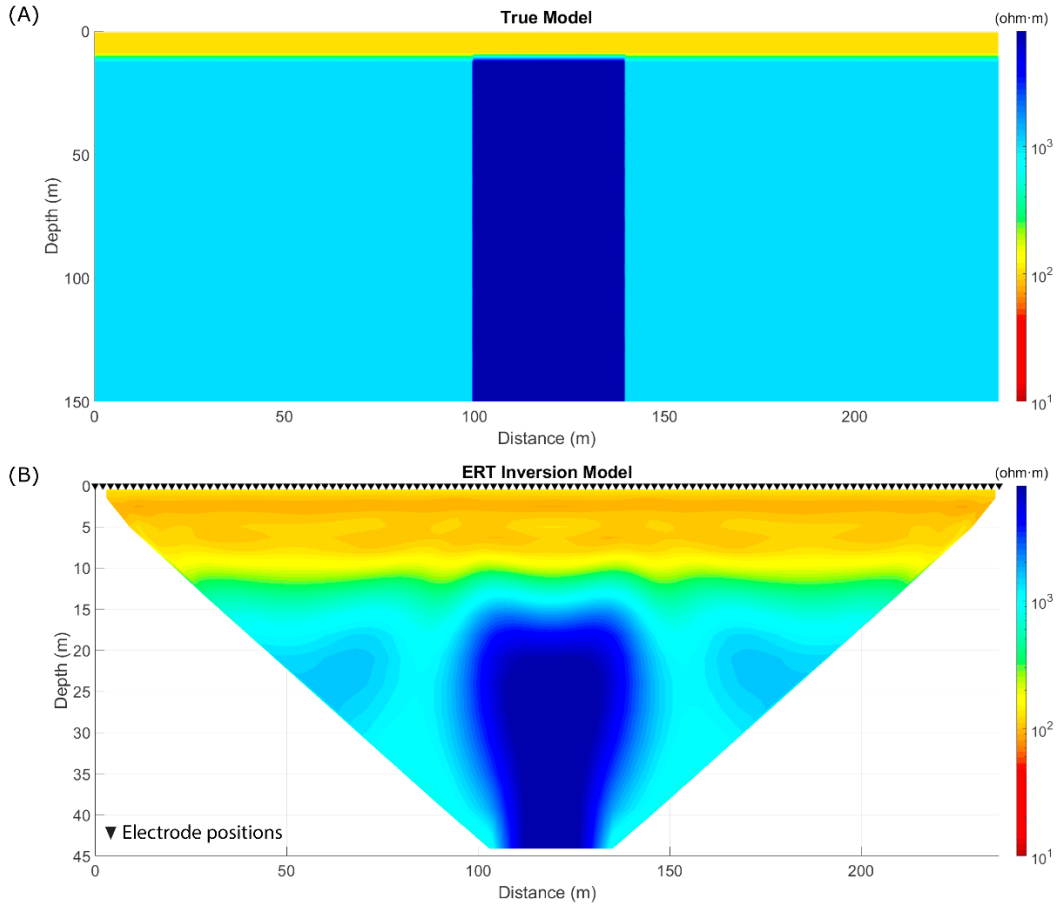


Figure 4.9. (A) True resistivity model with a conductive (100 Ω·m) overburden to a depth of 10 m and an underlying resistive (8000 Ω·m) dyke embedded in a 1000 Ω·m half-space. (B) ERT inverse model with an RMSE of 0.3. The resistive dyke and the conductive overburden is recovered in the inverse model.

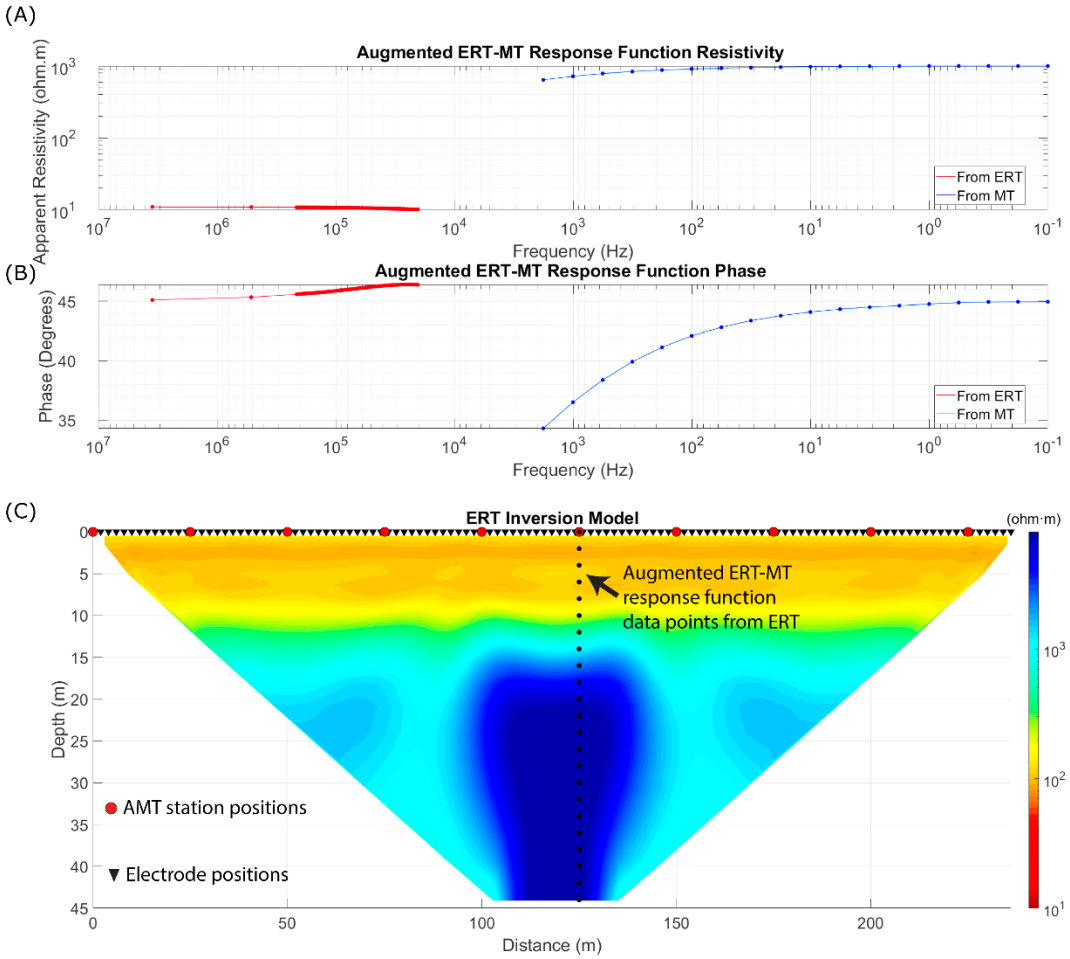


Figure 4.10. (A) Calculated apparent magnetotelluric resistivity response from ERT (red) and audio magnetotelluric (blue) data. Calculated phase response from ERT (red) and MT (blue) data. (C) ERT inverse model used to calculate the augmented ERT-MT response function. The black dots show the location of data points derived from the augmented ERT-MT response function. The gap between ~1000 Hz- 100000 Hz is due to the shorter ERT array so the depth penetration is insufficient for frequency overlap

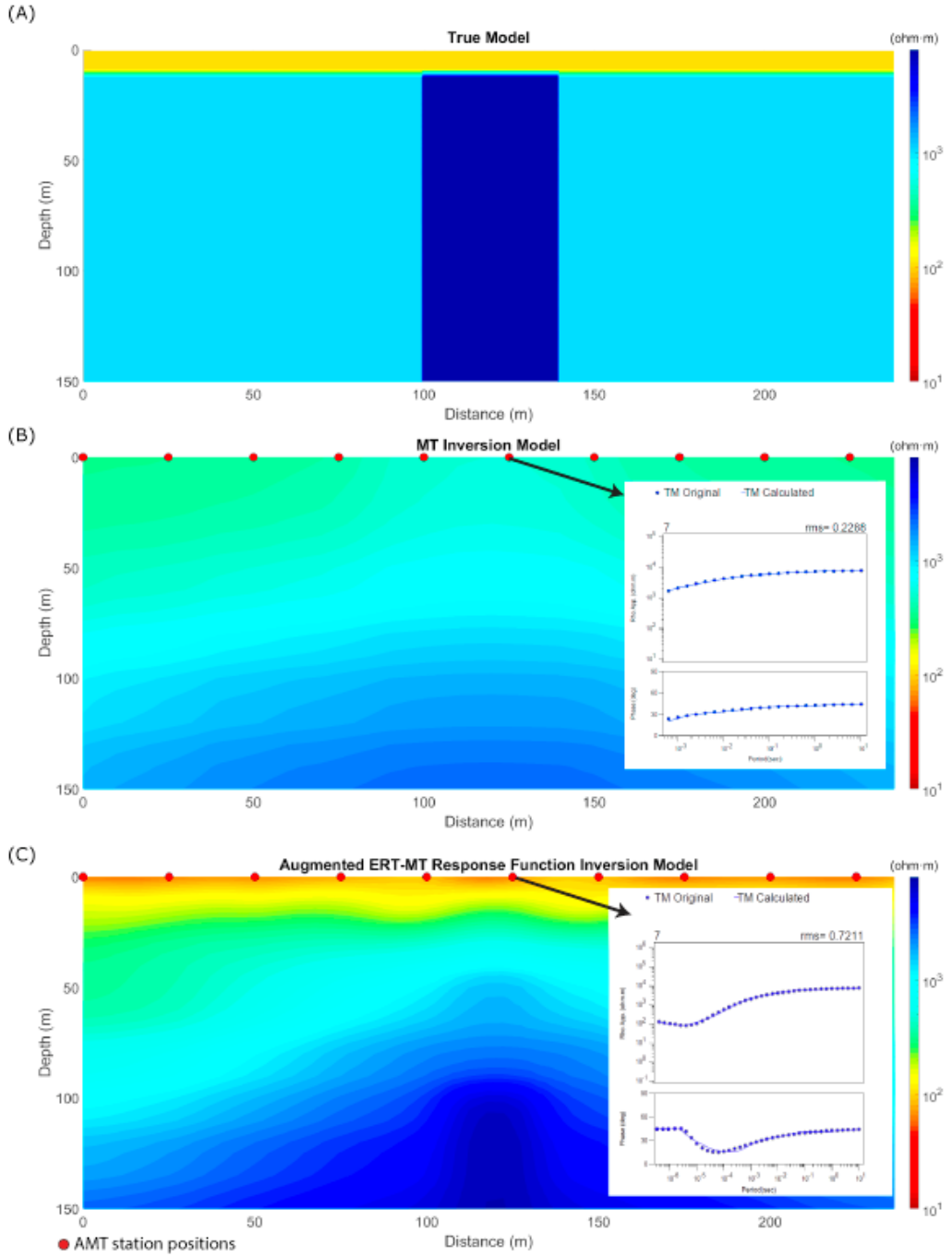


Figure 4.11. (A) The true resistivity model has a conductive (100 Ω·m) overburden, to a depth of 10 m, and an underlying resistive (8000 Ω·m) dyke embedded in a 1000 Ω·m half-space. The model is 238 m in length almost half the size of the previous model tested. (B) Resistivity inverse model only using audio magnetotelluric data. No clear resistor is mapped at 300 m along the profile. Again, the conductive overburden is absent in this inverse model. The inverse model had an RMSE of 0.3. (C) Resistivity inverse model using the augmented ERT-MT response function. A resistor is mapped at 300 m along the profile but is constrained to ~100 m. Also, the conductive overburden is again mapped in this inverse model. The inverse model had an RMSE of 0.3.

Since both the 1-D and 2-D experiments are showing promising results, when using the augmented ERT-MT response function for inverse modelling, for the second half of the paper we will consider a real case study.

4.5. Case study

4.5.1. Introduction

The study area is in a platinum mining region within the eastern limb of the Bushveld Complex, South Africa (Figure 4.12). The region of interest is in a aggradation valley where a dyke swarm has halted mining operations due to safety risks (Figure 4.14). We targeted one of the dolerite dykes interpreted from magnetic data. The dyke intrudes into Main Zone norites. The Main zone consists of recurring gabbronorites, anorthosites, and magnetite that overlies the Critical zone (Barnes et al., 2004). The Critical zone contains platinum rich reefs such as the UG-2, Merensky and Plat reefs.

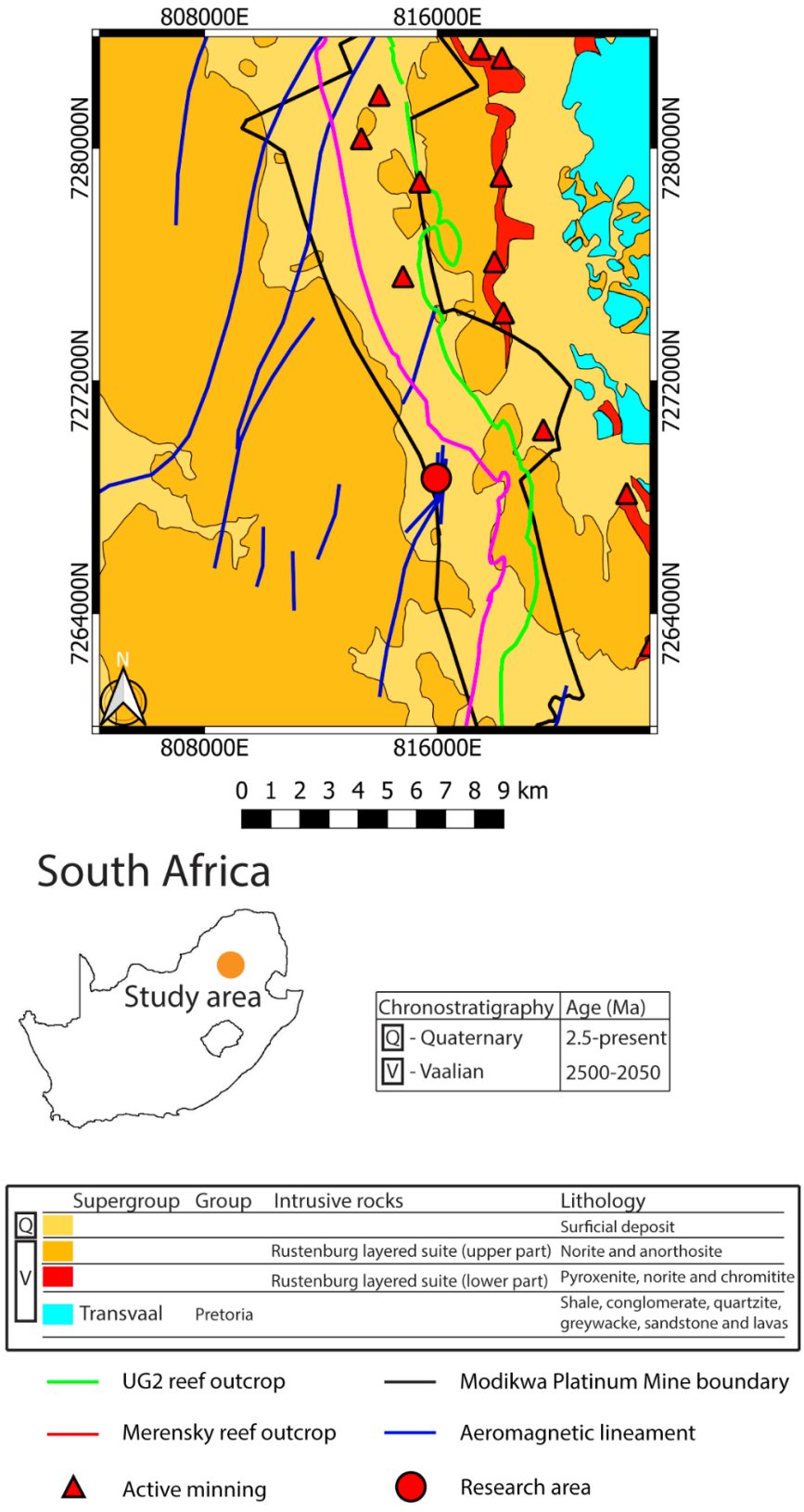


Figure 4.12. Regional geology map showing the ERT and MT survey site as a red circle and the dark blue lines represent aeromagnetic lineaments interpreted as a dyke swarm in the area (modified from Steyn, 1990).

The magnetic survey consists of 10 lines, striking east-west, of 300 m to 400 m in length and a line spacing of ~30 m (Figure 4.14(A)). The Geometrics G859 cesium vapor magnetometer was used to collect the magnetic data at a one - second sampling rate. Two Geometrics G856AX proton precession magnetometers were used as base stations, with a sampling rate of 15 and 30 seconds respectively. The diurnal, collected from the base station data, and spikes were removed from the collected magnetic data set. The data set was then used to calculate a 3-D magnetic susceptibility inverse model (Figure 4.14(C)).

The magnetic susceptibility inverse model was calculated using the 3-D magnetic inversion algorithms MAG3D, of Li and Oldenburg (1996) and Li and Oldenburg (1997). The 3-D magnetic susceptibility inverse model had a starting model of 0.1 SI and the upper and lower bounds for the inversion calculations were set to 0 SI and 2 SI respectively. The model contained a total of 1998920 cells in a 154 by 110 by 118 mesh. The predicted and misfit data is shown in Figure 4.13. A 20 m to 30 m wide dyke, represented by a isovolume of ~0.6 SI to isolate the dyke feature, is modeled from the collected magnetic data (Figure 4.14(C)).

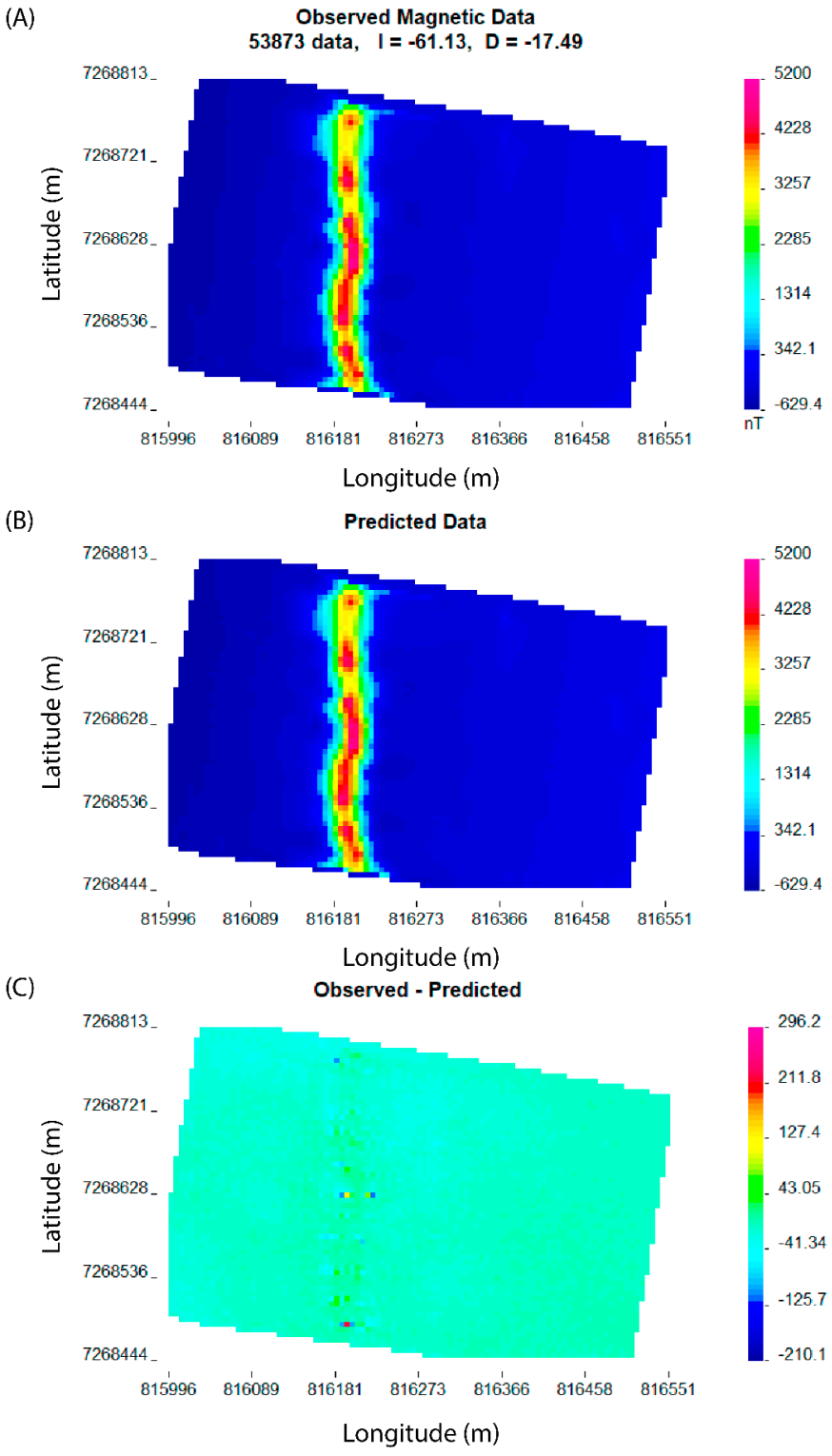


Figure 4.13. (A) The observed magnetic data collected over our research site. (B) Predicted magnetic data calculated from the inversion algorithm. (C) The misfit map is created by subtracting the predicted data from the observed data and the resulting difference is mapped as a misfit value on the map.

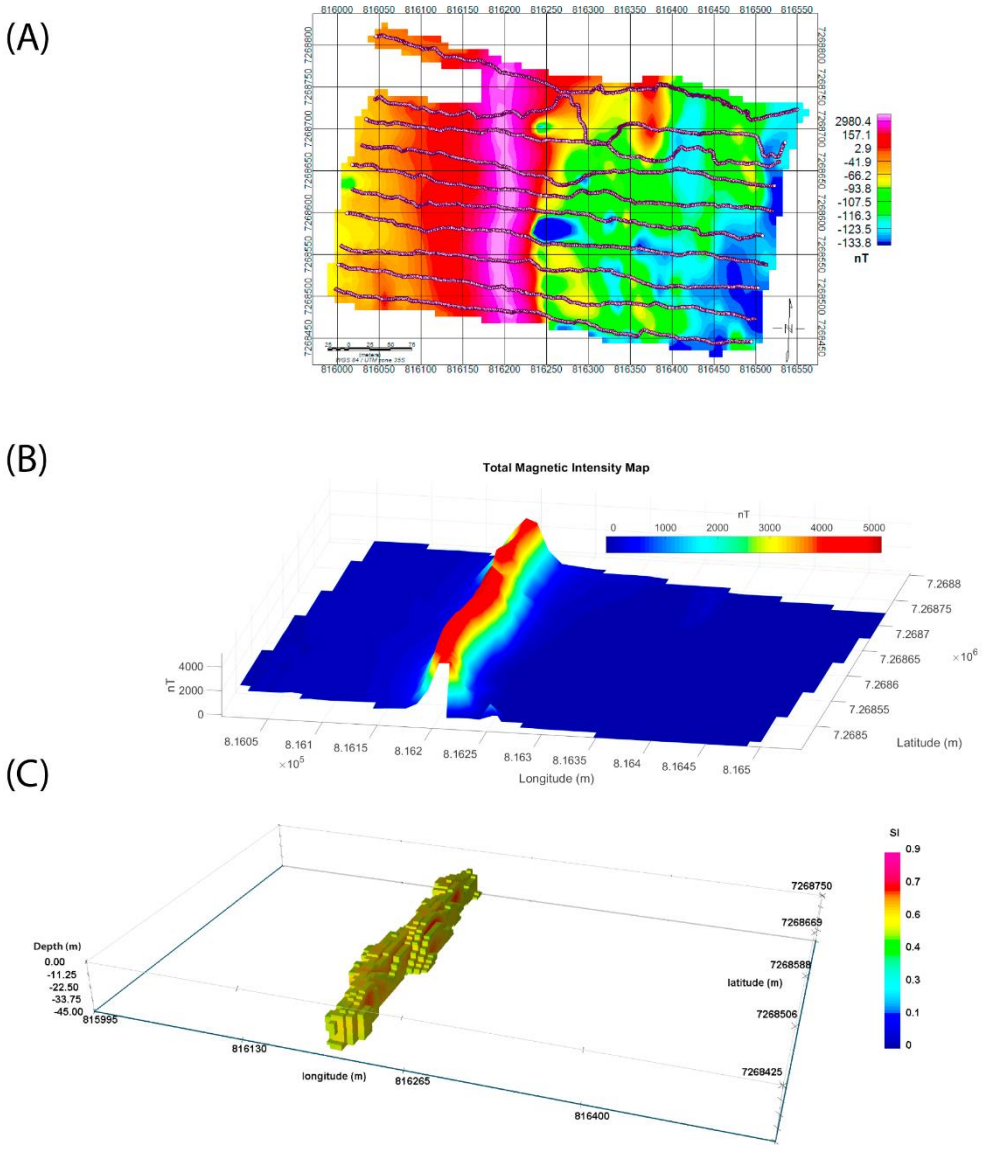


Figure 4.14. (A) Total magnetic intensity map of the magnetic data collected over the study area. White dots indicate actual magnetic readings from the magnetometer. (B) Total magnetic intensity observation data grid used for the 3-D magnetic susceptibility inverse model calculation. (C) The 3-D magnetic susceptibility inverse model shows a ~30 m wide dyke isovolume with a magnetic susceptibility of ~0.6 SI with a north-south strike in our study area.

4.5.2. Survey design

Two ERT surveys, with survey direction east-west and north-south respectively, were conducted perpendicular to each other (Figure 4.15). The Wenner-Schlumberger ERT array had an electrode spacing of 5 m and a total survey length of 400 m. We conducted an AMT survey over the east-west ERT survey line with a station spacing of 20 m (Figure 4.15). The AMT survey was also 400 m in length with a dipole length of 10 m and station spacing of 25 m. The frequency range for the AMT system is 10 Hz to 100 kHz. Possible noise sources in the area is a 50 Hz powerline ~600 m from the survey line, mining infrastructure below the surface and a workshop ~200 m away from the survey line. The survey was conducted during non-operational hours on the mine to prevent some of the possible noise sources mentioned effecting the AMT data. The GF Instruments ARES resistivity unit was used for the acquisition of the ERT data and we used the Geometrics Stratagem AMT system for AMT data collection.

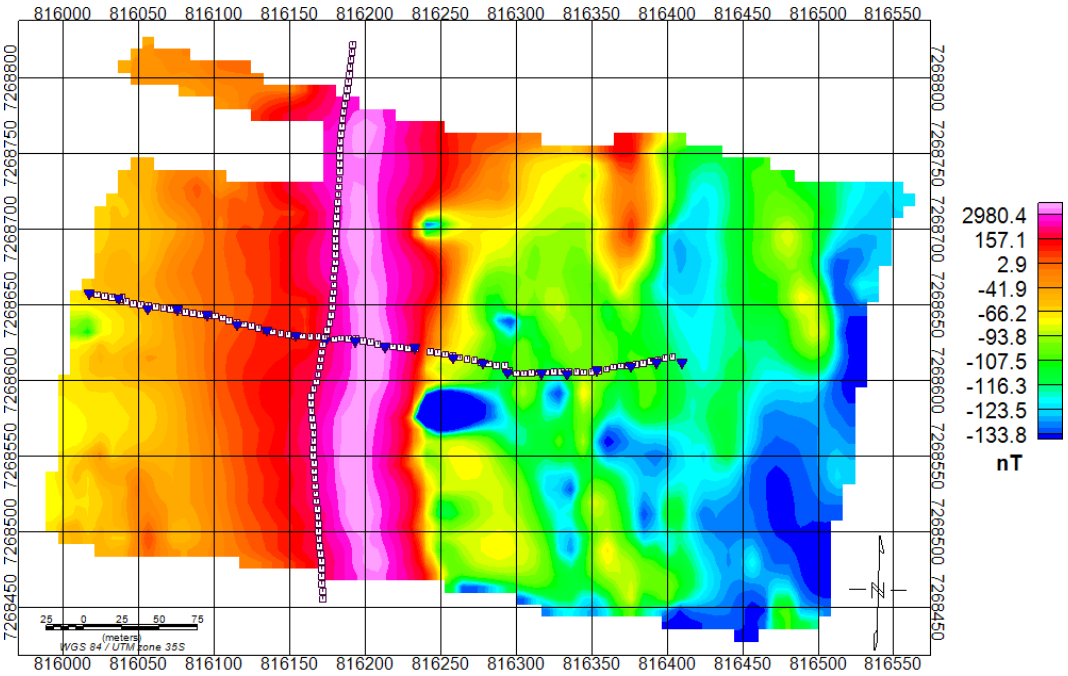


Figure 4.15. Total magnetic intensity map of the study area. White squares represent ERT electrode positions. Blue triangles show AMT station positions. The east-west survey lines run perpendicular to the strike of the target dyke in our study area.

4.5.3. Results

The 2-D inverse model on the east-west ERT line clearly shows the mapping of a dyke like structure from approximately ~100 m to ~200 m distance, with a resistivity of ~9000 Ω·m (Figure 4.16(A)). The model is also characterized by a conductive (~100 Ω·m) near-surface layer to a depth of 10-20 m. The 2-D inverse model for the north-south ERT survey line also shows the dolerite dyke with a similar resistivity of ~9000 Ω·m (Figure 4.16(B)). In the north-south ERT line, the dyke is prominent at the southern end of the line. This is because the line did not fully cross the dyke.

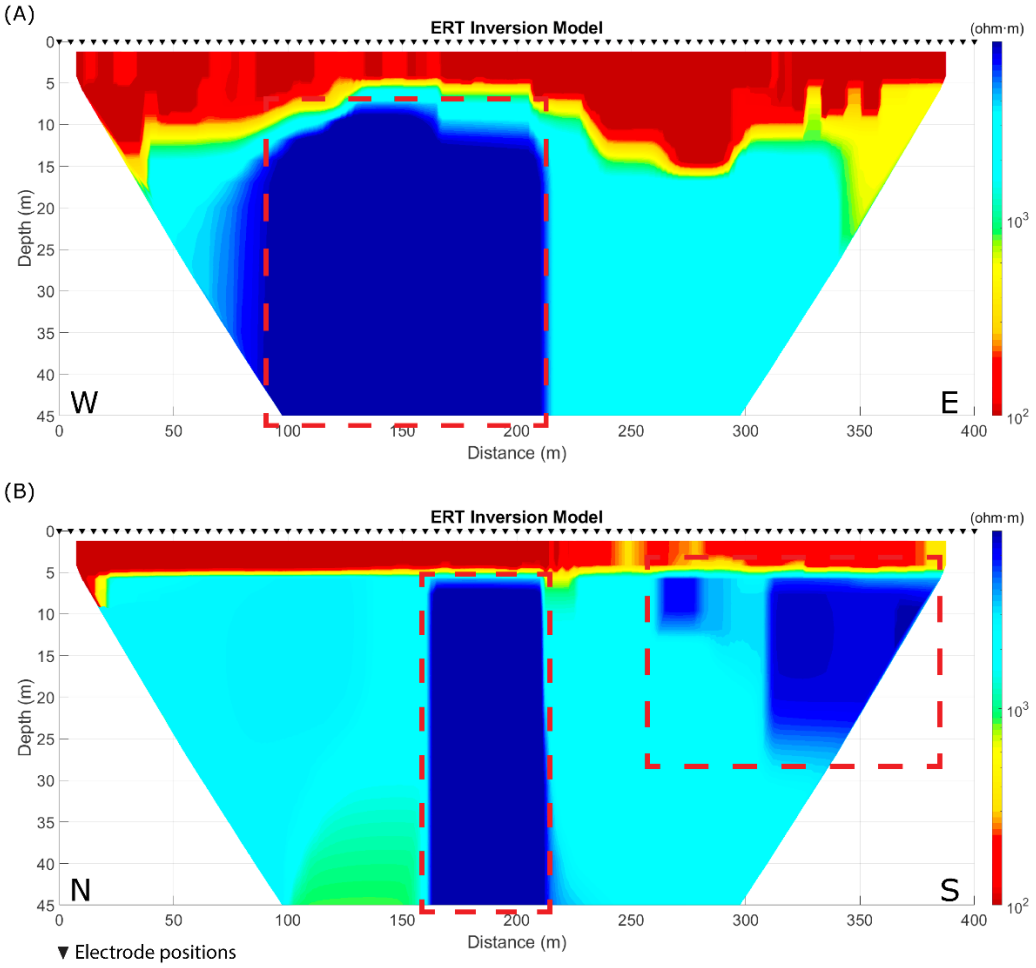


Figure 4.16. (A) East-west ERT 2-D inversion model highlighting the dolerite dyke location with a dashed red box. The resistivity inverse model has a root mean square error of 1.8. (B) North-south ERT 2-D inversion model. The dyke was intersected twice along the ERT line indicated by the two red dashed boxes. The resistivity inverse model has a root mean square error of 1.7.

We then calculate the augmented ERT-MT response function from the east-west ERT line. Figure 4.17 and 18 show two sample locations along the east-west ERT line, both the augmented ERT-MT response function and the AMT field data are plotted together for comparison. Once the AMT data is acquired, we rotate the data, so the X and Y direction is perpendicular and parallel to the strike of the dyke. We then assign TM and the TE modes to the phase and apparent resistivity curves. The TM mode strikes perpendicular to the dyke while the TE mode strikes

parallel to the dyke. Data points were masked in the 1 kHz dead band and >31 kHz where signal strength was low (Figure 4.19). noisy spikes were removed and smooth (D+) curves fitted to the remaining data points, to bridge the gap between the augmented ERT-MT response function data and the real AMT data (Figure 4.20). Once the data processing is complete, we calculate resistivity inverse models using the conjugant gradient code developed by Rodi and Mackie (2001). The full processing sequence is described in table 4.1.

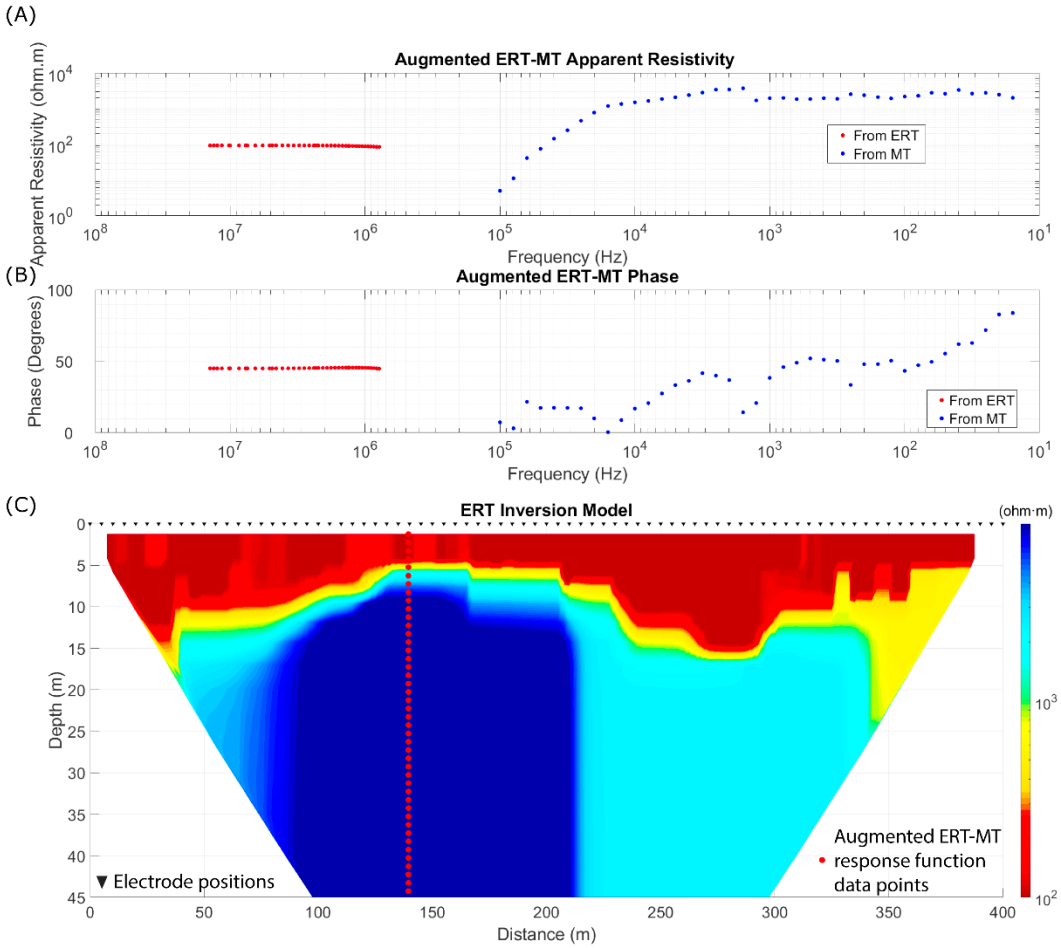


Figure 4.17. (A) Calculated apparent magnetotelluric resistivity response from ERT data (red) and collected audio magnetotelluric (blue) data. (B) Calculated apparent magnetotelluric phase response from ERT data (red) and collected audio magnetotelluric (blue) data. (C) The ERT inverse model used to calculate the augmented ERT-MT response function. The black dots show the location of data points used for the augmented ERT-MT response function.

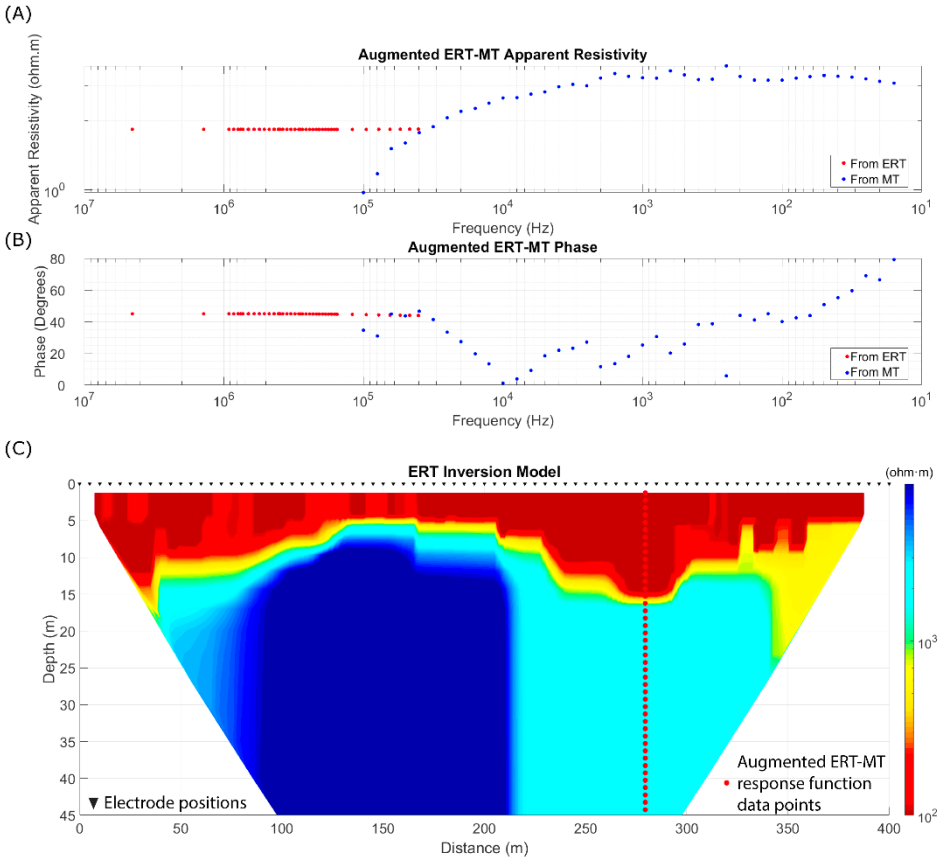


Figure 4.18. (A) Calculated apparent magnetotelluric resistivity response from ERT data (red) and collected audio magnetotelluric (blue) data. (B) Calculated apparent magnetotelluric phase response from ERT data (red) and collected audio magnetotelluric (blue) data. (C) The ERT inverse model used to calculate the augmented ERT-MT response function. The black dots show the location of data points used for the augmented ERT-MT response function. For this station the high frequency data calculated from the ERT data overlap with the AMT data.

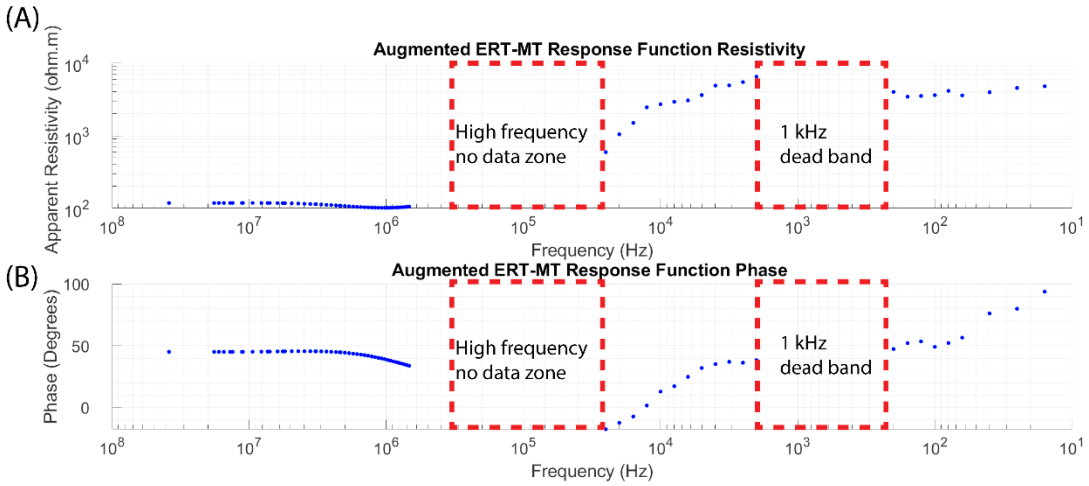


Figure 4.19. (A) Edited augmented ERT-MT response function resistivity data. (B) Edited augmented ERT-MT response function phase data.

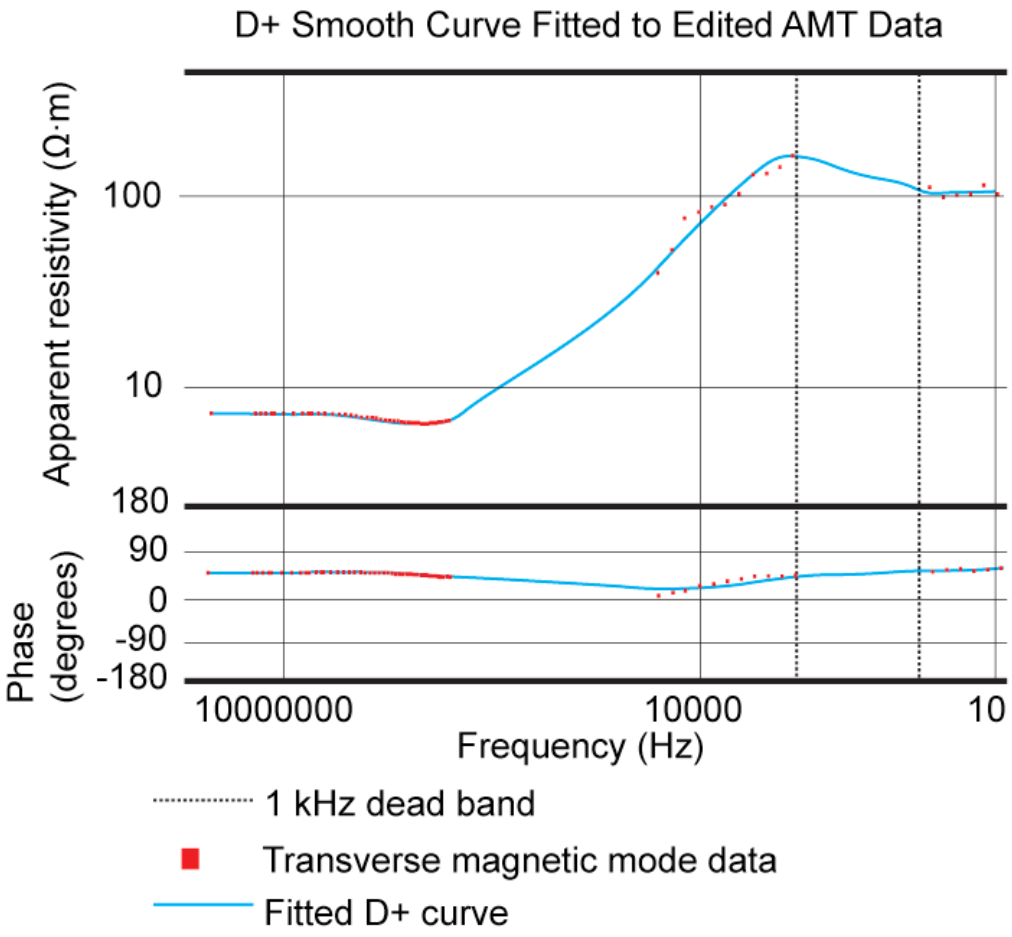


Figure 4.20. Edited augmented ERT-MT response function resistivity and phase curve (red squares). The calculated D+ smooth curve is represented as a blue line.

Table 4.1: Processing sequence of MT data

1.	MT impedance tensor was rotated perpendicular to geological strike.
2.	Assigned TM and TE modes. TM mode trends perpendicular to geological strike. TE mode trends parallel to geological strike.
3.	Masked data in the MT 1 kHz dead band.
4.	Masked low energy, high-frequency (> 10000 Hz) data.
5.	Fitted smooth D+ curves to data.
6.	Calculated 2-D conjugant gradient resistivity inverse model from code developed by Rodi and Mackie (2001). • An Initial 1000 Ω·m half-space is used as a starting model. • The minimum and maximum frequencies are set to 0.001 Hz and 10000 Hz. • The objective function is set to solve for the smoothest variation away from the starting model. • The standard Laplacian operator minimises the integral of the Laplacian. • Tau operator is set as 3. • A weighting function is enabled to prevent the model from becoming too blocky.

Two 2-D resistivity inverse models were calculated; the first model used only AMT data while the second model makes use of the augmented ERT-MT response functions (Figure 4.21). The inverse model using only the AMT data maps the conductive (5-10 Ω·m) overburden to a depth of ~ 20 m (Figure 4.21(A)). A vertical conductive (500 Ω·m) feature is mapped at 360 m along the profile. The vertical conductor at 360 m along the profile is related to the main north-south trending fault zone, with a throw up to ~120 m, in the area. The dyke that is mapped at ~145 m by the ERT inverse models and magnetic data is absent in this inverse model.

The second inverse model makes use of the augmented ERT-MT response function technique (Figure 4.21(B)). The conductive overburden is again mapped

to a depth of ~ 15-20 m. The north-south trending fault is also mapped as a vertical conductor at 360 m along the profile. The fault is ~10-100 Ω·m, which is more conductive than in the AMT only inverse model (~500 Ω·m). This is because of the addition of the high frequency data through the augmented ERT-MT response function which shows apparent resistivities < 100 Ω·m for frequencies greater than 10^6 Hz above the fault zone. Therefore, the inverse model fits the more conductive apparent resistivities, which are absent in the AMT invers model, resulting in a more conductive fault zone. The augmented ERT-MT response function inverse model maps a resistor, 145 m along the profile, where the dyke is predicted to be and was absent in the inverse model only using AMT data. The conductive regions to the west and east of the dyke are interpreted as a fracture region hosting groundwater because of the dyke intrusion. The resistor is in the same location as the resistor mapped in the east-west ERT inverse model (Figure 4.23).

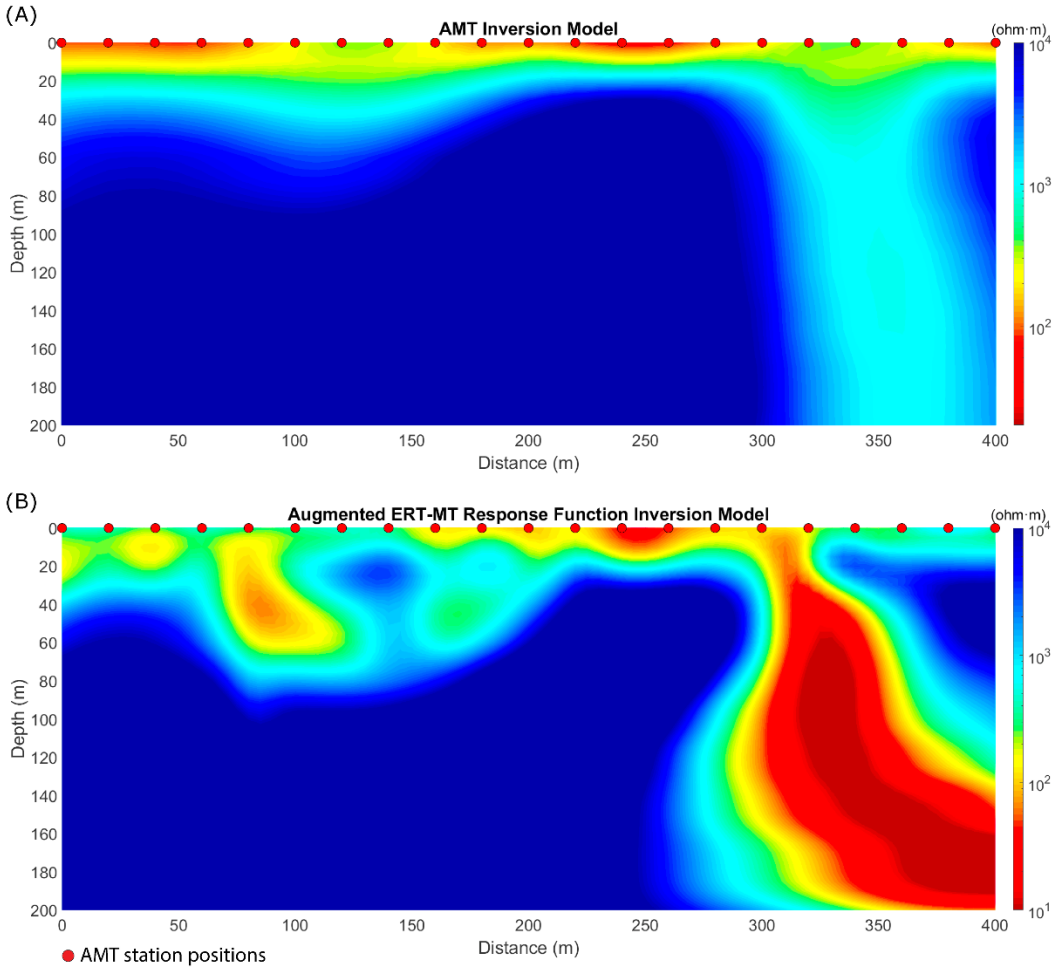


Figure 4.21. (A) Resistivity inverse model only using audio magnetotelluric data. The conductive (15-20 Ω·m) overburden is mapped to a depth of ~15 m. The inverse model had an RMSE of 2.9. (B) Resistivity inverse model using the augmented ERT-MT response function. A resistor is mapped at 150 m along the profile, which was absent in the inverse model using audio magnetotelluric data only. The inverse model had an RMSE of 2.1.

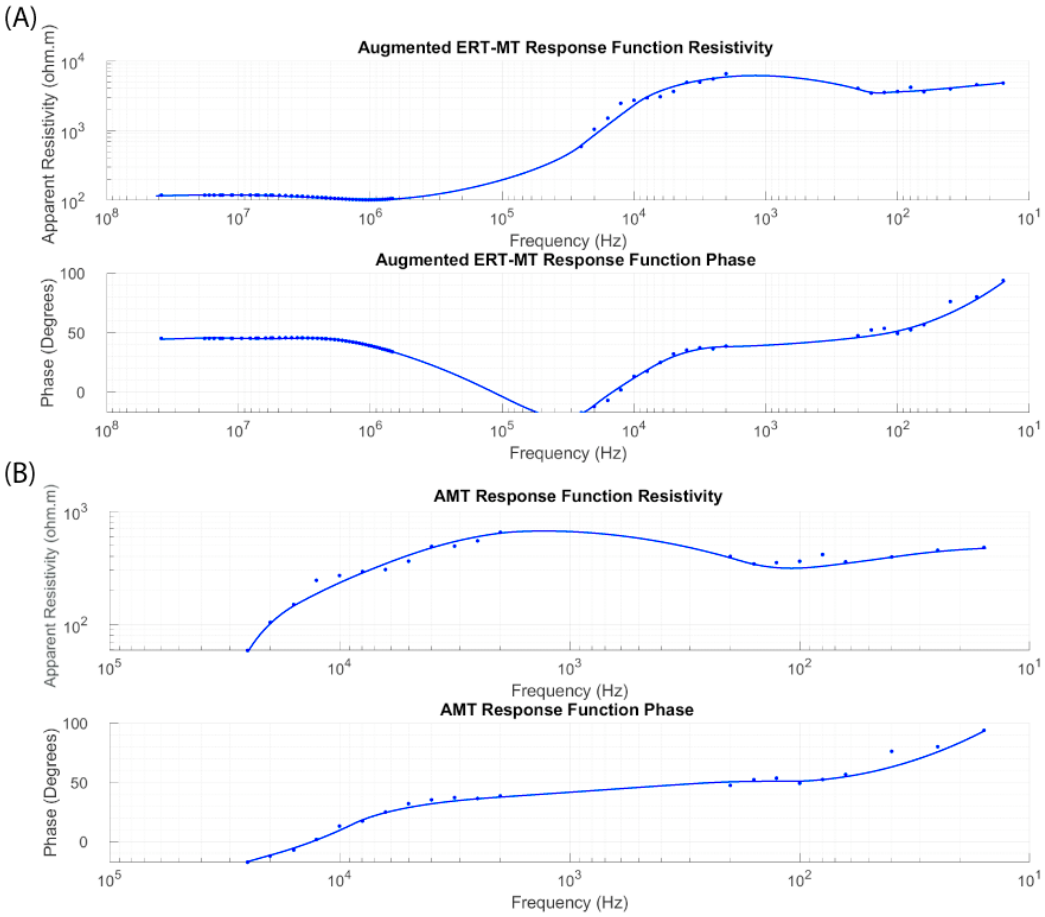


Figure 4.22. (A) Augmented ERT-MT response function resistivity and phase data fit from station 8 for the 2-D inverse model calculation shown in Figure 4.21. (B) . (A) AMT response function resistivity and phase data fit from station 8 for the 2-D inverse model calculation shown in Figure 4.21.

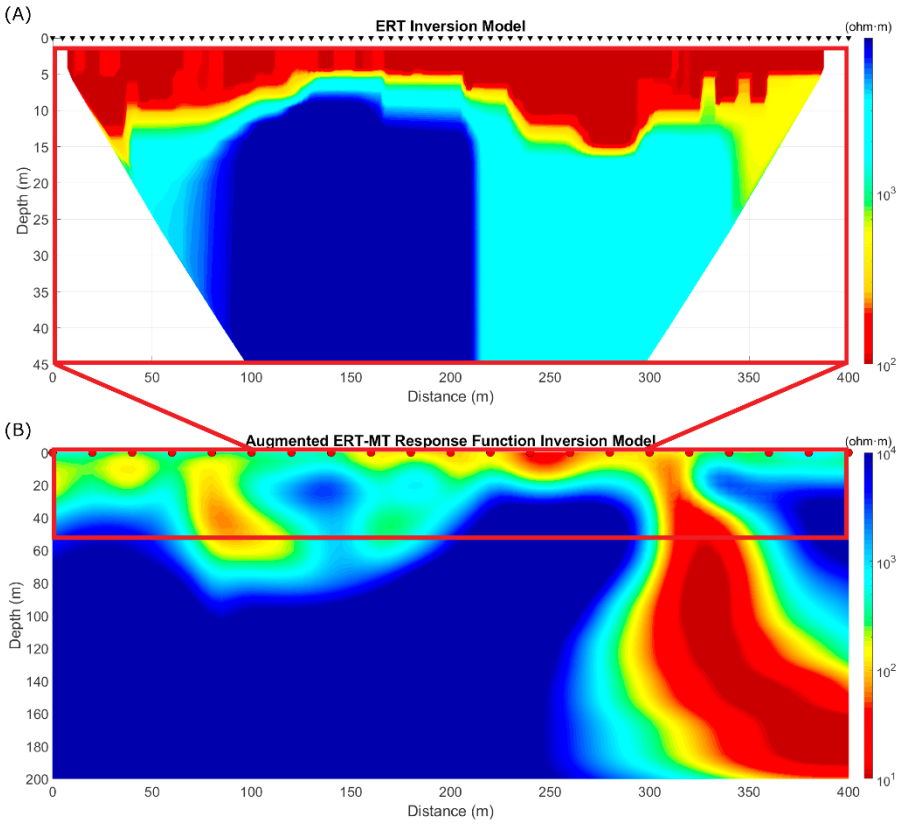


Figure 4.23. (A) East-west ERT inverse model over the audiomagnetotelluric line. (B) Resistivity inverse model using the augmented ERT-MT response function. The resistor at 150 m is mapped in both the ERT and augmented ERT-MT response function inverse model.

A comparison showing the augmented ERT-MT response function resistivity inverse model to a slice of the magnetic susceptibility inverse model that runs along the same AMT line is given in Figure 4.24. The resistive dyke, labeled “A” in Figure 4.24(B), lines up with the magnetic dyke, labeled “A” in Figure 4.24(A). The magnetic susceptibility inverse model also maps the north-south fault, labeled “B” in Figure 4.24(A), which also lines up with the conductive fault labeled “B” in the resistivity inverse model. Without the use of the augmented ERT-MT response function, the resistivity inverse model would have differed from the magnetic susceptibility inverse model since the dyke would have been absent in the model.

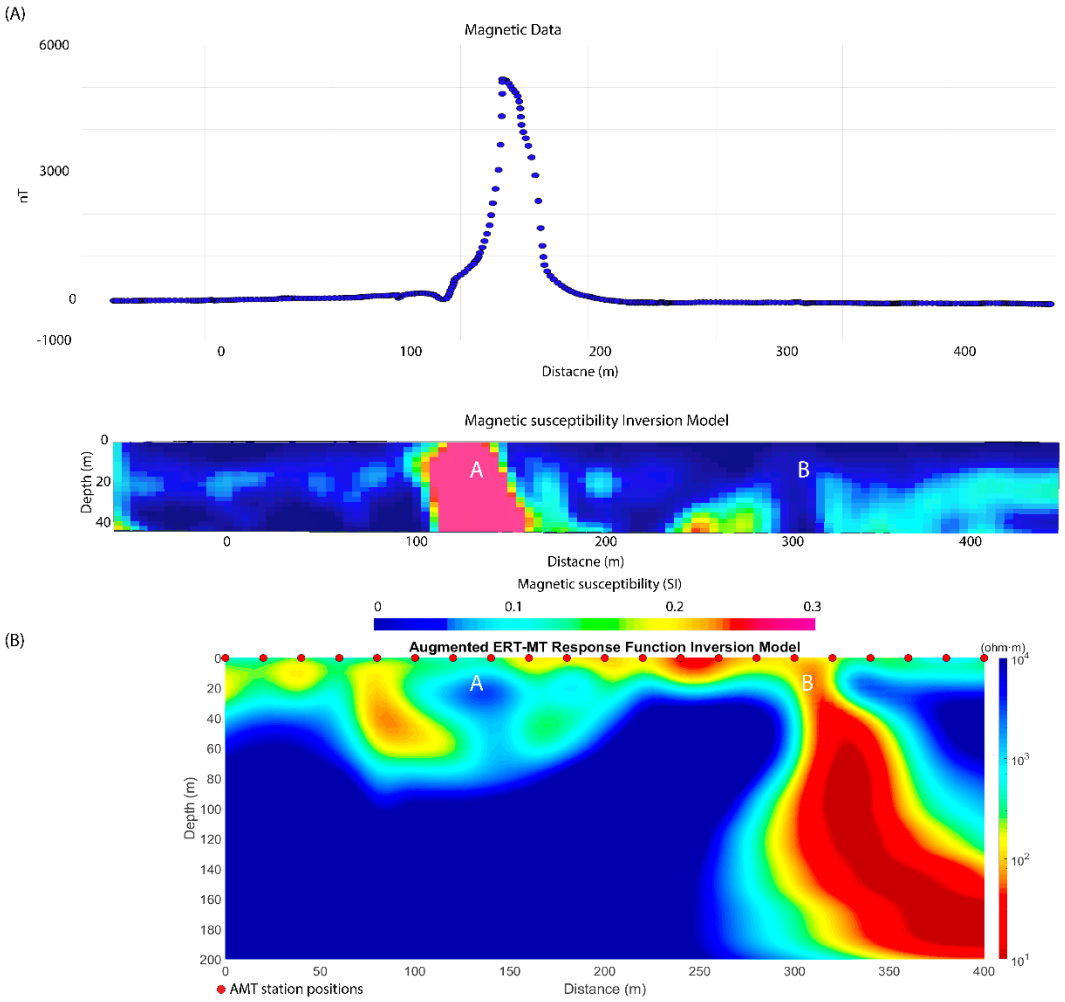


Figure 4.24. (A) A slice from the magnetic susceptibility inverse model along the AMT line shows the magnetic dyke, labeled "A", and the north-south fault, labeled "B". (B) The resistivity inverse model, calculated from the augmented ERT-MT response function, shows that both the dyke and the fault zone in both inverse models line up.

4.5.4. Discussion

It was demonstrated that by calculating an augmented ERT-MT response function from ERT data that we could improve the mapping of resistors beneath conductors in resistivity inverse models. In the theoretical models for both the 1-D and 2-D case, the resistor is recovered when using the augmented ERT-MT response function than if only the AMT data is used.

The same technique was applied to field data collected on a mining site in the Eastern Limb of the Bushveld Complex, South Africa. The inverse model using the augmented ERT-MT response function resolved a resistive dyke beneath a conductive overburden. The dyke and fault positions in this resistivity inverse model also correlated with the dyke and fault positions in the magnetic susceptibility inverse model. However, in the inverse model that only used AMT data, the dyke was absent. This finding agrees with both the 1-D and 2-D theoretical modeling, that using the augmented ERT-MT response function will improve the resolving power of resistivity inverse modeling for resistors beneath a conductive overburden.

Since the MT data is augmented before the inversion calculation is started only a single inversion parameter is inverted, unlike when a joint or cooperative inversion is needed to integrate both the ERT and AMT data sets. This reduces the overall computational time needed to invert both data sets with the same objective function. When using the augmented ERT-MT response function, in its current form, weightings on the different data sets are unnecessary. While in joint inversions, weighting the different data sets is required and can be a complex and computationally intense problem to solve as shown in Vozoff and Jupp (1975), Monteiro Santos et al., (2007) and Meqbeland Ritter (2015). The augmented ERT-MT response function can still be used in joint inversions but as an additional processing step to prepare the data for inversion. Therefore, improving computational time and recovery of resistivity models in joint inversion calculations by adding additional high frequency MT data.

It is also important to note that the augmented ERT-MT response function was only applied to the TM mode along the survey strike. This is because we only used the ERT data collected along the profile to calculate augmented ERT-MT response functions. Future work would involve the use of 3-D ERT modeling to calculate augmented ERT-MT response function for both the TM and TE mode and perform a joint inversion using both modes. As this new method uses a simplified equation for the MT current density, more complex cases might not see the same improvements. The effects of more complicated geometry may be under modelled but in the examples shown the equation provides greater resistivity model recovery when calculating resistivity inverse models. Also, if there is insufficient ERT data and the gap between the pseudo-MT data, calculated from the ERT data, and the real MT data is more than four orders of magnitude in the frequency range the inversion calculations will become unstable, as shown in Figure 4.3(B), (D) and (F), and the recovery of the expected resistivity inverse model will be unsuccessful. These problems can be solved by designing a suitable ERT survey beforehand, using D+ curve fitting and in the future by developing and calculating a more general from of the MT current density equation or at least a numerical approximation.

The improvement seen in mapping resistors with the augmented ERT-MT response function can be useful in many cases. One of them, other than dyke mapping shown in this paper, is that this method can be used to better map sandstones aquifers beneath conductive clay aquitards. In the case shown in our study area, a resistive feature, like a dolerite dyke, buried below a conductive layer will be resolved better when using the ERT-MT response function method.

4.5.5. Conclusion

We have shown that by using ERT data, to add additional high-frequency content in the MT response function, we can calculate augmented ERT-MT response functions that can be used in resistivity inverse modeling. The inverse models for both 1-D and 2-D theoretical modeling showed improvements in mapping resistive features beneath a conductive layer. In the 2-D case, the augmented ERT-MT response function helped to constrain the width and depth of a resistor that was partially mapped or completely absent before.

When the augmented ERT-MT response function technique is applied to field data, a resistive dyke that was absent in the initial inverse modeling is mapped. The dyke location and a fault zone correlate with the same positions in the magnetic susceptibility inverse model.

We have shown that the augmented ERT-MT response function technique improves the resolving power of the MT method for resistors beneath a conductive overburden for both the theoretical and experimental case.

4.5.6. Acknowledgments

The support of the DST-NRF Centre of Excellence for Integrated Mineral and Energy Resource Analysis (DST-NRF CIMERA) towards this research is hereby acknowledged. Opinions expressed and conclusions arrived at, are those of the authors and are not necessarily to be attributed to the CoE.

Jan van der Walt from GES Geophysics is also acknowledged for his support in providing an EH-4 Stratagem AMT system used throughout this research.

We would also like to acknowledge the UBC-Geophysical Inversion Facility from the Department of Earth and Ocean Sciences, University of British Columbia for providing us with MAG3D. MAG3D is a program library for the forward modelling and inversion of magnetic data over 3-D structures.

Chapter 5 : Evaluating the Augmented ERT-MT Response Function on Conductive Targets

5.1. Introduction

This research described in this chapter follows on form the development of the augmented ERT-MT response function in the previous chapter, Chapter 4. In this chapter the augmented ERT-MT response function is tested on conductive targets, karst aquifers and faults, overlain by resistive lithology (dolomites). This second study site is used to evaluate the newly developed augmented ERT-MT response function in a different environment, instead of a conductor (conductive overburden) overlying a resistor (dyke) at this site resistive dolomites overly conductive faults zones and karst aquifers.

Research on groundwater in deep South African goldmines has produced remarkable findings from methane-groundwater interaction (Manzi et al., 2012) to the discovery of a diverse archaeal biosphere in deep fissures (Takai et al., 2001). These findings are significant as they act as a template for the discovery of possible life on other planets like Mars. These deep biospheres could mirror one of the only possible ways life could be preserved on other planets, since rock-hosted life would have the highest probability of preservation on these planets (Onstott et al., 2019).

Evidence of life in the deep subsurface is found in the Witwatersrand goldfields of South Africa, but how these organisms originated in these locations is still unknown (Borgonie et al., 2019). One of the main questions is if these deep (~3 km deep) fissure zones, where archaeal life is being studied, have access to near-surface (< 1 km deep) aquifers and if they are truly isolated from surface groundwater sources. If this system is isolated, it would contain water that is millions to billions of years old as discussed by Heard et al. (2018). One of the active research sites studying groundwater biodiversity, ~3.1 km deep, in the Witwatersrand basin is located at the Moab Khotsong gold mine (Rusley et al., 2018). A few kilometres above this site are the dolomites or dolostone of the Transvaal Supergroup which host groundwater aquifers recharged by surface water flow. It is unknown if the fissures below the dolomites and faults in the dolomites are connected.

In this paper we find that legacy seismic, AMT, ERT and magnetic data can be used to efficiently distinguish faults and aquifers systems hosting freshwater in the dolomites and the connectivity of each system. By understanding where these structures are located, we can investigate structural linkages between the near-surface and deep biosphere in the Witwatersrand Basin.

5.2. Regional Geological and Hydrogeological Setting

The Moab Khotsong Gold mine is situated in the Klerksdorp goldfields of the Witwatersrand Basin, ~150 km south-west of the city of Johannesburg (Figure 5.1). The goldfield is of economic importance since it contains the gold-bearing conglomerates, which holds one of the largest known gold reserves in the world, confined in the Witwatersrand Supergroup. The Witwatersrand Supergroup is

made up of 5-7 km thick, ~2.97 billion-year-old, predominantly metasedimentary rock layer which unconformably overlies the Dominion Group (McCarthy and Rubridge, 2013). Unconformably overlying the Witwatersrand Supergroup is the Ventersdorp Supergroup. The Ventersdorp Supergroup consists of ~4500 m thick andesitic lava layer with interlayer agglomerate and conglomerate tuffs (Van der Westhuizen et al., 1991; Coward et al., 1995; Jolley et al., 2004). Capping the Ventersdorp Supergroup is a sedimentary succession of quartz-pebble conglomerate known as the Black Reef Formation (BLR) (Fuchs et al., 2016). The BLR is a basal lithostratigraphic unit forming part of the overlying Transvaal Supergroup. The Paleoproterozoic Transvaal Supergroup is made up of mafic lavas and alluvial-fluvial deposits (Eriksson and Reczko, 1995). The Transvaal Supergroup is segmented into two groups, namely the Chuniespoort Group and the Pretoria Group. The Chuniespoort Group contains the Malmani Subgroup where substantial groundwater is stored in the dolomitic aquifers. Further details on the geological and structural setting of the Witwatersrand basin and associating supergroups are well documented by the following authors, Coward et al. (1995), Gibson et al. (2000), Jolley et al. (2004), Dankert and Hein (2010) and McCarthy and Rubridge (2013).

The Malmani Subgroup dolomites is the primary focus of our study. The dolomites host unconfined to semi-confined fractured karst aquifers (Mndaweni et al., 2019). The aquifers display compartmentalization by vertical and/or sub-vertical dolerite dykes acting as aquitards. Both the contact zone between the dykes and dolomite aquifers and fault zones allow dolomite dissolution,

karstification and leaching for hydraulic conductivity in the area (Fleisher, 1981; Dippenaar, 2019).

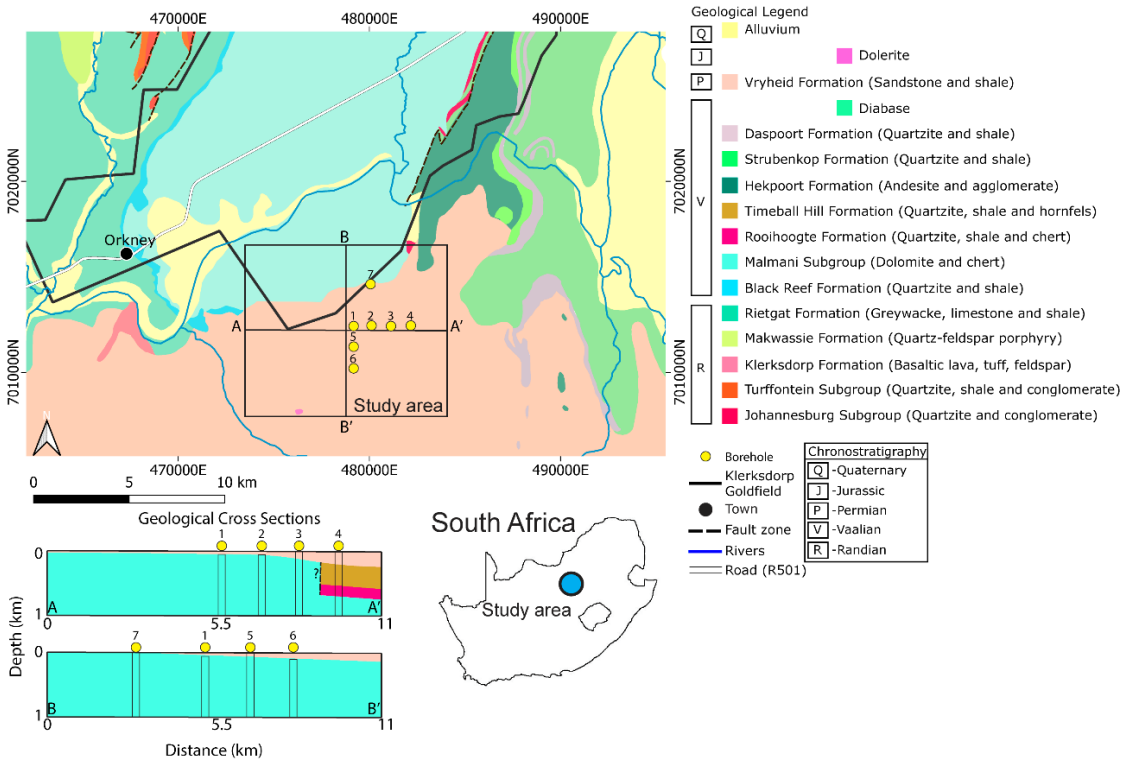


Figure 5.1. Geological map (modified from the following maps sheets, Wilkinson, K.J., and Coetsee, F., 1986; Retief, P.F., 2000) of surrounding the study area at the edge of the Klerksdorp Goldfield situated on the Witwatersrand Basin.

5.3. Legacy Seismic Data

The seismic data used in this study were acquired in 1983 by the Gold Division of the Anglo-American Corporation (now Anglo Gold Ashanti Ltd.). The surveys were designed to map gold-bearing horizons (known as reefs), at depths between 2.5 km and 3.8 km, in the Witwatersrand Basin (Manzi et al., 2018). In this study we will calculate refraction travel time inverse models using this seismic data up to a depth of ~400 m depending on ray path depths. Seismic profiles AV 1, AV 2, AV 4, AV 5, AV 6 and AV 7 (Figure 5.2). Were used and were received from Anglo Gold Ashanti as raw shot gathers in SEG-Y format and the information about the acquisition parameters were obtained from the field observers' reports. The seismic profiles were acquired in the 1980s using Vibroseis trucks as energy sources. All surveys were designed with a sweep length of 28 s and a frequency sweep of 10 – 90 Hz at a sampling rate of 4 ms for high-resolution imaging of the deeper targets. Profiles have 25 m shot and receiver spacing, and the resonance frequency of the receivers is 10 Hz (vertical single component) with a low-cut recording filter of 3 Hz. The survey parameters of these lines are summarized in Table 1. For the purpose of this study we were only interested in the seismic velocities of the near surface, thus only refraction tomography models were considered for each seismic profile.

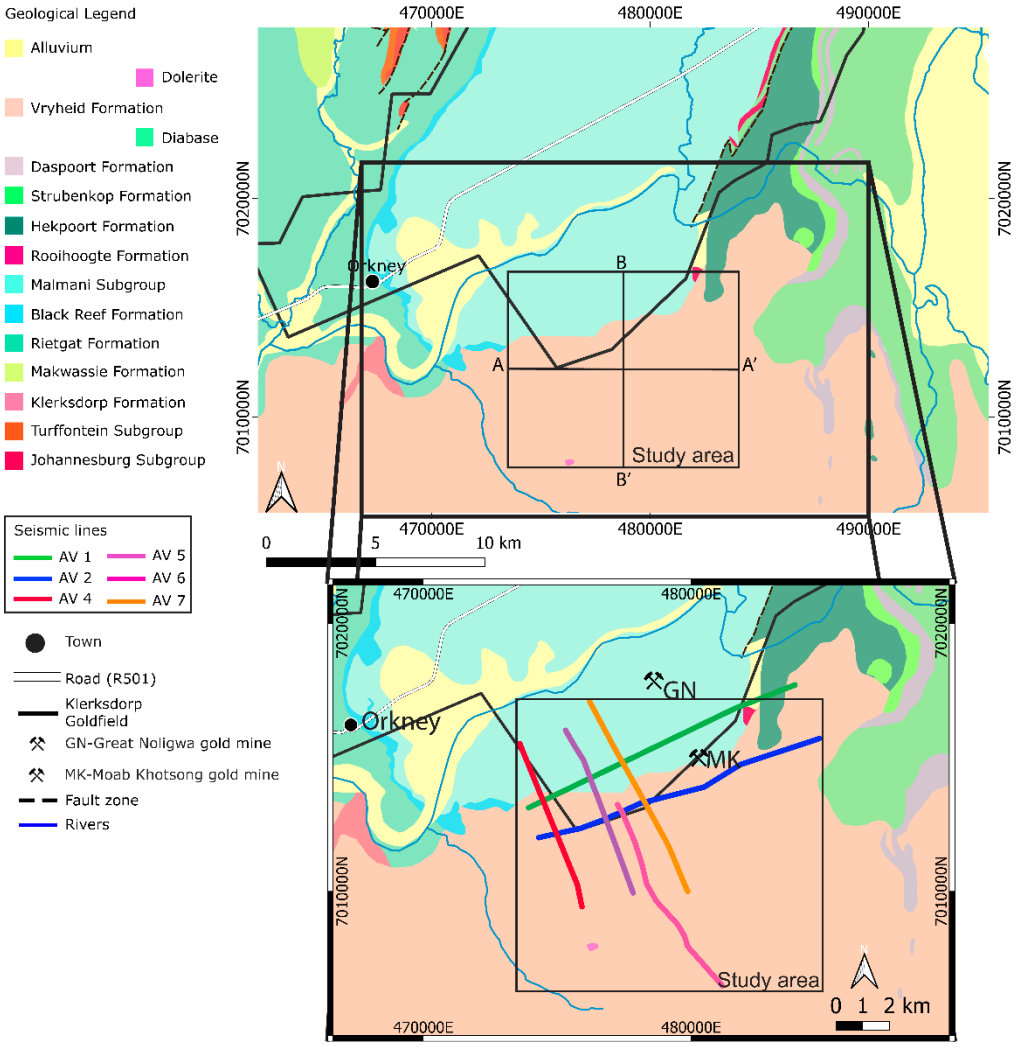


Figure 5.2. Geological map (modified from the following maps sheets, Wilkinson, K.J., and Coetsee, F., 1986; Retief, P.F., 2000) with seismic line positions collected by Gold Division of the Anglo-American Corporation in 1983.

Table 5.1: Field acquisition parameters for 1983 2D Moab Khotsong seismic surveys.

Recorded by	Rockplan (Pty.) Ltd.	Crew 240
Instrumentation	System	Sercel 338 HR/ Addit
	Geophones	III
	Data format	SM4V 10 Hz
	Record length	SEGB 9TRK 1600 BPI
	Sample interval	6 s
	System polarity	4 ms
		SEG
Parameters	Number of channels	
	Source interval	96
	Receiver interval	25 m
	Number of shots	25 m
	Nominal fold	~223
Source		48
	Vibroseis	
	Pattern	4 Vibs ¼ S Taper
	Sweep	28 s 10-90.5 Hz, 30-89.5 Hz
		8 sweeps/V_p

In order to calculate a refraction travel time inversion from the legacy data the trace headers and zero false values had to be edited, for example -9999 values found in the source depth header and this also included updating the headers to conventional header titles. Additionally, the geometry data had to be corrected, namely elevation data that were not in agreement for the both the source and receiver locations. The stored elevation data were replaced with interpolated values, using nearest neighbour interpolation and shuttle radar topography mission (SRTM) elevation data (Farr et al., 2007). After the preliminary preparation of the legacy seismic data, the first breaks were picked (Figure 5.3) along the shot gathers followed by calculating a P-wave seismic refraction tomography inverse

model. The inversion is a non-linear refraction travel time inversion, and in this case, Tikhonov Regularization was used (Tikhonov, 1943; Foster, 1961).

The inversion is minimizing the difference between synthetic travel times, raytraced through the velocity model, and the input travel times from our first break picks (Figure 5.4). The ray paths are further used to control the model alpha values. If a ray path is present the alpha value is set to one but if it is absent the alpha value is set to zero making that cell transparent. Therefore, when the final P-wave seismic tomography inverse model is visualized only sections of the model that have ray paths associated with the cells are visible.

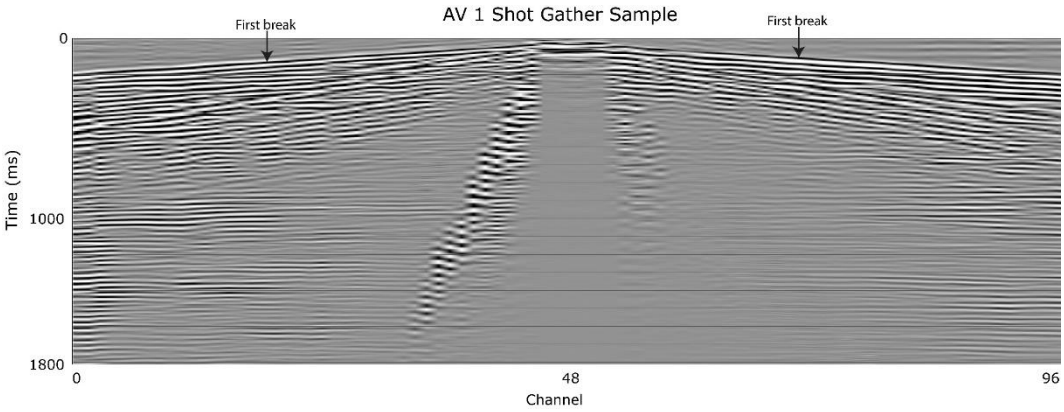


Figure 5.3 Shot gather taken from seismic line AV 1 showing the location of picked first breaks.

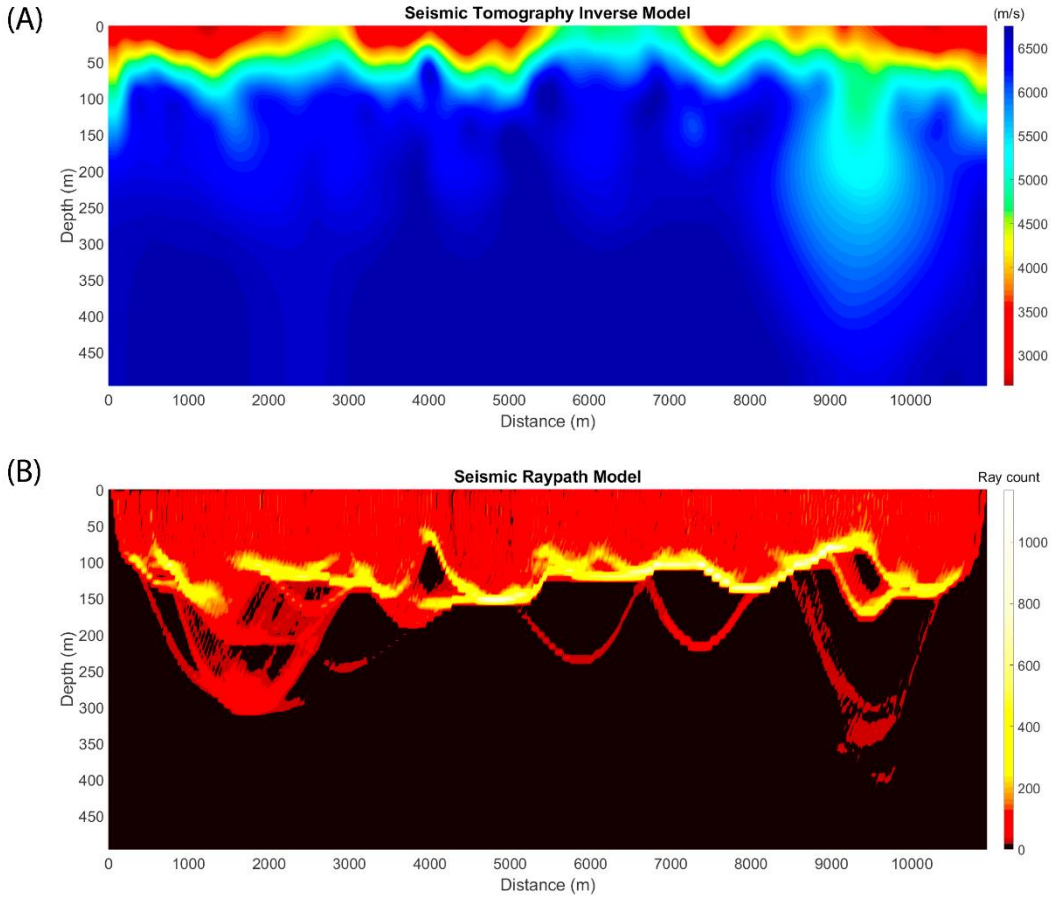


Figure 5.4. (A) P-wave seismic tomography inverse model of seismic line AV 1. The inverse model has a root mean square error of 6 ms. (B) The seismic ray paths raytraced through the velocity model. Black areas indicate zones with no ray traces.

The east-west striking seismic lines AV 1 and AV 2 (Figure 5.5) will be investigated first. Firstly, the refraction tomography models exhibit low velocity zones (~ 3000 – 3500 m/s) at depth between 0 and 50 m, which is interpreted as the weathered top rocks. Secondly, the model is characterized by relatively low velocity zone (3500 – 5500 m/s) at depths between 50 and 100 m, which is interpreted as the fresh top rocks. Below 100 m, the model shows the mapping of the high velocity zones (> 5500 m/s), which is interpreted as the bedrock. To constrain our model, the surface exploration holes drilled in the area (see Figure 5.1) were used. summary, the seismic velocities vary between ~5000 and 6000

m/s (blue) and represent the Malmani subgroup since they correlate with depths of the Malmani subgroup in borehole logs from boreholes MMB1 and MZA5. These rocks represent the Eccles, Lyttelton and upper Monte Christo Formations of the Malmani subgroup. The above velocities are consistent with those observed in the reflection seismic studies by Manzi et at. (2019) in the Moab Khotsong gold mine.

Further inspection of the AV 1 P-wave seismic tomography inverse model indicates the mapping of a relatively low velocity (<~5000 m/s) plunging structure situated at ~9500 m along the profile (Figure 5.5(A)). This is interpreted as the possible continuation of an existing north-south trending fault zone depicted in Figure 5.2 further to the north. The fault on Figure 5.5(A) is also north-south trending, west-dipping, and extends to a depth of ~400 m. Another second, east-west dipping, shallower (~150 m deep) fault is mapped at ~1500 m along the profile. The fault continuation marked as f1 in Figure 5.5(A) originates from a fault zone ~1.7 km to the north-east. This fault zone cuts the Vaal River and would provide a source of surface recharge for the dolomitic aquifers below the surface. Dolerite dykes, mapped from mine geological maps, exhibit ~6000 m/s velocity and compartmentalize the dolomitic aquifers of the Malmani subgroup.

The continuation of the fault can be seen again, marked as f2, as a relatively low velocity (~5000 m/s) plunging structure at location ~8500 m along the AV 2 P-wave seismic tomography inverse model (Figure 5.5(B)). Therefore, the fault zone continues another ~ 4 km south-west than previously mapped. Again, dykes that compartmentalize the dolomitic aquifers and are represented as 6000 m/s seismic velocity near-vertical features.

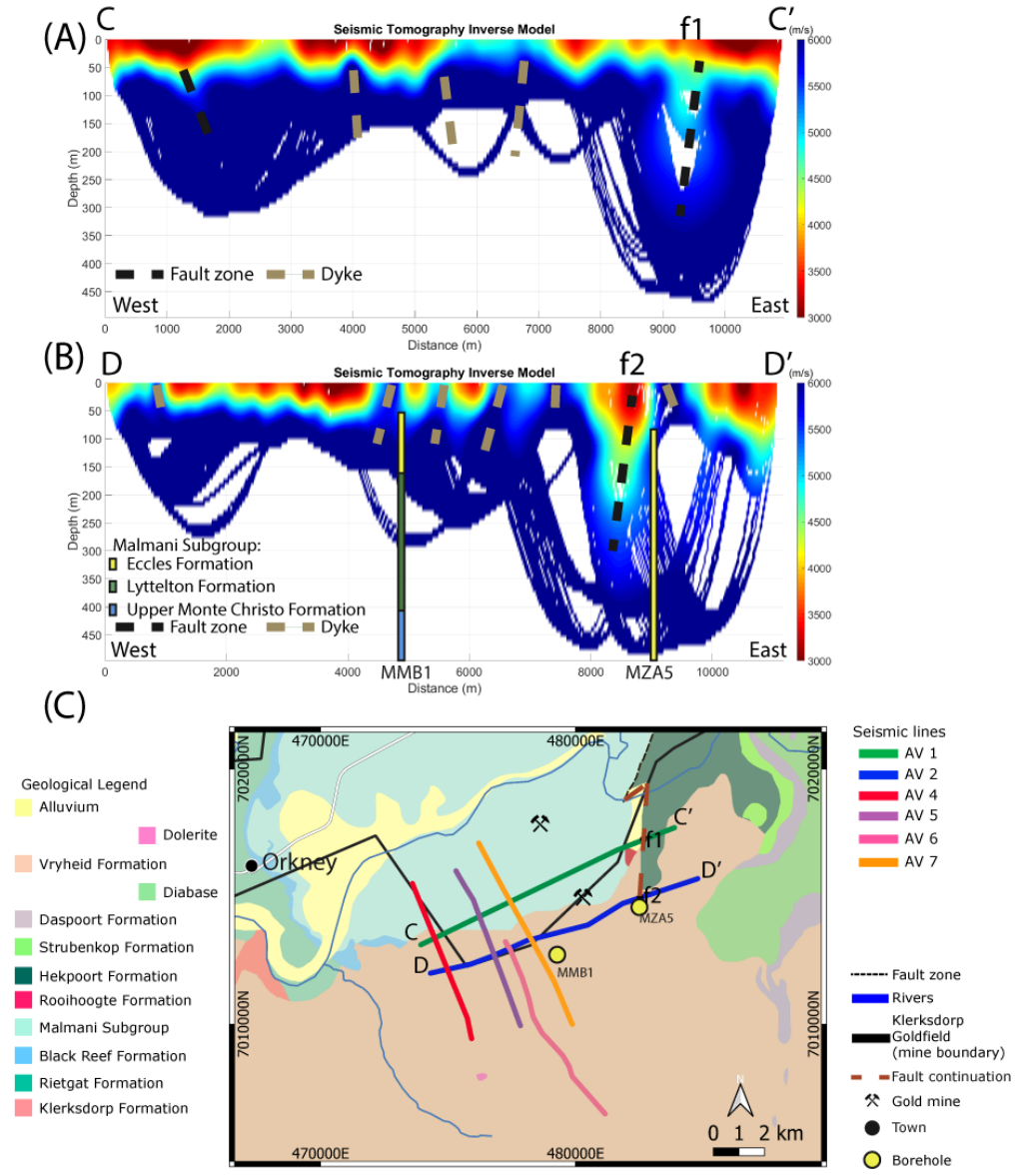


Figure 5.5. (A) P-wave seismic tomography inverse model of seismic line AV 1 with a root mean square error of 6 ms. A fault zone, with low velocities dipping down to a ~350 m depth, shown at position f1 maps the continuation of the fault depicted on the existing geological map of the area. Velocities between ~5000-6000 m/s (blue) represent the Malmani subgroup, and velocities between ~3000-4500 m/s indicate the Vryheid Formation, part of the Karoo supergroup, overlaying the Malmani subgroup, part of the Transvaal Supergroup. Dykes and faults are mapped from underground mapping and subsurface boreholes. (B) P-wave seismic tomography inverse model of seismic line AV 2 with a root mean square error of 7 ms. Position f2 shows the fault zone continuing from AV 1 with a low-velocity zone being traced down to a ~300 m deep. Dykes and faults are mapped from underground mapping and subsurface boreholes. (C) Geological map showing the position of the seismic lines and boreholes being indicated by yellow circles. The continuation of the existing fault zone between position f1 and f2 is indicated with a red line between AV 1 and AV 2.

Secondly, we will interpret the P-wave seismic tomography inverse models calculated for northwest-southeast striking seismic lines AV 4, AV 5, AV 6 and AV 7 (Figure 5.6). The P-wave seismic tomography inverse model calculated for seismic line AV 4 shows two shallow relatively low-velocity (<~5000 m/s) fault zones ~800 m and ~3900 m along the profile. The inverse model calculated for seismic line AV 5 shows the low-velocity (<~3000-4500 m/s) Vryheid and Dwyka Formations, from the Karroo Supergroup, mapped to a depth of ~48 m to the south of the line, correlating with the same depth measured in borehole MGR5 along the profile. A shallow relatively low-velocity (<~5000 m/s) fault zone is mapped at ~2500 m along the profile. The P-wave seismic tomography inverse model calculated for seismic line AV 4 shows the transition of the low-velocity (<~3000-4500 m/s) Karroo Supergroup to the south, 0-1000 m along the profile, and the higher velocity Transvaal Supergroup (~5500-6000 m/s) to the north. Again, vertical high-velocity (~5000 m/s) features in the inverse model correlate with dykes mapped on mine plans in the area. Line AV 7 has three boreholes, MHH1, MGR6, and MMB1, along the survey line to the south. The inverse model for AV 7 tracks the high-velocity Malmani subgroup to similar depths (~50-100 m deep) seen in all three boreholes. In all 4 inverse models discussed in Figure 5.6, the fault zones mapped are shallow with a depth extent ranging from ~100-250 m deep. The faults mapped in all the P-wave seismic tomography inverse models propagate no deeper than ~350 m. P-wave seismic velocities observed for the Karoo Supergroup (<~3000-4500 m/s) and dykes are in agreement with the published seismic velocities for these rocks in the Witwatersrand Basin (e.g., Manzi et al., 2019; Tinker et al., 2002).

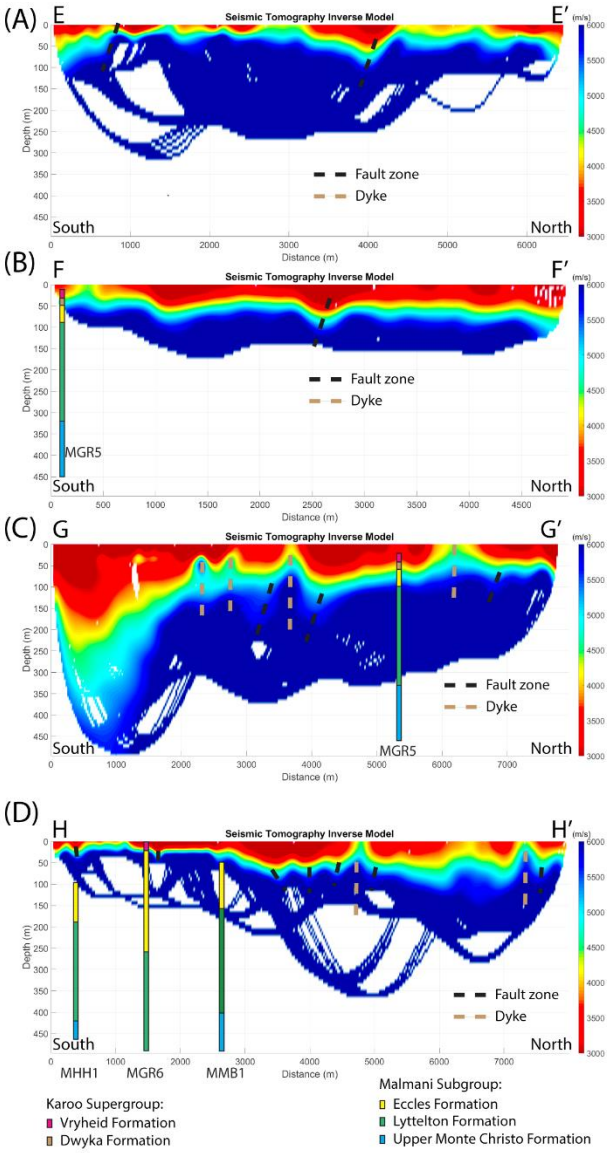


Figure 5.6. (A) P-wave seismic tomography inverse model of seismic line AV 4 with a root mean square error of 5 ms. Two fault zones are mapped in the dolomites. (B) P-wave seismic tomography inverse model of seismic line AV 5 with a root mean square error of 4 ms. Velocities between ~3000-4500 m/s map the Karoo supergroup and matches the borehole log MGR5. Velocities between ~5000-6000 m/s (blue) representing the Malmani subgroup also match the borehole log. A fault zone is mapped at ~2500 m along the profile. (C) P-wave seismic tomography inverse model of seismic line AV 6 with a root mean square error of 9 ms. Faults and dykes can be seen clearly compartmentalizing the dolomites in the inverse model. (D) P-wave seismic tomography inverse model of seismic line AV 7 with a root mean square error of 7 ms. Velocities between ~5000-6000 m/s (blue) in the Malmani subgroup correlate with all three boreholes along the survey line. Again, faults and dykes can be seen compartmentalizing the dolomites. Dykes and faults are mapped from underground mapping and subsurface boreholes.

When all 6 P-wave seismic tomography inverse model are plotted in a three-dimensional space, the continuation of the previously mapped fault zone can be seen propagating through the P-wave seismic tomography inverse model associated with seismic lines AV 1 and AV 2 at positions f1 and f2 (Figure 5.7). A possible fault zone can be seen mapped across seismic lines AV 2, AV 5, AV 6 and AV 7 (Figure 5.7). The low-velocity zones, labelled f3, correspond with a large fault zone mapped within the mining region. This low velocity zone will be the focus of the following localized integrated geophysical study.

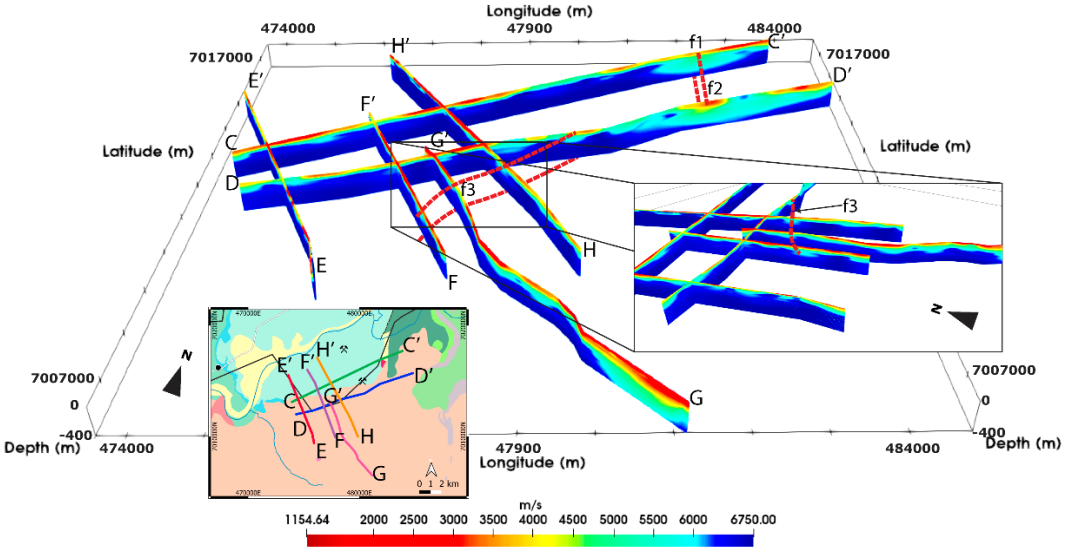


Figure 5.7. A three-dimensional spatial representation of all 6 seismic lines in our study area. Low velocity zones at Position f1 and f2 correspond with the fault continuation. The red line labeled f3 shows a love velocity zone propagating through P-wave seismic tomography inverse models associated with seismic lines AV 2, AV 5, AV 6 and AV 7.

5.4. Seismic Low Velocity Zone Investigation

In order to study the local low-velocity zone found in the seismic tomography inverse models, we identified a farm, situated within the low-velocity zone, and gathered magnetic, electrical resistivity tomography (ERT) and audio magnetotelluric (AMT) data in the study area (Figure 5.8 and data from 5 ERT survey lines, 11 AMT stations, and 15 magnetic survey lines were collected.

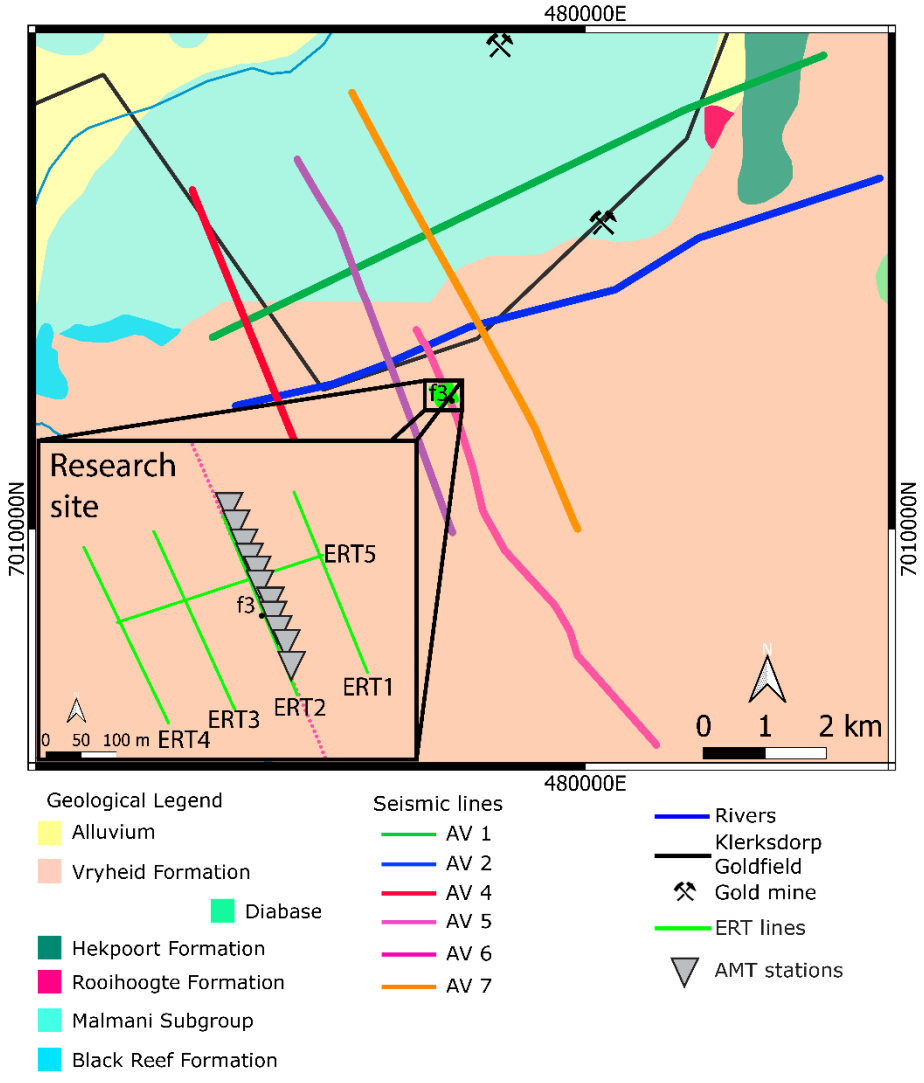


Figure 5.8. A geological map showing the planned survey site targeting low-velocity zones mapped in the P-wave seismic tomography inverse model. We collected data from 5 electrical resistivity tomography survey lines, 11 audio magnetotelluric stations, and 15 magnetic survey lines. Seismic line AV 6 runs through the center of our research site.

For the magnetic survey, a Geometrics G859 cesium vapor magnetometer was used as the rover and two Geometrics G856AX proton precession magnetometers for the base stations. The rovers sampling rate was set to one reading per second while the two base stations were set to take readings at 1 and 5 seconds respectively. The line spacing was set to ~25-35 m depending on the terrain, with an average line length of ~330 m. Once the data were collected, the diurnal, collected from the base stations was removed, resulting in the residual magnetic map (Figure 5.9(B)). We also leveled the aeromagnetic data using the Naudy-Fuller space domain filter which incorporates both a Butterworth and directional cosine filter (Fraser et al., 1966; Naudy and Dreyer, 1968). An 8th order Butterworth high-pass filter window is set to four times the line spacing (100 m) so to only pass frequencies less than the line spacing. The directional cosine filter is set to the line strike direction to only allow wavelengths through in the same direction. The resulting grid contains the leveling errors at each grid cell. This error grid is subtracted from the reduced magnetic grid resulting in a leveled magnetic grid (Figure 5.9(B)).

The reduced leveled magnetic map shown in (Figure 5.9(B)), depict two residual magnetic low intensity (~-11 nT) zones at positions A and B. A low magnetic intensity (~0 to -5 nT) area is also highlighted between the stippled lines for the zone labelled C. A linear high intensity residual magnetic (~2 nT) feature, trending north-west to south-east, is labeled D and could be offset by zone C. Position f3 shows the location of the low velocity zone seen along P-wave seismic tomography inverse model for seismic line AV 6. The white gaps in the reduced leveled magnetic map are due to cultural features such as pipes affecting the

magnetic signal along those lines, therefore those lines are not included in the final map.

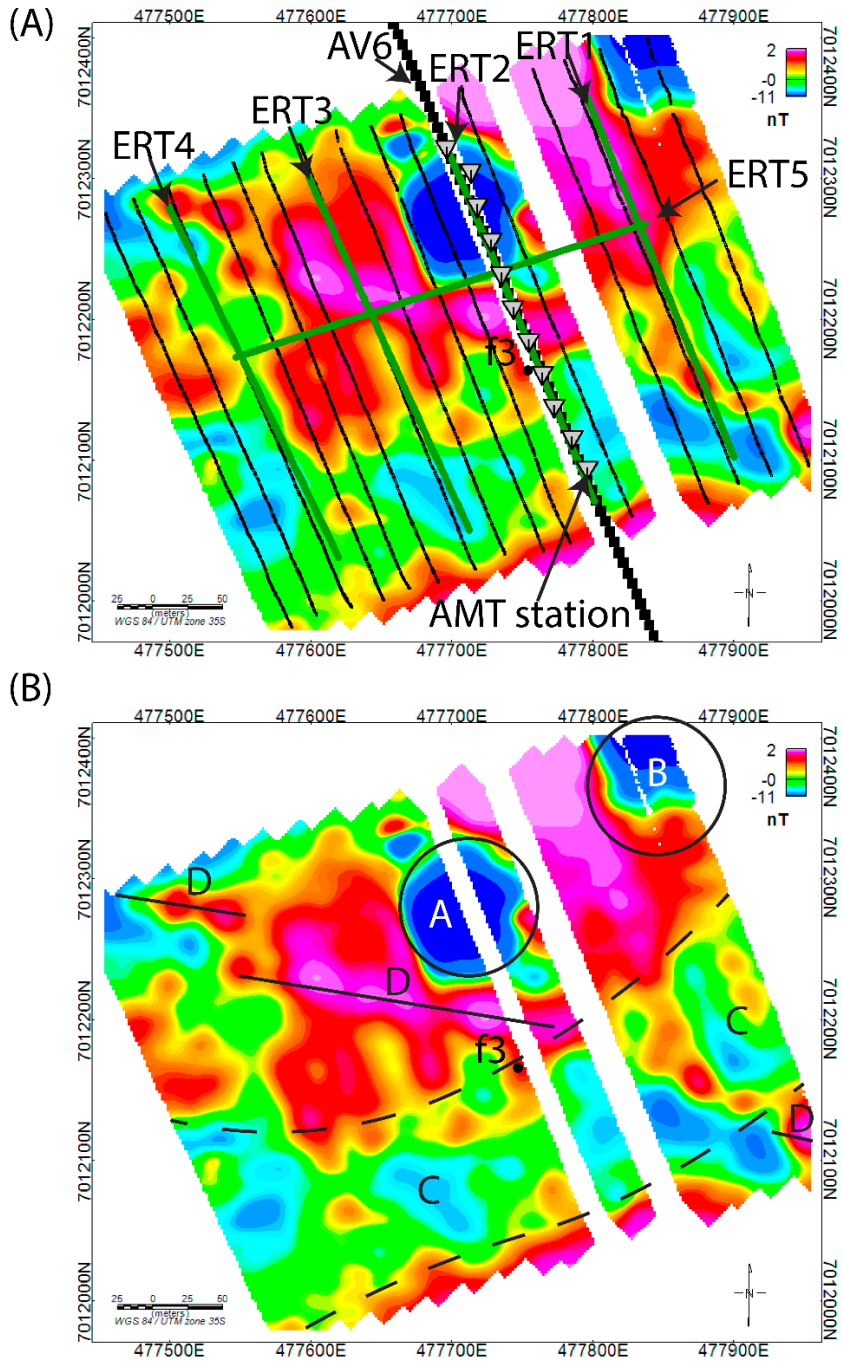


Figure 5.9. (A) Reduced and leveled magnetic map with black dots representing the magnetic readings collected along the survey lines. Black squares show the receiver positions for a portion of the seismic line AV 6. (B) Reduced and leveled magnetic data collected at our research site. Positions A and B show two negative residual magnetic intensity (~-11 nT) zones. Zone C, marked by the black stippled line, offsets the positive residual magnetic intensity lineament marked as D. Position f3 shows the location of the low velocity zone seen along P-wave seismic tomography inverse model for seismic line AV 6.

The reduced levelled residual magnetic grid was used to calculate a susceptibility inverse model using the MAG3D inverse algorithm developed by the University of British Columbia Geophysical Inversion Facility (Li and Oldenburg, 1996; Li and Oldenburg, 1997). A starting model of a 0.001 SI half-space was used in the magnetic susceptibility inverse model, the upper and lower bounds for the inverse model were set to 0 and 1 SI respectively. The mesh used for the inverse model had cells 10 m by 10 m with a mesh dimensionality of 55 by 50 by 45 cells with a total of 123750 cells in the inverse model. The absolute maximum misfit calculated for a cell in the inverse model was ~1.5 nT. The average misfit for the cells in the inverse model was ~0.2 nT. The target misfit, with the χ factor set to 1, was reached in 10 iterations.

From the magnetic susceptibility inverse model, a drop in the depth to solid dolomite (susceptibility 0.0004-0.0006 SI) from 15 m to ~110 m deep is modelled along the black stippled line, marking area C, in Figure 5.10(B and C). The drop-in dolomite depth in the region marked by area C correlates with the low-velocity zones f3. The negative residual magnetic intensity (~-11 nT) zone at position A, coincides with a cavity in the dolomites at the same position in the magnetic susceptibility inverse model where the low occurs.

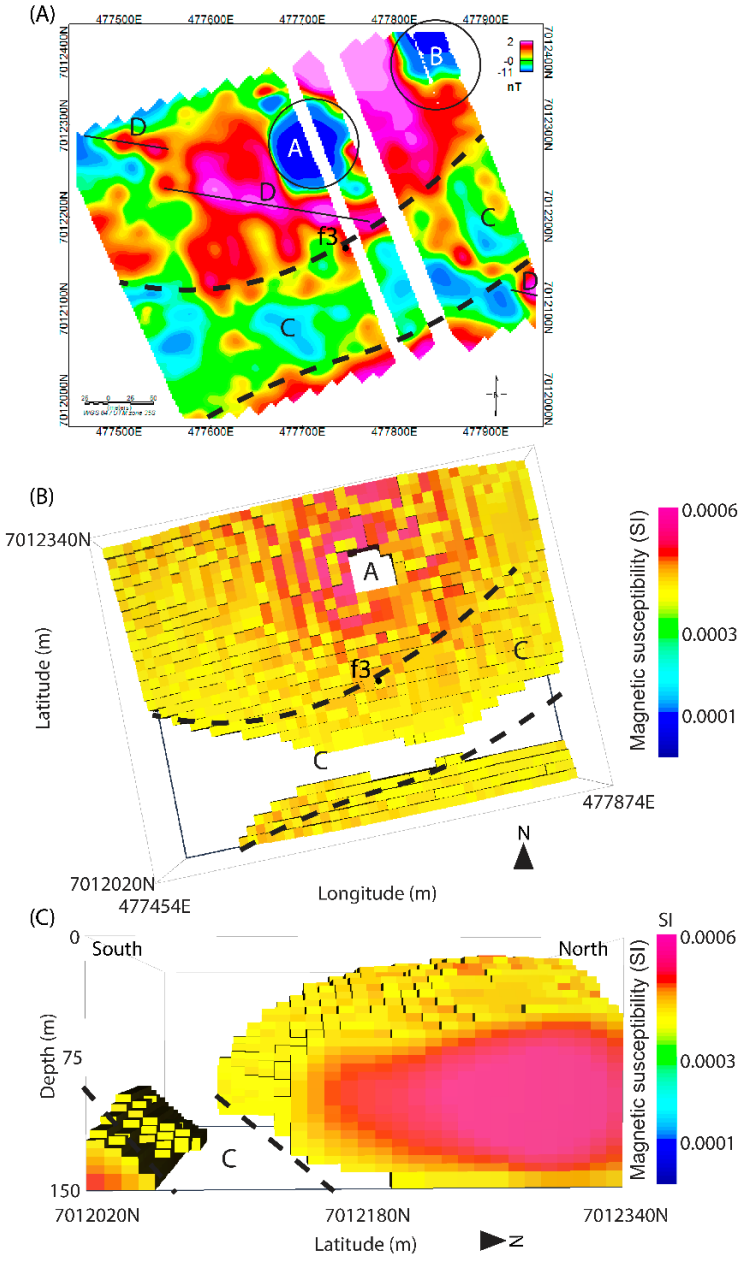


Figure 5.10. (A) Reduced and leveled magnetic map. Positions A and B show two negative magnetic intensity (~-11 nT) zones. Zone C, marked by the black stippled line, offsets the positive magnetic intensity lineament marked as D. Position f3 shows the location of the low velocity zone seen along P-wave seismic tomography inverse model for seismic line AV 6. (B) A top down view of the magnetic susceptibility inverse model calculated from the reduced and leveled residual magnetic grid. An isovolume of susceptibilities between 0.0004 and 0.0006 SI shows a 'break' in the dolomites in the area labeled C. The residual negative magnetic intensity (~-11 nT) zone at position A, correlates with a cavity in the dolomites at that same position in the magnetic susceptibility inverse model. (C) Easterly side view of the magnetic susceptibility inverse model. An isovolume of susceptibilities between 0.0004 and 0.0006 SI shows a drop in depth in the dolomites from ~15 m to ~110 m deep in the area labeled C.

For the ERT surveys, an electrode spacing of 5 m was used for ERT lines ERT1, ERT2, ERT3 and ERT4, which results in a maximum survey length of 275 m each. An electrode spacing of 5.5 m is used for ERT5 with a maximum survey length of 302.5 m. The GF Instruments ARES resistivity unit was used for the acquisition of the ERT data. The dipole-dipole ERT array configuration was used throughout the ERT data collection since we wanted to use an ERT array with the highest sensitivity to lateral changes in lithology (Loke, 2011) to map the vertical fault zone seen in the magnetic data. Data was difficult to collect due to the porous weathered dolomitic sands and cavities, resulting in higher than usual RMSE values in some resistivity inverse models.

Once the data were collected, we masked data spikes induced by cultural noise or high contact resistance between the electrodes and ground. The data were then used to calculate an electrical resistivity inverse model using the least-squares quasi-Newton inversion algorithm RES2DINV developed by Loke and Barker (1996). The finite difference forward modelling and inversion routine used for the ERT data is RES2DMOD and RES2DINV. A value of 0.16 is used for the initial damping factor value for the first iteration then halved after each iteration with a minimum allowed value of 0.015. The subsurface is discretized into rectangular cells, based on the position of available data points. The deepest layer in the model is equivalent to the depth of investigation of the data points where the total number of cells equals the number of available data points in the mesh. Topography values is also included in the mesh if available.

The ERT2 resistivity inverse model is compared to a cross section, along ERT2, from the 3-D magnetic susceptibility inverse model (Figure 5.11). The remaining

ERT lines are shown in the appendix in Figure A.11. The resistivity inverse model for ERT2 (Figure 5.11(B)) shows the resistive dolomites (~ 800 Ω·m) discontinued ~170 m along the profile by a conductor (~100 Ω·m) at the same position f3 where the low velocity zone is situated (Figure 5.11(B)). The slightly magnetic dolomites are also discontinued at position f3 in the cross-section from the magnetic susceptibility inverse model. The resistivity inverse model for ERT2 also shows a vertical resistor (1200-1400 Ω·m), ~60-150 m along the profile, situated in the same location as the cavity in the magnetic susceptibility inverse model.

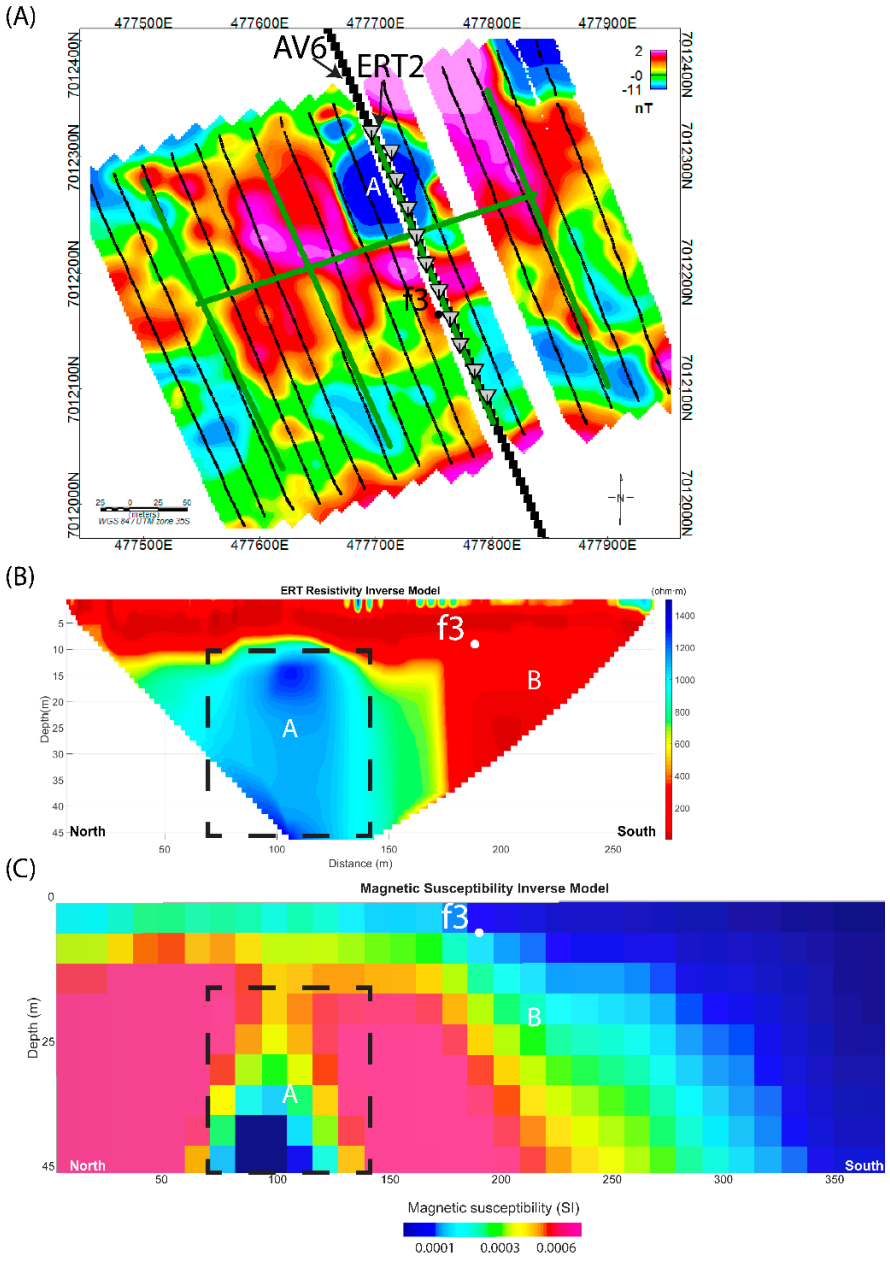


Figure 5.11. (A) Reduced and leveled magnetic map with black dots representing the magnetic readings collected along the survey lines. Green lines show the position of the ERT lines and 11 audio magnetotelluric stations are shown as grey triangles. Black squares show the receiver positions for a portion of seismic line AV 6. (B) Resistivity inverse model for ERT2, with a root mean square error of 5. The resistive dolomites (~ 800 Ω·m) are discontinued ~170 m along the profile by a conductor (~100 Ω·m) interpreted as a fault zone, labeled B. A vertical resistor (1200-1400 Ω·m), labeled A, ~60-150 m along the profile, is situated in the same location as the inferred cavity mapped on the reduced and leveled magnetic map. (C) 3-D Magnetic susceptibility inverse model slice along survey line ERT2. Both the position of the low susceptibility (~0.0001) fault zone and the inferred cavity match the position seen in the resistivity inverse model for the same line.

Once the displacement zone C was identified from the ERT and magnetic inverse models an AMT survey of 11 stations was planned over survey line ERT2. The station spacing for the AMT survey is ~25 m, with a dipole length of ~10 m. It is important to note that the AMT survey was conducted ~4 km south-west of operational mines and ~ 4 km west of a national power grid substation. Figure 5.12 shows a representative sample of data collected in the area; this data comes from station AMT1. Since the electromagnetic fields measured in the AMT method are orthogonal to each other they can be decomposed into two modes that relate to the polarization of the electromagnetic fields. The first mode is known as the transverse magnetic (TM) mode where the magnetic field is polarized parallel to the lithological strike. The second mode is called the transverse electric (TE) mode where the electric field is polarized parallel to lithological strike. The TE mode in our survey is affected most by the powerline noise since the strike of the TE mode is parallel with powerlines in the area. In some cases, the TE mode is completely saturated with noise and is left out of the resistivity inversion model calculations. Therefore, for the rest of this paper, we will only be considering the TM mode for inverse calculations.

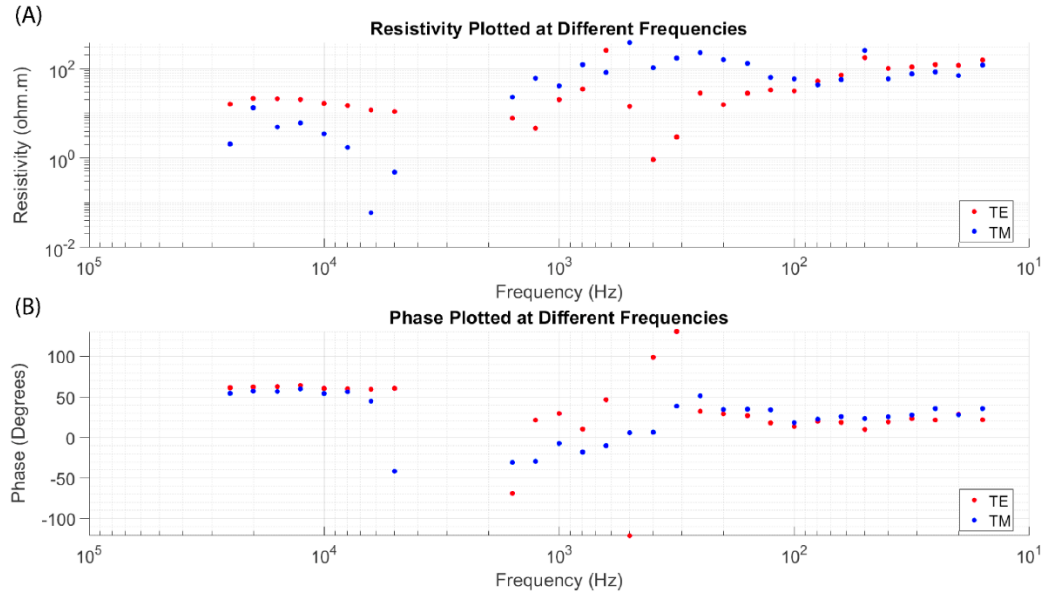


Figure 5.12. (A) TE and TM resistivity values collected from AMT station AMT1. (B) TE and TM phase values collected from AMT station AMT1. The TE mode is more susceptible to noise saturation since the TE mode strikes parallel with the surrounding powerlines in the study area.

Once the AMT data is acquired, the TM and the TE modes are assigned to the phase and resistivity curves. The TM mode is perpendicular to the displaced zone C shown in the magnetic and resistivity inverse models. The TE mode is parallel to the general strike direction of the displacement zone C. Subsequently data points were masked in the 1 kHz dead band and data points >31 kHz where signal strength was low. Noisy spikes were removed and smooth D+ curves fitted, following Beamish and Travassos (1992), to the remaining data points, since magnetotelluric data must be smoothly varying. The augmented response functions were then calculated from the resistivity inverse model along the survey line ERT2.

Once the data editing was completed and the augmented response function was calculated, the one-dimensional (1-D) and two-dimensional (2-D) resistivity inverse models were calculated using the conjugant gradient code developed by

Rodi and Mackie (2001). The minimum and maximum frequency set for the inverse model calculations is 15.6 Hz and 100000 Hz respectively, which replicates the frequency range of the data collected. A starting model of 1000 Ω·m is used for the initial inverse calculation. The objective function is set to first find the smoothest model with a standard Laplacian operator focusing on minimizing the integral of the gradients of the model with a Tau value of 3. Once the first inverse model is calculated the resulting model is used as a starting model for the second inverse model calculation. The objective function is now set to solve for the smoothest variation away from the starting model with a standard Laplacian operator focusing on minimizing the integral of the Laplacian. For this inverse calculation, the Tau operator is set as 3 with weighting functions enabled to prevent the model from becoming too blocky. This inversion methodology allows for an initial smooth model to be calculated from a 1000 Ω·m half-space and then the resulting smooth model is used as a starting model for a second inverse calculation that is focused on fitting the observed data. We use the 2-D resistivity inverse models calculated from just the TM, since the TE mode in most stations is saturated by noise, to interpret the underlying lithological structures. Once the 2-D inverse models are calculated, the model confidence assessment algorithm is run on the model and once again the resulting alpha map is used to modify the translucency of cells in the inverse model corresponding to the misfit magnitude calculated by model confidence assessment algorithm. Cells that are white show areas in the model with the least amount of confidence.

Figure 5.13 compares the standard AMT resistivity inverse model Figure 5.13(A) to the resistivity inverse model using the augmented ERT-MT response function

(developed in Chapter 4) Figure 5.13(B). As expected, greater detail is seen in the near surface (< 100 m deep) of the augmented ERT-MT response function resistivity inverse model while retaining the deeper features from the standard AMT resistivity inverse model. The confidence threshold is set at 0.3 of the maximum normalized misfit calculated by the confidence assessment algorithm. This can be seen with the white areas, of low confidence, in the AMT resistivity inverse model primarily isolated in the top 100 m of the model (Figure 5.13 (A)). This is because of poor AMT data quality or completely absent data in the high frequency band due to cultural noise in the AMT data. Generally, if noise free AMT data is collected in this area the near surface conductor would be resolved but due to cultural noise this is not the case for the current AMT data set. The augmented ERT-MT response function supplements the original AMT data with new pseudo-MT high frequency data. The effects of the augmented ERT-MT response function on the resistivity inverse model can be seen in the resistivity inverse model in Figure 5.13 (B), where much of the near surface low confidence zones are absent due to high misfits associated within these mesh regions. The root mean square error for the augmented ERT-MT response function resistivity inverse model is 2.3 while the minimum root mean square error the standard AMT resistivity inverse model could achieve is 5 in this noisy mining environment.

A conductor (~100 Ω·m) is seen between ~100-400 m deep in the augmented ERT-MT response function resistivity inverse model (Figure 5.13(B)). A conductive feature at position f3, correlates with the low velocity zone in the p-wave seismic tomography inverse model for seismic line AV 6 and the displacement seen in the dolomites in both the ERT and magnetic susceptibility

inverse models. The conductor has a maximum depth of ~400 m in the resistivity inverse model. At position A (Figure 5.13(B)) in the augmented ERT-MT response function resistivity inverse model show more resistive values are resolved at position A than in the lateral extent overlying conductor, which is at the same location as the cavity seen in both the ERT and magnetic susceptibility inverse models.

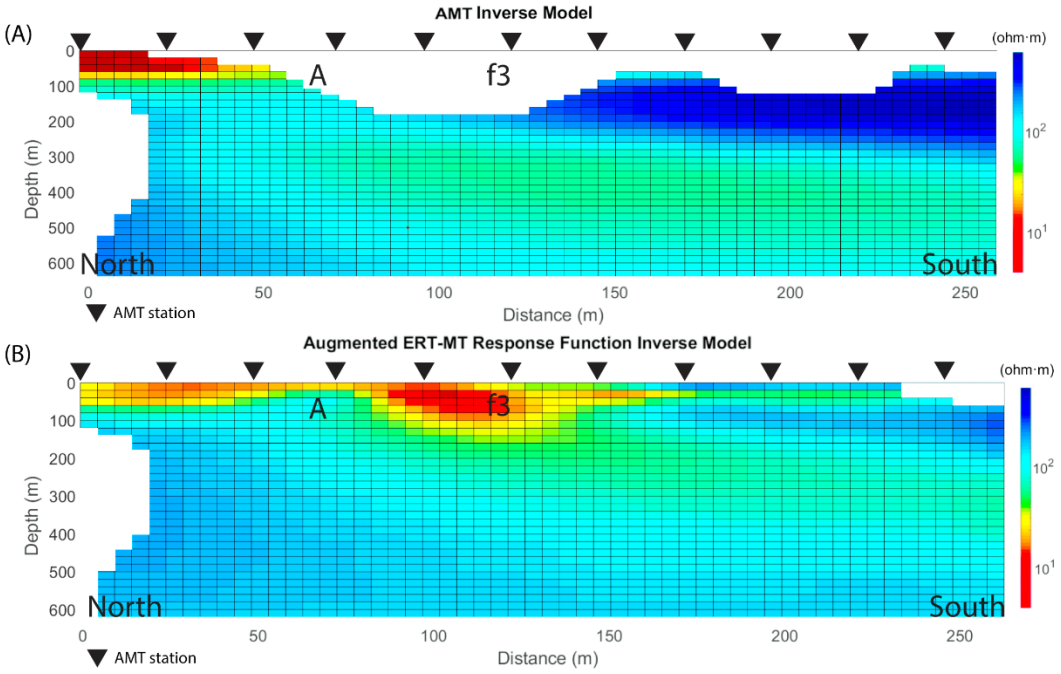


Figure 5.13. (A) Standard AMT resistivity inverse model with a minimum root mean square error of 5. (B) Augmented ERT-MT response function resistivity inverse model with a root mean square error of 2.3. Greater detail is seen in the near surface (< 100 m deep) of the augmented response function resistivity inverse model while retaining the deeper features from the standard AMT resistivity inverse model. f3 marks the location of the low velocity zone in the P-wave seismic tomography inverse model for a portion seismic line AV 6. Position A marks the location of the cavity seen in both the ERT and magnetic susceptibility inverse models. The white cells in these models represent cells with low confidence calculated from the model confidence assessment algorithm.

5.5. Discussion

It was shown that the deepest low velocity propagation zone interpreted as fault zones, mapped by the P-wave seismic tomography inverse models occur at ~400

m depth. From this it is inferred that meaningful groundwater conduits for surface recharge in the research area are possibly confined within the top ~400 m of the Malmani subgroup. Also, conductive features in the resistivity inverse models could also result from wafer thin layers of carbonaceous material, of high conductivity (~ 1000 Siemens), in the Malmani dolomites and not necessarily from geohydrological changes.

The displacement interpreted in the dolomites, from the magnetic susceptibility, ERT resistivity and augmented ERT-MT response function resistivity inverse models within the localized integrated geophysical survey are all consistent with the interpretation of a fault zone at location f3. This fault zone also correlates with the low velocity zone, f3, seen in the P-wave seismic tomography inverse models generated from seismic lines AV 2, AV 5, AV 6 and AV 7. The fault zone has an average width of ~ 115 m as interpreted from the reduced and leveled magnetic map and magnetic susceptibility inverse model. The fault zone has displaced the dolomites to the south up to ~95 m. The circular magnetic lows, at location A and B on the reduced and leveled magnetic map shown in Figure 5.9(B), are interpreted as potential cavity prone localities near the fault zone. These lows can also indicate the edges of magnetic materials in the area but due to depressions in the soil, seen at the surface within these lows most likely indicate a cavity beneath. Fractures from the fault zone likely allowed surface water access to the underlying dolomites triggering the dissolution of the surrounding dolomites and resulting in subsurface cavities.

The ~100 Ω·m conductor situated between ~100-400 m depths in the augmented ERT-MT response function resistivity inverse model is interpreted as being a fracture karst aquifer (Figure 5.14).

The deepest fault zone, mapped in the augmented ERT-MT response function resistivity inverse model, is too shallow for any meaningful interaction with deeper fault zones in the Witwatersrand Supergroup below. As the deepest extent of the conductor in Figure 5.13(B) is ~200 m. Therefore, the bottom of the fault has been resolved at ~200 m deep.

Therefore, a continuous conduit between the near-surface (< 1 km deep) biosphere and the deep (>2 km) biosphere is absent in all the geophysical inverse models calculated in our study area.

To fully comprehend the interconnectivity of the near-surface groundwater biosphere and the deep biosphere, future work using reflection seismic profiles should be used to model the deep faults and fissures. Once the deep faults and fissures are mapped, they can be compared to the faults mapped in the dolomites in our study area. This future work will be incorporated with the research done in this chapter and written up as a future publication.

With the use of multiple geophysical data sets and new processing techniques for ERT and AMT data, we conclude that the deep biosphere, in our study area, could be isolated from near-surface groundwater interactions. Therefore, if the deeper Witwatersrand Supergroup, which lies beneath the Transvaal and Ventersdorp Supergroups, is isolated there is potential for preserved ancient water, perhaps even as old as the Archean as shown in Rusley et al., (2018) and Borgonie et al.,

(2019). This ancient fissure that could resemble the most likely location to find a living biosphere on other planets (Takai et al., 2001; Onstott et al., 2019).

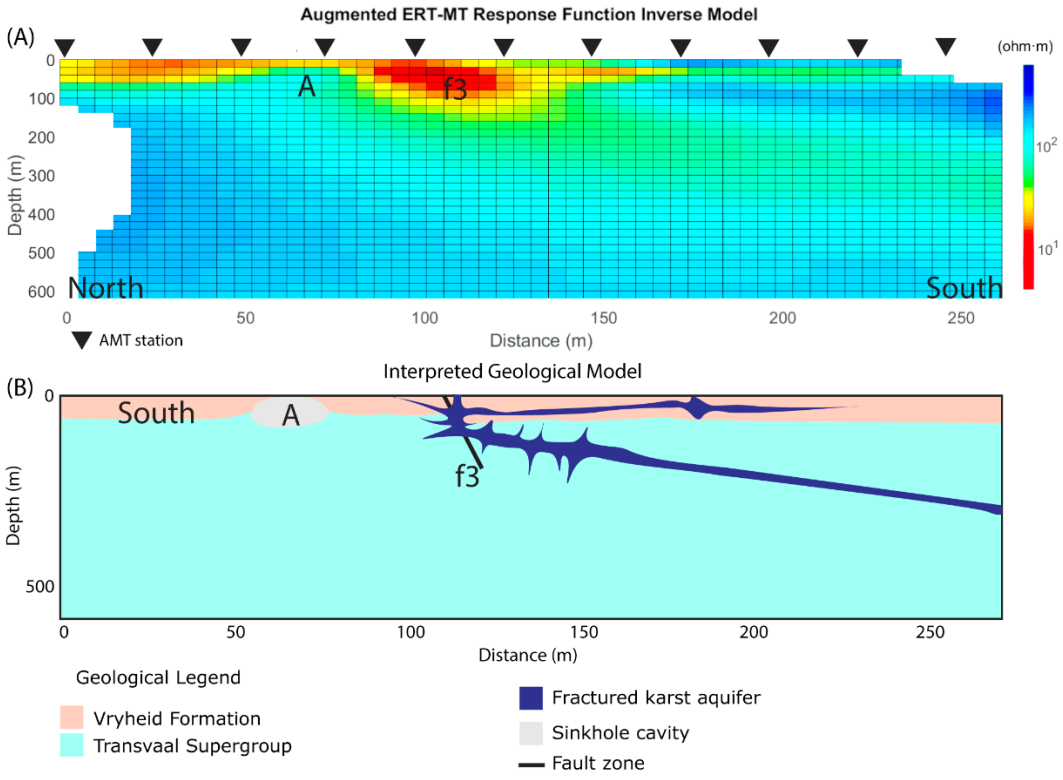


Figure 5.14. (A) Augmented ERT-MT response function resistivity inverse model along survey line ERT2. The white cells in this model represent cells with low confidence calculated from the model confidence assessment algorithm. (B) A geological model interpreted from the augmented ERT-MT response function resistivity inverse model along survey line ERT2. The fractured karst aquifer is confined between ~100-400 m deep. A inferred cavity is interpreted at position A.

It was shown that the augmented ERT-MT response function also improves the resistivity inverse models significantly even for the case of a resistor (dolomites) overlying a conductor (karst aquifer and fault). Greater detail is seen in the near surface (< 100 m deep) while maintaining the deeper features from the standard AMT resistivity inverse model. The root mean square error for the augmented ERT-MT response function resistivity inverse model is 2 and 5 for the AMT

inverse model in this noisy mining environment. In this case, the additional high-frequency data provided from the augmented ERT-MT response function assisted in stabilizing the inversion algorithm, with the additional data, resulting in a lower root mean square error than if only the AMT data was used. The augmented ERT-MT response function can also be used to improve MT inversion models in areas where data is noisy or difficult to acquire. Since if the area had low cultural noise the conductor at position f3 would be mapped by the AMT data only

5.6. Conclusion

We have shown that by utilizing multiple geophysical data sets, such as legacy seismic, ERT, AMT and magnetic data, we can identify fault zones and aquifers in the Malmani subgroup dolomites.

The results from multiple geophysical inverse models calculated for this chapter show that groundwater conduits, fault zones and fractured karst aquifer systems, in our study area are confined to the upper (< 500 m deep) Malmani subgroup dolomites. Therefore, it is unlikely that groundwater systems, recharged by surface water, have any meaningful interaction with deeper groundwater networks in our study area.

Hence the near-surface biosphere and the deep biosphere is disconnected in our study area. This means that the deep (> 2 km deep) fracture aquifers, hosting archaeal life in the present study area, are isolated from surface water recharge. Therefore, the deep gold mines here are an ideal example of how archaeal biospheres can be preserved and studied in deep confined fissures on other planets.

5.7. Acknowledgments

The support of the DST-NRF Centre of Excellence for Integrated Mineral and Energy Resource Analysis (DST-NRF CIMERA) towards this research is hereby acknowledged. Opinions expressed and conclusions arrived at, are those of the authors and are not necessarily to be attributed to the CoE.

GES Geophysics and De Beers Group South Africa are also acknowledged for their support in providing EH-4 Stratagem AMT systems for the period of the research project. We would also like to acknowledge Ian James from HiSeis, for his guidance and assistance throughout the p-wave seismic tomography inversion modelling process. We would also like to acknowledge the UBC-Geophysical Inversion Facility from the Department of Earth and Ocean Sciences at the University of British Columbia for providing us with MAG3D. MAG3D is a program library for the forward modelling and inversion of magnetic data over 3-D structures.

Lastly, we would like to thank Harmony Gold for allowing us to conduct this research on the Moab Khotsong gold mine property and providing borehole log information for our study area.

Chapter 6 : Concluding Remarks

6.1. Conclusion

In this thesis, it is shown that the AMT geophysical method's sensitivity to fault zones, intrusions such as dykes and groundwater bearing features such as aquifers and aquitards can be improved if the newly developed augmented ERT-MT response function is used when calculating resistivity inverse models.

On the farm Waterboerskraal, new ancient dune fields were mapped that recharge groundwater boreholes in the area. These ancient dune fields outcrop and allow for the storage and transmittance of fresh surface water into a Cenozoic sedimentary succession aquifer situated below an electrically conductive calcrete and clay aquitard. During the processing of the AMT data, it was noticed that the electrically conductive calcrete and clay aquitard masks any detail in the electrically resistive sedimentary aquifer below. As this is a general problem in frequency domain EM (FDEM) and the MT technique is a FDEM method that conductive layers mask resistors lying below a solution was sought which is the crux of this thesis being presented here.

To solve the magnetotelluric methods natural insensitivity to resistors below conductors, we developed the augmented ERT-MT response function. This method uses ERT data, through an analytically derived relationship, to augment the MT response function with high-frequency data. We showed that the

resistivity inverse models for both 1-D and 2-D theoretical modelling showed improvements, up to 90%, in recovering resistive features beneath a conductive layer and better constrain near-surface resistivity layers. In a case study, at the Modikwa Platinum mine, it was shown that the augmented ERT-MT response function helped to constrain the width and depth of a resistive dyke that was completely absent before in the singular MT data inversion image. Since the MT data is augmented before the inversion calculation commences only a single inversion parameter is inverted, unlike when a joint or cooperative inversion is needed to integrate both the ERT and AMT data sets. This reduces the overall computational time needed to invert both data sets with the same objective function.

To test the augmented ERT-MT response function on conductive targets in a different environment at a second study site, it was found that conductive fault zones and aquifers were identified as targets in the groundwater biosphere study, Chapter 5. In this case, the resistivity inverse models using the augmented ERT-MT response function mapped a fault zone, recharging a fractured karst aquifer, that was absent in the AMT only data resistivity inverse model. Therefore, for both conductive and resistive features augmented ERT-MT response function improved the AMT resistivity inverse models by mapping features that were absent before. It was shown that the augmented ERT-MT response function technique improves the resolving power of the MT method for both the theoretical and practical case. The augmented ERT-MT response function can also be used to improve MT inversion models in areas where data is noisy or difficult to acquire.

This is achieved by supplementing the noisy MT data with additional high frequency data that can assist in constraining the MT response function.

It was also shown in this thesis that the results from multiple geophysical methods helped in the interpretation and constraining of AMT resistivity inverse models. Without the use of multiple geophysical models, it would be difficult to develop and measure improvements in AMT inverse models. Independent geophysical data sets should always be used as a reference when attempting to derive new model algorithms or analytical derivations for new geophysical methods.

Some important secondary findings, from this thesis, that fall outside the original scope, include the discovery and mapping of a new ancient dune network in the Swartland Terrane. I also discovered a relationship between the proximity of productive wells to ancient dune outcrops on the Waterboerskraal farm. The Pliocene shoreline boundary in the Swartland Terrane was extended using geophysical techniques. It was illustrated that the near-surface biosphere and the deep biosphere is disconnected in our study area on the Witwatersrand Basin. This means that the deep gold mines in our study area can be an ideal example of how archaeal biospheres can be preserved in deep confined fissures on other planets.

6.2. Future studies

Possible future research projects include the further development of the augmented ERT-MT response function in a 3-D space. As it stands the augmented ERT-MT response function can only correct a single mode in the MT method. To apply the augmented ERT-MT response function to both TM and TE modes, a 3-

D ERT resistivity inverse model should be included in a new 3-D derivation of the augmented ERT-MT response function.

In this thesis, I only explored the benefits of using the augmented ERT-MT response function in MT inversion modelling. The derivation described in this thesis allows for the transformation of MT data into ERT data that can be used in an ERT resistivity inversion scheme. The augmented ERT-MT response function can easily be expanded to include other methods such as time-domain electromagnetic data.

Future work using reflection seismic profiles should be used to model the deep faults and fissures, around the Moab Khotsong Gold mine study area in Chapter 6, which is also planned. Once the deep faults and fissures are mapped, they can be compared to the faults mapped in the dolomites in the study area.

Chapter 7 : References

Alenitsyn, A.G., Butikov, E.I. and Kondratyev, A.S., (1997), Concise handbook of Mathematics and Physics, CRC Press, 488-490.

Ashcroft, N.W. and Mermin, N.D., (1976), Solid state physics, Saunders College Publishing, 131-329.

Baranov, V. and Naudy, H., (1964), Numerical calculation of the formula of reduction to the magnetic pole, Geophysics, 29(1), 67-79.

Barnes, S.J., Maier, W.D. and Ashwal, L.D., (2004), Platinum-group element distribution in the main zone and upper zone of the Bushveld Complex, South Africa, Chemical Geology, 208(1-4), 293-317.

Beamish, D., and Travassos, J.M., (1992), The use of the D+ solution in magnetotelluric interpretation, Journal of Applied Geophysics, 29, 1-19.

Belcher, R.W., (2003), Tectonostratigraphic evolution of the Swartland region and aspects of orogenic lode-gold mineralisation in the Pan-African Saldania Belt, Western Cape, South Africa, Doctoral dissertation, Stellenbosch University, 5-105.

Berdichevsky, M.N. and Dmitriev, V.I., (2002), Magnetotellurics in the context of the theory of ill-posed problems, Society of Exploration Geophysicists, 31-108.

Borgonie, G., Magnabosco, C., García-Moyano, A., Linage-Alvarez, B., Ojo, A.O., Freese, L.B., Van Jaarsveld, C., Van Rooyen, C., Kuloyo, O., Cason, E.D. and Vermeulen, J., (2019), New ecosystems in the deep subsurface follow the flow of water driven by geological activity, Scientific reports, 9.

Cagniard, L., (1953) Basic theory of the magneto-telluric method of geophysical prospecting, Geophysics, 18(3), 605-635.

Campbell, W. H., C. E. Barton, F. H. Chamalaun, and H. W. Welsh (1998), Quiet-day ionospheric currents and their application to upper mantle conductivity in Australia: Earth, Planets, and Space, 50, 347–360,

Chapman, S. and Price, A.T., (1930), The electric and magnetic state of the interior of the earth, as inferred from terrestrial magnetic variations, Philosophical Transactions of the Royal Society of London, 229(670-680), 427-460.

Chapman, S., (1919), The solar and lunar diurnal variations of terrestrial magnetism, Philosophical Transactions of the Royal Society of London, 218(561-569), 1-118.

Chave, A.D. and Jones, A.G. eds., (2012), The magnetotelluric method: Theory and practice, Cambridge University Press, 19-421.

Compton, J.S. and Franceschini, G., (2005), Holocene geoarchaeology of the sixteen mile beach barrier dunes in the Western Cape, South Africa, Quaternary Research, 63(1), 99-107.

Compton, J.S., (2001), Holocene sea-level fluctuations inferred from the evolution of depositional environments of the southern Langebaan Lagoon salt marsh, South Africa, The Holocene, 11(4), 395-405.

Conrad, J., Nel, J. and Wentzel, J., (2004), The challenges and implications of assessing groundwater recharge: A case study–northern Sandveld, Western Cape, South Africa, Water SA, 30(5), 75-81.

Constable, C., (2016), Earth's electromagnetic environment, Surveys in Geophysics, 37(1), 27-45.

Constable, S. and Weiss, C.J., (2006), Mapping thin resistors and hydrocarbons with marine EM methods: Insights from 1D modeling, Geophysics, 71(2), G43-G51.

Constable, S. and Weiss, C.J., (2006), Mapping thin resistors and hydrocarbons with marine EM methods: Insights from 1D modeling, Geophysics, 71(2), G43-G51.

Coward, M.P., Spencer, R.M. and Spencer, C.E., (1995), Development of the Witwatersrand Basin, South Africa, Geological Society, London, Special Publications, 95(1), 243-269.

Dalziel, I.W., Dalla Salda, L.H. and Gahagan, L.M., (1994), Paleozoic Laurentia-Gondwana interaction and the origin of the Appalachian-Andean mountain system, Geological Society of America Bulletin, 106(2), 243-252.

Dankert, B.T. and Hein, K.A., (2010), Evaluating the structural character and tectonic history of the Witwatersrand Basin, Precambrian Research, 177(1-2), 1-22.

deGroot-Hedlin, C., (1991), Removal of static shift in two dimensions by regularized inversion, Geophysics, 56(12), 2102-2106.

Dentith, M. and Mudge, S.T., (2014), Geophysics for the mineral exploration geoscientist, Cambridge University Press, 235-255.

Dippenaar, M.A., van Rooy, J.L. and Diamond, R.E., (2019), Engineering, hydrogeological and vadose zone hydrological aspects of Proterozoic dolomites (South Africa), Journal of African Earth Sciences, 150, 511-521.

Eriksson, P.G. and Reczko, B.F.F., (1995), The sedimentary and tectonic setting of the Transvaal Supergroup floor rocks to the Bushveld Complex, Journal of African Earth Sciences, 21(4), 487-504.

Everard, M., Jones, L. and Watts, B., (2010), Have we neglected the societal importance of sand dunes? An ecosystem services perspective: Aquatic Conservation, Marine and Freshwater Ecosystems, 20(4), 476-487.

Farr, T.G., Rosen, P.A., Caro, E., Crippen, R., Duren, R., Hensley, S., Kobrick, M., Paller, M., Rodriguez, E., Roth, L., Seal, D., Shaffer, S., Shimada, J., Umland, J., Werner, M., Oskin, M., Burbank, D., and Alsdorf, D.E., (2007), The shuttle radar topography mission, Reviews of Geophysics, v. 45, no. 2, RG2004, at https://doi.org/10.1029/2005RG000183.

Fleisher, J.N.E., (1981), The geohydrology of the dolomite aquifers of the Malmani Subgroup in the south-western Transvaal, Republic of South Africa, Doctoral dissertation, University of the Free State.

Flemming, B.W., (1977), Langebaan Lagoon: a mixed carbonate-siliciclastic tidal environment in a semi-arid climate, Sedimentary geology, 18(1-3), 61-95.

Flügel, W.A., (1995), River salination due to dryland agriculture in the Western Cape Province, Republic of South Africa, Environment International, 21(5), 679-686.

Foster, M., (1961), An application of the Wiener-Kolmogorov smoothing theory to matrix inversion, Journal of the Society for Industrial and Applied Mathematics, 9(3), 387-392.

Franceschini, G. and Compton, J.S., (2006), Holocene evolution of the sixteen mile beach complex, Western Cape, South Africa, Journal of Coastal Research, 1158-1166.

Fraser, D.C., Fuller, B.D. and Ward, S.H., (1966), Some numerical techniques for application in mining exploration, Geophysics, 31(6), 1066-1077.

Frimmel, H.E., Basei, M.A., Correa, V.X. and Mbangula, N., (2013), A new lithostratigraphic subdivision and geodynamic model for the Pan-African western Saldania Belt, South Africa, Precambrian Research, 231, 218-235.

Fuchs, S., Williams-Jones, A.E. and Przybylowicz, W.J., (2016), The origin of the gold and uranium ores of the Black Reef Formation, Transvaal Supergroup, South Africa, Ore Geology Reviews, 72, 149-164.

Gibson, M.A., Jolley, S.J. and Barnicoat, A.C., (2000), Interpretation of the Western Ultra Deep Levels 3-D seismic survey, The Leading Edge, 19(7), 730-735.

Glover, P.W., (2010), A generalized Archie's law for n phases, Geophysics, 75(6), E247-E265.

Heard, A.W., Warr, O., Borgonie, G., Linage, B., Kuloyo, O., Fellowes, J.W., Magnabosco, C., Lau, M.C., Erasmus, M., Cason, E.D. and van Heerden, E., (2018), South African crustal fracture fluids preserve paleometeoric water signatures for up to tens of millions of years, Chemical Geology, 493, 379-395.

Heckman, S.J., Williams, E. and Boldi, B., (1998), Total global lightning inferred from Schumann resonance measurements, Journal of Geophysical Research: Atmospheres, 103(D24), 31775-31779.

Hirayama, M., (1934), On the relations between the variations of earth potential gradient and terrestrial magnetism, Journal of the Meteorological Society of Japan, 12(1), 16-22.

Jolley, S.J., Freeman, S.R., Barnicoat, A.C., Phillips, G.M., Knipe, R.J., Pather, A., Fox, N.P.C., Strydom, D., Birch, M.T.G., Henderson, I.H.C. and Rowland, T.W., (2004), Structural controls on Witwatersrand gold mineralization, Journal of Structural Geology, 26(6-7), 1067-1086.

Jones, A.G., (1988), Static shift of magnetotelluric data and its removal in a sedimentary basin environment, Geophysics, 53(7), 967-978.

Jones, M.L.M., Reynolds, B., Brittain, S.A., Norris, D.A., Rhind, P.M. and Jones, R.E., (2006), Complex hydrological controls on wet dune slacks: the importance of local variability, Science of the Total Environment, 372(1), 266-277.

Kamish, W., (2008), Hydrosalinity modelling of the Berg River using ACRUSalinity, Doctoral dissertation, Stellenbosch University, 26-59.

Kandel, A.W., Felix-Henningsen, P. and Conard, N.J., (2003), An overview of the spatial archaeology of the Geelbek Dunes, Western Cape, South Africa, BAR International Series, 1163, 37-44.

Kisters, A. and Belcher, R., (2018), The stratigraphy and structure of the western saldania belt, south africa and geodynamic implications, in S. Siegesmund, M. A. S. Basei, P. Oyhantçabal, S. Oriolo, eds., Geology of Southwest Gondwana, Springer International Publishing, 387-410.

Kisters, A.F., Belcher, R.W., Scheepers, R., Rozendaal, A., Jordaan, L.S. and Armstrong, R.A., (2002), Timing and kinematics of the Colenso Fault: The Early Paleozoic shift from collisional to extensional tectonics in the Pan-African Saldania Belt, South Africa, South African Journal of Geology, 105(3), 257-270.

Lamb, H., (1883), On electrical motions in a spherical conductor, Philosophical Transactions of the Royal Society of London, 174, 519-549.

Ledwaba, L., Dingoko, O., Cole, P. and Havenga, M., (2009), Compilation of survey specifications for all the old regional airborne geophysical surveys conducted over South Africa, Council for Geoscience Report, 40.

Lee, T.D., (1950), Hydrogen content and energy-productive mechanism of white dwarfs, The Astrophysical Journal, 111, 625.

Lelièvre, P.G., Farquharson, C.G. and Hurich, C.A., (2012), Joint inversion of seismic traveltimes and gravity data on unstructured grids with application to mineral exploration, Geophysics, 77(1), K1-K15.

Li, Y. and Oldenburg, D.W., (1996), 3-D inversion of magnetic data, Geophysics, 61(2), 394-408.

Li, Y. and Oldenburg, D.W., (1997), Fast inversion of large scale magnetic data using wavelets, SEG Technical Program Expanded Abstracts 1997, 490-493.

Loke, M.H. and Barker, R.D., (1996), Rapid least-squares inversion of apparent resistivity pseudosections by a quasi-Newton method 1, Geophysical prospecting, 44(1), 131-152.

Loke, M.H., (2011), Electrical resistivity surveys and data interpretation, in Arora, K., Cazenave, A., Engdahl, E.R., Kind, R., Manglik, A., Roy, S., Sain, K. and Uyeda, S., Encyclopedia of solid earth Geophysics, Springer Science & Business Media., 276-283.

Manzi, M., Malehmir, A. and Durrheim, R.J., (2018), Improved Subsurface Imaging through Re-processing of Legacy 2D Seismic Data-A Case Study from a Deep South African Gold Mine, Presented at the 2nd Conference on Geophysics for Mineral Exploration and Mining, EAGE.

Manzi, M.S., Durrheim, R.J., Hein, K.A. and King, N., (2012), 3D edge detection seismic attributes used to map potential conduits for water and methane in deep gold mines in the Witwatersrand basin, South Africa, Geophysics, 77(5), WC133-WC147.

Manzi, MSD, Hunt, J., and Durrheim, R.J., (2019), 3D Reflection Seismic Imaging for Gold and Platinum Exploration, Mine Development, and Safety: Case Studies from the Witwatersrand Basin and Bushveld Complex (South Africa), Ore Deposits: Origin and Exploitation, Geophysical Monograph 242, First Edition. Edited by Sophie Decrée and Laurence Robb, 237-256.

Mare, L.P. (1999), Council for Geoscience, Physical property Database. Data set accessed 20 June 2018 at https://www.geoscience.org.za/index.php/publication/284-geophysical-data

Masante, D., McCormick, N., Vogt, J., Carmona-Moreno, C., Cordano, E., Ameztoy, I., (2018), Drought and Water Crisis in Southern Africa, European Commission, JRC Technical Reports, JRC111596, 1-27.

Maxwell, J.C., (1873), A treatise on electricity and magnetism: Oxford: Clarendon Press, 1.

McCarthy, T., and Rubridge, B., (2013), The story of earth & life: a southern African perspective on a 4.6-billion-year journey, Penguin Random House South Africa, 92-242.

Meqbel, N. and Ritter, O., (2015), Joint 3D inversion of multiple electromagnetic datasets, Geophysical Prospecting, 63(6), 1450-1467.

Mestel, L., (1950), On the thermal conductivity in dense stars, In Mathematical Proceedings of the Cambridge Philosophical Society, Cambridge University Press, 46(2), 331-338.

Mndaweni, S.S.E., Naicker, S. and Blake, D., (2019), Hydrostratigraphy of the Malmani Subgroup dolomites within the northeastern escarpment (Limpopo and Mpumalanga, South Africa), South African Journal of Geology, 122(3), 283-298.

Monteiro Santos, F.A., Afonso, A.R.A. and Dupis, A., (2007), 2D joint inversion of dc and scalar audio-magnetotelluric data in the evaluation of low enthalpy geothermal fields, Journal of Geophysics and Engineering, 4(1), 53-62.

Moorkamp, M., Heincke, B., Jegen, M., Roberts, A.W. and Hobbs, R.W., (2011), A framework for 3-D joint inversion of MT, gravity and seismic refraction data, Geophysical Journal International, 184(1), 477-493.

Moorkamp, M., Jones, A.G. and Fishwick, S., (2010), Joint inversion of receiver functions, surface wave dispersion, and magnetotelluric data, Journal of Geophysical Research: Solid Earth, 115(B4).

Nabighian, M.N., (1987), Electromagnetic methods in applied geophysics: (Volume 1). Theory, Society of Exploration Geophysicists, 5-44.

Nabighian, M.N., (1991), Electromagnetic Methods in Applied Geophysics (Volume 2), Society of Exploration Geophysicists, 641-806.

Naudy, H. and Dreyer, H., (1968), Non-linear filtering applied to aeromagnetic profiles, Geophysical Prospecting, 16(2), 171-178.

Onstott, T.C., Ehlmann, B.L., Sapers, H., Coleman, M., Ivarsson, M., Marlow, J.J., Neubeck, A. and Niles, P., (2019), Paleo-Rock-Hosted Life on Earth and the Search on Mars, A Review and Strategy for Exploration: Astrobiology, 19(10), 1230-1262.

Palacky, G.V., (1987), Resistivity characteristics of geologic targets, Electromagnetic Methods in Applied Geophysics, SEG, 1351.

Park, S.K. and Livelybrooks, D.W., (1989), Quantitative interpretation of rotationally invariant parameters in magnetotellurics, Geophysics, 54(11), 1483-1490.

Pauli, W., (1925), On the connection of the conclusion of the electron groups in the atom with the complex structure of the spectra, Journal of Physics A Hadrons and Nuclei , 31 (1), 765-783.

Pedersen, L.B. and Gharibi, M., (2000), Automatic 1-D inversion of magnetotelluric data, Finding the simplest possible model that fits the data: Geophysics, 65(3), 773-782.

Penrose, R., (1955), A generalized inverse for matrices, In Mathematical proceedings of the Cambridge philosophical society, Cambridge University Press, 51(3), 406-413.

Peter, Y.U. and Cardona, M., (2010), Fundamentals of semiconductors: physics and materials properties, Springer Science & Business Media, 17-105.

Potts, W.M., Götz, A. and James, N., (2015), Review of the projected impacts of climate change on coastal fishes in southern Africa, Reviews in Fish Biology and Fisheries, 25(4), 603-630.

Price, A.T., (1962), The theory of magnetotelluric methods when the source field is considered, Journal of Geophysical Research, 67(5), 1907-1918.

Retief, P.F., (2000), 1:250 000 Geological Series, 2726 Kroonstad, Pretoria: Geological Survey of South Africa.

Rikitake, T., (1948), Notes on the Electromagnetic Induction within the Earth, Bulletin of the Earthquake Research Institute, University of Tokyo, 24(1), 1-9.

Roberts, D.L., Matthews, T., Herries, A.I., Boulter, C., Scott, L., Dondo, C., Mtembi, P., Browning, C., Smith, R.M., Haarhoff, P. and Bateman, M.D., (2011), Regional and global context of the Late Cenozoic Langebaanweg (LBW) palaeontological site: West Coast of South Africa, Earth-Science Reviews, 106(3-4), 191-214.

Rodi, W. and Mackie, R.L. (2001), Nonlinear conjugate gradients algorithm for 2-D magnetotelluric inversion, Geophysics, 66(1), 174-187.

Rozendaal, A., Gresse, P.G., Scheepers, R. and Le Roux, J.P., (1999), Neoproterozoic to early Cambrian crustal evolution of the Pan-African Saldania belt, South Africa, Precambrian research, 97(3-4), 303-323.

Rusley, C., Onstott, T.C., Liang, R., Higgins, J.A., Slater, N.W., Ogasawara, H., Cason, E.D., Sherwood Lollar, B., Wiersberg, T., Zimmer, M. and van Heerden, E., (2018), Exploring the Limits of Life in a South African Deep Subsurface Brine, In AGU 2018 Fall Meeting Abstracts.

Schuster, A., (1889), The diurnal variation of terrestrial magnetism, Philosophical Transactions of the Royal Society of London, 180, 467-518.

Seyler, H., Hay, R., Hartnady, C. and Groenewal, L. (2008), The Assessment of Water Availability in The Berg Catchment (WMA 19) by Means of Water Resource Related Models, Groundwater Model Report Langebaan Road and Elandsfontein Aquifer, 6, 1-138.

Sternberg, B.K., Washburne, J.C. and Anderson, R.G., (1985), Investigation of MT static shift correction methods, In SEG Technical Program Expanded Abstracts 1985, Society of Exploration Geophysicists, 264-267.

Sternberg, B.K., Washburne, J.C. and Pellerin, L., (1988), Correction for the static shift in magnetotellurics using transient electromagnetic soundings, Geophysics, 53(11), 1459-1468.

Steyn, J.H., (1990), 1:250 000 Geological Series, 2430 Pilgrims Rest geological sheet, Pretoria, Geological Survey of South Africa.

Streich, R., Becken, M. and Ritter, O., (2010), Imaging of CO2 storage sites, geothermal reservoirs, and gas shales using controlled-source magnetotellurics: Modeling studies, Chemie Der Erde-Geochemistry, 70, 63-75.

Streich, R., Becken, M. and Ritter, O., (2010), Imaging of CO2 storage sites, geothermal reservoirs, and gas shales using controlled-source magnetotellurics: Modeling studies, Chemie Der Erde-Geochemistry, 70, 63-75.

Stuyfzand, P.J., (1995), The impact of land reclamation on groundwater quality and future drinking water supply in the Netherlands, Water Science and Technology, 31(8), 47-57.

Surkov, V. and Hayakawa, M., (2014), Ionospheric Alfvén Resonator (IAR). In Ultra and Extremely Low Frequency Electromagnetic Fields, Springer, 145-207.

Takai, K.E.N., Moser, D.P., DeFlaun, M., Onstott, T.C. and Fredrickson, J.K., (2001), Archaeal diversity in waters from deep South African gold mines, Applied Environmental Microbiology, 67(12), 5750-5760.

Tankard, A.J. (1976), Pleistocene history and coastal morphology of the Ysterfontein-Eland's Bay area, Cape Province, Annals of the South African Museum 69, 73-119.

Tarits, P., (1994), Electromagnetic studies of global geodynamic processes, Surveys in Geophysics, 15(2), 209-238.

Telford, W.M., Geldart, L.P., and Sheriff, R.E., (2001), Applied geophysics (Vol. 2), Cambridge university press, 283-538.

Theron, J.N. (1990), 1:250 000 Geological Series, 3318 Cape Town geological sheet, Pretoria, Geological Survey of South Africa.

Tietze, K., Ritter, O., Egbert, G. D., (2015), 3-D joint inversion of the magnetotelluric phase tensor and vertical magnetic transfer functions, Geophysical Journal International, 203, 2, 1128-1148.

Tikhonov, A. N. (1950), On determination of electric characteristics of deep layers of the Earth's crust, Doklady Akademii Nauk SSSR, 151, 295-297.

Tikhonov, A.N., (1943), On the stability of inverse problems, Doklady Akademii Nauk SSSR, 39, 195-198.

Tinker, J., De Wit, and M., Grotzinger, J., (2002), Seismic stratigraphic constrained on Neoarchean – Paleoproterozoic evolution of the western margin of the Kaapvaal craton, South Africa, South African Journal of Geology, 105, 107–134.

Van der Westhuizen, W.A., De Bruiyn, H. and Meintjes, P.G., (1991), The Ventersdorp supergroup: an overview, Journal of African Earth Sciences (and the Middle East), 13(1), 83-105.

Van Zijl, J.S.V., (1977), A practical manual on the resistivity method, National Physical Research Laboratory, CSIR Report FIS 142, 132.

Visser, H.N. and Theron, J.N. (1973), 1:250 000 Geological Series, 3218 Clanwilliam geological sheet, Geological Survey of South Africa.

Vozoff, K. and Jupp, D.L.B., (1975), Joint inversion of geophysical data. Geophysical Journal International, 42(3), 977-991.

Vozoff, K., (1991), The magnetotelluric method. In Electromagnetic methods in applied geophysics: Volume 2, application, parts A and B, Society of exploration geophysicists, 641-712.

Weckmann, U., Magunia, A. and Ritter, O., (2005), Effective noise separation for magnetotelluric single site data processing using a frequency domain selection scheme, Geophysical Journal International, 161(3), 635-652.

Wilkinson, K.J., and Coetsee, F., (1986), 1:250 000 Geological Series, 2626 Wes-Rand, Pretoria, Geological Survey of South Africa.

Chapter 8 : Appendix

A.1. Magnetotelluric forward modelling MATLAB code

The following code was developed and used throughout Chapter 3 and Chapter 5. The code is based on the magnetotelluric theory described above. The code allows the forward modelling of the MT response function for a one-dimensional layered case.

```
function MT1DMOD_v2

%%%%%%%%%%%%%%%%%%%%%%%%%%%%%%%%%%%%%%%%%%%%%%%%%%%%%%%%%%%%%%%%%%%%%%%%%%%%%%%
% Wesley Harrison 2017/11/09
% University of the Witwatersrand
% One dimensional MT forward modelling code
%%%%%%%%%%%%%%%%%%%%%%%%%%%%%%%%%%%%%%%%%%%%%%%%%%%%%%%%%%%%%%%%%%%%%%%%%%%%%%%

%%%%%%%%%%%%%%%%%%%%% Variable Index %%%%%%%%%%%%%%%%%%%%%%%%%%%%%%%%%%%%%%%%%
% w         = Angular Frequency (Radians)
% freq      = Frequency band (Hz).
% mu        = Magnetic Permeability (H/m)
% p         = Resistivity of layers
% Ap        = Calculated apparent resistivity
% TH        = Layer thickness
% k         = Wave propagation term.
% ZT        = Surface impedances
% ZL        = Layer impedances
% Zb        = Basement layer impedance
%%%%%%%%%%%%%%%%%%%%%%%%%%%%%%%%%%%%%%%%%%%%%%%%%%%%%%%%%%%%%%%%%%%%%%%%%%%%%%%

%%%%%%%%%%%%%%%%  Inputs and constants %%%%%%%%%%%%%%%%%%%%%%%%%%%%%%%%%%%%%%%
%  freq1  = 15:20:1000;         % Low-range frequency band.
%  freq2  = 1000:300:3000;      % Mid-range frequency band.
%  freq3  = 3000:500:10000;     % High-range frequency band.

freq   = logspace(-2,8,100);    % Consolidate frequency bands into a single long range frequency band.
w      = 2*pi*freq;             % Angular Frequency calculation.
mu     = 4*pi*1E-7;             % Magnetic Permeability calculation.
p      = [100 8000];            % Layer resistivity inputs, shallowest layer first.
TH     = [10];                  % Layer thickness inputs, shallowest layer first.
n      = length(p);             % Number of resistivity values.
Dep    = cumsum(TH);            % layer thicknesses.
%%%%%%%%%%%%%%%%%%%%%%%%%%%%%%%%%%%%%%%%%%%%%%%%%%%%%%%%%%%%%%%%%%%%%%%%%%%%%%%

%%%%%%%%%%%%%%%%%%%%%%%%%%% Initialize %%%%%%%%%%%%%%%%%%%%%%%%%%%%%%%%%%%%%%%
Zb=zeros(1,length(freq));       % Initialize basement impedance matrix.
ZL=zeros(1,length(freq));       % Initialize layer impedance matrix.
ZT=zeros(1,length(freq));       % Initialize surface impedance matrix.
Depth=zeros(1,length(freq));    % Initialize layer depth matrix.
Ap=zeros(1,length(freq));       % Initialize apparent resistivity matrix.
phasee=zeros(1,length(freq));   % Initialize phase matrix.
%%%%%%%%%%%%%%%%%%%%%%%%%%%%%%%%%%%%%%%%%%%%%%%%%%%%%%%%%%%%%%%%%%%%%%%%%%%%%%%

%%%%%%%%%%%%%%%%%%%% calculate impedances %%%%%%%%%%%%%%%%%%%%%%%%%%%%%%%%%%%%

parfor iii=1:length(freq);
                                %
    w1=w(iii);                                                  %
    kb=sqrt(sqrt(-1)*w1*mu*(1/p(n)));                           %
    Zbb=(w1*mu)/kb;                                             % Compute basement impedances using parallel
    Zb(iii)=Zbb;                                                % computing.
                                                                %
    Mon=(iii/length(freq))*100;                                 %
    disp(['Calculating basement impedance ' num2str(Mon) '%']); %
end;


for iii=1:length(freq);                                                 %
    ZL(iii)=Zb(iii);                                                    %
    w1=w(iii);                                                          %
        for jjj=n-1:-1:1;                                               % Compute layer impedances
              k1     =sqrt(sqrt(-1)*w1*mu*(1/p(jjj)));                  % from basement impedances until
              IB     =(acoth((k1*ZL(iii))/(w1*mu))-(sqrt(-1)*k1*Dep(jjj))); % all impedances are calculated.
              OB     =coth(IB);                                         %
              ZT1    =((w1*mu)/k1)*OB;                                  %
            ZL(iii)=ZT1;                                                %
        end;
  ZT(iii)=ZL(iii); % Store surface impedances.

  Mon=(iii/length(freq))*100;
  disp(['Calculating surface impedance ' num2str(Mon) '%']);

end;
%%%%%%%%%%%%%%%%%%%%%%%%%%%%%%%%%%%%%%%%%%%%%%%%%%%%%%%%%%%%%%%%%%%%%%%%%%%%%%%

%%%%%%%%%%%%%%%%%%%% calculate apparent resistivity %%%%%%%%%%%%%%%%%%%%%%%%%%
```

```
parfor iii=1:length(freq);                                  %
    Zt1=ZT(iii);                                            %
    w1=w(iii);                                              % Compute observed apparent resistivity values at
                    absZt=abs(Zt1);                         % different frequencies.
                    App=(1/(w1*mu))*(absZt*absZt);          %
    Ap(iii)=App;                                            % Store apparent resistivity values.

    Mon=(iii/length(freq))*100;
    disp(['Calculating apparent resistivity ' num2str(Mon) '%']);

end;
%%%%%%%%%%%%%%%%%%%%%%%%%%%%%%%%%%%%%%%%%%%%%%%%%%%%%%%%%%%%%%%%%%%%%%%%%%%%%%%

%%%%%%%%%%%%%%%%%%%%%%%%%% Phase Lead EF%%%%%%%%%%%%%%%%%%%%%%%%%%%%%%%%%%%%%%
parfor iii=1:length(freq);                          %
    Zt1=ZT(iii);                                    % Compute phase values at different frequencies.

                phase1=-atan(imag(Zt1)/real(Zt1))*57.2958;
    phasee(iii)=phase1; % Store phase values.

    Mon=(iii/length(freq))*100;
    disp(['Calculating phase ' num2str(Mon) '%']);
end;

%%%%%%%%%%%%%%%%%%%%%%%%%% Skin Depth %%%%%%%%%%%%%%%%%%%%%%%%%%%%%%%%%%%%%%%%
SkinDepth=zeros(n,1);

parfor III=1:1:length(freq);
       SkinDepth(III)=sqrt(Ap(III)/(mu*w(III)));
end;


%%%%%%%%%%%%%%%%%%%%%%%%%% Plotting Data %%%%%%%%%%%%%%%%%%%%%%%%%%%%%%%%%%%%%%
subplot(3,1,1);
plot(freq,Ap,'color','k');hold on;scatter(freq,Ap,'fill','k');
set(gca, 'YScale', 'log')
set(gca, 'XScale', 'log')
xlabel('Frequency (Hz)','fontsize',25);
ylabel('Apparent Resistivity (ohm.m)','fontsize',25);
title('Apparent Resistivity','fontsize',25);hold on;
set(gca,'fontsize',15);
set(gca, 'XDir','reverse')
grid on;
grid minor

subplot(3,1,2);
plot(freq,phasee,'color','b');hold on;scatter(freq,phasee,'fill','b');hold off;
ylabel('Phase (Degrees)','fontsize',25);
title('Apparent Phase Plotted','fontsize',25);hold on;
set(gca,'fontsize',15);
set(gca, 'XScale', 'log')
set(gca, 'XDir','reverse')
grid on;
grid minor

ZZ=cumsum(TH);
ZZ=[0 ZZ max(ZZ)+max(ZZ)*2];
PP=[p p(length(p))];
subplot(3,1,3);
stairs(ZZ,PP,'r','LineWidth',2);
% set(gca, 'XScale', 'log')
set(gca, 'YScale', 'log')
title('1-D Resistivity Model','fontsize',25);
xlabel('Depth (m)','fontsize',25);
ylabel('Resistivity (ohm.m)','fontsize',25);
ylim([0 max(PP)]);
grid on;
grid minor
set(gca,'fontsize',15);
axis tight;
%%%%%%%%%%%%%%%%%%%%%%%%%%%%%%%%%%%%%%%%%%%%%%%%%%%%%%%%%%%%%%%%%%%%%%%%%%%%%%%

%%%%%%%%%%%%%%%%%%%%%%%%%%%%%% Saving Data %%%%%%%%%%%%%%%%%%%%%%%%%%%%%%%%%%%%
disp('Saving data.');
save('MTData','Ap','freq','w','phasee','ZT','p','TH','SkinDepth');
AP2=Ap';
FREQ2=(freq');
PHASE2=phasee';
save('MTData_L','AP2','FREQ2','PHASE2');
disp('completed.');

L_EDI=[FREQ2 AP2 PHASE2 AP2 PHASE2];
L_EDI=L_EDI';

N=length(freq);
Freq=reshape(freq,[5 N/5]);
APP=reshape(Ap,[5 N/5]);
PH=reshape(phasee,[5 N/5]);
err=zeros(length(Freq(:,1)),length(Freq(1,:)));

Filedate =date;
FN=sprintf('MT_1D.EDI');

fid = fopen(FN,'w');
fprintf(fid,'>HEAD \r\n');
fprintf(fid,'DATAID="1" \r\n');
fprintf(fid,'FILEBY="" \r\n');
fprintf(fid,'ACQDATE=05/01/19 \r\n');
```

```
fprintf(fid,'FILEDATE=05/01/19 \r\n');
fprintf(fid,'PROSPECT="Test" \r\n');
fprintf(fid,'LOC="Test" \r\n');
fprintf(fid,'LAT=-27:02:01.2323 \r\n');
fprintf(fid,'LONG=26:37:18.5726 \r\n');
fprintf(fid,'ELEV=0 \r\n');
fprintf(fid,'STDVERS="SEG 1.0" \r\n');
fprintf(fid,'PROGVERS="WINGLINK EDI 1.0.22" \r\n');
fprintf(fid,'PROGDATE=04/23/02 \r\n');
fprintf(fid,'MAXSECT=999 \r\n');
fprintf(fid,'EMPTY=1.0e+32 \r\n');
fprintf(fid,'\r\n');
fprintf(fid,'>INFO \r\n');
fprintf(fid,'MAXINFO=999 \r\n');
fprintf(fid,'SURVEY ID:Test \r\n');
fprintf(fid,'SURVEY CO: \r\n');
fprintf(fid,'CLIENT CO: \r\n');
fprintf(fid,'AREA:Test \r\n');
fprintf(fid,'ROTATION= \r\n');
fprintf(fid,'\r\n');

fprintf(fid,'>=DEFINEMEAS \r\n');
fprintf(fid,'MAXCHAN=7 \r\n');
fprintf(fid,'MAXRUN=999 \r\n');
fprintf(fid,'MAXMEAS=9999 \r\n');
fprintf(fid,'UNITS=M \r\n');
fprintf(fid,'REFTYPE=CART \r\n');
fprintf(fid,'REFLOC="1" \r\n');
fprintf(fid,'REFLAT=-27:02:01.2323 \r\n');
fprintf(fid,'REFLONG=26:37:18.5726 \r\n');
fprintf(fid,'REFELEV=0 \r\n');
fprintf(fid,'>HMEAS ID=101.001 CHTYPE=HX X=0.0 Y=0.0 Z=0.0 AZM=0.0  \r\n');
fprintf(fid,'>HMEAS ID=102.001 CHTYPE=HY X=0.0 Y=0.0 Z=0.0 AZM=90.0  \r\n');
fprintf(fid,'>HMEAS ID=103.001 CHTYPE=HZ X=0.0 Y=0.0 Z=0.0 AZM=0.0  \r\n');
fprintf(fid,'>EMEAS ID=104.001 CHTYPE=EX X=0.0 Y=0.0 Z=0.0 X2=0.0 Y2=0.0 Z2=0.0  \r\n');
fprintf(fid,'>EMEAS ID=105.001 CHTYPE=EY X=0.0 Y=0.0 Z=0.0 X2=0.0 Y2=0.0 Z2=0.0  \r\n');
fprintf(fid,'>HMEAS ID=106.001 CHTYPE=HX X=0.0 Y=0.0 Z=0.0 AZM=0.0  \r\n');
fprintf(fid,'HMEAS ID=107.001 CHTYPE=HY X=0.0 Y=0.0 Z=0.0 AZM=90.0  \r\n');
fprintf(fid,'\r\n');

fprintf(fid,'>=MTSECT \r\n');
fprintf(fid,'SECTID="1" \r\n');
fprintf(fid,'NFREQ=%.0f \r\n',N);
fprintf(fid,'HX=101.001 \r\n');
fprintf(fid,'HY=102.001 \r\n');
fprintf(fid,'HZ=103.001 \r\n');
fprintf(fid,'EX=104.001 \r\n');
fprintf(fid,'EY=105.001 \r\n');
fprintf(fid,'RX=106.001 \r\n');
fprintf(fid,'RY=107.001 \r\n');
fprintf(fid,'\r\n');


fprintf(fid,'>!****FREQUENCIES****! \r\n');
fprintf(fid,'>FREQ //%.0f \r\n',N);
fprintf(fid,'  %8e %8e %8e %8e %8e \r\n',Freq);
fprintf(fid,'>!****APPARENT RESISTIVITIES AND PHASES****! \r\n');
fprintf(fid,'>RHOXY ROT=RHOROT //%.0f \r\n',N);
fprintf(fid,'  %8e %8e %8e %8e %8e \r\n',APP);
fprintf(fid,'>RHOXY.ERR ROT=RHOROT //%.0f \r\n',N);
fprintf(fid,'  %8e %8e %8e %8e %8e \r\n',err);
fprintf(fid,'>RHOYX ROT=RHOROT //%.0f \r\n',N);
fprintf(fid,'  %8e %8e %8e %8e %8e \r\n',APP);
fprintf(fid,'>RHOYX.ERR ROT=RHOROT //%.0f \r\n',N);
fprintf(fid,'  %8e %8e %8e %8e %8e \r\n',err);
fprintf(fid,'>PHSXY ROT=RHOROT //%.0f \r\n',N);
fprintf(fid,'  %8e %8e %8e %8e %8e \r\n',PH);
fprintf(fid,'>PHSXY.ERR ROT=RHOROT //%.0f \r\n',N);
fprintf(fid,'  %8e %8e %8e %8e %8e \r\n',err);
fprintf(fid,'>PHSYX ROT=RHOROT //%.0f \r\n',N);
fprintf(fid,'  %8e %8e %8e %8e %8e \r\n',PH);
fprintf(fid,'>PHSYX.ERR ROT=RHOROT //%.0f \r\n',N);
fprintf(fid,'  %8e %8e %8e %8e %8e \r\n',err);
fprintf(fid,'\r\n');

fprintf(fid,'>END');
fclose(fid);%%%%%%%%%%%%%%%%%%%%%%%%%%%%%%%%%%%%%%%%%%%%%%%%%%%%%%%%%%%%%%%%%%%%%%%%%%%
%%%%%%%%%%%%%%%%%%%%%%%%%%%%%%%%%%%%%%%%%%%%%%%%%%%%%%%%%%%%%%%%%%%%%%%%%%%
```

A.2. Magnetotelluric inversion modelling MATLAB code

A.2.1. Constrained tandem random model generator one dimensional magnetotelluric layer resistivity least squares damped weighted inversion MatLab code

This code is used in Chapter 2. This code makes use of the one-dimensional MT forward modelling code described in appendix A.1. to generate two sets of random models that attempt to fit the observed data by randomising layer resistivity only. The first set of random models can vary an order of magnitude more than the second set of random models. Once the first set of random models is calculated the best fitting model is used in the second set of random model calculations to improve the fit of calculated MT response function with the observed MT response function.

```
function MT1DINV_Resistivity
% Wesley Harrison 2017
% University of the Witwatersrand
% Constrained tandem random model generator one dimensional magnetotelluric
% layer resistivity least squares damped weighted inversion code

%%%%%%%%%%%%%%%%%%%% Variable Index %%%%%%%%%%%%%%%%%%%%%%%%%%%%%%%%%%%%%%%%

% AI            = Area of interest (m)
% Ap            = Calculated apparent resistivity
% Cell          = Number of model layers
% D             = Observed data
% Dep           = layer depths
% freq          = Frequency
% FRMG          = Number of fine random models to generate
% Iterations    = Number of iterations to run
% M             = Layer resistivities
% Max           = Maximum resistivity allowed in the conductivity model
% Mii           = Starting model resistivity half space
% Min           = Minimum resistivity allowed in the conductivity model
% mu            = Magnetic Permeability (H/m)
% Padding       = Number of model padding layers
% RA1           = Rough random model generator random value range in Ω·m
% RA2           = Fine random model generator random value range in Ω·m
% RA3           = Inversion random model generator random value range in Ω·m
% RMS           = Root mean square error
% RRMG          = Number of rough random models to generate
% RS            = Rough random model generator smoothing window
% THH           = Layer thicknesses
% w             = Angular Frequency (Radians)

%%%%%%%%%%%%%%%%%%%%%%%%%%%%%%%%%%%%%%%%%%%%%%%%%%%%%%%%%%%%%%%%%%%%%%%%%%%%

%%%%%%%%%%%%%%%%%%%%%%%%%%% Inputs %%%%%%%%%%%%%%%%%%%%%%%%%%%%%%%%%%%%%%%%%

load('MTData.mat')
D           =Ap';
D           =awgn(D,10,'measured');
freq        =freq';
AI          =300;
THF         =100;
Mii         =4000;
Iterations  =8000;
w           =(2*pi*freq);
mu          = 4*pi*1E-7;
MAX         =5000;
```

```
MIN          =1;
RRMG         =400;
RA1          =4000;
FRMG         =400;
RA2          =100;
RA3          =10;
RS           =20;

%%%%%%%%%%%%%%%%%%%%%%%%%%% Initialise %%%%%%%%%%%%%%%%%%%%%%%%%%%%%%%%%%%%%%%

MP=p';
MTH=[0;TH'];
MD=cumsum(MTH);
Cell=(AI/THF)+1;
Padding=Cell+6;
n=Padding;
TH=zeros(Padding,1);

%%%%%%%%%%%%%%%%%%%%%%%%%%% Area of Interest
for LLL=1:1:Cell;    %
    TH1=THF;         % Order layers for area of interest
    TH(LLL)=TH1;     %
end;

%%%%%%%%%%%%%%%%%%%%%%%%%%% Padding
for LLL=Cell:1:Padding;      %
    TH1=TH(LLL-1)+2000;      % Insert padding layers
    TH(LLL)=TH1;             %
end;

%%%%%%%%%%%%%%%%%%%%%%%%%%% Starting Model
Mi         = zeros(n+1,1);
for LLL=1:1:n+1;         %
    Mii1=Mii;            % Create starting model half space
    Mi(LLL)=Mii1;        %
end;

RMS=zeros(1,Iterations+1);
f=length(freq);
M=zeros(length(Mi),Iterations+1);
AP=zeros(length(D),Iterations);

%%%%%%%%%%%%%%%%%%%%%%%%%%%%%%%%%%%%%%%%%%%%%%%%%%%%%%%%%%%%%%%%%%%%%%%%%%%%%%%

%%%%%%%%%%%%%%%%%%%%%%%%%% Random model generator 1%%%%%%%%%%%%%%%%%%%%%%%%%%
r1=randi([-RA1,RA1],length(Mi)-1,RRMG); %
                                        %
G=Mi;                                   %
G(length(Mi))=[];                       %
G=repmat(G,1,RRMG);                     % Calculate and order rough random
MC=r1+G;                                % models
A=Mi(length(Mi));                       %
A=repmat(A,1,RRMG);                     %
MC=[MC;A];                              %



for NNN=1:1:length(G(:,1));                 %
                                            %
          for KKK=1:1:length(G(1,:));       % Check if random models are
                if  MC(NNN,KKK)<MIN;        % within the maximum and minimum
                    MC(NNN,KKK)=Mi(NNN);    % resistivity values
            elseif  MC(NNN,KKK)>MAX;        %
                    MC(NNN,KKK)=Mi(NNN);    %
                                            %
              end;
          end;
end;


for TTT=1:1:RRMG;
    MCS=smooth(MC(:,TTT),'moving',RS);      % Smooth random models
    MC(:,TTT)=MCS;
end;

%%%% Forward model random models and calculate the RMS value for each model

APR=zeros(length(D),RRMG);

for AAA=1:1:RRMG;
      Zb=zeros(1,length(D));
            Zt=zeros(1,length(D));
            ZL=zeros(length(D),length(Mi));
            ZT=zeros(1,length(D));

           n=length(MC(:,1));
            Dep=cumsum(TH);

            for xxx=1:f;
            w1=w(xxx);
            kb=sqrt(sqrt(-1)*w1*mu*(1/MC(n,AAA)));
            Zbb=(w1*mu)/kb;
            Zb(xxx)=Zbb;
            end;

            for xxx=1:f;
                Zt(xxx)=Zb(xxx);
                w1=w(xxx);
```

```
                    for jjj=n-1:-1:1;
                          k1     =sqrt(sqrt(-1)*w1*mu*(1/MC(jjj,AAA)));
                          IB     =(acoth((k1*Zt(xxx))/(w1*mu))-(sqrt(-1)*k1*Dep(jjj)));
                          OB     =coth(IB);
                          ZT1    =((w1*mu)/k1)*OB;
                        Zt(xxx)=ZT1;
                        ZL(:,jjj) =ZT1;
                    end;
               ZT(xxx)=Zt(xxx);
            end;

            for xxx=1:f;
                Zt1=ZT(xxx);
                w1=w(xxx);
                                  absZt=abs(Zt1);
                                  App=(1/(w1*mu))*(absZt*absZt);
                APR(xxx,AAA)=(App);
            end;
     IT=(AAA);
                disp(['Rough Random Model: ' num2str(IT) ]);


end;

RMSR=zeros(1,RRMG);

for LLL=1:1:RRMG;

   RMSRI = sqrt((1/length(D))*(sum((D-APR(:,LLL)).^2)));
   RMSR(LLL)=RMSRI;
end;

%%%%%%%%%%%%%%%%%%%%%%%%%%%%%%%%%%%%%%%%%%%%%%%%%%%%%%%%%%%%%%%%%%%%%%%%%%%%%%%

%%%%%% Plot random models against model RMSE
[ER,BM] = min(RMSR(:));
figure(1);clf;
scatter(1:1:RRMG,RMSR,'filled');
xlabel('Random Model');
ylabel('RMS Error');
title('Generated Random Models RMS Errors ');hold on;
%%%%%%

 M1=MC(:,BM); % Best rough random model is chosen based on RMSE

%%%%%%%%%%%%%%%%%%%%%%%%%%%%%%%%%%%%%%%%%%%%%%%%%%%%%%%%%%%%%%%%%%%%%%%%%%%%%%%

%%%%%%%%%%%%%%%%%%%%%%%%%% Random model generator 2%%%%%%%%%%%%%%%%%%%%%%%%%%
r2=randi([-RA2,RA2],length(Mi)-1,FRMG);      %
                                             %
G2=M1;                                       %
G2(length(M1))=[];                           % Calculate and order fine random
G2=repmat(G2,1,FRMG);                        % models
MC2=r2+G2;                                   %
A=Mi(length(Mi));                            %
A=repmat(A,1,FRMG);                          %
MC2=[MC2;A];                                 %

for NNN=1:1:length(G2(:,1));

          for KKK=1:1:length(G2(1,:));       %
                if  MC2(NNN,KKK)<MIN;        % Check if random models are
                    MC2(NNN,KKK)=Mi(NNN);    % within the maximum and minimum
            elseif  MC2(NNN,KKK)>MAX;        % resistivity values
                    MC2(NNN,KKK)=Mi(NNN);    %

              end;
          end;
end;
%%%% Forward model random models and calculate the RMS value for each model

APR=zeros(length(D),FRMG);

for AAA=1:1:FRMG;
      Zb=zeros(1,length(D));
            Zt=zeros(1,length(D));
            ZL=zeros(length(D),length(Mi));
            ZT=zeros(1,length(D));

           n=length(MC2(:,1));
            Dep=cumsum(TH);

            for xxx=1:f;
            w1=w(xxx);
            kb=sqrt(sqrt(-1)*w1*mu*(1/MC2(n,AAA)));
            Zbb=(w1*mu)/kb;
            Zb(xxx)=Zbb;
            end;

            for xxx=1:f;
                Zt(xxx)=Zb(xxx);
                w1=w(xxx);
                    for jjj=n-1:-1:1;
                          k1     =sqrt(sqrt(-1)*w1*mu*(1/MC2(jjj,AAA)));
                          IB     =(acoth((k1*Zt(xxx))/(w1*mu))-(sqrt(-1)*k1*Dep(jjj)));
                          OB     =coth(IB);
                          ZT1    =((w1*mu)/k1)*OB;
                        Zt(xxx)=ZT1;
```

```
                        ZL(:,jjj) =ZT1;
                    end;
              ZT(xxx)=Zt(xxx);
            end;

            for xxx=1:f;
                Zt1=ZT(xxx);
                w1=w(xxx);
                                absZt=abs(Zt1);
                                App=(1/(w1*mu))*(absZt*absZt);
                APR(xxx,AAA)=(App);
            end;
          IT=(AAA);
                disp(['Refined Random Model: ' num2str(IT) ]);


end;

RMSR2=zeros(1,FRMG);

for LLL=1:1:FRMG;

   RMSRI = sqrt((1/length(D))*(sum((D-APR(:,LLL)).^2)));
   RMSR2(LLL)=RMSRI;
end;
%%%%%%%%%%%%%%%%%%%%%%%%%%%%%%%%%%%%%%%%%%%%%%%%%%%%%%%%%%%%%%%%%%%%%%%%%%%%%%%

%%%%%% Plot random models against model RMSE

[ER2,BM2] = min(RMSR2(:));
figure(1);
scatter(1:1:FRMG,RMSR2,'filled','r');legend('Rough Random Model','Refined Random Model');

if ER>ER2;
text2=['Best Model RMS: ',num2str(ER)];
text(BM2,ER2,text2);
elseif ER<ER2;
text2=['Best Model RMS: ',num2str(ER)];
text(BM,ER,text2);
end;
hold off;
%%%%%% Best random model is chosen based on RMSE
if ER>ER2;
 M(:,1)=MC2(:,BM2);
 RMS(1)=ER2;
elseif ER<ER2;
     M(:,1)=MC(:,BM);
 RMS(1)=ER;
end;
%%%%%

%%%%%%%%%%%%%%%%%%%%%%%%%%%% Inversion %%%%%%%%%%%%%%%%%%%%%%%%%%%%%%%%%%%%%%
for III=1:1:Iterations;
          %%%%%%%%%%%%%%%%%%%%%%%%%%%%%% Calculated model response
            Zb=zeros(1,length(D));
            Zt=zeros(1,length(D));
            ZL=zeros(length(D),length(Mi));
            ZT=zeros(1,length(D));

            n=length(Mi);
            Dep=cumsum(TH);

            for xxx=1:length(freq);
            w1=w(xxx);
            kb=sqrt(sqrt(-1)*w1*mu*(1/M(n,III)));
            Zbb=(w1*mu)/kb;
            Zb(xxx)=Zbb;
            end;

            k=zeros(n-1,length(freq));


            for xxx=1:length(freq);
                Zt(xxx)=Zb(xxx);
                w1=w(xxx);
                    for jjj=n-1:-1:1;
                          k1     =sqrt(sqrt(-1)*w1*mu*(1/M(jjj,III)));
                          IB     =(acoth((k1*Zt(xxx))/(w1*mu))-(sqrt(-1)*k1*Dep(jjj)));
                          OB     =coth(IB);
                          ZT1    =((w1*mu)/k1)*OB;

                        k(jjj,III)=k1;
                        Zt(xxx)=ZT1;
                        ZL(:,jjj) =ZT1;
                    end;
              ZT(xxx)=Zt(xxx);
            end;

            for xxx=1:length(freq);
                Zt1=ZT(xxx);
                w1=w(xxx);
                                absZt=abs(Zt1);
                                App=(1/(w1*mu))*(absZt*absZt);
                AP(xxx,III)=(App);
            end;

        %%%%%%%%%%%%%%%%%%%%%%%%%%%%%% Calculate sensitivity matrix
        J=zeros(length(D),length(Mi));
```

```
        for KKK=1:1:length(Mi);
            for kkk=1:1:length(D);
                J1=(2*ZT(kkk))/sqrt(AP(KKK,III)*mu*w(KKK));
                J(kkk,KKK)=J1;
            end;
        end;
        JT=J';

        %%%%%%%%%%%%%%%%%%%%%%%%%%%%%% Calculate dampening  matrix
        if III==1;
            Damp=real(sqrt((sum(J))))';
        end;

        EYE=eye(length(Mi));
        DAMP=zeros(length(Mi),length(Mi));

        for KKK=1:1:length(Mi);
            DAMP1=Damp(KKK)*EYE(KKK,KKK);
            DAMP(KKK,KKK)=DAMP1;
        end;


         %%%%%%%%%%%%%%%%%%%%%%%%%%%%%% Calculate weighted matrix

         W=zeros(length(D),length(Mi));
         WW=zeros(length(D),1);

         for BBB=1:1:length(D);
             w1=100/AP(BBB,III);
             WW(BBB)=w1;
         end;

         for TTT=1:1:length(Mi);
             W(:,TTT)=WW;
         end;
         WT=W';
        %%%%%%%%%%%%%%%%%%%%%%%%%%%% Least square weighted damped inversion

                  DE=D-AP(:,III);
                  I1=JT*W*WT*J+DAMP;
                  INVI1=inv(I1);
                  I2=JT*W*WT*DE;
                  Mrec=INVI1*I2;

                  Mrec1=Mrec; % Model change vector

         M(:,III+1)=M(:,III)+(Mrec1);
         RMS(III+1)=sqrt((1/length(D))*(sum((D-AP(:,III)).^2)));

        %%%%%%%%%%%%%%%%%%%%%%%%%%%%%% Layer resistivity constraints

              if RMS(III+1)>RMS(III);

                        DAMP=DAMP*2;
                       M(:,III+1)=M(:,III);

              elseif RMS(III+1)<RMS(III);
                        DAMP=DAMP/2;

              else RMS(III+1)=RMS(III);
                    DAMP=DAMP*2;
                   [err,Mod] = min(RMS(RMS>0));
                   RR=randi([-RA3,RA3],length(Mi)-1,1);
                   RR=[RR;0];
                   M(:,III+1)=M(:,Mod)+RR;
              end;


            IT=(III);
                disp(['Iteration: ' num2str(IT) ' out of ' num2str(Iterations)]);

     for NNN=1:1:length(M(:,1));
            if  M(NNN,III+1)<0;
                M(NNN,III+1)=M(NNN,III);
            end;
     end;

     for NNN=1:1:length(M(:,1));
                if  M(NNN,III+1)<MIN;
                    M(NNN,III+1)=M(NNN,III);
            elseif  M(NNN,III+1)>MAX;
                    M(NNN,III+1)=M(NNN,III);

              end;
     end;
     if RMS(III+1)==0;
         break
     end;
 end;
%%%%%%%%%%%%%%%%%%%%%%%%%%%%%%%%%%%%%%%%%%%%%%%%%%%%%%%%%%%%%%%%%%%%%%%%%%%%%%%%

%%%%%%%%%%%%%%%%%%%%%%%%% Plots %%%%%%%%%%%%%%%%%%%%%%%%%%%%%%%%%%%%%%%%%%%%%%%
TH1=TH;
TH1=[0;TH1];
Depths=cumsum(TH1);
Depths=Depths(1:Cell);
```

```
[ERR,ERII] = min(RMS(:));

ITT=ERII-1;
ER=ERR;
RessS=Mi;
RessS=RessS(1:Cell);
RESS1=M(:,Iterations+1);
RESS1=RESS1(1:Cell);
RESS2=M(:,ERII);
RESS2=RESS2(1:Cell);
RESS3=M(:,1);
RESS3=RESS3(1:Cell);


P=(1./freq);
PL=log(P);
RMS(1)=[];
figure(2);clf;subplot(3,1,1);scatter(PL,D,8,'fill','r');hold on;
subplot(3,1,1);plot(PL,AP(:,IT),'color','b');
xlabel('Log Period (s)');
ylabel('Apparent Resistivity (ohm.m)');
legend('Observed data','Calculated data');
title('Apparent Resistivity Comparison Between Collected Data and Calculated Data ','fontsize',15);

subplot(3,1,2);plot(1:1:IT,RMS(:,1:1:IT));
xlabel('Iterations');
ylabel('RMS Error');
title('RMSE Tracker');

subplot(3,1,3);
stairs(Depths,RESS1,'b');hold on;stairs(Depths,RESS3,'r','LineStyle','--');hold on;
stairs(MD,MP,'g');hold on;stairs(Depths,RessS,'c','Marker','*');

xlabel('Depth (m)');
ylabel('Apparent Resistivity (ohm.m)');
title('Final Inverted Model');
legend('Final Inverted Model','Best Random Model','Actual Model','Starting Model');

figure(3);clf;

subplot(2,1,1);scatter(PL,D,8,'fill','r');hold on;plot(PL,AP(:,ITT),'color','b');
xlabel('Log Period (s)');
ylabel('Apparent Resistivity (ohm.m)');
legend('Observed data','Calculated data');
title(['Best Calculated Model: Iteration ' num2str(ITT) ' RMSE ' num2str(ER)] ,'fontsize',15);


subplot(2,1,2);
stairs(Depths,RESS2,'b');
xlabel('Depth (m)');
ylabel('Apparent Resistivity (ohm.m)');
title('Best Inverted Model');hold on;stairs(Depths,RESS3,'r','LineStyle','--');hold on;
stairs(MD,MP,'g');hold on;stairs(Depths,RessS,'c','Marker','*');

legend('Best Inverted Model','Best Random Model','Actual Model','Starting Model');


hold off;
```

A.2.2. Constrained tandem random model generator one dimensional magnetotelluric layer thickness least squares damped weighted inversion MatLab code

This code is used in Chapter 2. This code makes use of the one-dimensional MT forward modelling code described in appendix A.1. to generate two sets of random models that attempt to fit the observed data by randomising layer thickness only. The first set of random models can vary an order of magnitude more than the second set of random models. Once the first set of random models is calculated the best fitting model is used in the second set of random model calculations to improve the fit of calculated MT response function with the observed MT response function.

```
function MT1DINV_Thickness
% Wesley Harrison 2017
% University of the Witwatersrand
% Constrained tandem random model generator one dimensional magnetotelluric
% layer thickness least squares damped weighted inversion code

%%%%%%%%%%%%%%%%%%%% Variable Index %%%%%%%%%%%%%%%%%%%%%%%%%%%%%%%%%%%%%%%%

% AI            = Area of interest (m)
% Ap            = Calculated apparent resistivity
% Cell          = Number of model layers
% DA            = Observed apparent resistivity data
% DP            = Observed phase data
% Dep           = layer depths
% freq          = Frequency
% FRMG          = Number of fine random models to generate
% Iterations    = Number of iterations to run
% M             = Layer resistivities
% Mii           = Starting model resistivity half space
% mu            = Magnetic Permeability (H/m)
% Padding       = Number of model padding layers
% phasee        = Phase
% RA1           = Rough random model generator random value range in Ω·m
% RA2           = Fine random model generator random value range in Ω·m
% RA3           = Inversion random model generator random value range in Ω·m
% RMSP           = Root mean square error
% RRMG          = Number of rough random models to generate
% RS            = Rough random model generator smoothing window
% THH           = Layer thicknesses
% w             = Angular Frequency (Radians)

%%%%%%%%%%%%%%%%%%%%%%%%%%%%%%%%%%%%%%%%%%%%%%%%%%%%%%%%%%%%%%%%%%%%%%%%%%%%

%%%%%%%%%%%%%%%%%%%%%%%%%% Inputs %%%%%%%%%%%%%%%%%%%%%%%%%%%%%%%%%%%%%%%%%%
load('MTData.mat');


DA          =Ap';
DP          = phasee';
DP          =awgn(DP,10,'measured');% Add white Gaussian noise
freq       = freq';
MP=p';
MTH=[0;TH'];
MD=cumsum(MTH);

THF=80;
Cell=3;
```

```
Padding=Cell+4;

Iterations =3000;
w    =(2*pi*freq);
mu   = 4*pi*1E-7;
RMSP=zeros(1,Iterations+1);
RV1=4000;
RA1=100;
RV2=4000;
RA2=10;
RA3=2;

%%%%%%%%%%%%%%%%%%%%%%%%%%%%%%%%%%%%%%%%%%%%%%%%%%%%%%%%%%%%%%%%%%%%%%%%%%%%%%%

%%%%%%%%%%%%%%%%%%%%%%%%%%% Initialise %%%%%%%%%%%%%%%%%%%%%%%%%%%%%%%%%%%%%%%

f=length(freq);
n=Padding;
TH=zeros(Padding,1);

%%%%%%%%%%%%%%%%%%%%%%%%%%% Area of Interest
for LLL=1:1:Cell;        %
    TH1=THF;             % Order layers for area of interest
    TH(LLL)=TH1;         %
end;

%%%%%%%%%%%%%%%%%%%%%%%%%%% Padding
for LLL=Cell+1:1:Padding; %
    TH1=TH(LLL-1)+100;    % Insert padding layers
    TH(LLL)=TH1;          %
end;

%%%%%%%%%%%%%%%%%%%%%%%%%%% Starting Model
Mi=[500 800 500 1000 1000 1000 1000 1000]; % Create starting model half space

THH=zeros(length(Mi)-1,Iterations+1);
AP=zeros(length(DA),Iterations);
Phase=zeros(length(DA),Iterations);
EYEb=eye(length(Mi)-1);
Mrec1QC=zeros(length(Mi),Iterations);
Mrec2QC=zeros(length(Mi)-1,Iterations);

%%%%%%%%%%%%%%%%%%%%%%%%%%%%%%%%%%%%%%%%%%%%%%%%%%%%%%%%%%%%%%%%%%%%%%%%%%%%%%%

%%%%%%%%%%%%%%%%%%%%%%%%%%% Random model generator 1%%%%%%%%%%%%%%%%%%%%%%%%%%
r1=randi([-RA1,RA1],length(Mi)-1,RV1);  %
G=TH;                                   % Calculate and order rough random
G=repmat(G,1,RV1);                      % models
MC=r1+G;                                %


for NNN=1:1:length(G(:,1));                 %
                                            %
          for KKK=1:1:length(G(1,:));       % Check if random models have
                if  MC(NNN,KKK)<0;          % zero layer thickness
                    MC(NNN,KKK)=Mi(NNN);    %
                end;                        %
                                            %
          end;                              %
end;

%%%% Forward model random models and calculate the RMS value for each model

APR=zeros(length(DA),RV1);

for AAA=1:1:RV1;
      Zb=zeros(1,length(DA));
            Zt=zeros(1,length(DA));
            ZL=zeros(length(Mi),length(DA));
            ZT=zeros(1,length(DA));

           n=length(MC(:,1));
            Dep=cumsum(MC(:,AAA));

            for xxx=1:f;
            w1=w(xxx);
            kb=sqrt(sqrt(-1)*w1*mu*(1/Mi(n)));
            Zbb=(w1*mu)/kb;
            Zb(xxx)=Zbb;
            end;

            for xxx=1:f;
                Zt(xxx)=Zb(xxx);
                w1=w(xxx);
                    for jjj=n-1:-1:1;
                          k1     =sqrt(sqrt(-1)*w1*mu*(1/Mi(jjj)));
                          IB     =(acoth((k1*Zt(xxx))/(w1*mu))-(sqrt(-1)*k1*Dep(jjj)));
                          OB     =coth(IB);
                          ZT1    =((w1*mu)/k1)*OB;
                        Zt(xxx)=ZT1;
                        ZL(jjj,xxx) =ZT1;
                    end;
              ZT(xxx)=Zt(xxx);
            end;

            for xxx=1:f;
                Zt1=ZT(xxx);
```

```
                w1=w(xxx);
                                absZt=abs(Zt1);
                                App=(1/(w1*mu))*(absZt*absZt);
                APR(xxx,AAA)=(App);
            end;


     IT=(AAA);
                disp(['Rough Random Model: ' num2str(IT) ]);


end;

RMSR=zeros(1,RV1);

for LLL=1:1:RV1;

   RMSRI = sqrt((1/length(DA))*(sum((DA-APR(:,LLL)).^2)));
   RMSR(LLL)=RMSRI;
end;
%%%%%%%%%%%%%%%%%%%%%%%%%%%%%%%%%%%%%%%%%%%%%%%%%%%%%%%%%%%%%%%%%%%%%%%%%%%%%%%

%%%%%% Plot random models against model RMSE

[ER,BM] = min(RMSR(:));
figure(1);clf;
scatter(1:1:RV1,RMSR,'filled');
xlabel('Random Model');
ylabel('RMS Error');
title('Generated Random Models RMS Errors ');hold on;
%%%%%%


 M1=MC(:,BM); % Best rough random model is chosen based on RMSE

%%%%%%%%%%%%%%%%%%%%%%%%%%%%%%%%%%%%%%%%%%%%%%%%%%%%%%%%%%%%%%%%%%%%%%%%%%%%%%%

%%%%%%%%%%%%%%%%%%%%%%%%%%%%%%%% Random model generator 2%%%%%%%%%%%%%%%%%%%%%%%%%%
r2=randi([-RA2,RA2],length(Mi)-1,RV2);       %
                                              %
G2=M1;                                        % Calculate and order fine random
G2=repmat(G2,1,RV2);                          % models
MC2=r2+G2;                                    %
                                              %


for NNN=1:1:length(G2(:,1));                  %
                                              %
          for KKK=1:1:length(G2(1,:));        % Check if random models have
                if  MC2(NNN,KKK)<0;           % zero layer thickness
                    MC2(NNN,KKK)=Mi(NNN);     %
               end;                           %
          end;                                %
end;

%%%% Forward model random models and calculate the RMS value for each model
APR=zeros(length(DA),RV2);

for AAA=1:1:RV2;
      Zb=zeros(1,length(DA));
            Zt=zeros(1,length(DA));
            ZL=zeros(length(DA),length(Mi));
            ZT=zeros(1,length(DA));

           n=length(MC2(:,1));
            Dep=cumsum(MC2(:,AAA));

            for xxx=1:f;
            w1=w(xxx);
            kb=sqrt(sqrt(-1)*w1*mu*(1/Mi(n)));
            Zbb=(w1*mu)/kb;
            Zb(xxx)=Zbb;
            end;

            for xxx=1:f;
                Zt(xxx)=Zb(xxx);
                w1=w(xxx);
                    for jjj=n-1:-1:1;
                          k1     =sqrt(sqrt(-1)*w1*mu*(1/Mi(jjj)));
                          IB     =(acoth((k1*Zt(xxx))/(w1*mu))-(sqrt(-1)*k1*Dep(jjj)));
                          OB     =coth(IB);
                          ZT1    =((w1*mu)/k1)*OB;
                       Zt(xxx)=ZT1;
                       ZL(:,jjj) =ZT1;
                    end;
              ZT(xxx)=Zt(xxx);
            end;

            for xxx=1:f;
                Zt1=ZT(xxx);
                w1=w(xxx);
                                absZt=abs(Zt1);
                                App=(1/(w1*mu))*(absZt*absZt);
                APR(xxx,AAA)=(App);
            end;
          IT=(AAA);
                disp(['Refined Random Model: ' num2str(IT) ]);
```

```
end;

RMSR2=zeros(1,RV2);

for LLL=1:1:RV2;

   RMSRI = sqrt((1/length(DA))*(sum((DA-APR(:,LLL)).^2)));
   RMSR2(LLL)=RMSRI;
end;
%%%%%%%%%%%%%%%%%%%%%%%%%%%%%%%%%%%%%%%%%%%%%%%%%%%%%%%%%%%%%%%%%%%%%%%%%%%%%%%%

%%%%%% Plot random models against model RMSE

[ER2,BM2] = min(RMSR2(:));
figure(1);
scatter(1:1:RV2,RMSR2,'filled','r');legend('Rough Random Model','Refined Random Model');

if ER>ER2;
text2=['Best Model RMS: ',num2str(ER)];
text(BM2,ER2,text2);
elseif ER<ER2;
text2=['Best Model RMS: ',num2str(ER)];
text(BM,ER,text2);
end;
hold off;

%%%%%% Best random model is chosen based on RMSE
if ER>ER2;
 THH(:,1)=MC2(:,BM2);
 RMSA(1)=ER2;
elseif ER<ER2;
    THH(:,1)=MC(:,BM);
 RMSA(1)=ER;
end;
%%%%%

%%%%%%%%%%%%%%%%%%%%%%%%%%%%% Inversion %%%%%%%%%%%%%%%%%%%%%%%%%%%%%%%%%%%%%%%
for III=1:1:Iterations;
         %%%%%%%%%%%%%%%%%%%%%%%%%%%%%% Calculated model response
        Zb=zeros(1,length(DP));
            Zt=zeros(1,length(DP));
            ZL=zeros(length(DP),length(Mi));
            ZT=zeros(1,length(DP));

            n=length(Mi);
            Dep=cumsum(THH(:,III));

            for xxx=1:length(freq);
            w1=w(xxx);
            kb=sqrt(sqrt(-1)*w1*mu*(1/Mi(n)));
            Zbb=(w1*mu)/kb;
            Zb(xxx)=Zbb;
            end;

            k=zeros(n-1,length(freq));


            for xxx=1:length(freq);
                Zt(xxx)=Zb(xxx);
                w1=w(xxx);
                    for jjj=n-1:-1:1;
                          k1     =sqrt(sqrt(-1)*w1*mu*(1/Mi(jjj)));
                          IB     =(acoth((k1*Zt(xxx))/(w1*mu))-(sqrt(-1)*k1*Dep(jjj)));
                          OB     =coth(IB);
                          ZT1    =((w1*mu)/k1)*OB;

                        k(jjj,III)=k1;
                        Zt(xxx)=ZT1;
                        ZL(:,jjj) =ZT1;
                    end;
              ZT(xxx)=Zt(xxx);
            end;

            for xxx=1:length(freq);
                Zt1=ZT(xxx);
                w1=w(xxx);
                                absZt=abs(Zt1);
                                App=(1/(w1*mu))*(absZt*absZt);
                AP(xxx,III)=(App);
            end;

            for iii=1:length(freq);
                Zt1=ZT(iii);
                                phase1=-angle(Zt1)*57.2958;
                Phase(iii,III)=phase1;

            end;

        %%%%%%%%%%%%%%%%%%%%%%%%%%%%%% Calculate sensitivity matrix
        J=zeros(length(DA),length(Mi)-1);

        JB1=zeros(length(DA),length(Mi)-1);

        for KKK=1:1:length(Mi)-1;
            for kkk=1:1:length(DA);
```

```
                JB11=(sqrt(-1))*mu*w(kkk)*(csch((sqrt(-1)*k(1,KKK)*THH(KKK,III)-
acoth((k(1,KKK)*ZL(2,KKK))/(w(kkk)*mu))).^2));
                JB1(kkk,KKK)=JB11;
            end;
        end;

        JB2=zeros(length(DA),1);

        for KKK=1:1:length(DA);
            JB21=1/(ZT(KKK)^2+1);
            JB2(KKK)=JB21;
        end;

         for KKK=1:1:length(Mi)-1;
            for kkk=1:1:length(DA);
                Jb1=JB2(kkk)*JB1(kkk,KKK);
                J(kkk,KKK)=Jb1;
            end;
        end;


        JT=J';
        %%%%%%%%%%%%%%%%%%%%%%%%%%%%% Calculate dampening matrix
         if III==1;
            Damp=real(sqrt((sum(J))))';
        end;

        EYE=eye(length(Mi)-1);
        DAMP=zeros(length(Mi)-1,length(Mi)-1);

        for KKK=1:1:length(Mi)-1;
            DAMP1=Damp(KKK)*EYE(KKK,KKK);
            DAMP(KKK,KKK)=DAMP1;
        end;

         %%%%%%%%%%%%%%%%%%%%%%%%%% Least square weighted damped inversion
                  DEP=DP-Phase(:,III);
                  I1=JT*J+DAMP;
                  INVI1=inv(I1);
                  I2=JT*DEP;
                  Mrec2=INVI1*I2;
                  Mrec2QC(:,III)=real((Mrec2));


         THH(:,III+1)=THH(:,III)+real(Mrec2); % Model change vector
         RMSP(III+1)=sqrt((1/length(DA))*(sum((DP-Phase(:,III)).^2)));

           %%%%%%%%%%%%%%%%%%%%%%% Layer thicknesses constraints
           if III==1;
               RMSP(1)=RMSP(III+1);
           end;

           for KKK=1:1:length(TH);
               if THH(KKK,III+1)<0;
                  THH(KKK,III+1)=THH(KKK,III);
               end;
           end;



       if RMSP(III+1)>RMSP(III);
                        DAMP=DAMP*2;
                        [err,Mod] = min(RMSP(RMSP>0));
                        THH(:,III+1)=THH(:,Mod);


       elseif RMSP(III+1)<RMSP(III);

                  if DAMP(1)>1;
                        DAMP=DAMP/2;
                  end;



      end;


         if III > 1;
             if RMSP(III+1)==RMSP(III);
                   DAMP=DAMP*2;
                   [err,Mod] = min(RMSP(RMSP>0));
                   RR=randi([-RA3,RA3],length(Mi)-1,1);
                   THH(:,III+1)=THH(:,Mod)+RR;
            end;
        end;


             IT=(III);
                 disp(['Iteration: ' num2str(IT) ' out of ' num2str(Iterations)]);



     if RMSP(III+1)==0;
         break
     end;

end;
%%%%%%%%%%%%%%%%%%%%%%%%%%%%%%%%%%%%%%%%%%%%%%%%%%%%%%%%%%%%%%%%%%%%%%%%%%%%%%%
```

```
%%%%%%%%%%%%%%%%%%%%%%%%% Plots %%%%%%%%%%%%%%%%%%%%%%%%%%%%%%%%%%%%%%%%%%%%%%%%

THN=THH(:,Iterations+1);
THN1=[0;THN];
DepthsN=cumsum(THN1);
DepthsN=DepthsN(1:Cell+1);

THS=TH;
THS1=[0;THS];
DepthsS=cumsum(THS1);
DepthsS=DepthsS(1:Cell+1);

 [ERR,ERII] = min(RMSP(:));

 ITT=ERII-1;
 ER=ERR;

THB=THH(:,ITT);
THB1=[0;THB];
DepthsB=cumsum(THB1);
DepthsB=DepthsB(1:Cell+1);

TH1=THH(:,1);
TH1=[0;TH1];
Depths=cumsum(TH1);
Depths=Depths(1:Cell+1);

RESS2=Mi;
RESS2=RESS2(1:Cell+1);
RESS3=Mi;
RESS3=RESS3(1:Cell+1);


P=(1./freq);
PL=log(P);

figure(2);clf;

subplot(3,1,1);
fig = figure(2);
left_color = [1 0 0];
right_color = [0 0 1];
set(fig,'defaultAxesColorOrder',[left_color; right_color]);
yyaxis left;
scatter(PL,DA,8,'fill');hold on;
plot(PL,AP(:,IT),'-');hold on;

xlabel('Log Period (s)');
ylabel('Apparent Resistivity (ohm.m)');


yyaxis right;
scatter(PL,DP,8,'fill');
hold on;
plot(PL,Phase(:,IT),'-');
ylabel('Phase(Degrees)');

legend('Observed Resistivity data','Calculated Resistivity data','Observed Phase data','Calculated Phase
data');
title('Comparison Between Collected Data and Calculated Data ','fontsize',15);
hold off;

subplot(3,1,2);

plot(1:1:IT,RMSP(:,1:1:IT));
ylabel('Phase RMS Error');
title('RMSE Tracker');

subplot(3,1,3);
RESS1=Mi;
RESS1=RESS1(1:Cell+1);
stairs(DepthsN,RESS1,'b');
xlabel('Depth (m)');
ylabel('Apparent Resistivity (ohm.m)');
title('Final Inverted Model');hold on;stairs(Depths,RESS3,'r','LineStyle','--');hold on;stairs(MD,MP,'g');hold
on;
stairs(DepthsS,RESS3,'c','Marker','*');
legend('Final Inverted Model','Best Random Model','Actual Model','Starting Model');


figure(3);clf;


subplot(2,1,1);

fig = figure(3);
left_color = [1 0 0];
right_color = [0 0 1];
set(fig,'defaultAxesColorOrder',[left_color; right_color]);
yyaxis left;

scatter(PL,DA,8,'fill');hold on;plot(PL,real((AP(:,ITT))));
xlabel('Log Period (s)');
ylabel('Apparent Resistivity (ohm.m)');

yyaxis right;
scatter(PL,DP,8,'fill');hold on;plot(PL,Phase(:,ITT));hold off;
```

```
legend('Observed Resistivity data','Calculated Resistivity data','Observed Phase data','Calculated Phase
data');
title(['Best Calculated Model: Iteration ' num2str(ITT) ' RMSE ' num2str(ER)] ,'fontsize',15);

subplot(2,1,2);stairs(DepthsB,RESS2,'b');
xlabel('Depth (m)');
ylabel('Apparent Resistivity (ohm.m)');
title('Best Inverted Model');hold on;stairs(Depths,RESS3,'r','LineStyle','--');hold on;
stairs(MD,MP,'g');hold on;
stairs(DepthsS,RESS3,'c','Marker','*');
legend('Best Inverted Model','Best Random Model','Actual Model','Starting Model');


hold off;
```

A.2.3. Constrained tandem random model generator joint one-dimensional magnetotelluric layer thickness and resistivity least squares damped weighted inversion MatLab code

This code is used in Chapter 2. This code makes use of the one-dimensional MT forward modelling code described in appendix A.1. to generate two sets of random models that attempt to fit the observed data by randomising layer resistivity and thickness by combining the codes described in appendix A.2.1. and A.2.2. The first set of random models can vary an order of magnitude more than the second set of random models. Once the first set of random models is calculated the best fitting model is used in the second set of random model calculations to improve the fit of calculated MT response function with the observed MT response function.

```
function Joint_Thickness_Resistivity_MT1DINV
% Wesley Harrison 2017
% University of the Witwatersrand
% Constrained tandem random model generator one dimensional magnetotelluric
% Joint layer resistivity and thickness least squares damped weighted inversion code

%%%%%%%%%%%%%%%%%%%% Variable Index %%%%%%%%%%%%%%%%%%%%%%%%%%%%%%%%%%%%%%%%

% Ap            = Calculated apparent resistivity
% Cell          = Number of model layers
% DA            = Observed apparent resistivity data
% Dep           = layer depths
% DP            = Observed phase data
% freq          = Frequency
% FRMG          = Number of fine random models to generate
% Iterations    = Number of iterations to run
% M             = Layer resistivities
% MAX_Res       = Maximum resistivity allowed in the conductivity model
% Max_TH        = Maximum layer thickness allowed in the conductivity model
% Mii           = Starting model resistivity half space
% MIN_Res       = Minimum resistivity allowed in the conductivity model
% Min_TH        = Minimum layer thickness allowed in the conductivity model
% mu            = Magnetic Permeability (H/m)
% Padding       = Number of model padding layers
% phasee        = Phase
% Phi_Fine      = Fine random model generator random value range in (m)
% Phi_Rough     = Rough random model generator random value range in (m)
% RA3           = Inversion random model generator random value range in ohm*m
% Rand_Phi_smooth = Rough layer thickness random model generator smoothing window
% Rand_Res_smooth = Rough layer resistivity random model generator smoothing window
% Res_Fine      = Fine random model generator random value range in ohm*m
% Res_Rough     = Rough random model generator random value range in ohm*m
% RMSA          = Apparent resistivity root mean square error
% RMSP          = Phase root mean square error
% RRMG          = Number of rough random models to generate
% THF           = Cell thicknesses
% THH           = Layer thicknesses
% w             = Angular Frequency (Radians)

%%%%%%%%%%%%%%%%%%%%%%%%%%% Inputs %%%%%%%%%%%%%%%%%%%%%%%%%%%%%%%%%%%%%%%%%%
% load('MTData.mat');


DA          =DATA(:,2);
DP          = DATA(:,3);
DA          =awgn(DA,50,'measured');
DP          =awgn(DP,50,'measured');
```

```
freq       = DATA(:,1);

Mii=50000;

THF=100;
Cell=10;
Padding=Cell+8;

Iterations =2300;
w    =(2*pi*freq);
mu   = 4*pi*1E-7;
RMSA=zeros(1,Iterations+1);
RMSP=zeros(1,Iterations+1);
MAX_Res=2000;
MIN_Res=1;
Max_TH=100;
Min_TH=2;

RRMG=1000;
Res_Rough=1000;
Phi_Rough=10;
FRMG=1000;
Res_Fine=100;
Phi_Fine=1;

Rand_Res_smooth=40;
Rand_Phi_smooth=10;
%%%%%%%%%%%%%%%%%%%%%%%%%%%%%%%%%%%%%%%%%%%%%%%%%%%%%%%%%%%%%%%%%%%%%%%%%%%%

%%%%%%%%%%%%%%%%%%%%%%%%%% Initialise %%%%%%%%%%%%%%%%%%%%%%%%%%%%%%%%%%%%%
f=length(freq);
n=Padding;
TH=zeros(Padding,1);
MP=p';
MTH=[0;TH'];
MD=cumsum(MTH);

%%%%%%%%%%%%%%%%%%%%%%%%%% Area of Interest
for LLL=1:1:Cell;   %
    TH1=THF;        % Order layers for area of interest
    TH(LLL)=TH1;    %
end;

%%%%%%%%%%%%%%%%%%%%%%%%%% Padding
for LLL=Cell+1:1:Padding;           %
    TH1=TH(LLL-1)+THF*(10)*(LLL);   % Insert padding layers
    TH(LLL)=TH1;                    %
end;

%%%%%%%%%%%%%%%%%%%%%%%%%% Starting Model

Mi        = zeros(n+1,1);   %
for LLL=1:1:n+1;            %
    Mii1=Mii;               % Create starting model half space
    Mi(LLL)=Mii1;           %
end;                        %

M=zeros(length(Mi),Iterations+1);
THH=zeros(length(Mi)-1,Iterations+1);
THH(:,1)=TH;
AP=zeros(length(DA),Iterations);
Phase=zeros(length(DA),Iterations);
Mrec1QC=zeros(length(Mi),Iterations);
Mrec2QC=zeros(length(Mi)-1,Iterations);

%%%%%%%%%%%%%%%%%%%%%%%%%%%%%%%%%%%%%%%%%%%%%%%%%%%%%%%%%%%%%%%%%%%%%%%%%%%%

%%%%%%%%%%%%%%%%%%%%%%%%%% Random model generator 1%%%%%%%%%%%%%%%%%%%%%%%%%

%%%%%%%%%%%%%%%%% Calculate and order rough random models

RZ=randi([-Res_Rough,Res_Rough],length(Mi)-1,RRMG);
RPhi=randi([-Phi_Rough,Phi_Rough],length(Mi)-1,RRMG);

Rres=Mi;
Rres(length(Mi))=[];
Rres=repmat(Rres,1,RRMG);
MC_Res=RZ+Rres;
A2=Mi(length(Mi));
A2=repmat(A2,1,RRMG);
MC_Res=[MC_Res;A2];

Rth2=TH;
Rth2=repmat(Rth2,1,RRMG);
MC_phi=RPhi+Rth2;
%%%%%%%%%%%%%%%%%%%%%%%%%%%%%%%%%%%%%%%%%%%%%%%%%%%%%%%%%%%%%%%%%%%%%%%%%%%%

%%%%%%%%%%%%%%%% Smooth random models
for TTT=1:1:RRMG;
    MCS_Res=smooth(MC_Res(:,TTT),'moving',Rand_Res_smooth);
    MCS_phi=smooth(MC_phi(:,TTT),'moving',Rand_Phi_smooth);

    MC_Res(:,TTT)=MCS_Res;
    MC_phi(:,TTT)=MCS_phi;
end;
%%%%%%%%%%%%%%%%

%Check if random models are within the maximum and minimum resistivity values
```

```
for NNN=1:1:length(Rres(:,1));

          for KKK=1:1:length(Rres(1,:));
                if  MC_Res(NNN,KKK)<MIN_Res;
                    MC_Res(NNN,KKK)=Mi(NNN);
            elseif  MC_Res(NNN,KKK)>MAX_Res;
                    MC_Res(NNN,KKK)=Mi(NNN);

              end;
          end;
end;
%%%%%%%%%%%%%%%%%%%%%%%%%%%%%%%%%%%%%%%%%%%%%%%%%%%%%%%%%%%%%%%%%%%%%%%%%%%%%%%

%%%%%%%%%%%%%%%%%%%%%%%%%% Check if random models have zero-layer thickness
for NNN=1:1:length(MC_phi(:,1));

          for KKK=1:1:length(MC_phi(1,:));
                if MC_phi(NNN,KKK)<0;
                   MC_phi(NNN,KKK)=Mi(NNN);
                end;

          end;
end;
%%%%%%%%%%%%%%%%%%%%%%%%%%%%%%%%%%%%%%%%%%%%%%%%%%%%%%%%%%%%%%%%%%%%%%%%%%%%%%%

%%%% Forward model random models and calculate the RMS value for each model
APR=zeros(length(DA),RRMG);

for AAA=1:1:RRMG;
      Zb=zeros(1,length(DA));
            Zt=zeros(1,length(DA));
            ZL=zeros(length(Mi),length(DA));
            ZT=zeros(1,length(DA));

           n=length(MC_Res(:,1));
            Dep=MC_phi(:,AAA);

            for xxx=1:f;
            w1=w(xxx);
            kb=sqrt(sqrt(-1)*w1*mu*(1/MC_Res(n,AAA)));
            Zbb=(w1*mu)/kb;
            Zb(xxx)=Zbb;
            end;

            for xxx=1:f;
                Zt(xxx)=Zb(xxx);
                w1=w(xxx);
                    for jjj=n-1:-1:1;
                          k1     =sqrt(sqrt(-1)*w1*mu*(1/MC_Res(jjj,AAA)));
                          IB     =(acoth((k1*Zt(xxx))/(w1*mu))-(sqrt(-1)*k1*Dep(jjj)));
                          OB     =coth(IB);
                          ZT1    =((w1*mu)/k1)*OB;
                        Zt(xxx)=ZT1;
                        ZL(jjj,xxx) =ZT1;
                    end;
              ZT(xxx)=Zt(xxx);
            end;

            for xxx=1:f;
                Zt1=ZT(xxx);
                w1=w(xxx);
                                  absZt=abs(Zt1);
                                  App=(1/(w1*mu))*(absZt*absZt);
                APR(xxx,AAA)=(App);
            end;


     IT=(AAA);
                disp(['Rough Random Model: ' num2str(IT) ]);


end;

RMSR=zeros(1,RRMG);

for LLL=1:1:RRMG;

   RMSRI = sqrt((1/length(DA))*(sum((DA-APR(:,LLL)).^2)));
   RMSR(LLL)=RMSRI;
end;
%%%%%%%%%%%%%%%%%%%%%%%%%%%%%%%%%%%%%%%%%%%%%%%%%%%%%%%%%%%%%%%%%%%%%%%%%%%%%%%

%%%%%% Plot random models against model RMSE


[ER,BM] = min(RMSR(:));
figure(1);clf;
scatter(1:1:RRMG,RMSR,'filled');
xlabel('Random Model');
ylabel('RMS Error');
title('Generated Random Models RMS Errors ');hold on;

% Best rough random model is chosen based on RMSE
 Best_RRMG_Res=MC_Res(:,BM);
 Best_RRMG_phi=MC_phi(:,BM);
%
```

```
%%%%%%%%%%%%%%%%%%%%%%%%%%%%%%%%%%%%%%%%%%%%%%%%%%%%%%%%%%%%%%%%%%%%%%%%%%%%%%%

%%%%%%%%%%%%%%%%%%%%%%%%%% Random model generator 2%%%%%%%%%%%%%%%%%%%%%%%%%

%%%%%%%%%%%%%%%%%% Calculate and order fine random models
RZ_2=randi([-Res_Fine,Res_Fine],length(Mi)-1,FRMG);
RPhi_2=randi([-Phi_Fine,Phi_Fine],length(Mi)-1,FRMG);

Rres_2=Best_RRMG_Res;
Rres_2(length(Best_RRMG_Res))=[];
Rres_2=repmat(Rres_2,1,FRMG);
MC2_Res=RZ_2+Rres_2;
A2=Mi(length(Mi));
A2=repmat(A2,1,FRMG);
MC2_Res=[MC2_Res;A2];

Rth2=Best_RRMG_phi;
Rth2=repmat(Rth2,1,FRMG);
MC2_phi=RPhi_2+Rth2;

%%%%%%%%%%%%%%%%%%

%Check if random models are within the maximum and minimum resistivity values
for NNN=1:1:length(Rres_2(:,1));

          for KKK=1:1:length(Rres_2(1,:));
                if  MC2_Res(NNN,KKK)<MIN_Res;
                    MC2_Res(NNN,KKK)=Mi(NNN);
              elseif  MC2_Res(NNN,KKK)>MAX_Res;
                    MC2_Res(NNN,KKK)=Mi(NNN);

                end;
          end;
end;
%%%%%%%%%%%%%%%%%%%%%%%%%%%%%%%%%%%%%%%%%%%%%%%%%%%%%%%%%%%%%%%%%%%%%%%%%%%%%%%

%%%%%%%%%%%%%%%%%%%%%%%%%% Check if random models have zero-layer thickness
for NNN=1:1:length(MC2_phi(:,1));

          for KKK=1:1:length(MC2_phi(:,1));
                if  MC2_phi(NNN,KKK)<0;
                    MC2_phi(NNN,KKK)=Best_RRMG_phi(NNN);
                end;

          end;
end;

for NNN=1:1:length(MC2_phi(:,1));

          for KKK=1:1:length(MC2_phi(1,:));
                if MC2_phi(NNN,KKK)<0;
                   MC2_phi(NNN,KKK)=Mi(NNN);
                end;

          end;
end;

%%%%%%%%%%%%%%%%%%%%%%%%%%%%%%%%%%%%%%%%%%%%%%%%%%%%%%%%%%%%%%%%%%%%%%%%%%%%%%%

%%%% Forward model random models and calculate the RMS value for each model

APR=zeros(length(DA),FRMG);

for AAA=1:1:FRMG;
      Zb=zeros(1,length(DA));
            Zt=zeros(1,length(DA));
            ZL=zeros(length(DA),length(Mi));
            ZT=zeros(1,length(DA));

           n=length(MC2_Res(:,1));
            Dep=cumsum(MC2_phi(:,AAA));

            for xxx=1:f;
            w1=w(xxx);
            kb=sqrt(sqrt(-1)*w1*mu*(1/MC2_Res(n,AAA)));
            Zbb=(w1*mu)/kb;
            Zb(xxx)=Zbb;
            end;

            for xxx=1:f;
                Zt(xxx)=Zb(xxx);
                w1=w(xxx);
                    for jjj=n-1:-1:1;
                          k1     =sqrt(sqrt(-1)*w1*mu*(1/MC2_Res(jjj,AAA)));
                          IB     =(acoth((k1*Zt(xxx))/(w1*mu))-(sqrt(-1)*k1*Dep(jjj)));
                          OB     =coth(IB);
                          ZT1    =((w1*mu)/k1)*OB;
                       Zt(xxx)=ZT1;
                       ZL(:,jjj) =ZT1;
                    end;
              ZT(xxx)=Zt(xxx);
            end;

            for xxx=1:f;
                Zt1=ZT(xxx);
                w1=w(xxx);
                                  absZt=abs(Zt1);
                                  App=(1/(w1*mu))*(absZt*absZt);
```

```
                APR(xxx,AAA)=(App);
            end;
          IT=(AAA);
                disp(['Refined Random Model: ' num2str(IT) ]);


end;

RMSR2=zeros(1,FRMG);

for LLL=1:1:FRMG;

   RMSRI = sqrt((1/length(DA))*(sum((DA-APR(:,LLL)).^2)));
   RMSR2(LLL)=RMSRI;
end;

%%%%%%%%%%%%%%%%%%%%%%%%%%%%%%%%%%%%%%%%%%%%%%%%%%%%%%%%%%%%%%%%%%%%%%%%%%%

%%%%%% Plot random models against model RMSE

[ER2,BM2] = min(RMSR2(:));
figure(1);
scatter(1:1:FRMG,RMSR2,'filled','r');legend('Rough Random Model','Refined Random Model');

%%%%%% Best random model is chosen based on RMSE
if ER>ER2;
text2=['Best Model RMS: ',num2str(ER)];
text(BM2,ER2,text2);
elseif ER<ER2;
text2=['Best Model RMS: ',num2str(ER)];
text(BM,ER,text2);
end;
hold off;

if ER>ER2;
 M(:,1)=MC2_Res(:,BM2);
 THH(:,1)=MC2_phi(:,BM2);
 RMSA(1)=ER2;
elseif ER<ER2;
     M(:,1)=MC_Res(:,BM);
     THH(:,1)=MC_phi(:,BM);
 RMSA(1)=ER;
end;
%%%%%%%%%%%%%%%%%%%%%%%%%%%%%%%%%%%%%%%%%%%%%%%%

%%%%%%%%%%%%%%%%%%%%%%%%%%% Inversion %%%%%%%%%%%%%%%%%%%%%%%%%%%%%%%%%%%%%
for III=1:1:Iterations;
         %%%%%%%%%%%%%%%%%%%%%%%%%%%%% Calculated model response
            Zb=zeros(1,length(DA));
            Zt=zeros(1,length(DA));
            ZL=zeros(length(Mi),length(DA));
            ZT=zeros(1,length(DA));

            n=length(M(:,III));
            Dep=cumsum(THH(:,III));

            for xxx=1:length(freq);
            w1=w(xxx);
            kb=sqrt(sqrt(-1)*w1*mu*(1/M(n,III)));
            Zbb=(w1*mu)/kb;
            Zb(xxx)=Zbb;
            end;

            k=zeros(n-1,length(freq));


            for xxx=1:length(freq);
                Zt(xxx)=Zb(xxx);
                w1=w(xxx);
                    for jjj=n-1:-1:1;
                          k1      =sqrt(sqrt(-1)*w1*mu*(1/M(jjj,III)));
                          IB      =(acoth((k1*Zt(xxx))/(w1*mu))-(sqrt(-1)*k1*Dep(jjj)));
                          OB      =coth(IB);
                          ZT1     =((w1*mu)/k1)*OB;

                        k(jjj,xxx)=k1;
                        Zt(xxx)=ZT1;
                        ZL(jjj,xxx) =ZT1;
                    end;
              ZT(xxx)=Zt(xxx);
            end;

            for xxx=1:length(freq);
                Zt1=ZT(xxx);
                w1=w(xxx);
                                 absZt=abs(Zt1);
                                 App=(1/(w1*mu))*(absZt*absZt);
                AP(xxx,III)=(App);
            end;

            for iii=1:length(freq);
                Zt1=ZT(iii);
                             phase1=-angle(Zt1)*57.2958;
                Phase(iii,III)=phase1;

            end;
```

```
        %%%%%%%%%%%%%%%%%%%%%%%%%%%%%% Calculate sensitivity matrix
        Jt=zeros(length(DA),length(Mi));
        Jb=zeros(length(DA),length(Mi)-1);


        for KKK=1:1:length(M(:,III));
            for kkk=1:1:length(DA);
                J1=(2*ZT(kkk))/sqrt(AP(KKK,III)*mu*w(KKK));
                Jt(kkk,KKK)=J1;
            end;
        end;


        JB1=zeros(length(DA),length(M(:,III))-1);

        for KKK=1:1:length(M(:,III))-1;
            for kkk=1:1:length(DA);
                JB11=(sqrt(-1))*mu*w(kkk)*(csch((sqrt(-1)*k(1,KKK)*THH(KKK,III)-
acoth((k(1,KKK)*ZL(2,KKK))/(w(kkk)*mu))).^2));
                JB1(kkk,KKK)=JB11;
            end;
        end;

        JB2=zeros(length(DA),1);

        for KKK=1:1:length(DA);
            JB21=1/(ZT(KKK)^2+1);
            JB2(KKK)=JB21;
        end;

         for KKK=1:1:length(M(:,III))-1;
            for kkk=1:1:length(DA);
                Jb1=JB2(kkk)*JB1(kkk,KKK);
                Jb(kkk,KKK)=Jb1;
            end;
        end;

        JTt=Jt';
        JTb=Jb';

       %%%%%%%%%%%%%%%%%%%%%%%%%%%%%% Calculate dampening matrix
        if III==1;
            Damp=real(sqrt((sum(Jt))))';
        end;

        if III==1;
        EYE=eye(length(M(:,III)));
        DAMP_Z=zeros(length(M(:,III)),length(M(:,III)));

        for KKK=1:1:length(M(:,III));
            DAMP1=Damp(KKK)*EYE(KKK,KKK);
            DAMP_Z(KKK,KKK)=DAMP1;
        end;
        end;
         if III==1;
            Damp=real(sqrt((sum(Jb))))';
        end;
        if III==1;
        EYE=eye(length(M(:,III))-1);
        DAMP_phi=zeros(length(Mi)-1,length(M(:,III))-1);

        for KKK=1:1:length(M(:,III))-1;
            DAMP1=Damp(KKK)*EYE(KKK,KKK);
            DAMP_phi(KKK,KKK)=DAMP1;
        end;
        end;
         %%%%%%%%%%%%%%%%%%%%%%%%%%%%%% Calculate weighted matrix

         W=zeros(length(DA),length(M(:,III)));
         WW=zeros(length(DA),1);

         for BBB=1:1:length(DA);
             w1=10/AP(BBB,III);
             WW(BBB)=w1;
         end;

         for TTT=1:1:length(M(:,III));
             W(:,TTT)=WW;
         end;
         WT=W';

          WP=zeros(length(DP),length(M(:,III)));
         WWP=zeros(length(DP),1);

         for BBB=1:1:length(DP);
             w1=Phase(BBB,III);
             WWP(BBB)=w1;
         end;

         for TTT=1:1:length(M(:,III));
             WP(:,TTT)=WWP;
         end;
         WPT=WP';
```

```
%%%%%%%%%%%%%%%%%%%%%%%%%%%% Weighted ridge regression damped inversion


              DEA=DA-AP(:,III);
              I1=JTt*W*WT*Jt+ DAMP_Z;
              INVI1=inv(I1);
              I2=JTt*W*WT*DEA;
              Mrec1=INVI1*I2;
              Mrec1QC(:,III)=real(Mrec1);

              DEP=DP-Phase(:,III);
              I1=JTb*WP*WPT*Jb+DAMP_phi;
              INVI1=inv(I1);
              I2=JTb*WP*WPT*DEP;
              Mrec2=INVI1*I2;
              Mrec2QC(:,III)=real((Mrec2));

      M(:,III+1)=M(:,III)+real(Mrec1);
      THH(:,III+1)=THH(:,III)+real((Mrec2));

        RMSA(III+1)=sqrt((1/length(DA))*(sum((DA-AP(:,III)).^2)));
        RMSP(III+1)=sqrt((1/length(DA))*(sum((DP-Phase(:,III)).^2)));

        %%%%%%%%%%%%%%%%%%%%%%%%%%%% Layer resistivity constraints

          if RMSA(III+1)>RMSA(III);

                      DAMP_Z=DAMP_Z*2;


                   M(:,III+1)=M(:,III);


           elseif RMSA(III+1)<RMSA(III);

                     DAMP_Z=DAMP_Z/2;


           else RMSA(III+1)=RMSA(III);
                 DAMP_Z=DAMP_Z*2;

           end;
%%%%%%%%%%%%%%%%%%%%%%%%%%%% Layer thicknesses constraints


       if III==1;
            RMSP(1)=RMSP(III+1);
        end;

        for KKK=1:1:length(THH(:,III));
            if THH(KKK,III+1)<0;
               THH(KKK,III+1)=THH(KKK,III);
            end;
        end;


        if RMSP(III+1)>RMSP(III);
                         DAMP_phi=DAMP_phi*2;
                         THH(:,III+1)=THH(:,III);


        elseif RMSP(III+1)<RMSP(III);


                         DAMP_phi=DAMP_phi/2;


        end;


      if III > 1;
          if RMSP(III+1)==RMSP(III);
                DAMP_phi=DAMP_phi*2;
      end;

      for LLL=1:1:length(THH(:,III));
          if THH(LLL,III+1)>Max_TH;
             THH(LLL,III+1)=THH(LLL,III);
          end;
           if THH(LLL,III+1)<Min_TH;
             THH(LLL,III+1)=THH(LLL,III);
          end;

      end;

%%%%%%%%%%%%%%%%%%%%%%%%%%%%%

           IT=(III);
               disp(['Iteration: ' num2str(IT) ' out of ' num2str(Iterations)]);

    for NNN=1:1:length(M(:,1));
          if  M(NNN,III+1)<0;
              M(NNN,III+1)=M(NNN,III);
          end;
    end;

    for NNN=1:1:length(M(:,III));
              if  M(NNN,III+1)<MIN_Res;
```

```
                    M(NNN,III+1)=M(NNN,III);
                elseif  M(NNN,III+1)>MAX_Res;
                    M(NNN,III+1)=M(NNN,III);

                end;
        end;

        Zeros=find(~THH(:,III));

        for MMM=1:1:length(Zeros);
            THH(Zeros(MMM),III)=[];
            M(Zeros(MMM),III)=[];
        end;
end;


%%%%%%%%%%%%%%%%%%%%%%%%%%%%%%%%%%%%%%%%%%%%%%%%%%%%%%%%%%%%%%%%%%%%%%%%%%%%%%%

%%%%%%%%%%%%%%%%%%%%%%%%% Plots %%%%%%%%%%%%%%%%%%%%%%%%%%%%%%%%%%%%%%%%%%%%%%
RMSP(1)=RMSP(2);
[ERR,ERII] = min(RMSA(:));
[ERRP,ERIIP] = min(RMSP(:));

 ITT=ERII;
 ER=ERR;

ITTP=ERIIP-1;
ERP=ERRP;

THBP=THH(:,ITTP);
THB1P=[0;THBP];
DepthsBP=cumsum(THB1P);
[c,indexBP] = min(abs(DepthsBP-(THF*Cell)));
DepthsBP=DepthsBP(1:indexBP);

THN=THH(:,Iterations+1);
THN1=[0;THN];
DepthsN=cumsum(THN1);
[c,indexN] = min(abs(DepthsN-(THF*Cell)));
DepthsN=DepthsN(1:indexN);

THS=TH;
THS1=[0;THS];
DepthsS=cumsum(THS1);
[c,indexS] = min(abs(DepthsS-(THF*Cell)));
DepthsS=DepthsS(1:indexS);

THB=THH(:,ITT);
THB1=[0;THB];
DepthsB=cumsum(THB1);
[c,indexB] = min(abs(DepthsB-(THF*Cell)));
DepthsB=DepthsB(1:indexB);

TH1=THH(:,1);
TH1=[0;TH1];
Depths=cumsum(TH1);
[c,index] = min(abs(Depths-(THF*Cell)));
Depths=Depths(1:index);

RessS=Mi;
RessS=RessS(1:indexS-1);
RessS=[RessS(1);RessS];

RESS1=M(:,Iterations);
RESS1=RESS1(1:indexN-1);
RESS1=[RESS1(1);RESS1];

RESS2=M(:,ERII);
RESS2=RESS2(1:indexB-1);
RESS2=[RESS2(1);RESS2];

RESS3=M(:,1);
RESS3=RESS3(1:index-1);
RESS3=[RESS3(1);RESS3];

RESS4=M(:,ERIIP);
RESS4=RESS4(1:indexBP-1);
RESS4=[RESS4(1);RESS4];

P=(1./freq);
PL=log(P);

figure(2);clf;

subplot(3,1,1);
fig = figure(2);
left_color = [1 0 0];
right_color = [0 0 1];
set(fig,'defaultAxesColorOrder',[left_color; right_color]);
yyaxis left;
scatter(PL,DA,8,'fill');hold on;plot(PL,AP(:,IT),'-');hold on;

xlabel('Log Period (s)');
ylabel('Apparent Resistivity (ohm.m)');


yyaxis right;
scatter(PL,DP,8,'fill');hold on;plot(PL,Phase(:,IT),'-');
```

```
ylabel('Phase(Degrees)');

legend('Observed Resistivity data','Calculated Resistivity data','Observed Phase data','Calculated Phase
data');
title('Comparison Between Collected Data and Calculated Data ','fontsize',15);
hold off;

subplot(3,1,2);

fig = figure(2);
left_color = [1 0 0];
right_color = [0 0 1];
set(fig,'defaultAxesColorOrder',[left_color; right_color]);
yyaxis left;
plot(1:1:IT,RMSA(:,1:1:IT));
xlabel('Iterations');
ylabel('Resistivity RMS Error');
hold on;

yyaxis right;
plot(1:1:IT,RMSP(:,1:1:IT));
legend('Resistivity RMS','Phase RMS');
ylabel('Phase RMS Error');
title('RMSE Tracker');

subplot(3,1,3);
stairs(DepthsN,RESS1,'b');
xlabel('Depth (m)');
ylabel('Apparent Resistivity (ohm.m)');
title('Final Inverted Model');hold on;stairs(Depths,RESS3,'r','LineStyle','--');hold on;stairs(MD,MP,'g');
hold on; stairs(DepthsS,RessS,'c','Marker','*');
legend('Final Inverted Model','Best Random Model','Actual Model','Starting Model' );


figure(3);clf;
 [ERR,ERII] = min(RMSA(:));

 ITT=ERII;
 ER=ERR;

subplot(3,1,1);

fig = figure(3);
left_color = [1 0 0];
right_color = [0 0 1];
set(fig,'defaultAxesColorOrder',[left_color; right_color]);
yyaxis left;

scatter(PL,DA,8,'fill');hold on;plot(PL,real((AP(:,ITT))));
xlabel('Log Period (s)');
ylabel('Apparent Resistivity (ohm.m)');

yyaxis right;
scatter(PL,DP,8,'fill');hold on;plot(PL,Phase(:,ITT));hold off;

legend('Observed Resistivity data','Calculated Resistivity data','Observed Phase data','Calculated Phase
data');
title(['Best Layer Resistivity Calculated Model: Iteration ' num2str(ITT) ' RMSE ' num2str(ER)]
,'fontsize',15);

subplot(3,1,2);

fig = figure(3);
left_color = [1 0 0];
right_color = [0 0 1];
set(fig,'defaultAxesColorOrder',[left_color; right_color]);
yyaxis left;

scatter(PL,DA,8,'fill');hold on;plot(PL,real((AP(:,ITTP))));
xlabel('Log Period (s)');
ylabel('Apparent Resistivity (ohm.m)');

yyaxis right;
scatter(PL,DP,8,'fill');hold on;plot(PL,Phase(:,ITTP));hold off;

legend('Observed Resistivity data','Calculated Resistivity data','Observed Phase data','Calculated Phase
data');
title(['Best Layer Thickness Calculated Model: Iteration ' num2str(ITTP) ' RMSE ' num2str(ERP)]
,'fontsize',15);

subplot(3,1,3);stairs(DepthsB,RESS2,'b');hold on;stairs(DepthsBP,RESS4,'k');hold on;
xlabel('Depth (m)');
ylabel('Apparent Resistivity (ohm.m)');
title('Best Inverted Model');hold on;stairs(Depths,RESS3,'r','LineStyle','--');hold on;
stairs(MD,MP,'g');hold on; stairs(DepthsS,RessS,'c','Marker','*');
legend('Best RMS Resistivity Inverted Model','Best RMS Thickness Inverted Model','Best Random Model','Actual
Model','Starting Model');
hold off;
```

A.3. Augmented ERT-MT response function MatLab code

This code is developed from the theory described in Chapter 4. The code is used to calculate the augmented ERT-MT response functions used in the resistivity inverse models described in Chapter 4 and Chapter 5.

```
function augmented_resistivity_curve_V3
% Wesley Harrison 2019
% University of the Witwatersrand
% A MatLab algorithm for calculating an augmented ERT-MT response function.

%%%%%%%%%%%%%%%%%%%% Variable Index %%%%%%%%%%%%%%%%%%%%%%%%%%%%%%%%%%%%%%%
% w         = Angular Frequency (Radians)
% freq      = Frequency band (Hz).
% mu        = Magnetic Permeability (H/m)
% p         = Resistivity of layers
% Ap        = Calculated apparent resistivity
% TH        = Layer thickness
% k         = Wave propagation term.
% ZT        = Surface impedances
% ZL        = Layer impedances
% Zb        = Basement layer impedance
%%%%%%%%%%%%%%%%%%%%%%%%%%%%%%%%%%%%%%%%%%%%%%%%%%%%%%%%%%%%%%%%%%%%%%%%%%%

StationLoc=119;              % MT location along ERT resistivity inverse model.

load('Depthdc.mat');         % Load depth values for ERT resistivity inverse model.
load('Resdc.mat');           % Load resistivity values for ERT resistivity inverse model.
load('Xdc.mat');             % Load distance values for ERT resistivity inverse model.

load('ResMT.mat');           % Load resistivity values from MT data.
load('PHMT.mat');            % Load phase values from MT data.
load('FreqMT.mat');          % Load frequency values from MT data.

mu     = 4*pi*1E-7;

%%Extracting resistivity values from ERT resistivity inverse model %%%%%%%%%%%%%%%%%%%%%%%%%%%%%%%%%%%%%%%%%%

[gx1,gz1]=meshgrid(min(Xdc):1:max(Xdc),min(Depthdc):1:max(Depthdc));
grid1=griddata(Xdc,Depthdc,Resdc,gx1,gz1);

FF=abs(gx1-StationLoc);
FFF=min(FF,[],'all');

[idx,idy]= find(FFF==FF);

XdcMT=gx1(:,idy(1));
ZdcMT=gz1(:,idy(1));
ResdcMT=grid1(:,idy(1));

[IDXnan,IDynan]=find(isnan(ResdcMT));
ResdcMT(IDXnan)=[];
XdcMT(IDXnan)=[];
ZdcMT(IDXnan)=[];

ResdcMT=[ResdcMT;ResdcMT(length(ResdcMT))];
n=length(ResdcMT);
freq=zeros(length(ZdcMT),1);

for III=1:1:length(ZdcMT)
 freq(III)=ResdcMT(III)/(2*pi*(ZdcMT(III)^2)*mu);
end


%%%%%%%%%%%%%%%%%%%%%%%%%%%% Initialize %%%%%%%%%%%%%%%%%%%%%%%%%%%%%%%%%%%
Zb=zeros(1,length(freq));       % Initialize basement impedance matrix.
ZL=zeros(1,length(freq));       % Initialize layer impedance matrix.
ZT=zeros(1,length(freq));       % Initialize surface impedance matrix.
Dep=ZdcMT;                      % Initialize layer depth matrix.
Ap=zeros(1,length(freq));       % Initialize apparent resistivity matrix.
phasee=zeros(1,length(freq));   % Initialize phase matrix.
%%%%%%%%%%%%%%%%%%%%%%%%%%%%%%%%%%%%%%%%%%%%%%%%%%%%%%%%%%%%%%%%%%%%%%%%%%%

%%%%%%%%%%%%%%%%%%%% calculate impedances %%%%%%%%%%%%%%%%%%%%%%%%%%%%%%%%%

parfor iii=1:length(freq);                                 %
    w1=2*pi*freq(iii);                                     %
    kb=sqrt(sqrt(-1)*w1*mu*(1/ResdcMT(n)));                %
    Zbb=(w1*mu)/kb;                                        % Compute basement impedances using parallel
computing.
    Zb(iii)=Zbb;                                           %
                                                           %
    Mon=(iii/length(freq))*100;                            %
    disp(['Calculating basement impedance ' num2str(Mon) '%']); %
end;
```

```
for iii=1:length(freq);                                                    %
    ZL(iii)=Zb(iii);                                                       %
    w1=2*pi*freq(iii);                                                     %
        for jjj=n-1:-1:1;                                                  % Compute layer impedances
              k1     =sqrt(sqrt(-1)*w1*mu*(1/ResdcMT(jjj)));               %
              IB     =(acoth((k1*ZL(iii))/(w1*mu))-(sqrt(-1)*k1*Dep(jjj))); %
              OB     =coth(IB);                                            %
              ZT1    =((w1*mu)/k1)*OB;                                     %
            ZL(iii)=ZT1;                                                   %
        end;
  ZT(iii)=ZL(iii); % Store surface impedances.

  Mon=(iii/length(freq))*100;
  disp(['Calculating surface impedance ' num2str(Mon) '%']);

end;
%%%%%%%%%%%%%%%%%%%%%%%%%%%%%%%%%%%%%%%%%%%%%%%%%%%%%%%%%%%%%%%%%%%%%%%%%%%

%%%%%%%%%%%%%%%%%%%%%% calculate apparent resistivity %%%%%%%%%%%%%%%%%%%%%%
parfor iii=1:length(freq);                                 %
    Zt1=ZT(iii);                                           %
    w1=2*pi*freq(iii);                                     % Compute observed apparent resistivity values at
                    absZt=abs(Zt1);                        % different frequencies.
                    App=(1/(w1*mu))*(absZt*absZt);         %
    Ap(iii)=App;                                           % Store apparent resistivity values.

    Mon=(iii/length(freq))*100;
    disp(['Calculating apparent resistivity ' num2str(Mon) '%']);

end;
%%%%%%%%%%%%%%%%%%%%%%%%%%%%%%%%%%%%%%%%%%%%%%%%%%%%%%%%%%%%%%%%%%%%%%%%%%%

%%%%%%%%%%%%%%%%%%%%%%%% Phase Lead EF%%%%%%%%%%%%%%%%%%%%%%%%%%%%%%%%%%%%%
parfor iii=1:length(freq);                        %
    Zt1=ZT(iii);                                  % Compute phase values at different frequencies.

                phase1=-atan(imag(Zt1)/real(Zt1))*57.2958;
    phasee(iii)=phase1; % Store phase values.

    Mon=(iii/length(freq))*100;
    disp(['Calculating phase ' num2str(Mon) '%']);
end;


AMT=[freq Ap' phasee'];
AMT = sortrows(AMT,1);

figure(1);
tri=delaunay(Xdc,Depthdc);
trimesh(tri,Xdc,Depthdc,Resdc,'FaceColor','interp','EdgeColor','interp');colormap(flipud(jet));caxis([100
8000]);hold on;scatter(XdcMT,ZdcMT,'fill','k');
xlabel('Distance (m)','fontsize',25); ylabel('Depth (m)','fontsize',25);title('Calculated Electrical
Resistivity Inversion Model','fontsize',25);
set(gca,'ColorScale','log')
hcb=colorbar;
colorTitleHandle = get(hcb,'Title');
titleString = '(ohm·m)';
set(colorTitleHandle ,'String',titleString);
set(gca,'fontsize',25);
view(0,-90);

figure(2);
subplot(2,1,1);
scatter(AMT(:,1),AMT(:,2),'fill','r');hold on;scatter(FreqMT,ResMT,'fill','b');
set(gca, 'YScale', 'log')
set(gca, 'XScale', 'log')
set(gca, 'XDir','reverse')
Ax = gca;
yt = Ax.YTick;
Ax.YTickLabel = compose('%.0f    ', yt);
xlabel('Frequency (Hz)','fontsize',25);
ylabel('Apparent Resistivity (ohm.m)','fontsize',25);
title('Augmented Apparent Resistivity Plotted at Different Frequencies','fontsize',30);hold on;
legend({'From Electrical Resistivity','From Magnetotelluric'},'Location','best');
set(gca,'fontsize',25);
grid on;
grid minor


subplot(2,1,2);
scatter(AMT(:,1),AMT(:,3),'fill','r');hold on;scatter(FreqMT,PHMT,'fill','b');
ylabel('Phase (Degrees)','fontsize',25);
xlabel('Frequency (Hz)','fontsize',25);
Ax = gca;
yt = Ax.YTick;
Ax.YTickLabel = compose('%.0f    ', yt);
title('Augmented Phase Plotted at Different Frequencies','fontsize',30);hold on;
legend({'From Electrical Resistivity','From Magnetotelluric'},'Location','best');
set(gca,'fontsize',25);
set(gca, 'XScale', 'log')
set(gca, 'XDir','reverse')
grid on;
grid minor

%%%%%%%%%%%%%%%%%%%%%%%%%%%%%% Saving Data %%%%%%%%%%%%%%%%%%%%%%%%%%%%%%%%
AllFreq=[freq; FreqMT];
AllAp=[Ap';ResMT];
AllPH=[phasee';PHMT];
```

```
N=length(AllFreq);
AZ=5*ceil(N/5);
AZ=AZ-N;
AZ=zeros(AZ,1);

AllFreq=[AllFreq; AZ];
AllAp=[AllAp;AZ];
AllPH=[AllPH;AZ];
N=length(AllFreq);

Freq=reshape(AllFreq,[5 ceil(N/5)]);
APP=reshape(AllAp,[5 ceil(N/5)]);
PH=reshape(AllPH,[5 ceil(N/5)]);
err=zeros(length(AllFreq(:,1)),length(AllFreq(1,:)));

Filedate =date;
FN=sprintf('AG_MT_119m_8.EDI');

fid = fopen(FN,'w');
fprintf(fid,'>HEAD \r\n');
fprintf(fid,'DATAID="1" \r\n');
fprintf(fid,'FILEBY="" \r\n');
fprintf(fid,'ACQDATE=05/01/19 \r\n');
fprintf(fid,'FILEDATE=05/01/19 \r\n');
fprintf(fid,'PROSPECT="Test" \r\n');
fprintf(fid,'LOC="Test" \r\n');
fprintf(fid,'LAT=-27:02:01.2323 \r\n');
fprintf(fid,'LONG=26:37:18.5726 \r\n');
fprintf(fid,'ELEV=0 \r\n');
fprintf(fid,'STDVERS="SEG 1.0" \r\n');
fprintf(fid,'PROGVERS="WINGLINK EDI 1.0.22" \r\n');
fprintf(fid,'PROGDATE=04/23/02 \r\n');
fprintf(fid,'MAXSECT=999 \r\n');
fprintf(fid,'EMPTY=1.0e+32 \r\n');
fprintf(fid,'\r\n');
fprintf(fid,'>INFO \r\n');
fprintf(fid,'MAXINFO=999 \r\n');
fprintf(fid,'SURVEY ID:Test \r\n');
fprintf(fid,'SURVEY CO: \r\n');
fprintf(fid,'CLIENT CO: \r\n');
fprintf(fid,'AREA:Test \r\n');
fprintf(fid,'ROTATION= \r\n');
fprintf(fid,'\r\n');

fprintf(fid,'>=DEFINEMEAS \r\n');
fprintf(fid,'MAXCHAN=7 \r\n');
fprintf(fid,'MAXRUN=999 \r\n');
fprintf(fid,'MAXMEAS=9999 \r\n');
fprintf(fid,'UNITS=M \r\n');
fprintf(fid,'REFTYPE=CART \r\n');
fprintf(fid,'REFLOC="1" \r\n');
fprintf(fid,'REFLAT=-27:02:01.2323 \r\n');
fprintf(fid,'REFLONG=26:37:18.5726 \r\n');
fprintf(fid,'REFELEV=0 \r\n');
fprintf(fid,'>HMEAS ID=101.001 CHTYPE=HX X=0.0 Y=0.0 Z=0.0 AZM=0.0  \r\n');
fprintf(fid,'>HMEAS ID=102.001 CHTYPE=HY X=0.0 Y=0.0 Z=0.0 AZM=90.0  \r\n');
fprintf(fid,'>HMEAS ID=103.001 CHTYPE=HZ X=0.0 Y=0.0 Z=0.0 AZM=0.0  \r\n');
fprintf(fid,'>EMEAS ID=104.001 CHTYPE=EX X=0.0 Y=0.0 Z=0.0 X2=0.0 Y2=0.0 Z2=0.0  \r\n');
fprintf(fid,'>EMEAS ID=105.001 CHTYPE=EY X=0.0 Y=0.0 Z=0.0 X2=0.0 Y2=0.0 Z2=0.0  \r\n');
fprintf(fid,'>HMEAS ID=106.001 CHTYPE=HX X=0.0 Y=0.0 Z=0.0 AZM=0.0  \r\n');
fprintf(fid,'HMEAS ID=107.001 CHTYPE=HY X=0.0 Y=0.0 Z=0.0 AZM=90.0  \r\n');
fprintf(fid,'\r\n');

fprintf(fid,'>=MTSECT \r\n');
fprintf(fid,'SECTID="1" \r\n');
fprintf(fid,'NFREQ=%.0f \r\n',N);
fprintf(fid,'HX=101.001 \r\n');
fprintf(fid,'HY=102.001 \r\n');
fprintf(fid,'HZ=103.001 \r\n');
fprintf(fid,'EX=104.001 \r\n');
fprintf(fid,'EY=105.001 \r\n');
fprintf(fid,'RX=106.001 \r\n');
fprintf(fid,'RY=107.001 \r\n');
fprintf(fid,'\r\n');


fprintf(fid,'>!****FREQUENCIES****! \r\n');
fprintf(fid,'>FREQ //%.0f \r\n',N);
fprintf(fid,'  %8e %8e %8e %8e %8e \r\n',Freq);
fprintf(fid,'>!****APPARENT RESISTIVITIES AND PHASES****! \r\n');
fprintf(fid,'>RHOXY ROT=RHOROT //%.0f \r\n',N);
fprintf(fid,'  %8e %8e %8e %8e %8e \r\n',APP);
fprintf(fid,'>RHOXY.ERR ROT=RHOROT //%.0f \r\n',N);
fprintf(fid,'  %8e %8e %8e %8e %8e \r\n',err);
fprintf(fid,'>RHOYX ROT=RHOROT //%.0f \r\n',N);
fprintf(fid,'  %8e %8e %8e %8e %8e \r\n',APP);
fprintf(fid,'>RHOYX.ERR ROT=RHOROT //%.0f \r\n',N);
fprintf(fid,'  %8e %8e %8e %8e %8e \r\n',err);
fprintf(fid,'>PHSXY ROT=RHOROT //%.0f \r\n',N);
fprintf(fid,'  %8e %8e %8e %8e %8e \r\n',PH);
fprintf(fid,'>PHSXY.ERR ROT=RHOROT //%.0f \r\n',N);
fprintf(fid,'  %8e %8e %8e %8e %8e \r\n',err);
fprintf(fid,'>PHSYX ROT=RHOROT //%.0f \r\n',N);
fprintf(fid,'  %8e %8e %8e %8e %8e \r\n',PH);
fprintf(fid,'>PHSYX.ERR ROT=RHOROT //%.0f \r\n',N);
fprintf(fid,'  %8e %8e %8e %8e %8e \r\n',err);
fprintf(fid,'\r\n');
```

```
fprintf(fid,'>END');
fclose(fid);
end
```

A.4. ERT Lines

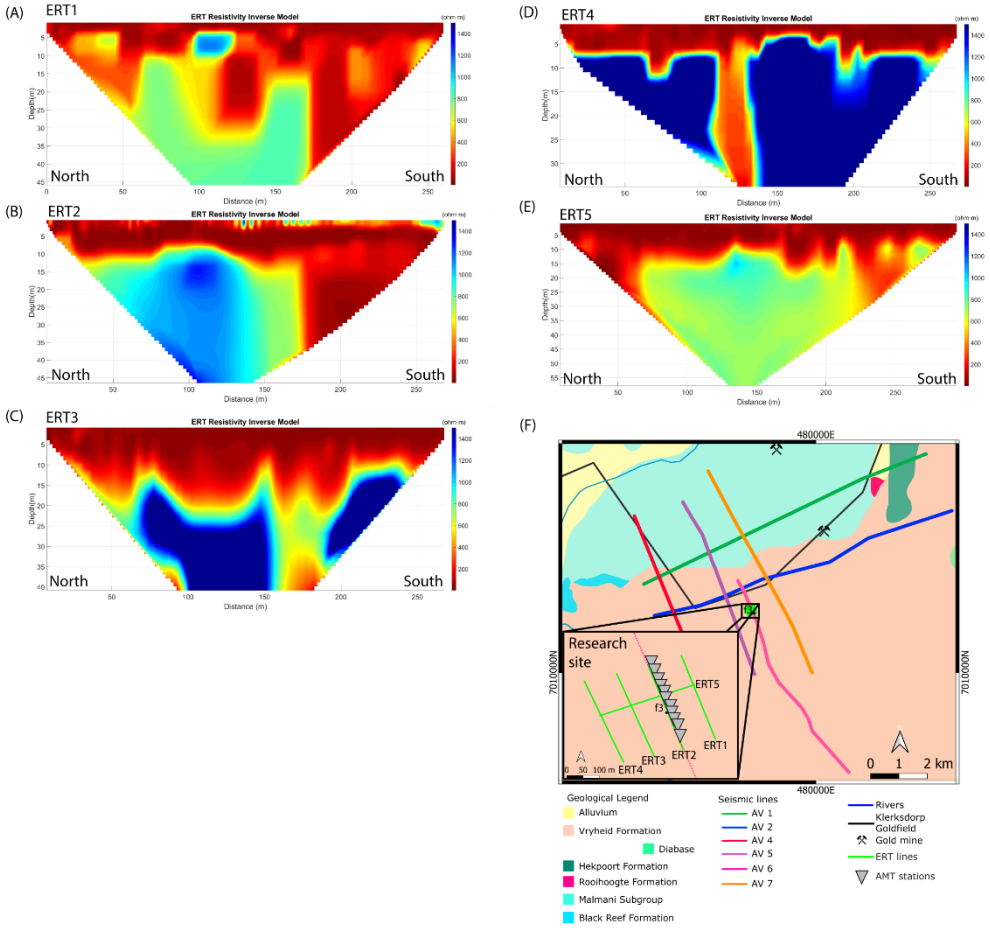


Figure 8.1. (A) ERT inverse model for ERT line: ERT1 with a root mean square error of 4.7. (B) ERT inverse model for ERT line: ERT2 with a root mean square error of 5. (C) ERT inverse model for ERT line: ERT3 with a root mean square error of 3.1. (D) ERT inverse model for ERT line: ERT4 with a root mean square error of 5.4. (E) ERT inverse model for ERT line: ERT5 with a root mean square error of 3.2. (F) ERT line locality map.

A.5. Publications

A.5.1. Conference abstracts

Conference abstracts resulting from the research completed in this thesis:

Harrison, W., Webb, S., (2017). Method Refinement of the DC Resistivity Method for Near Surface Exploration and Hazard Detection, presented at the 6th International Symposium in Three-Dimensional

Electromagnetics held from March 28-30, 2017, 3DEM-6, the University of California Berkeley, San Francisco, United Sates of America.

Harrison, W., Webb, S., (2017). DC Resistivity Noise Reduction Methods within Mining Environments, presentenced at the 12th Annual Africa Array Workshop held from 27 June - 1 July, 2017, School of Geosciences, University of the Witwatersrand, Johannesburg, South Africa.

Harrison, W., Webb, S., (2017). Method Refinement of the DC Resistivity Method for Near Surface Exploration and Hazard Detection, presented at the 15th SAGA Biennial Conference & Exhibition held from 10 - 13 September, 2017, Lord Charles Hotel, Cape Town, South Africa.

Harrison, W. and Webb, S., (2018), DC Resistivity and Magnetotellurics: efficient geophysical methods for evaluating ground water drilling sites for drought relief, presented at Geocongress held from 18-20 July, 2018, University of Johannesburg, South Africa.

Harrison, W. and Webb, S., (2018), Investigation of methods for determining DC static shift factors for MT corrections with application to a resistive dyke in the Bushveld Complex, South Africa, presented at the American Geophysical Union Fall Meeting held from 10-14 December, 2018, Walter E. Washington Convention Center, Washington, D.C., United Sates of America.

Harrison, W., Pellerin, L. and Webb, S., (2019), Geophysical Investigation of Lithological Groundwater Control on the Waterboerskraal Farm in the Semi-Arid Swartland Terrane, South Africa, presented at the 16th Saga Biennial Conference & Exhibition, held from 6-9 October, 2019, Elangeni & Maharani, Durban, South Africa.

A.5.2. Publications

Westgate, M., Musa, S. D. M., James. I., **Harrison, W.,** (2020), New insights from legacy seismic data: reprocessing of legacy 2D seismic data for imaging of iron oxide mineralisation near Sishen Mine, South Africa, Geophysical Prospecting, DOI: https://doi.org/10.1111/1365-2478.12996